Numerical approximation of thin structures using stabilized mixed formulations for Infinitesimal and Finite Strain theories, including Fluid-Structure Interaction problem applications

Universitat Politècnica de Catalunya - Barcelona Tech

Doctoral Program in Structural Analysis
Department of Civil & Environmental Engineering
School of Civil Engineering

Alejandro Aguirre Ruz
Advisors: Ramon Codina Rovira – Joan Baiges Aznar

April 16, 2024

To my wife, my family and for the animals

Contents

List of Figures

List of Tables

Abstract

The theories of thin structures can be classified into two main branches depending upon whether shear deformation in the transverse direction is taken into consideration or not. In this context, theories accounting for shear deformations prove suitable for modeling structures with both thin and thick profiles. However, when approximated by using the standard Finite Element method, numerical instabilities appear. These instabilities, known as numerical locking, result in an artificial stiffening of the structure, whose effect becomes more pronounced for thinner structures. Various forms of numerical locking can be triggered, influenced not only by the slenderness of the structure but also by its shape and the nature of the applied loads. In this context, flat structures are prone to shear locking when exposed to transverse loads. Conversely, curved structures may confront different mechanisms leading to various forms of numerical locking, namely membrane, thickness, and trapezoidal locking. This thesis mainly focuses on overcoming challenges associated with thin structures when employing the conventional Galerkin Finite Element approach and seeks solutions through stabilized methods, specifically within the Variational Multiscale framework.

The initial part of the study aims to develop a specialized framework to address instabilities of flat structures in the context of Reissner-Mindlin and Timoshenko theories. Subsequently, the second part of the study aims to expand the framework to effectively address instabilities arising in curved structures in the context of Solid-Shell elements. The locking problem is approached by means of a mixed formulation that considers displacements and stress as unknowns in a curvilinear coordinate framework. This approach allows to isolate the components of the stress tensor in order to study the mechanisms in which each type of numerical locking is triggered. The third part of the thesis is dedicated to integrating the previous developments into Finite Strain analysis by the inclusion of standard hyperelastic constitutive behavior. The complexity of the problem is higly increased in this case because of the non-linearity and the large deformations of the shell. Lastly, the fourth and final part is dedicated to addressing the Fluid-Structure Interaction problem using an embedded mesh approach, which has consistently been a frequent research topic in the literature because of its wide variety of applications. This problem introduces a variety of challenges that have to be properly addressed: the discontinuous pressure field arising for the structure separating the fluid domain, the computation and imposition of transmission conditions between domains, the coupling strategy, and the algorithmic work needed to join all of these ingredients together.

The formulations developed through the investigations have proven to be robust, allowing to model locking-free thin structures efficiently, and to accurately describe the physics of thin shells immersed in fluid flows and being subject to large deformations.

Resumen

Las teorías de estructuras delgadas pueden clasificarse en dos ramas principales dependiendo de si se tiene en cuenta o no la deformación por corte en la dirección transversal. Las teorías que tienen en cuenta las deformaciones por corte son adecuadas para modelar estructuras con perfiles tanto delgados como gruesos. En el contexto del Método de Elementos Finitos, se las denomina teorías C0, debido al orden mínimo de continuidad de las funciones de forma requerido para plantear una aproximación discretizada. Sin embargo, existen incompatibilidades espaciales en la aproximación discreta estándar que exhiben soluciones espurias, especialmente evidentes en estructuras delgadas. Estas inestabilidades, conocidas como bloqueo numérico, resultan en un endurecimiento artificial de la estructura, cuyo efecto se hace más pronunciado a medida que disminuye su espesor. Se pueden desencadenar varias formas de bloqueo numérico, influenciadas no solo por la esbeltez de la estructura, sino también por su forma y la naturaleza de las cargas aplicadas.

La parte inicial del estudio tiene como objetivo desarrollar un marco especializado para abordar las inestabilidades de estructuras planas usando la teoría de placas de Reissner-Mindlin. Posteriormente, la segunda parte del estudio tiene como objetivo expandir el marco para abordar eficazmente las inestabilidades que surgen en estructuras curvas usando elementos de tipo Solid-Shell. El problema de bloqueo se aborda mediante una formulación mixta que considera desplazamientos y tensiones como incógnitas en un marco de coordenadas curvilíneas. Este enfoque permite aislar los componentes del tensor de tensiones para estudiar los mecanismos en los que se desencadenan cada tipo de bloqueo numérico. La tercera parte de la tesis está dedicada a integrar los avances anteriores en el análisis de deformaciones finitas mediante la inclusión de un comportamiento constitutivo hiperelástico estándar. Con este enfoque, el problema se vuelve aún más difícil de resolver debido a la no-linealidad y las grandes deformaciones a las que está sujeta la estructura. Por último, la cuarta y última parte está dedicada a abordar el problema de Interacción Fluido-Estructura utilizando un enfoque de malla embebida, que ha sido consistentemente un tema de gran interés en la literatura debido a su complejidad y amplia variedad de aplicaciones. Este problema introduce una variedad de desafíos que deben abordarse adecuadamente: el campo de presión discontinuo que surge para la estructura separando el dominio del fluido, el cálculo y la imposición de condiciones de transmisión entre dominios, la estrategia de acoplamiento y el trabajo algorítmico necesario para unir todos estos ingredientes.

Esta tesis se centra principalmente en superar los desafíos asociados con estructuras delgadas al emplear método de Elementos Finitos de Galerkin. Busca soluciones a través de métodos estabilizados, específicamente dentro del marco Variacional Multiescala. Como resultado, las formulaciones desarrolladas a través de las investigaciones han demostrado ser robustas, lo que permite modelar eficientemente estructuras delgadas libres de bloqueo y describir con precisión la física de las láminas delgadas inmersas en flujos de fluidos y sujetas a grandes deformaciones.

Acknowledgments

First and foremost I shall express my most profound gratitude to my advisors Ramon Codina and Joan Baiges. I am sincerely grateful for the opportunity to work with them in pursuing my PhD. Their support has been invaluable to me, to the extent that I find myself wondering if I truly deserve such care. Their dedication to my training and personal growth is something that will stay with me forever. In return I have tried my best to live up to their teachings. In fact, I have devoted my utmost attention to every word and every scribble they have provided me, whether on loose sheets or on their blackboards. In fact, I believe I can recall everything in my mind, owing to how much thought I have given to each concept.

I would also like to thank all the members of the FEMUSS team and the people of C102 office, the fishbowl and the whole building. I am thankful to everyone, even to those who I did not work with, because not everything is about work, sometimes it is about having fun or simply being together. I thank Gabriel for all the bad jokes and compliments he provides in a daily basis, I thank my comrade Arnau for teaching me the love for chess even if he was not usually present, I thank Samuel for all the laughs and good vibes, I thank Carlinhos and his dog for being brazilian. I thank Ignacio for always being so nice to me, you always helped me a lot in everything. However, there are people that supported me so much that I must honor them properly. First of all, I would like to thank Laura, who was the first one to finish the PhD and physically leaving the office, but not before teaching me and helping me a lot in the moments when I needed it most. Dear Laura, I hold the belief that you possess exceptional qualities and attributes as a person, and you are also a great mathematician. Next I would like to thank Ino, who acted like a true brother for me. You supported me a lot with so much patience and expecting nothing in return. Without your support, none of this thesis would have been possible, you should be a co-author of this thesis. Lastly, the last part of the work would not have been possible without Ruben, you were really nice to me and you dedicated me a lot of your time, I will never forget that.

You are all great people and I would really enjoy to stay to see you every so often. But I have to leave.

That takes me to the next topic: the where. During our stay in Barcelona, we have met a lot of incredible people, who also give me strength to keep going. Those moments at the merken house with Valentina and Olaya were just unique and I will really miss them. To Oscar and Alican, who visited us and we visited them so many times, I am happy to see that we could strengthen our bonds, we will be waiting for you in Chile.

Speaking of returning, the acknowledgments cannot be complete without mentioning all the people who supported me from afar. I thank my parents Ismael and Sandra, my sisters Joce and Vilma, my brother Ismael, my sister in law Fernanda, my brother in law Carlos, my nephew Angel and my niece Renata, for always been there rooting for me, without your

support, I would have never been able to even get anywhere. I thank my grandmother Yorka for waiting all of this time, I know it was difficult, and I wanted to be with you when Juan left us. The acknowledgments cannot be complete without mentioning the in-law members of my family, thank you for your support Carlos, Lucia and Makako from the mountains, you have adopted me as a member of the family from the first moment we met. I want to mention my closest friends, who I also consider to be part of my family. Belen, my earliest friend, we have always been there for each other, I really miss spending time together. Axel, my adoptive brother, I think we have been synchronized in some manner since the first time we met. Rocio, my dear friend, you have always been attentive to my progress and rooting for me. Juan Pablo, my other adoptive brother, your friendship has always been invaluable for me, you may be the most reliable person I have ever met. Natalia Paz, I think my life would have been completely different if I had not met you, you gave me strength and advice when I needed it the most. I really want to see all of you again.

I also thank the person who initiated me to the world of research and gave me the opportunity to get a master's degree and later to pursue a PhD. Thank you Ernesto, you have been really important for me in many aspects of my life, you have helped me a lot in everything you have been able to. You made all of this possible, I will never forget what you have done for me, so consider yourself as a member of my family. I will honor your effort and dedication for me.

I want to close with the most important person in my life, my wife, my love. Camila, I will never forget the first time I saw you, the first time you held my hand, the moment we fell in love, the day we got married, and of course, our everyday life together. Who would have suspected that, not long after we met, you would build up courage and join the trip? I know it was hard, and I am really grateful to you in countless ways. I am glad we stood together from the beginning to the end of this long trip. I hope that this is only the first part of our journey, because I want to stay together with you until the very end. I really love you.

Introduction 1

1.1 Motivation

Throughout evolution, it becomes evident that most living organisms on Earth have evolved distinct mechanisms to efficiently manage specific loads, driven by necessity. This adaptation often takes the form of slender structures, chosen for their effectiveness in load-bearing while minimizing material usage. Consequently, thin structures stand out as the most prevalent architectural form in nature. In the same manner that a bird has ability to soar gracefully with its slender wings and lightweight physique, the sturdy support provided by towering trees allows them to stand with their lengthy, slender trunks and branches. Through exhaustive observation, rigorous study, and extensive testing, scientists have amassed knowledge and formulated theories that uncover the underlying principles governing the physics inherent in nature. This thesis work aims to create both theoretical frameworks and computer implementations for simulating and analyzing structural elements in engineering applications. The focal point of this effort is the advancement of Finite Element Method (FEM) technologies with special focus on its capability to effectively address the complexities associated with thin structures, encompassing beams, plates and shells.

1.2 Overview

The theories of thin structures can be classified into two main branches depending upon whether shear deformation in the transverse direction is taken into consideration or not. The reason to neglect transverse behavior during bending is because transverse strains diminish for thinner structures. Hence, theories neglecting shear deformation are confined to modeling particularly thin structures. Conversely, theories accounting for shear deformations prove suitable for modeling structures with both thin and thick profiles. In the Finite Element (FE) context, they are referred to as $C1$ and $C0$ theories, respectively, due to the minimum continuity order of shape

[1]: Oñate (2013), *Structural analysis with the finite element method. Linear statics: volume 2: beams, plates and shells*

functions required to pose a discretized approximation [1]. Due to the continuity requirements, the latter is typically the preferred choice in the existing literature, and it is also the approach adopted in the present study. However, standard Finite Element approximations of the equations of thin structures accounting for shear deformation exhibit spurious numerical oscillations„ particularly evident in thin structures. These instabilities, known as *numerical locking*, practically result in an artificial stiffening of the structure, with the effect becoming more pronounced for thinner structures. Various forms of numerical locking can be triggered, influenced not only by the slenderness of the structure but also by its shape and the nature of the applied loads. In this context, flat structures are prone to shear locking when exposed to transverse loads. Conversely, curved structures may confront different mechanisms leading to various forms of numerical locking, namely membrane, thickness, and trapezoidal locking.

This thesis mainly focuses on overcoming challenges associated with shear deformable structures when employing the conventional Galerkin FE approach. It seeks solutions through stabilized methods, specifically within the Variational Multiscale (VMS) framework. The VMS framework was firstly introduced by Hughes in the nineties [2, 3]. The initial part of the study aims to develop a specialized framework to address instabilities in the context of flat structures. Subsequently, the second part of the study aims to expand the framework to effectively address instabilities arising in the context of curved structures.

[2]: Hughes (1995), *Multiscale phenomena: Green's functions, the Dirichlet-to-Neumann formulation, subgrid scale models, bubbles and the origins of stabilized methods*

[3]: Hughes et al. (1998), *The variational multiscale method - A paradigm for computational mechanics*

Successfully overcoming the initial challenge of numerical locking opens the path for a multitude of research possibilities. However, considering the necessity to delimit the thesis scope, a specific path must be chosen. Building on the study of numerical locking, a logical next step would be to address the numerical locking associated with incompressibility. This concern extends beyond thin structures as it is also a recurrent topic within solid mechanics fields. Nevertheless, there have already been developments that can handle the incompressible limit with ease [4]. Another possibility would be to address material anisotropy by refining existing implementations to accommodate distinct material properties. This can be achieved by taking advantage of the locally defined coordinate systems typically used in structural mechanics [5]. An interesting option could also be to apply the

[4]: Castañar et al. (2020), *A stabilized mixed finite element approximation for incompressible finite strain solid dynamics using a total Lagrangian formulation*

[5]: Valdés Vázquez (2007), *Nonlinear Analysis of Orthotropic Membrane and Shell Structures Including Fluid-Structure Interaction.*

developments in conjunction with a Fluid Dynamic solver to study coupled problems involving aerodynamically-induced fluttering [6]. While various potential applications arise in the field of renewable energies [7] and structural analysis [8], the infinitesimal strain approach is very restrictive for more comprehensive research purposes.

[6]: DOWELL (1966), *Nonlinear oscillations of a fluttering plate.*

[7]: McCarthy et al. (2016), *Fluttering energy harvesters in the wind: A review*

[8]: Bueno et al. (2015), *Flutter analysis including structural uncertainties*

A more faithful continuation, aligned with the developments thus far and also expanding the research scopes, would be addressing non-linearity. Although infinitesimal strain theory has a wide variety of applications in fields like construction, aerodynamics, hydrodynamics and automotive engineering, most fields would greatly benefit from incorporating highly flexible elements into the structural analysis. Therefore, the third part of the thesis is dedicated to integrating the earlier advancements into Finite Strain analysis [9]. For this matter, the inclusion of standard hyperelastic constitutive behavior is considered, which introduces several difficulties to the FE analysis. Firstly, it introduces the need of treating the non-linear terms in the equations through a linearization process. Consequently, the problem requires to be solved through small increments and correction steps. Secondly, the initial and current configurations of the deformation process are not necessarily the same. Therefore, the deformation gradient cannot be approximated as the identity, implying that the constitutive tensor is not constant. It is crucial to ensure that the Jacobian, computed as the determinant of the deformation gradient, remains positive across the entire domain to avoid non-physical results [10]. Consequently, both the constitutive tensor and Jacobian have to be computed element wise across the domain with each iteration.

[9]: Belytschko et al. (2014), *Nonlinear finite elements for continua and structures*

[10]: Bonet et al. (1997), *Nonlinear continuum mechanics for finite element analysis*

With the first three parts of the thesis being successful in addressing the linear infinitesimal strain and non-linear finite strain approach, with flat and curved elements, there are several analysis tools at our disposal. Considering the implementations developed during the investigation, the fourth and final part is dedicated to addressing the Fluid-Structure Interaction (FSI) problem. This decision is justified for several reasons. Over the years, the FSI problem has consistently been a topic of great research interest that is always worth to explore. In that sense, from a practical perspective, it would be wise to exploit the fluid mechanics solver already available in the research group's code. From the implementation point of view, beams, plates, rods and shells are usually modeled as volumeless bodies [11], making them suitable for addressing

[11]: Bischoff et al. (2004), *Models and finite elements for thin-walled structures*

the FSI problem using an embedded mesh approach instead of a body fitted one. Lastly, developing a tool to properly couple structural elements to other physical problems would extend the future research possibilities even further.

1.3 Goals

The goal of this thesis is to develop new numerical schemes, formulations and techniques to address the analysis of slender structural elements, considering infinitesimal and finite strains and fluid-structure interaction. These numerical schemes are all based on the Finite Element Method, and the stabilization techniques are developed in the Variational Multiscale (VMS) framework. All the developments are implemented in FEMUSS (Finite Element Using Subgrid Scales), a High Performance Computing Environment code.

The investigation has been organized in a manner that the mathematical and computational developments have continuity. Therefore, the previous advances serve as a background of the next ones. Consequently, the objectives of the thesis are organized as follows:

- To develop an efficient and accurate strategy to handle structural analysis of thin structures involving the numerical locking of plate and beam elements, based on the Reissner-Mindlin and Timoshenko theories.
- To develop a robust locking-free structural analysis strategy involving shell structures, based on the construction of Solid-Shell elements using a mixed formulation and taking into consideration the effect of the domain curvature.
- To extend the Solid-Shell approach for structural analysis to handle Finite Strain deformations of hyperelastic materials.
- To couple the the Finite-Strain Solid-Shell solver to a Fluid Mechanics solver by using an embedded mesh approach to solve Fluid-Structure Interaction problems.

1.4 Expected impact

The impact of this thesis can be delineated into two main contributions: scientific and industrial. Scientifically, the advancements presented in this research significantly contribute to the state of the art in thin structures, namely beams, plates, rods, and shells. The introduced novel approaches not only compete with traditional methods but also offer additional benefits, including enhanced computational stability and improved result accuracy. From an industrial perspective, the developments align with the needs in the analysis and design of structures across various engineering fields. The advancements introduced in this research align with the technology provided by existing Finite Element software, offering reliable precision and accuracy in results, making it a viable option for easy incorporation.

1.5 Outline

The content of the thesis is organized in four self-contained but interrelated chapters that have been developed progressively, presented as follows:

- **Chapter 2: Stabilized formulations for Reissner-Mindlin plates and Timoshenko beams**
  This chapter focuses on the development of a novel formulation for flat structural elements based on the Reissner-Mindlin plate and Timoshenko beam theories. These theories are known for their low requirement of continuity in their interpolation, but also for being subject to shear-locking at high slenderness ratios. The stabilized formulations are based on the Variational Multiscale framework, and are designed through numerical analysis to eliminate shear-locking and enhance their overall performance.
- **Chapter 3: Stress-displacement formulations for Solid-Shell Finite Elements**
  The previously discussed theories for thin structures do not take into account the effects of curvature into the analysis. This limitation is overcome by shifting the approach to a solid-shell finite element approximation. This chapter is a comprehensive study on the nature and mechanisms that trigger numerical locking

effects inherent to solid-shell elements, namely shear, thickness, membrane and trapezoidal locking. As a solution, a mixed formulation that consider displacements and stress as unknowns is implemented. Due to incompatibility of spaces between these two variables, a stabilization technique, based on the Variational Multiscale framework, has been employed. The study shows how the approximation of each component of the stress tensor resolves each one of the locking effects. Results prove the necessity of using a mixed formulation to properly address them, resulting in a locking- free formulation.

- **Chapter 4: Finite strain hyperelasticity formulations for Solid-Shell Finite Elements**
  The mixed formulation approach has proven to be a proper approach to deal with numerical locking in solid-shell elements. Consequently, the mixed formulation is extended to a non-linear Finite-Strain formulation for hyperelastic materials. The aim of introducing stabilization is to obtain a robust formulation that greatly enhances the accuracy of the stress field in the approximations.
- **Chapter 5: Embedded Fluid-structure interaction problems using discontinuous functions**
  Considering the improvements in accuracy of the mixed formulation for Finite-Strain deformations, the approach is now extended to solve Fluid-Structure Interaction problems. The proposed approach utilizes an embedded mesh method to establish a coupling interface between the fluid and structural domains. The approach requires several tools for its implementation. Nevertheless, the presented framework proves to be robust even for highly flexible bodies and is able to handle complex flow environments.
- **Chapter 6: Conclusion**
  To finalize, the achievements of the research and the final concluding remarks are summarized.

Every chapter is based on scientific papers, implying that all of them are self-contained; therefore, they are independent of each other in terms of content. As consequence, some information is repeated between chapters for better readability and understanding. Likewise, conclusions related to the specific contents of each chapter are pointed out at the end of them.

1.6 Research dissemination

This manuscript gathers most of the developments performed during the PhD research. The following lists organize the original contributions of this manuscript depending on the relation with the thesis.

1.6.1 Conference proccedings

The advances and results of the research have been presented in the following international and specialized conferences:

- ”Formulación estabilizada de tipo Variational Multiscale para placas de Reissner- Mindlin y vigas de Timoshenko” In *XIX Jornadas de Mecánica Computacional.* October 7-8, 2021, Valparaiso, Chile.
- ”Stabilized finite element formulations for Reissner-Mindlin plates and Timoshenko beams based in the VMS framework”. In *Congress in Numerical Methods in Engineering (CMN).* September 12-14, 2022, Las Palmas de Gran Canaria, Spain.

1.6.2 Scientific journal papers

- “A variational multiscale stabilized finite element formulation for Reissner-Mindlin plates and Timoshenko beams”. Published in *Finite Elements in Analysis and Design. 2023, vol. 217, p. 103908.* https://doi.org/10.1016/j.finel.2023.103908.
- “Stress-displacement stabilized finite element analysis of thin structures using solid-shell elements-Part I: On the need of interpolating the stresses”
  To appear in in *Finite Elements in Analysis and Design.*
- “Stress-displacement stabilized finite element analysis of thin structures using solid-shell elements-Part II: Finite strain hyperelasticity”
  Submitted.
- ”Fluid-structure interaction approximation with embedded solid-shell finite elements using discontinuous shape functions”
  Submitted

1.7 FEMUSS

All algorithms developed in this thesis are implemented within FEMUSS (Finite Element Method Using Subgrid Scales), an object-oriented, Fortran-based finite element code. FEMUSS adopts a modular approach for multiphysics interaction and conducts parallel computations under MPI directives, establishing a High-Performance Computing (HPC) environment. It has a modular structure that allows for an easy driver-oriented coupling strategies between different physical problems, including fluid dynamics modules for incompressible and compressible equations, waves, low Mach models, etc., solid mechanics modules for beams, plates, shells, compressible and incompressible materials, etc., and thermal problems, among others.

FEMUSS makes use of PETSc, a suite of data routines and algorithms designed for scalable (parallel) solution of applications modeled by Partial Differential Equations (PDEs). PETSc incorporates a broad range of parallel linear solvers that can be integrated with different application codes. FEMUSS utilizes PETSc not only as a solver library but also as a partitioner and communicator among subdomains, owing to its diverse capabilities. Interaction between FEMUSS and PETSc is facilitated through an abstract and independent interface, enabling effortless substitution of PETSc with alternative libraries if needed, such as Trilinos.

For preprocessing, GiD, a processing system for computer analysis in science and engineering developed by CIMNE, is employed [12]. Postprocessing tasks can be either performed by GiD or by utilizing Paraview through the VTK library.

[12]: Melendo et al. (2018), *www.gidhome.com*

A key strength of FEMUSS, being predominantly a research-oriented code, lies in its straightforward code organization and accessibility, facilitating the integration of new models and algorithms. Consequently, it is continually evolving; implementing new formulations necessitates additional enhancements that align with the objectives of the research group.

Stabilized formulations for Reissner-Mindlin plates and Timoshenko beams

2

2.1 Abstract

The theories for thick plates and beams, namely Reissner-Mindlin's and Timoshenko's theories, are well known to suffer numerical locking when approximated using the standard Galerkin finite element method for small thicknesses. This occurs when the same interpolations are used for displacement and rotations, reason for which stabilization becomes necessary. To overcome this problem, a Variational Multiscale stabilization method is analyzed in this paper. In this framework, two different approaches are presented: the Algebraic Sub-Grid Scale formulation and the Orthogonal Sub-Grid Scale formulation. Stability and convergence is proved for both approaches, explaining why the latter performs much better. Although the numerical examples show that the Algebraic Sub-Grid Scale approach is in some cases able to overcome the numerical locking, it is highly sensitive to stabilization parameters and presents difficulties to converge optimally with respect to the element size in the L^2 norm. In this regard, the Orthogonal Sub-Grid Scale approach, which considers the space of the sub-grid scales to be orthogonal to the finite element space, is shown to be stable and optimally convergent independently of the thickness of the solid. The final formulation is similar to approaches developed previously, thus justifying them in the frame of the Variational Multiscale concept.

2.2 Introduction

In the context of computational mechanics, plates and beams are structural elements that are able to represent three dimensional objects in which the length of one or two of its dimensions is significantly smaller than the others. This dimensional reduction allows engineers to model complex structures at the cost of introducing rotations as independent variables. The Reissner-Mindlin equations are commonly used to describe the behavior of thin and moderately thick plates under transverse loads. This model differs from the Poisson-Kirchhoff equations for thin plates by considering the shear deformations due to distortion. In a physical sense, it is assumed that a straight line normal to the undeformed middle plane will remain straight but not necessarily perpendicular to the middle plane after deformation. The same analogy applies to the Timoshenko equations for thin-thick beams, with respect to the Euler-Bernoulli equations for thin beams. This leads to two groups of equations: the thin-thick theories, referred to as Reissner-Mindlin plates and Timoshenko beams, and the thin theories, referred to as Poisson-Kirchhoff plates and Euler-Bernoulli beams.

This paper is focused on the Finite Element (FE) stabilization of thin-thick theories of plates and beams, founded on the fact that applications in engineering usually fall into this category, and in the interest of using C^0 interpolations for displacement and rotations that are not possible using thin theories. In this context, both in Reissner-Mindlin plate and Timoshenko beam theories, the thickness of the structure appears explicitly in the partial differential equations, which results in a dominance of the shear term as it tends to the slender limit case. This fact together with the zero shear strain constraint leads to *numerical locking* when the equations are solved using the same interpolation for deflection and rotations, and it is the reason it needs to be stabilized. In the case of beams, the way locking occurs can be explicitly analyzed from the stiffness matrix of the elements [13].

[13]: Rakowski (1990), *The interpretation of the shear locking in beam elements*

A considerable amount of work has been put into the design of *locking-free* elements, namely that the order of convergence does not depend on the thickness of the structure. The existing approaches can be classified depending on whether or not the problem is dealt with in the irreducible form or if the shear strain is interpolated as an additional variable

of the problem, which alleviates the zero shear constraint. In the irreducible approach, the equations are presented in terms of deflections and rotations only, and if these equations are discretized using standard polynomial spaces, the numerically simulated structure behaves with a stiffness larger than it should for small thicknesses [1]. This pure numerical response is known as numerical locking, and for this particular case, it is often called *shear-locking* because it occurs due to the inability to reproduce a zero shear strain field. In that regard, the numerical locking will occur for any loading that results in a pure bending state of the structure. On the other hand, the mixed formulation approach consists in interpolating the shear strain from the constitutive equations as an additional unknown. This can be extended, although not necessarily, to the dual-mixed formulation by also interpolating the bending strain. This type of implementations is used to avoid restrictive constraints; however, they are inf-sup deficient and also require stabilization. For a better understanding of the FE approach to plates the reader can refer to [14, 15].

The most common approach used to solve the problem, independently of which variables are interpolated, is to use MITC (Mixed Interpolation of Tensorial Components) elements, that allows one to use different interpolations for each unknown. These approaches have been, and are still being developed for different types of problems [16, 17]. The reader can refer to [18] for a general overview, and also to [19] for a general analysis of the design procedure of MITC elements based on the velocity-pressure pair of the Stokes problem. The main challenge of this approach is to develop a stabilized formulation that converges optimally for every unknown using the lowest possible order of interpolation. A good insight of this in relation to the plate problem can be followed from [20], where it was established that shear stress is convergent if the bending moment converges at a high enough rate. This led to further developments using a variational approach [21] that was valid for any element of high enough order of interpolation for MITC elements, limited to using at least quadratic interpolations for the displacements. This limitation was improved in [22] by adding some consistent terms to the formulation. This type of elements has also been extended to shells [23], although some sort of stabilization is also required in this framework [24].

A search of the literature shows that another common method-

[1]: Oñate (2013), *Structural analysis with the finite element method. Linear statics: volume 2: beams, plates and shells*

[14]: Bathe (2001), *The inf–sup condition and its evaluation for mixed finite element methods*

[15]: Chapelle et al. (2010), *The finite element analysis of shells-fundamentals*

[16]: Durán et al. (1992), *On mixed finite element methods for the Reissner-Mindlin plate model*

[17]: Lovadina (1998), *Analysis of a mixed finite element method for the Reissner-Mindlin plate problems*

[18]: Falk et al. (2000), *Locking-free finite elements for the Reissner-Mindlin plate*

[19]: Brezzi et al. (1989), *Mixed-interpolated elements for Reissner–Mindlin plates*

[20]: Hughes et al. (1988), *Convergence of transverse shear stresses in the finite element analysis of plates*

[21]: Hughes et al. (1988), *A mixed finite element formulation for Reissner-Mindlin plate theory: Uniform convergence of all higher-order spaces*

[22]: Stenberg (1995), *A new finite element formulation for the plate bending problem*

[23]: Lee et al. (2004), *Development of MITC isotropic triangular shell finite elements*

[24]: Veiga et al. (2007), *Towards improving the MITC6 triangular shell element*

ology to treat shear-locking is by using different types of selective integration [25, 26]. This, however, is limited to particular element shapes and element orders (for example for bilinear quads), but it is not a general approach. Stabilization of shear locking can be achieved through many different approaches such as using Lagrange multipliers [27, 28], non-conforming method approaches [29, 30] which have also been a common topic of discussion, or discontinuous Petrov-Galerkin methods [31, 32], to name a few. Another approach was taken in [33], where the dual mixed formulation was stabilized using inter-elemental jumps of the unknowns. This approach provides optimal convergence of all the unknowns using linear interpolations only. A completely different approach was followed in [34], where a locking-free formulation is obtained from general polygonal space discretization rather than from standard finite elements.

Another methodology consists in formulating the stabilization from the multiscale perspective. It started from the introduction of the Galerkin-Least Squares method [21] and was further developed in [35]. Another least-squares type formulation was developed in [36] by introducing stabilization terms using the shear stress computed from the equilibrium equations. A rather different approach was used in [37], where a preconditioner was obtained using a multigrid method that was initially proposed in [38], where a conjugate gradient iterative algorithm was used to solve the linear system. The mixed formulation was also solved in [39] by introducing different interpolations for bending and shear effects. Also, in [40] a method was developed using a modified version of the formulation presented in [41], where an additional term was added to the mixed form. A similar approach to one of the stabilization methods to be described in the following was adopted in [42], in particular applied to the Discrete Shear Gap (DSG) formulation, which was already designed to avoid shear locking.

In this paper, the Reissner-Mindlin plate and the Timoshenko beam problems are addressed using the Variational Multiscale (VMS) method, a framework to develop stabilized formulations originally introduced in [2, 3]. In these formulations, the original Galerkin formulation is modified as little as possible using residual-based terms, making it consistent. The stabilized formulations presented in this paper share some characteristics with other formulations presented in the literature, such as [15, 18, 22]; however, the final outcome is not

[25]: Lepe et al. (2014), *Locking-free finite element method for a bending moment formulation of Timoshenko beams*

[26]: Toolabi et al. (2018), *Enhanced mixed interpolation XFEM formulations for discontinuous Timoshenko beam and Mindlin-Reissner plate*

[27]: Darrall et al. (2014), *Finite element Lagrange multiplier formulation for size-dependent skew-symmetric couple-stress planar elasticity*

[28]: Veiga et al. (2013), *Numerical analysis of a locking-free mixed finite element method for a bending moment formulation of Reissner-Mindlin plate model*

[29]: Brezzi et al. (2003), *A nonconforming element for the Reissner–Mindlin plate*

[30]: Chinosi et al. (2006), *Non-conforming locking-free finite elements for Reissner–Mindlin plates*

[31]: Calo et al. (2014), *Analysis of the discontinuous Petrov–Galerkin method with optimal test functions for the Reissner–Mindlin plate bending model*

[32]: Führer et al. (2021), *A locking-free DPG scheme for Timoshenko beams*

[33]: Barrenechea et al. (2015), *Stabilised finite element methods for a bending moment formulation of the Reissner-Mindlin plate model*

[34]: Videla et al. (2019), *A new locking-free polygonal plate element for thin and thick plates based on Reissner-Mindlin plate theory and assumed shear strain fields*

[35]: Peisker (1991), *A multigrid method for Reissner-Mindlin plates*

[36]: Kouhia (2008), *On stabilized finite element methods for the Reissner–Mindlin plate model*

[37]: Schöberl et al. (2009), *Multigrid methods for a stabilized Reissner–Mindlin plate formulation*

exactly the same and the motivation to derive the methods we propose is completely different [43].

The paper is organized as follows: A brief overview of the physical problem is presented in section 2.3 and the variational form is given in section 2.4. The general form of the stabilized FE formulation is explained in section 2.5 and its implementation for the plate and beam problems is presented in section 2.6. The numerical analysis in which the method is proven to be stable and convergent is presented in section 2.7 and lastly, numerical results are shown in section 2.8.

2.3 Continuous boundary value problem

Consider a general definition of the transverse deflection w and the rotation $\boldsymbol{\theta}$ of a structure. In the case of plates, the rotation is a vector that contains the rotations that make it bend in the x and y directions as $\boldsymbol{\theta} = \left[\theta_x, \theta_y\right]$. Since the beam problem is a dimensional reduction of the plate problem, a single rotation in the z direction is considered in this case, as $\boldsymbol{\theta} = \theta = \theta_z$.

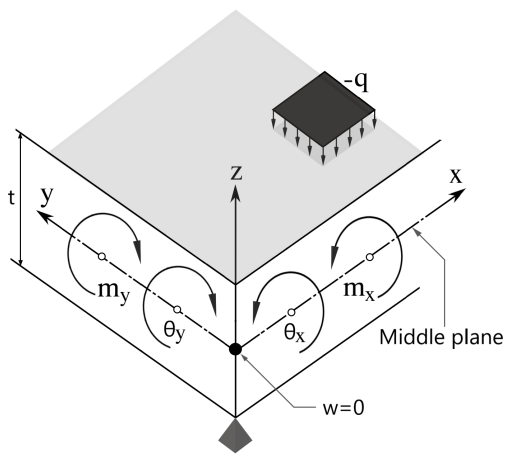

Figure 2.1: Coordinate system and definition of variables in plates.

In the problems presented below, the geometries and coordinate systems are defined under the convention presented in

[38]: Peisker et al. (1990), *Iterative solution methods for plate bending problems: multigrid and preconditioned cg algorithm*

[39]: Bathe et al. (1985), *A four-node plate bending element based on Mindlin/Reissner plate theory and a mixed interpolation*

[40]: Chapelle et al. (1998), *An optimal low-order locking-free finite element method for Reissner–Mindlin plates*

[41]: Arnold et al. (1993), *Some new elements for the Reissner-Mindlin plate model*

[42]: Bischoff et al. (2004), *Improving stability and accuracy of Reissner–Mindlin plate finite elements via algebraic subgrid scale stabilization*

[2]: Hughes (1995), *Multiscale phenomena: Green's functions, the Dirichlet-to-Neumann formulation, subgrid scale models, bubbles and the origins of stabilized methods*

[3]: Hughes et al. (1998), *The variational multiscale method - A paradigm for computational mechanics*

[43]: Codina (2000), *Stabilization of incompressibility and convection through orthogonal sub-scales in finite element methods*

Figs. 2.1-2.2. Only beams in the plane will be considered, the extension to 3D beams being straightforward.

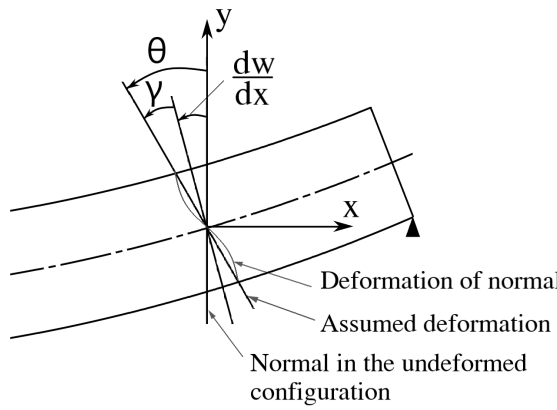

Figure 2.2: Coordinate system and definition of variables in beams.

Let us define a domain in a general manner as Ω and its boundary $\Gamma = \partial\Omega$. Then Ω can be particularized for plates as $\Omega = \Omega_P$ and for beams as $\Omega = \Omega_B$, with their corresponding boundaries Γ_P and Γ_B. The irreducible form of the Reissner-Mindlin plate problem consists in finding $\mathbf{u} = [\boldsymbol{\theta}, w]$ in the domain Ω_P of $\mathbb{R}^2$ with boundary Γ_P as the solution to

Reissner-Mindlin plate equations

$$-k_1\Delta\boldsymbol{\theta} - k_2\nabla(\nabla\cdot\boldsymbol{\theta}) - \frac{1}{\varepsilon}(\nabla w - \boldsymbol{\theta}) = \mathbf{m} \quad \text{in } \Omega_P, \tag{2.1}$$

$$-\frac{1}{\varepsilon}\nabla\cdot(\nabla w - \boldsymbol{\theta}) = q \quad \text{in } \Omega_P, \tag{2.2}$$

$$w = 0 \quad \text{in } \Gamma_P, \tag{2.3}$$

$$\boldsymbol{\theta} = \mathbf{0} \quad \text{in } \Gamma_P, \tag{2.4}$$

for properly defined external loading moments $\mathbf{m} = [m_x, m_y]$, transverse loads q and

$$k_1 = \frac{Et^3}{24(1+\nu)}, \qquad k_2 = \frac{Et^3}{24(1-\nu)}, \qquad \varepsilon = \frac{2(1+\nu)}{E\kappa t},$$

where E is the Young modulus, ν the Poisson ratio, t the thickness and κ the shear correction factor. In the development presented below, only homogeneous Dirichlet conditions are considered in (2.3) and (2.4), for simplicity. Note that $\varepsilon \to \infty$ as $t \to 0$. However, k_1 and k_2 are $O(t^3)$, whereas ε^{-1} is $O(t)$.

We have used the symbol ε^{-1} for the shear stiffness to emphasize that it dominates the bending stiffnesses as $t \to 0$.

Similarly, the Timoshenko beam problem consists in finding $\mathbf{u} = [\theta, w]$ defined in the domain Ω_B of $\mathbb{R}$ with boundary Γ_B such that

Timoshenko beam equations

$$-\frac{d}{dx}\left(EI\frac{d\theta}{dx}\right) - GA^*\left(\frac{dw}{dx} - \theta\right) = m \qquad \text{in} \quad \Omega_B, \tag{2.5}$$

$$-\frac{d}{dx}\left[GA^*\left(\frac{dw}{dx} - \theta\right)\right] = q \qquad \text{in} \quad \Omega_B, \tag{2.6}$$

$$w = 0 \qquad \text{in } \Gamma_B, \tag{2.7}$$

$$\theta = 0 \qquad \text{in } \Gamma_B, \tag{2.8}$$

where G is the shear modulus, I is the inertia in the bending axis, and A^* is the traverse reduced section area of the beam. The equilibrium equations are completed by the external moment, in this case $\mathbf{m} = m = m_z$, and external loads q. Comparing the beam and the plate equations, clearly EI plays the role of k_1 and k_2, whereas GA^* plays the role of ε^{-1}. Note that indeed both EI and k_1, k_2 are $O(t^3)$, whereas GA^* and ε^{-1} are $O(t)$, and the later become dominant when $t \to 0$.

It is important to mention that thick theories account for the shear strains $\boldsymbol{\gamma} := \nabla w - \boldsymbol{\theta}$, contrary to the $\boldsymbol{\gamma} = \mathbf{0}$ assumption of thin theories. Nevertheless, thick theories should converge to the corresponding thin theory solution when approaching the thin limit $t \to 0$.

Additional notation is necessary to build the formulations to be described below. Let us define, in a general manner, a linear differential operator $\mathscr{L}$, the trace operator $\mathscr{D}$ that makes the problem well defined, and a external force vector $\mathbf{f}$. Either the plate or beam problems can now be written as: find $\mathbf{u} : \Omega \to \mathbb{R}^n$ such that

$$\mathscr{L}\mathbf{u} = \mathbf{f} \qquad \text{in} \quad \Omega, \tag{2.9}$$

$$\mathscr{D}\mathbf{u} = \bar{\mathbf{u}} \qquad \text{on} \quad \Gamma. \tag{2.10}$$

For the problems we consider, $\mathscr{D}\mathbf{u}$ is just the trace of $\mathbf{u}$ on Γ. As it has been mentioned, we will take $\bar{\mathbf{u}} = \mathbf{0}$ for simplicity.

We can refer to the Reissner-Mindlin plate problem when $n = 3$, $\mathscr{L} = \mathscr{L}_{\mathrm{RM}}$ and $\mathbf{f} = \mathbf{f}_{\mathrm{RM}}$, given by

$$\mathscr{L}_{\mathrm{RM}}\mathbf{u} = \begin{bmatrix} -k_1\Delta\boldsymbol{\theta} - k_2\nabla(\nabla\cdot\boldsymbol{\theta}) - \frac{1}{\varepsilon}(\nabla w - \boldsymbol{\theta}) \\ -\frac{1}{\varepsilon}\nabla\cdot(\nabla w - \boldsymbol{\theta}) \end{bmatrix}, \tag{2.11}$$

$$\mathbf{f}_{RM} = \begin{bmatrix} \mathbf{m} \\ q \end{bmatrix}, \tag{2.12}$$

and to the Timoshenko beam problem when $n = 2$, $\mathscr{L} = \mathscr{L}_{\mathrm{T}}$ and $\mathbf{f} = \mathbf{f}_{\mathrm{T}}$, given by

$$\mathscr{L}_{\mathrm{T}}\mathbf{u} = \begin{bmatrix} -\frac{d}{dx}\left(EI\frac{d\theta}{dx}\right) - GA^*\left(\frac{dw}{dx} - \theta\right) \\ -\frac{d}{dx}\left(GA^*\left(\frac{dw}{dx} - \theta\right)\right) \end{bmatrix}, \tag{2.13}$$

$$\mathbf{f}_{\mathrm{T}} = \begin{bmatrix} m \\ q \end{bmatrix}. \tag{2.14}$$

To build the variational method below, it also is necessary to define the flux operator $\mathscr{F}$. Following the same notation as before, the flux operator corresponds to the Reissner-Mindlin problem when $\mathscr{F} = \mathscr{F}_{\mathrm{RM}}$, defined as

$$\mathscr{F}_{\mathrm{RM}}(\mathbf{u}) = \begin{bmatrix} k_1\mathbf{n}\cdot\nabla\boldsymbol{\theta} + k_2\mathbf{n}\nabla\cdot\boldsymbol{\theta} \\ \mathbf{n}\cdot\frac{1}{\varepsilon}(\nabla w - \boldsymbol{\theta}) \end{bmatrix}, \tag{2.15}$$

and to the Timoshenko beam problem when $\mathscr{F} = \mathscr{F}_{\mathrm{T}}$, given by

$$\mathscr{F}_{\mathrm{T}}(\mathbf{u}) = \begin{bmatrix} EI\frac{d\theta}{dx} \\ GA^*\left(\frac{dw}{dx} - \theta\right) \end{bmatrix}. \tag{2.16}$$

2.4 Variational Form

Consider $H^1(\Omega)$ as the space of functions in $L^2(\Omega)$ whose derivatives belong to $L^2(\Omega)$ and $H^1_0(\Omega)$ the subspace of $H^1(\Omega)$ of functions vanishing on Γ. In both specific problems, we denote the space of the deflection as $\mathscr{V} = H^1_0(\Omega)$; the space of the rotations $\mathscr{Q}$ will correspond to $\mathscr{Q} = H^1_0(\Omega)^2$ when referring to plates and to $\mathscr{Q} = H^1_0(\Omega)$ when referring to beams.

Let us denote by $(\cdot,\cdot)_\Omega$ the L^2-inner product and define $\langle\cdot,\cdot\rangle_\Omega$ as the integral of the product of two functions in Ω. We also denote as $\mathscr{X} = \mathscr{V}\times\mathscr{Q}$ the spaces where the weak problem is defined, whose test functions are $\mathbf{v} = [\boldsymbol{\phi}, v] \in \mathscr{X}$. Let us

introduce the bilinear form of the problem B and the linear form L as

$$B(\mathbf{u}, \mathbf{v}) = \langle \mathscr{L}\mathbf{u}, \mathbf{v} \rangle_\Omega + \langle \mathscr{F}\mathbf{u}, \mathscr{D}\mathbf{v} \rangle_{\partial\Omega}\,, \tag{2.17}$$

$$L(\mathbf{v}) = \langle \mathbf{f}, \mathbf{v} \rangle_\Omega\,. \tag{2.18}$$

With all the above, the general problem in (2.9) and (2.10) is equivalent to the weak form of the problem, which consists in finding $\mathbf{u} \in \mathscr{X}$ such that

$$B(\mathbf{u}, \mathbf{v}) = L(\mathbf{v}), \tag{2.19}$$

for all $\mathbf{v} \in X$.

2.5 Stabilized Finite Element Formulation

The standard FE discretization consists in taking a finite partition $\{K\}$ of the domain Ω. Let the functional space where the continuous problem is posed be denoted by $\mathscr{X}$ from which the constructed conforming FE space $\mathscr{X}_h$ is a subset. Then the Galerkin FE approximation consists in finding $\mathbf{u}_h \in \mathscr{X}$ such that

$$B(\mathbf{u}_h, \mathbf{v}_h) = L(\mathbf{v}_h) \qquad \forall\, \mathbf{v}_h \in \mathscr{X}_h. \tag{2.20}$$

The stabilized formulation analyzed in this paper is constructed in the VMS framework. The idea is to add additional terms to the Galerkin formulation of the problem that enhance stability without upsetting accuracy. This is achieved by splitting the space of unknowns as $\mathscr{X} = \mathscr{X}_h \oplus \mathscr{X}'$, where $\mathscr{X}_h$ is the part that can be solved in the FE space and $\mathscr{X}'$ is the remainder, or sub-grid scale, part. This leads to the splitting of the unknowns $\mathbf{u} = \mathbf{u}_h + \mathbf{u}'$ and test functions $\mathbf{v} = \mathbf{v}_h + \mathbf{v}'$. This splitting modifies the original formulation shown in (2.20) and turns the problem into: find $\mathbf{u}_h \in \mathscr{X}_h$ and $\mathbf{u}' \in \mathscr{X}'$ such that

$$B(\mathbf{u}_h, \mathbf{v}_h) + B(\mathbf{u}', \mathbf{v}_h) = L(\mathbf{v}_h) \qquad \forall\, \mathbf{v}_h \in \mathscr{X}_h, \tag{2.21}$$

$$B(\mathbf{u}_h, \mathbf{v}') + B(\mathbf{u}', \mathbf{v}') = L(\mathbf{v}') \qquad \forall\, \mathbf{v}' \in \mathscr{X}'. \tag{2.22}$$

The way this formulation is constructed requires an approximation of the sub-grid scales to be complete, which will be computed as a function of the FE part, as shown below. Note

that choosing $\mathcal{X}' = \{0\}$ yields the Galerkin method, making this method consistent by construction.

2.5.1 Sub-grid scales in the element interiors

At this point, the approximation requires to solve more variables than the initial problem. This is dealt with by modifying (2.21) by using the additivity of the integral and the identity of the bilinear operator:

$$\begin{aligned} B(\mathbf{u},\mathbf{v}) &= \sum_K \langle \mathscr{L}\mathbf{u},\mathbf{v}\rangle_K + \sum_K \langle \mathscr{F}\mathbf{u},\mathscr{D}\mathbf{v}\rangle_{\partial K} \\ &= \sum_K \langle \mathbf{u},\mathscr{L}^*\mathbf{v}\rangle_K + \sum_K \langle \mathscr{D}\mathbf{u},\mathscr{F}^*\mathbf{v}\rangle_{\partial K}\,, \end{aligned} \tag{2.23}$$

where the superscript * denotes the adjoint of an operator. In the current problems, the operators involved are self-adjoint, which means that $\mathscr{L}^* = \mathscr{L}$ and $\mathscr{F}^* = \mathscr{F}$; nevertheless, the superscript is left as a reference. In this manner, equation (2.21) can be written as

$$B(\mathbf{u}_h,\mathbf{v}_h) + \sum_K \left[\langle \mathbf{u}',\mathscr{L}^*\mathbf{v}_h\rangle_K + \langle \mathscr{D}\mathbf{u}',\mathscr{F}^*\mathbf{v}_h\rangle_{\partial K}\right] = L(\mathbf{v}_h). \tag{2.24}$$

Then the problem reduces to find a proper approximation for $\mathbf{u}'$. This can be achieved in (2.22) by approximating $\mathbf{u}'$ in terms of $\mathbf{u}_h$. We have that

$$\begin{aligned} B(\mathbf{u}',\mathbf{v}') &= L(\mathbf{v}') - B(\mathbf{u}_h,\mathbf{v}')\,, \\ &= L(\mathbf{v}') - \sum_K \left[\langle \mathscr{L}\mathbf{u}_h,\mathbf{v}'\rangle_K + \langle \mathscr{F}\mathbf{u}_h,\mathscr{D}\mathbf{v}'\rangle_{\partial K}\right], \\ &= \sum_K \left[\langle \mathscr{R}\mathbf{u}_h,\mathbf{v}'\rangle_K + \langle \mathscr{F}\mathbf{u}_h,\mathscr{D}\mathbf{v}'\rangle_{\partial K}\right], \end{aligned} \tag{2.25}$$

where $\mathscr{R}\mathbf{u}_h = \mathbf{f} - \mathscr{L}\mathbf{u}_h$ is the FE residual. For now let us impose that $\mathscr{D}\mathbf{u}' = \mathbf{0}$ on ∂K in an essential way, making the sub-grid scale test function satisfy $\mathscr{D}\mathbf{v}' = \mathbf{0}$ on ∂K. This yields the following approximation

$$\mathbf{u}' = \mathscr{L}^{-1}\left(\mathscr{R}\mathbf{u}_h + \mathbf{v}'^{\perp}\right), \tag{2.26}$$

where $\mathbf{v}'^{\perp}$ guarantees that $\mathbf{u}' \in X'$. In this expression, $\mathscr{L}^{-1}$ cannot be computed directly, so it is approximated element by element as

$$\mathbf{u}'\,|_K \approx \boldsymbol{\tau}_K\left(\mathscr{R}\mathbf{u}_h + \mathbf{v}'^{\perp}\right)|_K, \tag{2.27}$$

where $\boldsymbol{\tau}_K$ is a matrix that approximates $\mathscr{L}^{-1}$ on each element K. The function $\mathbf{v}'^{\perp}$ depends on the space of the sub-grid scales, so it can be written in a general form as

$$\mathbf{u}' \,|_K \approx \boldsymbol{\tau}_K P' \left(\mathscr{R}\mathbf{u}_h\right)|_K, \tag{2.28}$$

where P' is the L^2 projection onto the sub-grid scale space $\mathscr{X}'$ and $P' = I - P'^{\perp}$, with I being the identity in $\mathscr{X}$. This approximation allows us to rewrite the modified version of the problem in (2.24) as a function of the FE variables, making the number of unknowns to be the same as the original problem, as follows

$$B(\mathbf{u}_h, \mathbf{v}_h) + \sum_K \langle \boldsymbol{\tau}_K P' \left(\mathscr{R}\mathbf{u}_h\right), \mathscr{L}^* \mathbf{v}_h \rangle_K = L(\mathbf{v}_h). \tag{2.29}$$

From this point onwards, it only remains to choose a proper projection of the residual. A typical choice of the sub-grid scale space is the identity $P' = I$, leading to the Algebraic Sub-Grid Scale (ASGS) formulation, which means $\mathbf{v}'^{\perp} = \mathbf{0}$. Choosing $P' = I - P_h := P_h^{\perp}$, where P_h is the L^2 projection onto the FE space (including boundary conditions) yields the Orthogonal Sub-Grid Scale (OSGS) formulation, because it corresponds to taking $\mathscr{X}'$ as the orthogonal complement of $\mathscr{X}_h$.

2.5.2 Sub-grid scales in the element edges

The common procedure for the VMS formulation is to neglect the contribution of the sub-grid scales to the inter-element boundaries; however, enhanced stability properties can be achieved by considering them [44]. With the approach we follow, it is important to note that the sub-grid scales in the element interiors do not account for the boundary values, and the sub-grid scales in the inter-element boundaries have to be computed afterwards.

[44]: Codina et al. (2018), *Variational multiscale methods in computational fluid dynamics*

Let $E_h = \{E\}$ the collection of interior edges of the FE partition, and $\mathbf{u}'_E$ the sub-grid scale on edge E, assumed to be uniquely valued. The sub-grid scales on the edges of the boundary of Ω are taken as zero. Then, we may write equa-

tion (2.24) as:

$$B(\mathbf{u}_h, \mathbf{v}_h) + \sum_K \langle \mathbf{u}', \mathscr{L}^* \mathbf{v}_h \rangle_K + \sum_E \left\langle \mathbf{u}'_E, [\![\mathscr{F}^* \mathbf{v}_h]\!] \right\rangle_E = L(\mathbf{v}_h). \tag{2.30}$$

where $[\![\mathscr{F}^* \mathbf{v}_h]\!]$ denotes the jump of $\mathscr{F}^* \mathbf{v}_h$ across E, i.e., the sum of the values of $\mathscr{F}^* \mathbf{v}_h$ computed with the normals exterior to the elements that share edge E.

Imposing that the total fluxes are continuous across inter-element boundaries, it is argued in [45] that the sub-grid scales on the edges of the FE partition can be approximated by

$$\mathbf{u}'_E \approx -\frac{\delta}{2} [\![\mathscr{F} \mathbf{u}_h]\!],$$

[45]: Codina et al. (2009), *Subscales on the element boundaries in the variational two-scale finite element method*

where $\delta = \delta_0 h$ and δ_0 is a dimensionless algorithmic parameter. Combining this with (2.28) we obtain the stabilized FE formulation:

$$B(\mathbf{u}_h, \mathbf{v}_h) + \sum_K \langle \boldsymbol{\tau}_K P' (\mathscr{R} \mathbf{u}_h), \mathscr{L}^* \mathbf{v}_h \rangle_K - \sum_E \frac{\delta}{2} \langle [\![\mathscr{F} \mathbf{u}_h]\!], [\![\mathscr{F}^* \mathbf{v}_h]\!] \rangle_E = L(\mathbf{v}_h). \tag{2.31}$$

2.6 Implementation

In this subsection, the stabilized formulation of the Reissner-Mindlin plate and the Timoshenko beam theories are presented. To simplify the exposition, in this section we consider only linear elements, and thus higher order derivatives in the element interiors are not considered. Nevertheless, the case of arbitrary order of interpolation will be analyzed in the following section.

Let us first write the Galerkin FE form of each problem:

Galerkin finite element form of Reissner-Mindlin plate problem

$$k_1 (\nabla \boldsymbol{\theta}_h, \nabla \boldsymbol{\phi}_h) + k_2 (\nabla \cdot \boldsymbol{\theta}_h, \nabla \cdot \boldsymbol{\phi}_h) + \frac{1}{\varepsilon} (\nabla w_h - \boldsymbol{\theta}_h, \nabla v_h - \boldsymbol{\phi}_h) = \langle \mathbf{m}, \boldsymbol{\phi}_h \rangle + \langle q, v_h \rangle. \tag{2.32}$$

Galerkin finite element form of Timoshenko beam problem

$$EI\left(\frac{d\theta_h}{dx}, \frac{d\phi_h}{dx}\right) + GA^*\left(\frac{dw_h}{dx} - \theta_h, \frac{dv_h}{dx} - \phi_h\right) = \left\langle m,\ \phi_h \right\rangle + \left\langle q,\ v_h \right\rangle. \tag{2.33}$$

Consider α and β as the constants that multiply the shear and bending terms, respectively, namely $\alpha = GA^*$ and $\beta = EI$ for beams and $\alpha = \varepsilon^{-1}$, $\beta = Et^3/24$ for plates. In a general manner, the formulation yields a system of equations of the form

$$\begin{bmatrix} \alpha S_1 & \alpha S_2 \\ \alpha S_3 & \alpha S_4 + \beta B \end{bmatrix} \begin{bmatrix} W \\ \Theta \end{bmatrix} = \begin{bmatrix} F \\ M \end{bmatrix}, \tag{2.34}$$

where W and Θ are the displacements and rotations arrays, respectively, F is the array coming from the transverse loads, M from the bending moments, B and S_i ($i = 1, 2, 3, 4$) are the components arising from the bending and shear terms, respectively (with $S_3 = S_2^T$). These notations can refer to matrix arrays depending on the problem. The standard formulations gives a symmetric system that locks when $t \to 0$ and $S_i \gg B$ (the inequality being understood component-wise), while in the stabilized formulations presented below, the stabilization terms allow the system to avoid the dominance of one term over the other.

In the following, the stabilization matrices are taken to be diagonal, of the form $\boldsymbol{\tau}_K = \text{diag}(\tau_\theta, \tau_\theta, \tau_w)$ for plates and $\boldsymbol{\tau}_K = \text{diag}(\tau_\theta, \tau_w)$ for beams, where τ_θ and τ_w are still to be defined. It is understood that these parameters are evaluated element by element.

We will start writing the stabilized formulations without subgrid scales on the inter-element boundaries. These will be introduced later, as they are the same for both the ASGS and the OSGS formulations.

2.6.1 Algebraic Sub-Grid Scales

We first consider the ASGS formulation, which corresponds to $\mathbf{v}'^{\perp} = \mathbf{0}$. Then P' is the identity on the element residuals, and thus $\mathbf{u}' = \boldsymbol{\tau}_K[\mathbf{f} - \mathscr{L}\mathbf{u}_h]$ in each element K. The formulation for linear elements and assuming constant stabilization parameters (i.e., constant element sizes) reads:

ASGS stabilization of Reissner-Mindlin plate problem

$$k_1\left(\nabla\boldsymbol{\theta}_h,\nabla\boldsymbol{\phi}_h\right)+k_2\left(\nabla\cdot\boldsymbol{\theta}_h,\nabla\cdot\boldsymbol{\phi}_h\right)+\frac{1}{\varepsilon}\left(\nabla w_h-\boldsymbol{\theta}_h,\nabla v_h-\boldsymbol{\phi}_h\right)$$
$$-\frac{\tau_w}{\varepsilon^2}\sum_K\langle\nabla\cdot\boldsymbol{\theta}_h,\nabla\cdot\boldsymbol{\phi}_h\rangle_K-\frac{\tau_\theta}{\varepsilon^2}\sum_K\langle\nabla w_h-\boldsymbol{\theta}_h,\nabla v_h-\boldsymbol{\phi}_h\rangle_K=\langle\mathbf{m},\boldsymbol{\phi}_h\rangle+\langle q,v_h\rangle\,. \tag{2.35}$$

ASGS stabilization of Timoshenko beam problem

$$EI\left(\frac{d\theta_h}{dx},\frac{d\phi_h}{dx}\right)+GA^*\left(\frac{dw_h}{dx}-\theta_h,\frac{dv_h}{dx}-\phi_h\right)$$
$$-\tau_w\left(GA^*\right)^2\sum_K\left\langle\frac{d\theta_h}{dx}\,,\,\frac{d\phi_h}{dx}\right\rangle_K-\tau_\theta\left(GA^*\right)^2\sum_K\left\langle\frac{dw_h}{dx}-\theta_h\,,\,\frac{dv_h}{dx}-\phi_h\right\rangle_K=\left\langle m,\,\phi_h\right\rangle+\left\langle q,\,v_h\right\rangle. \tag{2.36}$$

In a general manner, their matrix version is

$$\begin{bmatrix}(\alpha-\tau_\theta\alpha^2)S_1 & (\alpha-\tau_\theta\alpha^2)S_2\\ (\alpha-\tau_\theta\alpha^2)S_3 & (\alpha-\tau_\theta\alpha^2)S_4+(\beta-\tau_w\alpha^2)B\end{bmatrix}\begin{bmatrix}W\\ \Theta\end{bmatrix}=\begin{bmatrix}F\\ M\end{bmatrix}. \tag{2.37}$$

This allows the system not to fall into shear dominance when $\boldsymbol{\tau}_K$ is properly designed. This part is crucial to obtain a locking-free formulation, and it will be explained below in more detail.

2.6.2 Orthogonal Sub-Grid Scales

For this approach, the sub-grid scales are computed considering the orthogonal component of the residual as $\mathbf{u}'=\boldsymbol{\tau}_K P^{\perp}[\mathbf{f}-\mathscr{L}\mathbf{u}_h]$ in each element K, i.e., $P'=P^{\perp}=I-P_h$. If we denote, in a general manner, $\boldsymbol{\xi}_h=[\boldsymbol{\xi}_\theta,\xi_w]$ to be the FE projections of the residual onto $\mathscr{X}_h$, and $\boldsymbol{\eta}_h=[\boldsymbol{\eta}_\theta,\eta_w]$ to be the respective test functions in $\mathscr{X}_h$, the formulations for plates and beams can be written as:

OSGS stabilization of Reissner-Mindlin plate problem

$$
\begin{aligned}
&k_1\left(\nabla\boldsymbol{\theta}_h,\nabla\boldsymbol{\phi}_h\right)+k_2\left(\nabla\cdot\boldsymbol{\theta}_h,\nabla\cdot\boldsymbol{\phi}_h\right)+\frac{1}{\varepsilon}\left(\nabla w_h-\boldsymbol{\theta}_h,\nabla v_h-\boldsymbol{\phi}_h\right)\\
&-\frac{\tau_w}{\varepsilon^2}\sum_K\langle\nabla\cdot\boldsymbol{\theta}_h,\nabla\cdot\boldsymbol{\phi}_h\rangle_K-\frac{\tau_\theta}{\varepsilon^2}\sum_K\langle\nabla w_h-\boldsymbol{\theta}_h,\nabla v_h-\boldsymbol{\phi}_h\rangle_K\\
&+\frac{\tau_w}{\varepsilon}\sum_K\langle\xi_w,\nabla\cdot\boldsymbol{\phi}_h\rangle_K+\frac{\tau_\theta}{\varepsilon}\sum_K\langle\boldsymbol{\xi}_\theta,\nabla v_h-\boldsymbol{\phi}_h\rangle_K=\langle\mathbf{m},\boldsymbol{\phi}_h\rangle+\langle q,v_h\rangle\,, \qquad (2.38)\\
&\frac{1}{\varepsilon}\left(\nabla\cdot\boldsymbol{\theta},\eta_w\right)-\left(\xi_w,\eta_w\right)=0, \qquad (2.39)\\
&\frac{1}{\varepsilon}\left(\nabla w_h-\boldsymbol{\theta}_h,\boldsymbol{\eta}_\theta\right)-\left(\boldsymbol{\xi}_\theta,\boldsymbol{\eta}_\theta\right)=0, \qquad (2.40)
\end{aligned}
$$

for all $[\boldsymbol{\phi}_h, v_h] \in X_h$ and $[\boldsymbol{\eta}_\theta, \eta_w] \in X_h$.

OSGS stabilization of Timoshenko beam problem

$$
\begin{aligned}
&EI\left(\frac{d\theta_h}{dx},\frac{d\phi_h}{dx}\right)+GA^*\left(\frac{dw_h}{dx}-\theta_h,\frac{dv_h}{dx}-\phi_h\right)\\
&-\tau_w(GA^*)^2\sum_K\left\langle\frac{d\theta_h}{dx}\,,\,\frac{d\phi_h}{dx}\right\rangle_K-\tau_\theta(GA^*)^2\sum_K\left\langle\frac{dw_h}{dx}-\theta_h\,,\,\frac{dv_h}{dx}-\phi_h\right\rangle_K\\
&+\tau_wGA^*\sum_K\left\langle\xi_w\,,\,\frac{d\phi_h}{dx}\right\rangle_K+\tau_\theta GA^*\sum_K\left\langle\xi_\theta\,,\,\frac{dv_h}{dx}-\phi_h\right\rangle_K=\left\langle m,\,\phi_h\right\rangle+\left\langle q,\,v_h\right\rangle, \qquad (2.41)\\
&GA^*\left(\frac{dw_h}{dx}-\theta_h\,,\,\eta_\theta\right)-\left(\xi_\theta\,,\,\eta_\theta\right)=0, \qquad (2.42)\\
&GA^*\left(\frac{d\theta_h}{dx}\,,\,\eta_w\right)-\left(\xi_w\,,\,\eta_w\right)=0, \qquad (2.43)
\end{aligned}
$$

for all $[\phi_h, v_h] \in X_h$ and $[\eta_\theta, \eta_w] \in X_h$.

For this formulation, the matrix version of the equations is:

$$
\begin{bmatrix}
(\alpha-\tau_\theta\alpha^2)S_1 & (\alpha-\tau_\theta\alpha^2)S_2 & \tau_\theta\alpha P_1^\theta & 0\\
(\alpha-\tau_\theta\alpha^2)S_3 & (\alpha-\tau_\theta\alpha^2)S_4+(\beta-\tau_w\alpha^2)B & \tau_\theta\alpha P_2^\theta & \tau_w\alpha P^w\\
\alpha Q_1^\theta & \alpha Q_2^\theta & N & 0\\
0 & \alpha Q^w & 0 & N
\end{bmatrix}
\begin{bmatrix} W\\ \Theta\\ \Xi_\theta\\ \Xi_w \end{bmatrix}=
\begin{bmatrix} F\\ M\\ 0\\ 0 \end{bmatrix}, \qquad (2.44)
$$

where N is the Gram matrix, P^w and P_i^θ $(i = 1, 2)$ are the

matrices containing ξ_w and ξ_θ, respectively, with the corresponding test function associated to the index. In the same manner, Q^w and Q_i^θ ($i = 1, 2$) are the matrices containing deflection and rotations terms, depending on the index, with the test functions of the projection equations. Note that the system can be symmetrized by multiplying the last two rows by τ_θ and τ_w, respectively, since $(Q_i^\theta)^T = P_i^\theta$, $i = 1, 2$.

The OSGS implementation yields a system that shares some similarities with the mixed form of the problem. The difference is that the later yields a saddle point problem that is usually addressed using a mixed interpolation of the unknowns [21]. Note that similar formulations have been obtained in [15, 18, 22], where the shear force is computed using the L^2 projection of the rotation onto the FE space in order to soothe the zero shear strain constraint of the problem, which differs from the sub-grid scale approach of the present work.

[21]: Hughes et al. (1988), *A mixed finite element formulation for Reissner-Mindlin plate theory: Uniform convergence of all higher-order spaces*

[15]: Chapelle et al. (2010), *The finite element analysis of shells-fundamentals*

[18]: Falk et al. (2000), *Locking-free finite elements for the Reissner-Mindlin plate*

[22]: Stenberg (1995), *A new finite element formulation for the plate bending problem*

The implementation given by Eq. (2.44) is useful for the presentation of the formulation, but in practice two other alternatives are possible eliminating the degrees of freedom of the projections. One is an iterative deffect-correction approach, evaluating these projections at the previous iteration when computing displacements and rotations and then updating them. The other is a condensation of the projections, which implies an increase of the stencil of the stiffness matrix. Both approaches are feasible because the matrix that multiplies the degrees of freedom of the rotations is a mass matrix, easily invertible (in a direct or in an iterative way). In this case, the formulation presented should be compared to those that do not introduce new variables, but solve only for displacements and rotations.

2.6.3 Inter-element edge stabilization

The stabilization using the sub-grid scales in the element edges can be implemented independently of the sub-grid scales in the element interiors, as stated in section 2.5. For the implementation, consider the terms from the sub-grid scale in the inter-element edges added to the Galerkin form of the problem. The resulting discrete problem is:

Reissner-Mindlin plate inter-element stabilization

$$
\begin{aligned}
&k_1\left(\nabla\boldsymbol{\theta}_h, \nabla\boldsymbol{\phi}_h\right) + k_2\left(\nabla\cdot\boldsymbol{\theta}_h, \nabla\cdot\boldsymbol{\phi}_h\right) + \frac{1}{\varepsilon}\left(\nabla w_h - \boldsymbol{\theta}_h, \nabla v_h - \boldsymbol{\phi}_h\right) \\
&-\frac{\delta k_1}{2}\sum_E \langle[\![\mathbf{n}\cdot\nabla\boldsymbol{\theta}_h]\!], [\![\mathbf{n}\cdot\nabla\boldsymbol{\phi}_h]\!]\rangle_E - \frac{\delta k_2}{2}\sum_E \langle[\![\mathbf{n}\nabla\cdot\boldsymbol{\theta}_h]\!], [\![\mathbf{n}\nabla\cdot\boldsymbol{\phi}_h]\!]\rangle_E \\
&\qquad -\frac{\delta}{2\varepsilon}\sum_E \langle[\![\mathbf{n}\cdot\nabla w_h]\!], [\![\mathbf{n}\cdot\nabla v_h]\!]\rangle_E = \langle \mathbf{m}, \boldsymbol{\phi}_h\rangle + \langle q, v_h\rangle . \qquad (2.45)
\end{aligned}
$$

Timoshenko beam inter-element stabilization

$$
\begin{aligned}
&EI\left(\frac{d\theta_h}{dx}, \frac{d\phi_h}{dx}\right) + GA^*\left(\frac{dw_h}{dx} - \theta_h, \frac{dv_h}{dx} - \phi_h\right) \\
&-\frac{\delta EI}{2}\sum_E \left\langle \left[\!\left[\frac{d\theta_h}{dx}\right]\!\right], \left[\!\left[\frac{d\phi_h}{dx}\right]\!\right] \right\rangle_E - \frac{\delta GA^*}{2}\sum_E \left\langle \left[\!\left[\frac{dw_h}{dx}\right]\!\right], \left[\!\left[\frac{dv_h}{dx}\right]\!\right] \right\rangle_E = \left\langle m,\ \phi_h \right\rangle + \left\langle q,\ v_h \right\rangle . \qquad (2.46)
\end{aligned}
$$

Recall that, in both problems, δ is a parameter of the order of the element size.

2.6.4 Stabilization parameters

The design of $\boldsymbol{\tau}_K$ is based on the definition proposed in [46] for the Reissner-Mindlin case, with some modifications. According to that work, shear dominance can be dealt with by just introducing the shear stabilization parameter τ_θ, and it was successful in that regard. However, convergence ratios were not tested. Taking this into consideration, the stabilization parameters are defined as

[46]: Codina (2000), *On stabilized finite element methods for linear systems of convection–diffusion-reaction equations*

Reissner-Mindlin plate stabilization parameters

$$
\begin{aligned}
\boldsymbol{\tau}_K &= \operatorname{diag}\left(\tau_\theta, \tau_\theta, \tau_w\right), \\
\tau_\theta &= \left(c_1\frac{k}{h^2} + c_2\varepsilon^{-1}\right)^{-1}, \\
\tau_w &= \left(c_3\frac{\varepsilon^{-1}}{h^2} + c_4\frac{\varepsilon^{-2}}{k}\right)^{-1}, \qquad (2.47)
\end{aligned}
$$

Timoshenko beam stabilization parameters

$$\begin{aligned}\boldsymbol{\tau}_K &= \operatorname{diag}(\tau_\theta, \tau_w),\\ \tau_\theta &= \left(c_1 \frac{EI}{h^2} + c_2 GA^*\right)^{-1},\\ \tau_w &= \left(c_3 \frac{GA^*}{h^2} + c_4 \frac{(GA^*)^2}{EI}\right)^{-1},\end{aligned} \tag{2.48}$$

where h is the element size, $k = k_1 + k_2$, and c_i, $i = 1, 2$ are constants to be defined. Note that in [46] the constant c_2 must be taken as $c_2 = 1$ to eliminate shear dominance; this is confirmed in the stability analysis in section 2.7. In [42] the ASGS formulation is used together with the DSG approach taking $\tau_w = 0$ and a similar expression of τ_θ to the one we propose, but taking also into account the possible anisotropy of the elements.

[42]: Bischoff et al. (2004), *Improving stability and accuracy of Reissner–Mindlin plate finite elements via algebraic subgrid scale stabilization*

To find which values of the stabilization constants can be used in the stabilization parameters, the matrix form of the equations using the ASGS formulation of (2.37) is compared to the exact solution of the elastic equations for the bending of an unloaded beam using Timoshenko's theory. Consider a two noded beam of length L, with nodal deflections w_i and rotations θ_i, for nodes $i = 1, 2$, and the corresponding nodal loads P_i and M_i. For $\mu = \frac{12EI}{GA^*L^2}$, the following system of equations is obtained:

$$\begin{bmatrix} \frac{12EI}{(1+\mu)L^3} & \frac{6EI}{(1+\mu)L^2} & -\frac{12EI}{(1+\mu)L^3} & \frac{6EI}{(1+\mu)L^2} \\ \frac{6EI}{(1+\mu)L^2} & \frac{(4+\mu)EI}{(1+\mu)L} & -\frac{12EI}{(1+\mu)L^2} & \frac{(2-\mu)EI}{(1+\mu)L} \\ -\frac{12EI}{(1+\mu)L^2} & -\frac{6EI}{(1+\mu)L^2} & \frac{12EI}{(1+\mu)L^2} & -\frac{6EI}{(1+\mu)L^2} \\ \frac{6EI}{(1+\mu)L^2} & \frac{(2-\mu)EI}{(1+\mu)L} & -\frac{12EI}{(1+\mu)L^2} & \frac{(4+\mu)EI}{(1+\mu)L} \end{bmatrix} \begin{bmatrix} w_1 \\ \theta_1 \\ w_2 \\ \theta_2 \end{bmatrix} = \begin{bmatrix} P_1 \\ M_1 \\ P_2 \\ M_2 \end{bmatrix}. \tag{2.49}$$

Comparing this system to the one obtained using the stabilized FE approximation we propose, we obtain that, in the ASGS formulation of beams, the stabilization constants can be taken as $c_1 = c_3 = 12$ and $c_2 = c_4 = 1$. In this case, the stiffness matrix of an element of length L is exactly the same as that of the elastic equations of a Timoshenko beam. The behavior of the FE formulation in response to this selection of constants as well as the constants used in the OSGS formulation will be discussed in section 2.8.

2.7 Numerical Analysis

In this section, the numerical analysis of the stabilized formulation for plates is analysed. The results are inherited by the beam problem since it is equivalent to the dimensional reduction of the plate problem.

Consider $\|\cdot\|$ to be the $L^2(\Omega)$ norm. Let us define some inequalities that will allow us to obtain a stability estimate. For simplicity, we will assume the FE partition to be quasi-uniform, of size h. We may thus assume that there is a constant C_{inv}, independent of the mesh size h, such that the following inverse estimate holds:

$$\|\nabla v_h\|_K \leq \frac{C_{\text{inv}}}{h}\|v_h\|_K, \tag{2.50}$$

for all FE functions v_h defined on the partition $\{K\}$. Similarly, the following trace inequality holds: there exists a a constant C_{trace} independent of h such that

$$\|v\|^2_{\partial K} \leq C_{\text{trace}}\left(\frac{1}{h}\|v\|^2_K + h\|\nabla v\|^2_K\right), \tag{2.51}$$

for functions $v \in H^1(K)$. In this expression, the last term is dropped if v is a polynomial on the element domain K.

Let now $E_h = \{E\}$ be the edges of the FE partition. For piecewise discontinuous polynomials φ_h and continuous polynomials ψ_h there holds:

$$\sum_E \| [\![\mathbf{n}\varphi_h]\!] \|^2_E \leq 2\frac{C_{\text{trace}}}{h}\sum_K \|\varphi_h\|^2_K, \tag{2.52}$$

$$\sum_E \|\psi_h\|^2_E \leq \frac{C_{\text{trace}}}{2h}\sum_K \|\psi_h\|^2_K. \tag{2.53}$$

In the following, C will denote a generic positive constant, not necessarily the same at different occurrences.

The stabilized FE formulation for elements of arbitrary polynomial degree can be written as:

$$B_{\text{stab}}(\mathbf{u}_h, \mathbf{v}_h) = L_{\text{stab}}(\mathbf{v}_h), \tag{2.54}$$

where

$$B_{\text{stab}}(\mathbf{u}_h, \mathbf{v}_h) = k_1 (\nabla\boldsymbol{\theta}_h, \nabla\boldsymbol{\phi}_h) + k_2 (\nabla\cdot\boldsymbol{\theta}_h, \nabla\cdot\boldsymbol{\phi}_h) + \frac{1}{\varepsilon}(\nabla w_h - \boldsymbol{\theta}_h, \nabla v_h - \boldsymbol{\phi}_h)$$
$$+ \tau_\theta \sum_K \left\langle P'\left[k_1\Delta\boldsymbol{\theta}_h + k_2\nabla(\nabla\cdot\boldsymbol{\theta}_h) + \frac{1}{\varepsilon}(\nabla w_h - \boldsymbol{\theta}_h)\right], -k_1\Delta\boldsymbol{\phi}_h - k_2\nabla(\nabla\cdot\boldsymbol{\phi}_h) - \frac{1}{\varepsilon}(\nabla v_h - \boldsymbol{\phi}_h)\right\rangle_K$$
$$+ \tau_w \sum_K \left\langle P'\left[\frac{1}{\varepsilon}\nabla\cdot(\nabla w_h - \boldsymbol{\theta}_h)\right], -\frac{1}{\varepsilon}\nabla\cdot(\nabla v_h - \boldsymbol{\phi}_h)\right\rangle_K, \tag{2.55}$$

and

$$L_{\text{stab}}(\mathbf{v}_h) = \langle \mathbf{m}, \boldsymbol{\phi}_h\rangle + \langle q, v_h\rangle - \tau_w \sum_K \left\langle P'[q], -\frac{1}{\varepsilon}\nabla\cdot(\nabla v_h - \boldsymbol{\phi}_h)\right\rangle_K,$$
$$- \tau_\theta \sum_K \left\langle P'[\mathbf{m}], -k_1\Delta\boldsymbol{\phi}_h - k_2\nabla(\nabla\cdot\boldsymbol{\phi}_h) - \frac{1}{\varepsilon}(\nabla v_h - \boldsymbol{\phi}_h)\right\rangle_K \tag{2.56}$$

where $P' = I$ for the ASGS formulation and $P' = P^\perp$ for the OSGS method.

2.7.1 Stability analysis of the Algebraic Sub-Grid Scale formulation

[46]: Codina (2000), *On stabilized finite element methods for linear systems of convection–diffusion-reaction equations*

Let us first recall the stability estimate presented in [46] for the plate problem, where the ASGS approach was considered. In that work the terms multiplied by τ_w were neglected because they were not needed to get rid of the numerical locking. This fact however, does not account for the convergence rate of the solution, and τ_w is indeed necessary for it to be optimal, as will be explained and numerically proven below. The formulation will now be extended in the same manner: for the stability estimate, take $\mathbf{v}_h = \mathbf{u}_h$ and consider $\boldsymbol{\gamma}_h = \nabla w_h - \boldsymbol{\theta}_h$. Using Schwarz's inequality leads to:

$$B_{\text{stab}}(\mathbf{u}_h, \mathbf{u}_h) \geq \sum_K \Big[k_1\|\nabla\boldsymbol{\theta}_h\|_K^2 + k_2\|\nabla\cdot\boldsymbol{\theta}_h\|_K^2 + \frac{1}{\varepsilon}\|\boldsymbol{\gamma}_h\|_K^2$$
$$- \tau_\theta k_1^2\|\Delta\boldsymbol{\theta}_h\|_K^2 - \tau_\theta k_2^2\|\nabla(\nabla\cdot\boldsymbol{\theta}_h)\|_K^2 - \tau_\theta\frac{1}{\varepsilon^2}\|\boldsymbol{\gamma}_h\|_K^2$$
$$- 2\tau_\theta\frac{k_1}{\varepsilon}\|\Delta\boldsymbol{\theta}_h\|_K\|\boldsymbol{\gamma}_h\|_K - 2\tau_\theta\frac{k_2}{\varepsilon}\|\nabla(\nabla\cdot\boldsymbol{\theta}_h)\|_K\|\boldsymbol{\gamma}_h\|_K$$
$$-2\tau_\theta k_1 k_2\|\Delta\boldsymbol{\theta}_h\|_K\|\nabla(\nabla\cdot\boldsymbol{\theta}_h)\|_K - \tau_w\frac{1}{\varepsilon^2}\|\nabla\cdot\boldsymbol{\gamma}_h\|_K^2\Big]. \tag{2.57}$$

Using the inverse estimate (2.50) and Young's inequality, we obtain:

$$
\begin{aligned}
B_{\text{stab}}(\mathbf{u}_h, \mathbf{u}_h) \geq \sum_K \Bigg[& k_1 \|\nabla \boldsymbol{\theta}_h\|_K^2 + k_2 \|\nabla \cdot \boldsymbol{\theta}_h\|_K^2 + \frac{1}{\varepsilon} \|\boldsymbol{\gamma}_h\|_K^2 - \tau_\theta k_1^2 \frac{C_{\text{inv}}^2}{h^2} \|\nabla \boldsymbol{\theta}_h\|_K^2 - \tau_\theta k_2^2 \frac{C_{\text{inv}}^2}{h^2} \|\nabla \cdot \boldsymbol{\theta}_h\|_K^2 \\
& - \tau_\theta \frac{1}{\varepsilon^2} \|\boldsymbol{\gamma}_h\|_K^2 - \tau_\theta \frac{k_1}{\varepsilon} \left(\|\nabla \boldsymbol{\theta}_h\|_K^2 + \frac{C_{\text{inv}}^2}{h^2} \|\boldsymbol{\gamma}_h\|_K^2 \right) - \tau_\theta \frac{k_2}{\varepsilon} \left(\|\nabla \cdot \boldsymbol{\theta}_h\|_K^2 + \frac{C_{\text{inv}}^2}{h^2} \|\boldsymbol{\gamma}_h\|_K^2 \right) \\
& - \tau_\theta \left(k_1^2 \frac{C_{\text{inv}}^2}{h^2} \|\nabla \boldsymbol{\theta}_h\|_K^2 + k_2^2 \frac{C_{\text{inv}}^2}{h^2} \|\nabla \cdot \boldsymbol{\theta}_h\|_K^2 \right) - \tau_w \frac{1}{\varepsilon^2} \frac{C_{\text{inv}}^2}{h^2} \|\boldsymbol{\gamma}_h\|_K^2 \Bigg] \\
= \sum_K & \Big[\beta_1 \|\nabla \boldsymbol{\theta}_h\|_K^2 + \beta_2 \|\nabla \cdot \boldsymbol{\theta}_h\|_K^2 + \beta_3 \|\boldsymbol{\gamma}_h\|_K^2 \Big],
\end{aligned} \tag{2.58}
$$

where

$$
\beta_1 = \tau_\theta \left[c_1 \frac{k_1^2}{h^2} + c_1 \frac{k_1 k_2}{h^2} + c_2 \frac{k_1}{\varepsilon} - 2 \frac{C_{\text{inv}}^2}{h^2} k_1^2 - \frac{k_1}{\varepsilon} \right], \tag{2.59}
$$

$$
\beta_2 = \tau_\theta \left[c_1 \frac{k_1 k_2}{h^2} + c_1 \frac{k_2^2}{h^2} + c_2 \frac{k_2}{\varepsilon} - 2 \frac{C_{\text{inv}}^2}{h^2} k_2^2 - \frac{k_2}{\varepsilon} \right], \tag{2.60}
$$

$$
\beta_3 = \tau_\theta \left[c_1 \frac{k}{h^2 \varepsilon} + c_2 \frac{1}{\varepsilon^2} - \frac{1}{\varepsilon^2} - \frac{k}{\varepsilon} \frac{C_{\text{inv}}^2}{h^2} - \frac{k}{\varepsilon} \frac{C_{\text{inv}}^2}{h^2} \left(\frac{c_1 k \varepsilon + c_2 h^2}{c_3 k \varepsilon + c_4 h^2} \right) \right]. \tag{2.61}
$$

Estimate (2.58) is not satisfactory because it does not provide a proper balance of the powers of the thickness in the different terms it involves. This occurs regardless of the selection of stabilization parameters, with the only exception of $c_1 = c_3 = 12$, and $c_2 = c_4 = 1$, which allow one to recover the stiffness matrix coming from the elastic equations (2.49). To understand the reason, suppose that the physical properties and the mesh size h are fixed and let us analyze the scaling of the parameters β_i, $i = 1, 2, 3$, with respect to the thickness t. Assuming $c_3 \geq c_1$, $c_4 \geq c_2$ and $c_1 > 2C_{\text{inv}}^2$ and noting that k_1, k_2 scale as t^3 and ε scales as t^{-1}, we have that

$$
\begin{aligned}
\beta_1, \beta_2 &\sim \tau_\theta t^4 \left[A_1 \frac{t^2}{h^2} + A_2 (c_2 - 1) \right], \\
\beta_3 &\sim \tau_\theta t^4 \left[B_1 \frac{1}{h^2} + \frac{B_2}{t^2} (c_2 - 1) \right],
\end{aligned} \tag{2.62}
$$

where $\sim$ stands for scaling and A_1, A_2, B_1, B_2 are independent of t and h. From this we observe that in order to avoid shear locking we need to take $c_2 = 1$, as it was observed in [46], but

[46]: Codina (2000), *On stabilized finite element methods for linear systems of convection–diffusion-reaction equations*

in this case also the last term in β_1, β_2 vanishes, and we have that $\beta_1,\ \beta_2 = O(\tau_\theta t^6)$ while $\beta_3 = O(\tau_\theta t^4)$ (for h fixed). Therefore, the stability estimate (2.58) does not provide a balanced control of the shear term and the derivatives of the rotation when $t \to 0$. We will see in the next subsection that the OSGS formulation does not suffer from this misbehavior.

2.7.2 Stability and convergence analysis of the Orthogonal Sub-Grid Scale formulation

The numerical analysis of the method considering the OSGS approach is presented next. For positive and dimensionally correct α_i ($i = 1, 2, 3$), the norm in which the results are presented is:

$$\|\mathbf{v}_h\|^2 := \alpha_1 \|\nabla \boldsymbol{\phi}_h\|^2 + \alpha_2 \|\nabla \cdot \boldsymbol{\phi}_h\|^2 + \alpha_3 \|\boldsymbol{\gamma}_h\|^2 . \tag{2.63}$$

This norm has the same form as for the Galerkin method and the ASGS formulation (see estimate (2.58)), but with the advantage that the constants α_i are such that locking is no longer possible, because they are designed in a manner that none of them can become dominant over the others. In particular, it will be shown that they behave as $\alpha_1,\ \alpha_2 = O(\tau_\theta t^4)$ and $\alpha_3 = O(\tau_\theta t^4 h^{-2})$.

In the following, it will be proved that the formulation is stable under the norm (2.63), in the form of the inf-sup condition.

Theorem 2.7.1 (Stability) *There is a constant $C > 0$ such that*

$$\inf_{\mathbf{u}_h \in \mathcal{X}_h} \sup_{\mathbf{v}_h \in \mathcal{X}_h} \frac{B_{\text{stab}}(\mathbf{u}_h, \mathbf{v}_h)}{\|\mathbf{u}_h\| \|\mathbf{v}_h\|} \geq C. \tag{2.64}$$

Proof. Let us start noting that for any function $\mathbf{u}_h \in \mathcal{X}_h$ we have

$$\begin{aligned} B_{\text{stab}}(\mathbf{u}_h, \mathbf{u}_h) =& k_1 \|\nabla \boldsymbol{\theta}_h\|^2 + k_2 \|\nabla \cdot \boldsymbol{\theta}_h\|^2 + \varepsilon^{-1} \|\boldsymbol{\gamma}_h\|^2 \\ & - \tau_\theta \sum_K \left\| P^\perp \left(k_1 \Delta \boldsymbol{\theta}_h + k_2 \nabla (\nabla \cdot \boldsymbol{\theta}_h) + \varepsilon^{-1} \boldsymbol{\gamma}_h \right) \right\|_K^2 \\ & - \tau_w \sum_K \left\| P^\perp \left(\varepsilon^{-1} \nabla \cdot \boldsymbol{\gamma}_h \right) \right\|_K^2 . \end{aligned} \tag{2.65}$$

It is important to note that the Galerkin terms of the bilinear form B have already the necessary terms to have control over the $\nabla\boldsymbol{\theta}_h$ and $\boldsymbol{\gamma}_h$. However, the problem arises when $t \to 0$ and becomes shear dominant. Because of this, the main idea is to obtain a stability estimate in which the shear dominance can be prevented. This estimate comes from the terms whose orthogonal projections appear in B_{stab}, which is obtained by bounding the bilinear form term by term as follows. Let us consider

$$\mathbf{v}_{h1} := (\tau_\theta \boldsymbol{\phi}_1, 0), \tag{2.66}$$

where $\boldsymbol{\phi}_1 = P_h\left(k_1\Delta\boldsymbol{\theta}_h + k_2\nabla(\nabla\cdot\boldsymbol{\theta}_h) + \varepsilon^{-1}\boldsymbol{\gamma}_h\right)$ and P_h is the L^2 projection onto the FE space. It is understood that the term inside the projection is evaluated element-wise. Taking $\mathbf{v}_{h1}$ as test function in the bilinear form, and integrating by parts the Galerkin terms, yields

$$\begin{aligned} B_{\text{stab}}(\mathbf{u}_h, \mathbf{v}_{h1}) = &- \sum_K \tau_\theta \left\langle k_1\Delta\boldsymbol{\theta}_h + k_2\nabla(\nabla\cdot\boldsymbol{\theta}_h) + \varepsilon^{-1}\boldsymbol{\gamma}_h, \boldsymbol{\phi}_1\right\rangle_K \\ &+ \tau_\theta \sum_E \left\langle [\![k_1\mathbf{n}\cdot\nabla\boldsymbol{\theta}_h]\!] + [\![k_2\mathbf{n}\nabla\cdot\boldsymbol{\theta}_h]\!], \boldsymbol{\phi}_1\right\rangle_E \\ &- \tau_\theta^2 \sum_K \left\langle P^\perp\left(k_1\Delta\boldsymbol{\theta}_h + k_2\nabla(\nabla\cdot\boldsymbol{\theta}_h) + \varepsilon^{-1}\boldsymbol{\gamma}_h\right), k_1\Delta\boldsymbol{\phi}_1 + k_2\nabla(\nabla\cdot\boldsymbol{\phi}_1) - \varepsilon^{-1}\boldsymbol{\phi}_1\right\rangle_K \\ &- \tau_\theta\tau_w \sum_K \left\langle P^\perp\left(\varepsilon^{-1}\nabla\cdot\boldsymbol{\gamma}_h\right), -\varepsilon^{-1}\nabla\cdot\boldsymbol{\phi}_1\right\rangle_K . \end{aligned} \tag{2.67}$$

Note that the equation contains terms projected in the space that is orthogonal to the FE space, which disappear when tested with $\boldsymbol{\phi}_1$ because it belongs to the FE space itself. Then, by using Schwarz's inequality and the inverse estimate (2.50), we obtain

$$\begin{aligned} B_{\text{stab}}(\mathbf{u}_h, \mathbf{v}_{h1}) \geq &- \tau_\theta \sum_K \|\boldsymbol{\phi}_1\|_K^2 - \tau_\theta \sum_E \|[\![k_1\mathbf{n}\cdot\nabla\boldsymbol{\theta}_h]\!]\|_E \|\boldsymbol{\phi}_1\|_E - \tau_\theta \sum_E \|[\![k_2\mathbf{n}\nabla\cdot\boldsymbol{\theta}_h]\!]\|_E \|\boldsymbol{\phi}_1\|_E \\ &- \tau_\theta^2 k \frac{C_{\text{inv}}^2}{h^2} \sum_K \left\|P^\perp\left(k_1\Delta\boldsymbol{\theta}_h + k_2\nabla(\nabla\cdot\boldsymbol{\theta}_h) + \varepsilon^{-1}\boldsymbol{\gamma}_h\right)\right\|_K \|\boldsymbol{\phi}_1\|_K \\ &- \tau_\theta\tau_w\varepsilon^{-1}\frac{C_{\text{inv}}}{h} \sum_K \left\|P^\perp\left(\varepsilon^{-1}\nabla\cdot\boldsymbol{\gamma}_h\right)\right\|_K \|\boldsymbol{\phi}_1\|_K . \end{aligned} \tag{2.68}$$

Then, using Young's inequality and the trace inequalities (2.53) it follows that

$$
\begin{aligned}
B_{\text{stab}}(\mathbf{u}_h, \mathbf{v}_{h1}) \geq & -\tau_\theta \sum_K \|\boldsymbol{\phi}_1\|_K^2 - \tau_\theta \sum_K \|\boldsymbol{\phi}_1\|_K^2 - \tau_\theta \frac{C_{\text{trace}}^2}{2h^2} \sum_K \|k_1 \nabla \boldsymbol{\theta}_h\|_K^2 - \tau_\theta \frac{C_{\text{trace}}^2}{2h^2} \sum_K \|k_2 \nabla \cdot \boldsymbol{\theta}_h\|_K^2 \\
& - \frac{\tau_\theta^2 k}{2} \frac{C_{\text{inv}}^2}{h^2} \sum_K \left(\|\boldsymbol{\phi}_1\|_K^2 + \left\| P^\perp \left(k_1 \Delta \boldsymbol{\theta}_h + k_2 \nabla (\nabla \cdot \boldsymbol{\theta}_h) + \varepsilon^{-1} \boldsymbol{\gamma}_h \right) \right\|_K^2 \right) \\
& - \tau_\theta \tau_w \frac{\varepsilon^{-1}}{2} \frac{C_{\text{inv}}^2}{h^2} \sum_K \|\boldsymbol{\phi}_1\|_K^2 - \tau_\theta \tau_w \frac{\varepsilon^{-1}}{2} \sum_K \left\| P^\perp \left(\varepsilon^{-1} \nabla \cdot \boldsymbol{\gamma}_h \right) \right\|_K^2 .
\end{aligned} \tag{2.69}
$$

Similarly, consider $\mathbf{v}_{h2} = (\mathbf{0}, \tau_w v_2)$, where $v_2 = P_h \left(\varepsilon^{-1} \nabla \cdot \boldsymbol{\gamma}_h \right)$, as test function in the bilinear form. We have that

$$
\begin{aligned}
B_{\text{stab}}(\mathbf{u}_h, \mathbf{v}_{h2}) = & -\tau_w \left(\varepsilon^{-1} \nabla \cdot \boldsymbol{\gamma}_h, v_2 \right) + \tau_w \sum_E \left\langle \varepsilon^{-1} \left[\!\left[\mathbf{n} \cdot \boldsymbol{\gamma}_h \right]\!\right], v_2 \right\rangle_E \\
& - \tau_w^2 \varepsilon^{-1} \sum_K \left\langle P^\perp \left(\varepsilon^{-1} \nabla \cdot \boldsymbol{\gamma}_h \right), \nabla \cdot \nabla v_2 \right\rangle_K \\
& - \tau_\theta \tau_w \varepsilon^{-1} \sum_K \left\langle P^\perp \left(k_1 \Delta \boldsymbol{\theta}_h + k_2 \nabla (\nabla \cdot \boldsymbol{\theta}_h) + \varepsilon^{-1} \boldsymbol{\gamma}_h \right), \nabla v_2 \right\rangle_K .
\end{aligned} \tag{2.70}
$$

Then following the same procedure as before, it follows that

$$
\begin{aligned}
B_{\text{stab}}(\mathbf{u}_h, \mathbf{v}_{h2}) \geq & -\tau_w \sum_K \|v_2\|_K^2 - \tau_w \sum_K \|v_2\|_K^2 - \tau_w \frac{C_{\text{trace}}^2}{4h^2} \sum_K \left\| \varepsilon^{-1} \boldsymbol{\gamma}_h \right\|_K^2 \\
& - \tau_w^2 \frac{\varepsilon^{-1}}{2} \frac{C_{\text{inv}}^2}{h^2} \sum_K \left(\|v_2\|_K^2 + \left\| P^\perp \left(\varepsilon^{-1} \nabla \cdot \boldsymbol{\gamma}_h \right) \right\|_K^2 \right) \\
& - \tau_\theta \tau_w \frac{\varepsilon^{-1}}{2} \sum_K \|v_2\|_K^2 - \tau_\theta \tau_w \frac{\varepsilon^{-1}}{2} \frac{C_{\text{inv}}^2}{h^2} \sum_K \left\| P^\perp \left(k_1 \Delta \boldsymbol{\theta}_h + k_2 \nabla (\nabla \cdot \boldsymbol{\theta}_h) + \varepsilon^{-1} \boldsymbol{\gamma}_h \right) \right\|_K^2 .
\end{aligned} \tag{2.71}
$$

Lastly, consider $\mathbf{v}_h = \mathbf{u}_h + \frac{1}{2}\mathbf{v}_{h1} + \frac{1}{2}\mathbf{v}_{h2}$, which is equivalent to adding up (2.65), $\frac{1}{2}$(2.69), and $\frac{1}{2}$(2.71). This yields

$$
\begin{aligned}
B_{\text{stab}}(\mathbf{u}_h, \mathbf{v}_h) \geq & \left(k_1 - \tau_\theta k_1^2 \frac{C_{\text{trace}}^2}{4h^2}\right) \|\nabla \boldsymbol{\theta}_h\|^2 + \left(k_2 - \tau_\theta k_2^2 \frac{C_{\text{trace}}^2}{4h^2}\right) \|\nabla \cdot \boldsymbol{\theta}_h\|^2 \\
& + \left(\varepsilon^{-1} - \tau_w \varepsilon^{-2} \frac{C_{\text{trace}}^2}{8h^2}\right) \|\boldsymbol{\gamma}_h\|^2 \\
& - \left(\tau_\theta + \frac{\tau_\theta^2 k}{2} \frac{C_{\text{inv}}^2}{h^2} + \tau_\theta \tau_w \frac{\varepsilon^{-1}}{2} \frac{C_{\text{inv}}^2}{h^2}\right) \sum_K \left\|k_1 \Delta \boldsymbol{\theta}_h + k_2 \nabla(\nabla \cdot \boldsymbol{\theta}_h) + \varepsilon^{-1} \boldsymbol{\gamma}_h\right\|_K^2 \\
& - \left(\tau_w + \tau_\theta \tau_w \frac{\varepsilon^{-1}}{2} + \tau_w^2 \frac{\varepsilon^{-1}}{2} \frac{C_{\text{inv}}^2}{h^2}\right) \sum_K \left\|\varepsilon^{-1} \nabla \cdot \boldsymbol{\gamma}_h\right\|_K^2 . \qquad (2.72)
\end{aligned}
$$

The last two terms can be separated using the triangular inequality, enabling us to write the expression in terms of the original variables only:

$$
B_{\text{stab}}(\mathbf{u}_h, \mathbf{v}_h) \geq \alpha_1 \|\nabla \boldsymbol{\theta}_h\|^2 + \alpha_2 \|\nabla \cdot \boldsymbol{\theta}_h\|^2 + \alpha_3 \|\boldsymbol{\gamma}_h\|^2 \equiv \|\mathbf{u}_h\|^2, \qquad (2.73)
$$

where

$$
\alpha_1 = \tau_\theta \left[c_1 \frac{k k_1}{h^2} + c_2 \frac{k_1}{\varepsilon} - k_1^2 \frac{C_{\text{inv}}^2}{4h^2} \left(\frac{C_{\text{inv}} k \varepsilon}{c_1 k \varepsilon + c_2 h^2}\right) - k_1^2 \frac{C_{\text{inv}}^2}{4h^2} \left(\frac{C_{\text{inv}}^2 k \varepsilon}{c_3 k \varepsilon + c_4 h^2}\right) - k_1^2 \frac{C_{\text{trace}}^2}{4h^2}\right], \qquad (2.74)
$$

$$
\alpha_2 = \tau_\theta \left[c_1 \frac{k k_2}{h^2} + c_2 \frac{k_2}{\varepsilon} - k_2^2 \frac{C_{\text{inv}}^2}{4h^2} \left(\frac{C_{\text{inv}} k \varepsilon}{c_1 k \varepsilon + c_2 h^2}\right) - k_2^2 \frac{C_{\text{inv}}^2}{4h^2} \left(\frac{C_{\text{inv}}^2 k \varepsilon}{c_3 k \varepsilon + c_4 h^2}\right) - k_2^2 \frac{C_{\text{trace}}^2}{4h^2}\right], \qquad (2.75)
$$

$$
\begin{aligned}
\alpha_3 = \tau_\theta \Bigg[& c_1 \frac{k \varepsilon^{-1}}{h^2} + \frac{c_2}{\varepsilon^2} - \frac{1}{\varepsilon^2} - \frac{k}{\varepsilon} \frac{C_{\text{inv}}^2}{4h^2} \left(\frac{h^2}{c_1 k \varepsilon + c_2 h^2}\right) - \frac{k}{\varepsilon} \frac{C_{\text{inv}}^2}{4h^2} \left(\frac{h^2}{c_3 k \varepsilon + c_4 h^2}\right) \\
& - \frac{k}{\varepsilon} \frac{C_{\text{trace}}^2}{8h^2} \left(\frac{c_1 k \varepsilon + c_2 h^2}{c_3 k \varepsilon + c_4 h^2}\right) - \frac{k}{\varepsilon} \frac{C_{\text{inv}}^2}{h^2} \left(\frac{c_1 k \varepsilon + c_2 h^2}{c_3 k \varepsilon + c_4 h^2}\right) \\
& - \frac{k}{\varepsilon} \frac{C_{\text{inv}}^2}{2h^2} \left(\frac{c_1 k \varepsilon + c_2 h^2}{c_3 k \varepsilon + c_4 h^2}\right) \left(\frac{C_{\text{inv}}^2 k \varepsilon^{-1}}{c_3 k \varepsilon^{-1} + c_4 \varepsilon^{-2} h^2}\right) \Bigg]. \qquad (2.76)
\end{aligned}
$$

From the expression in (2.76) it can be verified again that the value $c_2 = 1$ is necessary to eliminate shear dominance and that the constants must satisfy $c_3 \geq c_1$ and $c_4 \geq c_2$. It is also needed that $c_1 > 2C_{\text{inv}}^2 + \frac{1}{4}C_{\text{trace}}^2$. In fact, for linear elements it suffices to take $c_1 > 0$, as the integration by parts in (2.67) is not needed (the terms multiplied by C_{trace} do not show up) and one may take the constant associated to the inverse es-

timate for second derivatives as $C_{\text{inv}} = 0$. Under all these conditions, it is readily checked that

$$\alpha_1, \alpha_2 \sim \tau_\theta t^4 \left[A_1' \frac{t^2}{h^2} + A_2' c_2 \right],$$
$$\alpha_3 \sim \tau_\theta t^4 \left[B_1' \frac{1}{h^2} + \frac{B_2'}{t^2}(c_2 - 1) \right], \tag{2.77}$$

where A_1', A_2', B_1', B_2' are independent of t and h. Comparing (2.77) with (2.62) it is observed that the last term in α_1, α_2 does not vanish when $c_2 = 1$, contrary to what happens for β_1, β_2. Thus, when $t \to 0$ we have that α_1, $\alpha_2 = O(\tau_\theta t^4)$ and $\alpha_3 = O(\tau_\theta t^4 h^{-2})$, as claimed earlier.

Therefore, we have proved that there is a positive constant C for which the following inequality holds:

$$B_{\text{stab}}(\mathbf{u}_h, \mathbf{v}_h) \geq C \|\mathbf{u}_h\|^2. \tag{2.78}$$

It is also easy to check that

$$\|\mathbf{v}_{h1}\|^2 \leq \tau_\theta^2 \frac{C_{\text{inv}}^4}{h^4}(\alpha_1 + \alpha_2)\left(k_1^2 \|\nabla \boldsymbol{\theta}_h\|_K^2 + k_2^2 \|\nabla \cdot \boldsymbol{\theta}_h\|_K^2\right)$$
$$+ \tau_\theta^2 \varepsilon^{-2} \frac{C_{\text{inv}}^2}{h^2}(\alpha_1 + \alpha_2)\|\boldsymbol{\gamma}_h\|_K^2 \leq C \|\mathbf{u}_h\|^2, \tag{2.79}$$
$$\|\mathbf{v}_{h2}\|^2 \leq \tau_w^2 \varepsilon^{-2} \alpha_3 \frac{C_{\text{inv}}^4}{h^4} \|\boldsymbol{\gamma}_h\|_K^2 \leq C \|\mathbf{u}_h\|^2, \tag{2.80}$$

and therefore $\|\mathbf{v}_h\|^2 \leq C\|\mathbf{u}_h\|^2$. From this result and (2.78) it follows that for each $\mathbf{u}_h \in \mathcal{X}_h$ there exists $\mathbf{v}_h \in \mathcal{X}_h$ such that $B_{\text{stab}}(\mathbf{u}_h, \mathbf{v}_h) \geq C\|\mathbf{u}_h\|\|\mathbf{v}_h\|$, from where the theorem follows. □

Once the stability is established, a standard procedure follows to prove convergence. There are two preliminary lemmas that are needed to achieve it, concerning the consistency and the interpolation error.

Lemma 2.7.2 (Consistency) *Let $\mathbf{u} \in \mathcal{X}$ be the solution of the continuous problem and $\mathbf{u}_h \in \mathcal{X}_h$ the FE solution of* (2.55). *If $\mathbf{u}$ is regular enough so that $B_{\text{stab}}(\mathbf{u}, \mathbf{v}_h)$ is well defined, then*

$$B_{\text{stab}}(\mathbf{u} - \mathbf{u}_h, \mathbf{v}_h) = 0, \quad \forall \mathbf{v}_h \in \mathcal{X}_h. \tag{2.81}$$

Proof. Since the stabilization terms are residual based and the Galerkin method does not contribute to the consistency

error, the lemma is satisfied by construction. □

The following lemma concerns an interpolation error in terms of the working norm $\|\cdot\|$ and the bilinear form B_{stab}. Let $\mathscr{W}_h$ be a generic FE space of degree k_v. The interpolation error $\epsilon_i(v)$ for any function $v \in H^{k_v'+1}(\Omega)$ for $i = 0, 1$ is defined as follows

$$\inf_{v_h \in \mathscr{W}_h} \sum_K \|v - v_h\|_{H^i(K)} \leq C h^{k_v''+1-i} \sum_K \|v\|_{H^{k_v''+1}(K)} =: \epsilon_i(v), \tag{2.82}$$

where $k_v'' = \min(k_v, k_v')$. Also consider $\tilde{v}_h$ to be the best approximation of v in $\mathscr{W}_h$. Note that $\epsilon_0(v) = h\epsilon_1(v)$. In particular, the notation will be $v = \boldsymbol{\theta}$ for the rotations and $v = w$ for the deflection, with orders of interpolation k_θ and k_w, respectively.

The error function of the method will be proven to be:

$$E(h) := \left(\sqrt{k_1} + \sqrt{k_2}\right)\epsilon_1(\boldsymbol{\theta}) + \frac{1}{\sqrt{\varepsilon}}\epsilon_0(\boldsymbol{\theta}) + \frac{1}{\sqrt{\varepsilon}}\epsilon_1(w). \tag{2.83}$$

Lemma 2.7.3 (Interpolation error) *Let $\mathbf{u} \in \mathscr{X}$ be the continuous solution, assumed to be regular enough, and $\tilde{\mathbf{u}}_h \in \mathscr{X}_h$ its best FE approximation. Then the following inequalities hold:*

$$B_{\text{stab}}(\mathbf{u} - \tilde{\mathbf{u}}_h, \mathbf{v}_h) \leq CE(h)\|\mathbf{v}_h\|, \tag{2.84}$$

$$\|\mathbf{u} - \tilde{\mathbf{u}}_h\| \leq CE(h). \tag{2.85}$$

Proof. Let us prove (2.85). Consider the definition of the working norm (2.63); it can be easily checked that

$$\|\mathbf{u} - \tilde{\mathbf{u}}_h\|^2 \leq C\left[\alpha_1\epsilon_1^2(\boldsymbol{\theta}) + \alpha_2\epsilon_1^2(\boldsymbol{\theta}) + \alpha_3\epsilon_1^2(w) + \alpha_3\epsilon_0^2(\boldsymbol{\theta})\right], \tag{2.86}$$

from where (2.85) follows using (2.47) for the expression of the stabilization parameters and (2.74)-(2.76) for the expression of α_i, $i = 1, 2, 3$.

Then consider $\mathbf{e}_u = \mathbf{u} - \tilde{\mathbf{u}}_h = [\mathbf{e}_\theta, e_w]$, where $\mathbf{e}_\theta = \boldsymbol{\theta} - \tilde{\boldsymbol{\theta}}_h$ and $e_w = w - \tilde{w}_h$; the proof of (2.84) is as follows:

$$
\begin{aligned}
B_{\text{stab}}(\mathbf{e}_u, \mathbf{v}_h) &= k_1 \left(\nabla \mathbf{e}_\theta, \nabla \boldsymbol{\phi}_h\right) + k_2 \left(\nabla \cdot \mathbf{e}_\theta, \nabla \cdot \boldsymbol{\phi}_h\right) + \frac{1}{\varepsilon} \left(\nabla e_w - \mathbf{e}_\theta, \nabla v_h - \boldsymbol{\phi}_h\right) \\
&+ \tau_\theta \sum_K \left\langle P_\theta^\perp \left[k_1 \Delta \mathbf{e}_\theta + k_2 \nabla(\nabla \cdot \mathbf{e}_\theta) + \frac{1}{\varepsilon} \left(\nabla e_w - \mathbf{e}_\theta\right) \right], P_\theta^\perp \left[-k_1 \Delta \boldsymbol{\phi}_h - k_2 \nabla(\nabla \cdot \boldsymbol{\phi}_h) - \frac{1}{\varepsilon} \boldsymbol{\gamma}_h \right] \right\rangle_K \\
&+ \tau_w \sum_K \left\langle P_w^\perp \left[\frac{1}{\varepsilon} \nabla \cdot \left(\nabla e_w - \mathbf{e}_\theta\right) \right], P_w^\perp \left[-\frac{1}{\varepsilon} \nabla \cdot \boldsymbol{\gamma}_h \right] \right\rangle_K \\
&\leq \sqrt{k_1} \|\nabla \mathbf{e}_\theta\| \sqrt{k_1} \|\nabla \boldsymbol{\phi}_h\| + \sqrt{k_2} \|\nabla \cdot \mathbf{e}_\theta\| \sqrt{k_2} \|\nabla \cdot \boldsymbol{\phi}_h\| + \frac{1}{\sqrt{\varepsilon}} \|\nabla e_w - \mathbf{e}_\theta\| \frac{1}{\sqrt{\varepsilon}} \|\boldsymbol{\gamma}_h\| \\
&+ \left(\tau_\theta \frac{k_1}{h} \|\nabla \mathbf{e}_\theta\| + \tau_\theta \frac{k_2}{h} \|\nabla \cdot \mathbf{e}_\theta\| + \frac{\tau_\theta}{\varepsilon} \left(\|\nabla e_w\| + \|\mathbf{e}_\theta\| \right) \right) \left(k_1 \frac{C_{\text{inv}}}{h} \|\nabla \boldsymbol{\phi}_h\| \right. \\
&\left. + k_2 \frac{C_{\text{inv}}}{h} \|\nabla \cdot \boldsymbol{\phi}_h\| + \frac{1}{\varepsilon} \|\boldsymbol{\gamma}_h\| \right) + \left(\tau_w \frac{1}{\varepsilon} \frac{1}{h} \|\nabla e_w\| + \tau_w \frac{1}{\varepsilon} \|\nabla \cdot \mathbf{e}_\theta\| \right) \frac{C_{\text{inv}}}{\varepsilon h} \|\boldsymbol{\gamma}_h\|
\end{aligned}
$$

$$
\begin{aligned}
B_{\text{stab}}(\mathbf{e}_u, \mathbf{v}_h) &\leq \left[\left(k_1 + \tau_\theta k_1^2 \frac{C_{\text{inv}}}{h^2} \right) \|\nabla \mathbf{e}_\theta\| + \tau_\theta k_1 k_2 \frac{C_{\text{inv}}}{h^2} \|\nabla \cdot \mathbf{e}_\theta\| + \tau_\theta \frac{k_1}{\varepsilon} \frac{C_{\text{inv}}}{h} \|\nabla e_w\| \right. \\
&\left. + \tau_\theta \frac{k_1}{\varepsilon} \frac{C_{\text{inv}}}{h^2} \|\mathbf{e}_\theta\| \right] \|\nabla \boldsymbol{\phi}_h\| + \left[\tau_\theta k_1 k_2 \frac{C_{\text{inv}}}{h^2} \|\nabla \mathbf{e}_\theta\| + \left(k_2 + \tau_\theta k_2^2 \frac{C_{\text{inv}}}{h^2} \right) \|\nabla \cdot \mathbf{e}_\theta\| \right. \\
&\left. + \tau_\theta \frac{k_2}{\varepsilon} \frac{C_{\text{inv}}}{h} \|\nabla e_w\| + \tau_\theta \frac{k_2}{\varepsilon} \frac{C_{\text{inv}}}{h^2} \|\mathbf{e}_\theta\| \right] \|\nabla \cdot \boldsymbol{\phi}_h\| \\
&+ \left[\tau_\theta \frac{k_1}{\varepsilon h} \|\nabla \mathbf{e}_\theta\| + \tau_\theta \frac{k_2}{\varepsilon h} \|\nabla \cdot \mathbf{e}_\theta\| + \left(\frac{1}{\varepsilon} + \frac{\tau_\theta}{\varepsilon^2} + \tau_w \frac{C_{\text{inv}}}{\varepsilon^2 h^2} \right) \left(\|\nabla e_w\| + \|\mathbf{e}_\theta\| \right) \right] \|\boldsymbol{\gamma}_h\| \\
&\leq C \left[k_1 \|\nabla \mathbf{e}_\theta\| + k_2 \|\nabla \cdot \mathbf{e}_\theta\| + \frac{h}{\varepsilon} \|\nabla e_w\| + \frac{h}{\varepsilon} \|\mathbf{e}_\theta\| \right] \left(\|\nabla \boldsymbol{\phi}_h\|_K + \|\nabla \cdot \boldsymbol{\phi}_h\| + \frac{1}{h} \|\boldsymbol{\gamma}_h\| \right) \\
&\leq C \left[\left(\sqrt{k_1} + \sqrt{k_2} \right) \epsilon_1(\boldsymbol{\theta}) + \frac{1}{\sqrt{\varepsilon}} \epsilon_0(\boldsymbol{\theta}) + \frac{1}{\sqrt{\varepsilon}} \epsilon_1(w) \right] \left(\sqrt{\alpha_1} \|\nabla \boldsymbol{\phi}_h\| + \sqrt{\alpha_2} \|\nabla \cdot \boldsymbol{\phi}_h\| + \sqrt{\alpha_3} \|\boldsymbol{\gamma}_h\| \right).
\end{aligned}
\tag{2.87}
$$

All the terms have been organized to see that it is clear that they are all bounded by $CE(h)\|\mathbf{v}_h\|$, from where (2.84) follows. □

With this, it only remains to prove convergence, which proceeds in a standard manner.

Theorem 2.7.4 (Convergence) *Let $\mathbf{u} \in \mathcal{X}$ be the solution of the continuous problem, assumed to be regular enough. There is a positive constant C such that*

$$
\|\mathbf{u} - \mathbf{u}_h\| \leq CE(h). \tag{2.88}
$$

Proof. Consider $\tilde{\mathbf{u}}_h - \mathbf{u}_h \in \mathcal{X}_h$, where $\tilde{\mathbf{u}}_h$ is the best FE approximation to $\mathbf{u}$. From the inf-sup condition (2.64) it follows that

there exists $\mathbf{v}_h \in \mathcal{X}_h$ such that from the consistency (2.81) and equation (2.84) it follows

$$\begin{aligned} C\|\tilde{\mathbf{u}}_h - \mathbf{u}_h\|\|\mathbf{v}_h\| &\leq B_{\text{stab}}(\tilde{\mathbf{u}}_h - \mathbf{u}_h, \mathbf{v}_h) \\ &= B_{\text{stab}}(\tilde{\mathbf{u}}_h - \mathbf{u}, \mathbf{v}_h) \\ &\leq CE(h)\|\mathbf{v}_h\| \end{aligned}$$

from where $\|\tilde{\mathbf{u}}_h - \mathbf{u}_h\| \leq CE(h)$. Subsequently, the theorem follows from the triangle inequality $\|\mathbf{u} - \mathbf{u}_h\| \leq \|\mathbf{u} - \tilde{\mathbf{u}}_h\| + \|\tilde{\mathbf{u}}_h - \mathbf{u}_h\|$ and the interpolation error estimate (2.85). □

From this result and the expression of the error function in (2.83) it follows that when t is 'large' the optimal combination of interpolation orders for rotations and displacements is $k_\theta = k_w$. However, when t is small, say $t < h$, the best is to take $k_\theta = k_w - 1$, since in this case rotations and deflection contribute with the same order of h to the error of the formulation.

2.8 Numerical results

All the examples of this section have been run considering linear continuous interpolation for both rotations and displacements, i.e., $k_\theta = k_w = 1$.

2.8.1 Shear-locking

In this section, the behavior of the ASGS and OSGS formulations is evaluated for the plate and beam problems. From the physical point of view, the formulations must be able to represent thin behavior, or in other words, the effects of shear deformations must become negligible for decreasing thickness. From the numerical point of view, this can be verified if the numerical results are free from shear-locking. This implies that the solution obtained using the Reissner-Mindlin and Timoshenko theories should coincide with the solution of the Kirchhoff and the Euler-Bernoulli beam theory, respectively, for small thicknesses.

To assess this behavior, let us consider a square plate of domain $\Omega = (0, L)^2$ clamped on all its sides and subject to a uniform load $q = 1$ and a cantilever beam of domain $\Omega = (0, L)$ with a point load $P = -1$ at the right end and clamped at

the left one. For the beam geometry we define a rectangular cross section of side $b = 1$ and thickness t, thus the inertia is $I = bt^3/12$. For the material properties we consider $E = 10^6$ and $\nu = 0.2$ in all cases (SI units can be assumed to fix ideas). The analytical deflection at the center of the plate and at the end of the beam according to the Kirchhoff and Euler-Bernoulli theories are, respectively:

$$w_{\mathrm{K}} = 0.01524\frac{qL^4(1-\nu^2)}{Et^3}, \qquad w_{\mathrm{E}} = \frac{PL^3}{3EI}. \tag{2.89}$$

For the numerical computations, we consider a mesh of 20×20 square elements for the plate and 50 linear elements for the beam. The ratios between the deflection obtained numerically from the stabilized formulations and the analytical solutions respect to the thickness are plotted in Figs. 2.3-2.4. Results show that both formulations are able to represent the thin limit behavior.

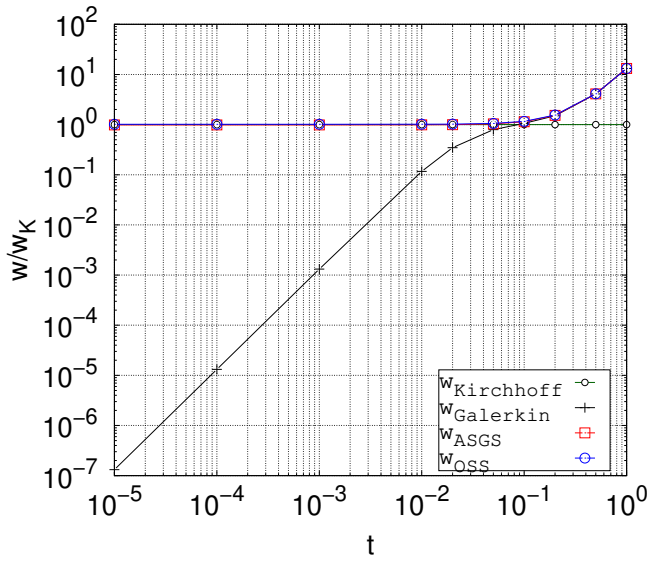

Figure 2.3: Comparison of deflection w from numerical results vs analytical solutions for different thicknesses of plates.

In order to have a reference of the performance of the methods proposed, the behavior of ASGS and OSGS formulations is compared to that obtained by the reduced integration of the shear terms, i.e., those that involve rotations. In the case of beams, Fig. 2.5 shows that both ASGS and OSGS converge slightly faster to the analytical solution compared to reduced integration; however, the convergence test presented below shall depict the true nature of the formulations discussed in the present work.

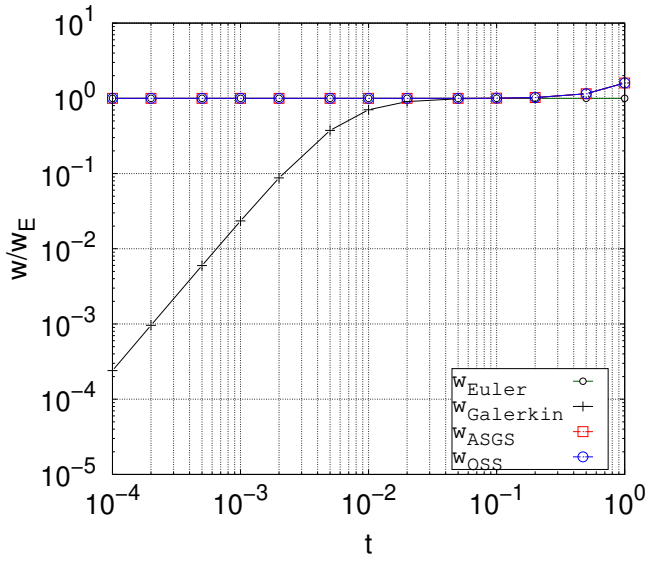

Figure 2.4: Comparison of deflection w from numerical results vs analytical solutions for different thicknesses of beams.

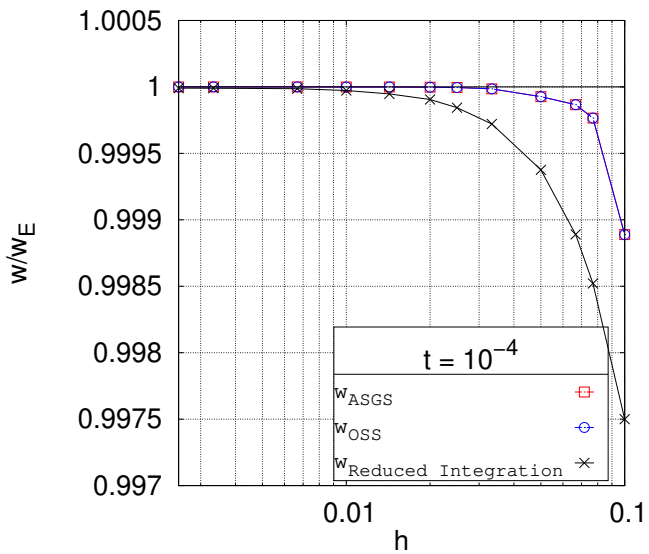

Figure 2.5: Comparison of relative deflection w from numerical results vs analytical solutions for different element sizes.

2.8.2 Convergence tests

Convergence for beams

To assess the convergence of the stabilized Timoshenko beam formulation, consider a beam oriented in the x direction clamped at both sides, a homogeneous load $q = 1$ on its entire length $L = 1$, and the same material and geometrical properties as

in the previous beam example. Since the formulation has to be able to represent the thin behavior, the solutions of the numerical method is compared to the analytical solution of the Euler-Bernoulli beam theory:

$$\theta_z(x) = \frac{qx}{12EI}(L-x)(1-2x), \tag{2.90}$$

$$w(x) = \frac{qx^2}{24EI}(L-x)^2. \tag{2.91}$$

The problem then is numerically solved for decreasing element sizes h, thicknesses of $t = 10^{-4}, 10^{-5}$ which correspond to slenderness ratios of $L/t = 10^4, 10^5$, respectively, and the error is evaluated in the L^2 norm. For comparison purposes, results are shown for the standard Galerkin, ASGS and OSGS formulations, as presented in Figs. 2.6-2.7. Results show that deflections and rotations are optimally convergent respect to the element size using any of the two stabilized formulations.

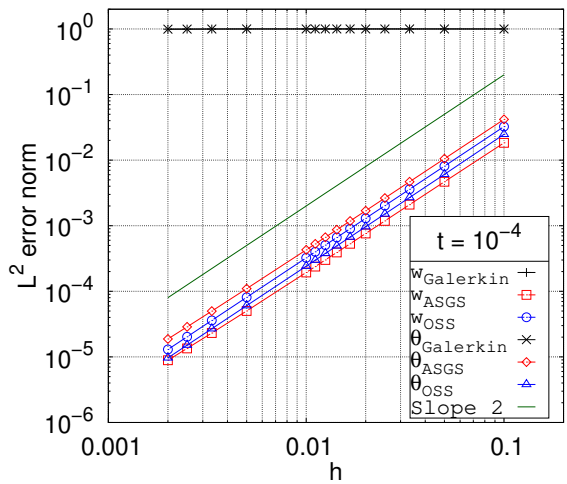

Figure 2.6: Beam L^2-error norm for Galerkin, ASGS and OSGS formulations for $L/t = 10^4$.

For the numerical tests, the stabilization constants chosen for the ASGS formulation are $c_1 = c_3 = 12$, as found in section 2.6. In the case of the OSGS formulation, the values of the constants have no justification from the exact solution, and were chosen by testing different values. Nevertheless, this selection is not arbitrary; it is known that the zero shear constraint is difficult to handle, and selecting small values of c_1 can alleviate it. Under this assumption, it was found that values of $c_1 \leq 10^{-3}$ have to be used to obtain optimally convergent results. Recall that for linear elements the only

condition needed for stability is that $c_1 > 0$, as discussed in section 2.7.

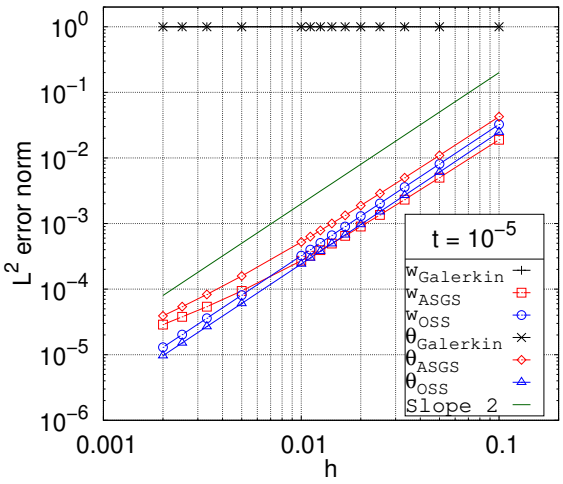

Figure 2.7: Beam L^2-error norm for Galerkin, ASGS and OSGS formulations for $L/t = 10^5$.

One important aspect of a locking-free formulation is that its convergence should be independent of the thickness, at least to some degree. To assess this dependence, the convergence curves of the displacements are plotted for different thicknesses. As presented in Figs. 2.8-2.9, the ASGS formulation becomes noticeable dependent on the thickness for low enough values, while the OSGS formulation shows a robust behavior since it is almost independent of it.

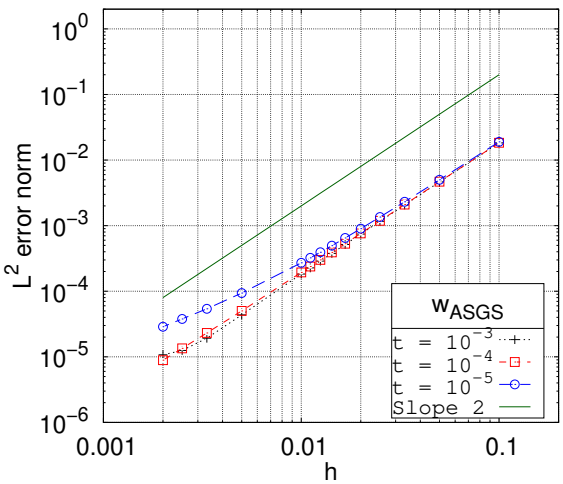

Figure 2.8: Beam displacement L^2-error norm for different thicknesses using ASGS stabilization.

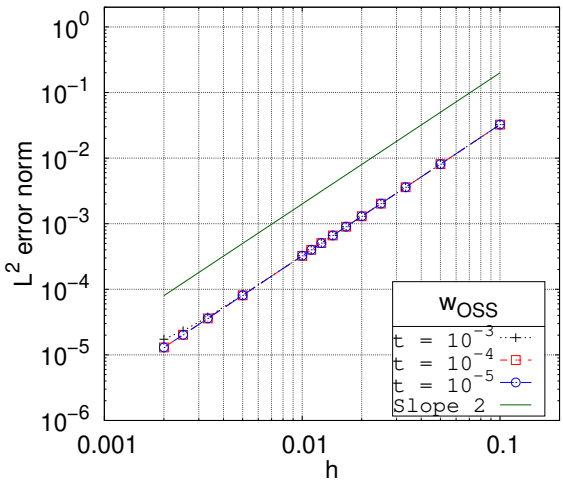

Figure 2.9: Beam displacement L^2-error norm for different thicknesses using OSGS stabilization.

Convergence for plates

[30]: Chinosi et al. (2006), *Non-conforming locking-free finite elements for Reissner–Mindlin plates*

To assess the convergence of the stabilized Reissner-Mindlin plate formulation, we consider a problem proposed in [30]. It consists in a square plate of domain $\Omega = (0, L)^2$ clamped on all sides, and loaded vertically using the following function:

$$q(x,y) = \frac{E}{12(1-\nu^2)}\left[12y(y-1)(5x^2-5x+1)(2y^2(y-1)^2+x(x-1)(5y^2-5y+1)) \right.$$
$$\left. +12x(x-1)(5y^2-5y+1)(2x^2(x-1)^2+y(y-1)(5x^2-5x+1))\right], \quad (2.92)$$

for which the exact solutions of displacements and rotations are given by

$$w(x,y) = \frac{x^3y^3}{3t^3}(x-1)^3(y-1)^3 - \frac{2}{5t(1-\nu)}\left[y^3(y-1)^3x(x-1)(5x^2-5x+1)\right.$$
$$\left. +x^3(x-1)^3y(y-1)(5y^2-5y+1)\right], \quad (2.93)$$
$$\theta_x(x,y) = \frac{y^3x^2}{t^3}(y-1)^3(x-1)^2(2x-1), \quad (2.94)$$
$$\theta_y(x,y) = \frac{x^3y^2}{t^3}(x-1)^3(y-1)^2(2y-1). \quad (2.95)$$

The load, displacement and rotation fields are showed graphically in Figs. 2.10-2.11-2.12, respectively.

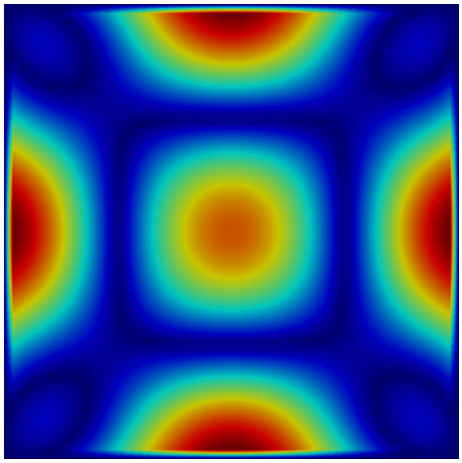

Figure 2.10: Plate convergence test: applied load.

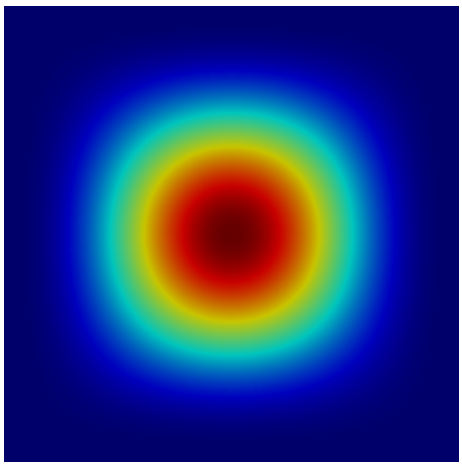

Figure 2.11: Plate convergence test: displacement field.

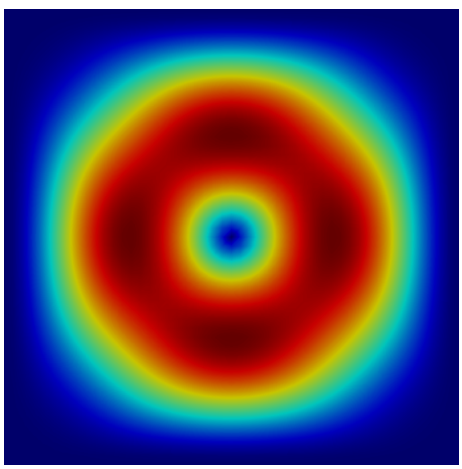

Figure 2.12: Plate convergence test: norm of rotation field.

The problem then is solved for decreasing element sizes h, considering a constant thicknesses of $t = 10^{-4}$, and 10^{-5} which correspond to slenderness ratios of $L/t = 10^4$ and 10^5, respectively, and the error is evaluated in the L^2 norm. Numerical tests have been computed to evaluate which stabilization parameters are best suited to obtain optimal convergence. In regard of this, the only constant that must remain fixed is $c_2 = 1$, as proven in the convergence analysis.

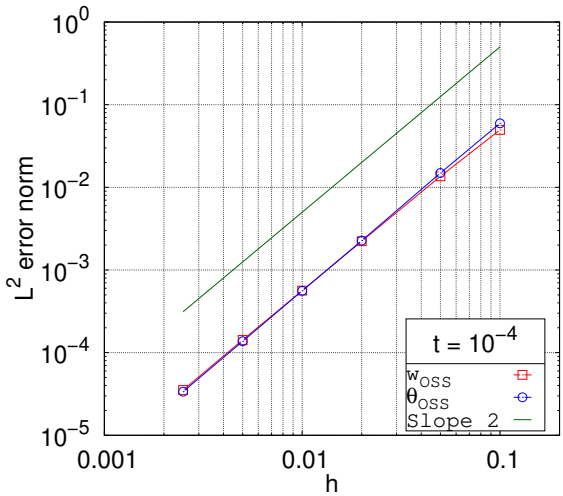

Figure 2.13: Plates L^2-error norm for OSGS formulation for $L/t = 10^4$.

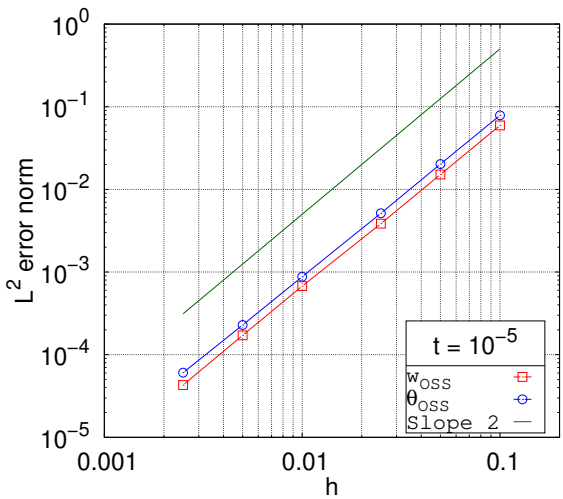

Figure 2.14: Plates L^2-error norm for OSGS formulation for $L/t = 10^5$.

As for the other constants, optimal values have not been found for the ASGS formulation, while in the OSGS formulation $c_1 \leq 10^{-3}$ has proven to give good results. As presented in

Figs. 2.13-2.14 for the OSGS formulation, results prove to converge optimally respect to the element size.

It is important to note that the constants c_3 and c_4, which are associated to τ_w, have little impact on the solution. This is explained in detail in subsection 2.8.3. Recall that the theory does not predict locking-free convergence for the ASGS formulation. Lastly, the dependency of the thickness is evaluated by comparing the L^2 error norm for the different thicknesses. As presented in Fig. 2.15, the accuracy of the solution does not depend on the thickness of the plate.

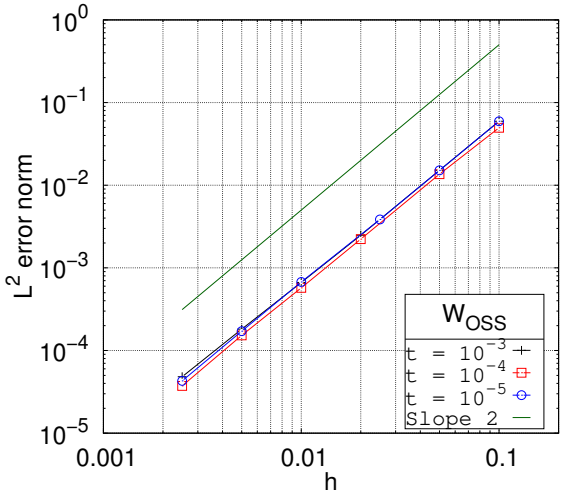

Figure 2.15: Plate displacement L^2-error norm for different thicknesses using OSGS stabilization.

2.8.3 Sensitivity to stabilization constants

In this subsection, the sensitivity of the numerical solution to the stabilization constants is checked using numerical examples. When evaluating the convergence of the ASGS formulation for beams, the stabilization parameters were set using the constants $c_1 = c_3 = 12$ obtained from the elastic equations, which is not possible in plates. Even though in the beam case the constants are well defined for the ASGS formulation, it is important to check the performance of both ASGS and OSGS formulations for any set of constants. To address this, consider the same clamped beam with uniform load discussed previously in this section, the problem is solved repeatedly for different values of c_1 and c_3, which are modified independently.

In the ASGS case, for the slenderness ratio of $L/t = 10^5$ several values of the stabilization constants are tested. The constant c_1 is tested for slightly perturbed values, namely 12 ± 0.1 and c_3 is tested for a set of values ranged in $[2, 20]$, as shown in Fig. 2.17. Results show that the best convergence ratio is obtained for $c_1 = c_3 = 12$, however, a slight variation of c_1 is enough to lock the problem in a constant error independently of the element size, while c_3 allows a more flexible range of working values. The numerical tests confirm that the values obtained from the elastic equations provide the best behavior of the solution, which cannot be found in the case of plates. Regarding this, the convergence ratio curves of the ASGS formulation for plates has the same behavior as the first image in Figs. 2.16-2.17. Since the values of $c_1 = c_3 = 12$ are not valid for plates and the constants that provide optimal convergence were were not found, results similar to Fig. 2.17 can not be replicated.

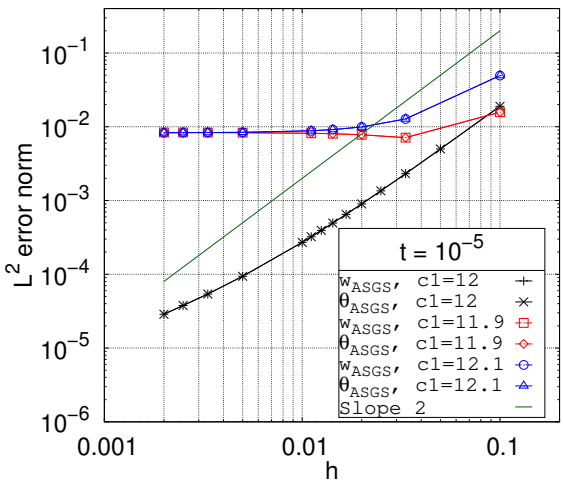

Figure 2.16: Sensitivity to c_1 in $L2$-error norm, for $L/t = 10^5$.

In the case of the OSGS formulation, the stabilization constants do not have a significant impact on the final solution when $c_1 \leq 10^{-3}$. In this regard, the flexibility to choose any value for c_3 has to be assessed properly. Let us compute the convergence curves for the same beam case presented above, but this time to compare the results of extreme values of c_3, as presented in Fig. 2.18.

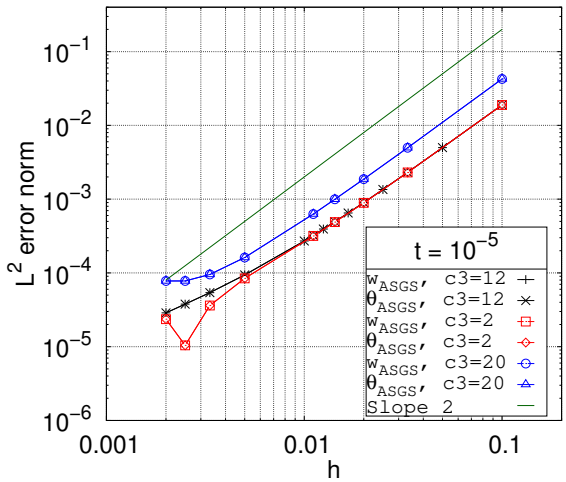

Figure 2.17: Sensitivity to c_3 in $L2$-error norm, for $L/t = 10^5$.

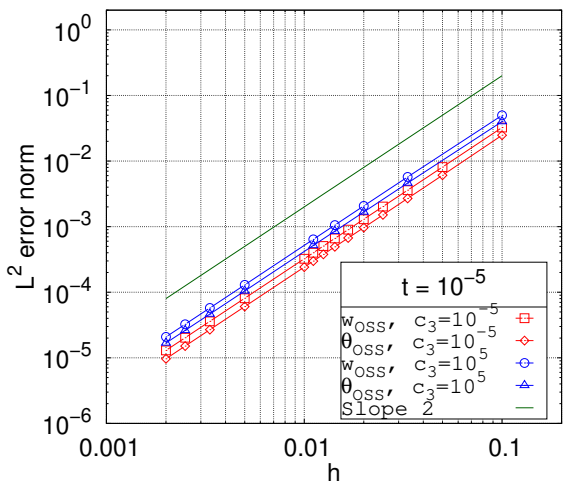

Figure 2.18: $L2$-error norm for different values of c_3, for $L/t = 10^5$.

Results show that the curves are almost identical independently of the value of c_3. This is, however, an important feature of the formulation: for high values of c_3, the influence of the terms that contain τ_w is reduced, and in fact, it would be more useful not to consider them at all. From the practical point of view, this is equivalent to remove the projection of the force equilibrium equation, or ξ_w, from the formulation, lowering the total number of degrees of freedom. This response to stabilization constants behaves exactly the same for plates as well, and the fact that the number of degrees of freedom of the formulation can be reduced is specially useful for lowering the cost of computations.

2.8.4 Applied examples

Three numerical examples are solved to illustrate the performance of the OSGS formulation with respect to the Galerkin formulation. The cases presented below are just a few of the many examples found in the literature. Results presented show that the OSGS formulation is free of locking and converges to the exact solution much faster than the locked solution obtained using the Galerkin approach. This behavior is independent of the thickness of the plate, which is consistent with the convergence tests presented in 2.8.2.

Clamped circular plate with uniform load

Consider a clamped circular plate of radius $R = 5$ loaded with an uniform load of $q = 1$. The geometry, mesh, and boundary conditions are set up as in standard manner described in the literature [47–50], the solution of circular loaded plates set with different boundary conditions are described in [51]. Due to the symmetry of the case, only a quarter of the geometry is modelled and symmetry boundary conditions are set in both straight sides. The mesh structure, which is built in three patches of square elements, and the deformed configuration are illustrated in Figs. 2.19-2.20.

[47]: Shang et al. (2015), *Two generalized conforming quadrilateral Mindlin–Reissner plate elements based on the displacement function*
[48]: Yunhua et al. (1999), *An alternative assumed strain method*
[49]: Ribarić et al. (2012), *Higher-order linked interpolation in quadrilateral thick plate finite elements*
[50]: Cen et al. (2014), *Hybrid displacement function element method: a simple hybrid-Trefftz stress element method for analysis of Mindlin–Reissner plate*
[51]: Young et al. (2012), *Roark's formulas for stress and strain*

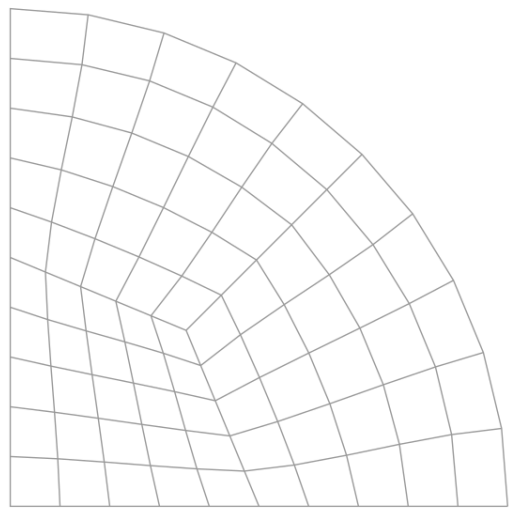

Figure 2.19: Clamped circular plate with uniform load: Mesh.

Cases are computed for two different thicknesses: $t = 0.1$ and $t = 0.01$ which correspond to slenderness ratios of $R/t = 50$

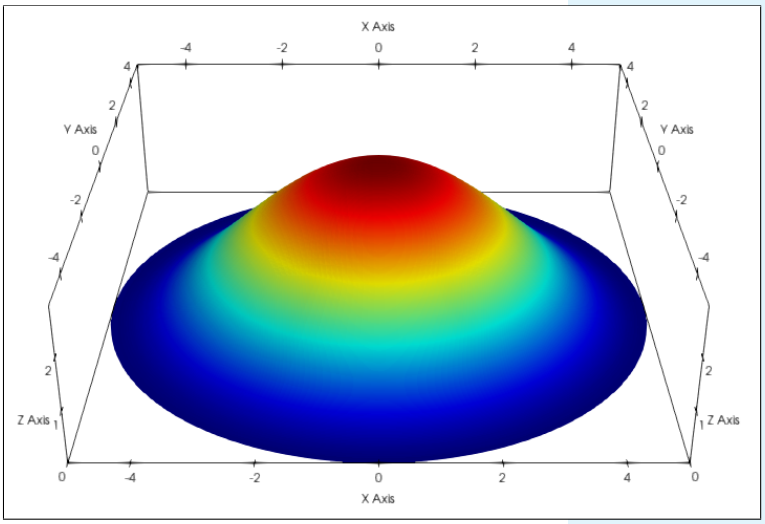

Figure 2.20: Clamped circular plate with uniform load: deformed configuration.

and $R/t = 500$, respectively. These values are chosen to test cases with high shear-locking effects. For the assessment, the displacements are tracked at the center of the plate ($R = 0$), where they reach their maximum values. Results are shown in Figs. 2.21-2.22.

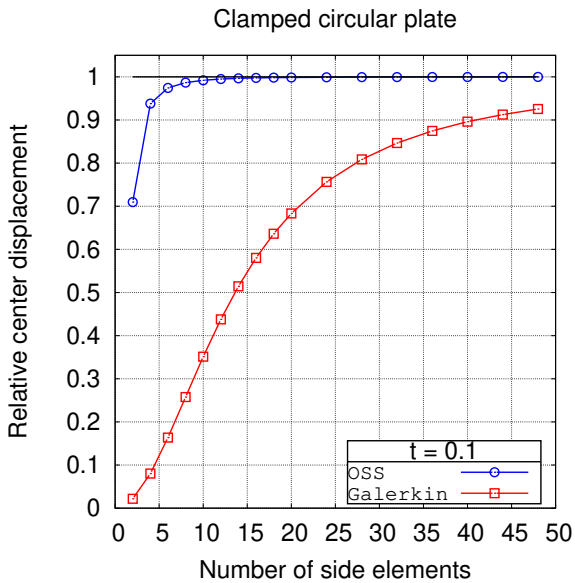

Figure 2.21: Clamped circular plate with uniform load: relative maximum displacements for $t = 0.1$.

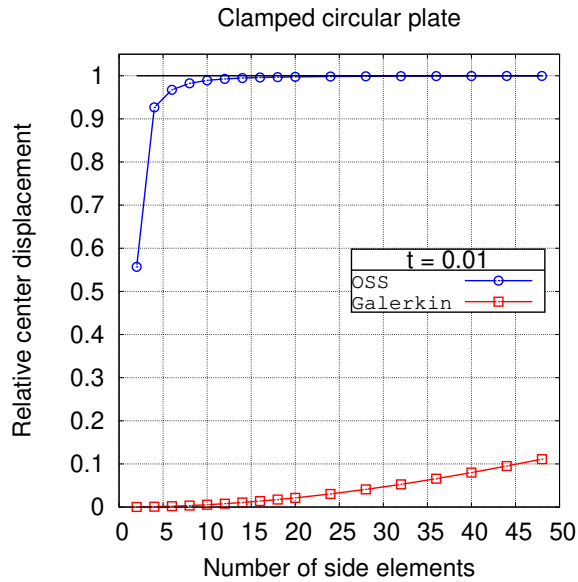

Figure 2.22: Clamped circular plate with uniform load: relative maximum displacements for $t = 0.01$.

Simply supported annular plate with uniform load

Consider a simply supported annular plate of inner radius of $R_i = 1.5$ and outter radius $R_o = 5$, which again correspond to slenderness ratios of $R_o/t = 50$ and $R_o/t = 500$, respectively, and loaded with an uniform load of $q = 1$. The solution of loaded annular plate problems are also described in [51].

[51]: Young et al. (2012), *Roark's formulas for stress and strain*

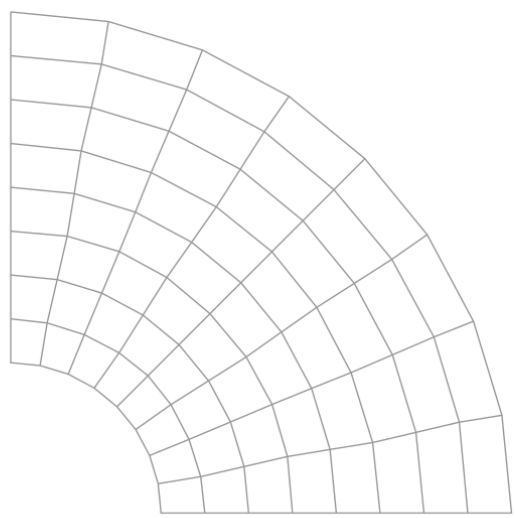

Figure 2.23: Simply supported annular plate with uniform load: Mesh.

As in the previous case, only a quarter of the geometry is needed and symmetry boundary conditions are set in the straight sides. The mesh, which consists square elements aligned in the radial direction, and the deformed configurations are illustrated in Figs. 2.23-2.24.

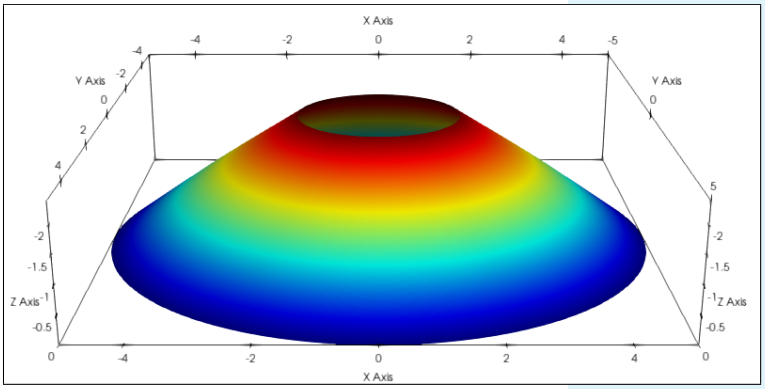

Figure 2.24: Simply supported annular plate with uniform load: deformed configuration.

The cases are computed using thicknesses of $t = 0.1$ and $t = 0.01$ for the same reason as the previous case. In this example the displacements are tracked at the inner radius of the plate, where they reach their maximum values. Results are shown in Figs. 2.25-2.26.

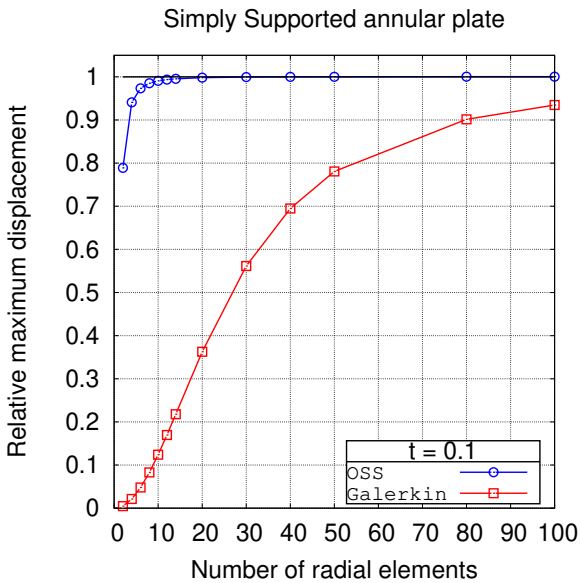

Figure 2.25: Simply supported annular plate with uniform load: relative maximum displacements for $t = 0.1$.

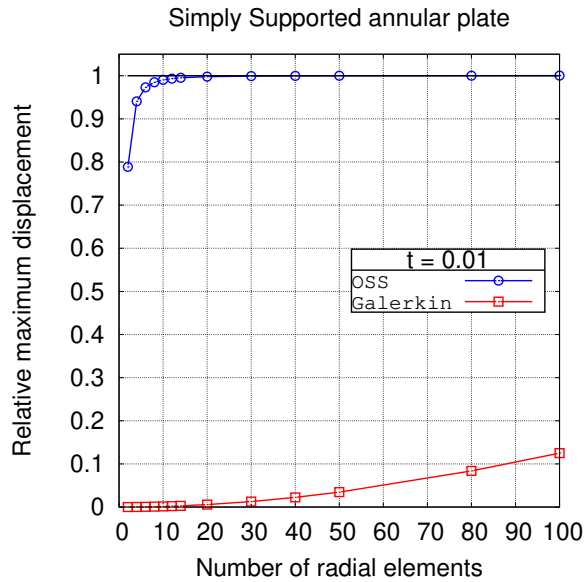

Figure 2.26: Simply supported annular plate with uniform load: relative maximum displacements for $t = 0.01$.

Cantilever plate with hole

The last case consists in a cantilever plate loaded with an uniform load of $q = 1$, clamped in the wider straight side. The geometry and mesh are illustrated in Fig. 2.27. The mesh is divided in four patches of four sides each, so that the mesh refinements depend only on the number of elements set in each side.

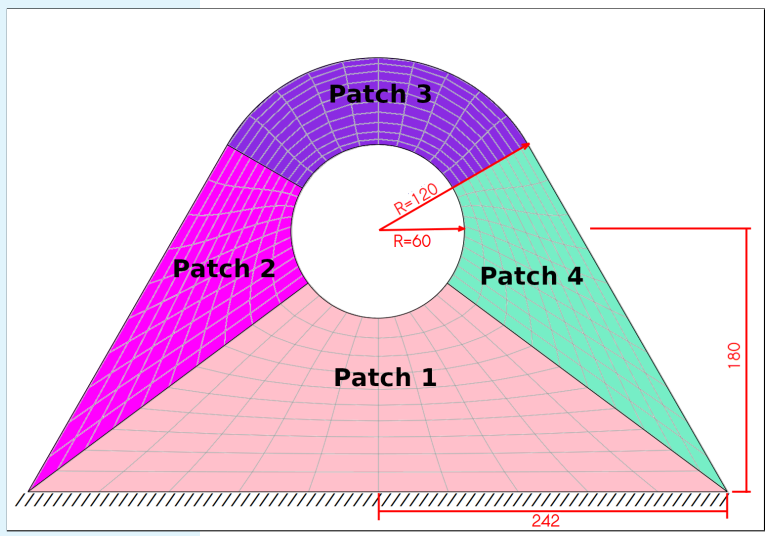

Figure 2.27: Cantilever plate with hole: geometry and mesh.

The cases are computed using thicknesses of $t = 20$ and $t = 5$, which correspond to slenderness ratios of $L/t = 15$ and $L/t = 60$, respectively, and displacements are tracked at the opposite end to the clamped side, where the displacement reach their maximum value, the deformed geometry is illustrated in Fig. 2.28. In the case of $t = 20$, results converge to $7.4341 \cdot 10^{-4}$ similar to those presented in [52]. In the more slender case of $t = 5$ the result converges to 0.046546 with mesh refinement. Note that since it is a linear elastic problem, result are proportional to the cube of the thickness, which is $(20/5)^3 = 64$, with respect to the known solution.

[52]: Du et al. (2015), *Nitsche method for isogeometric analysis of Reissner–Mindlin plate with non-conforming multi-patches*

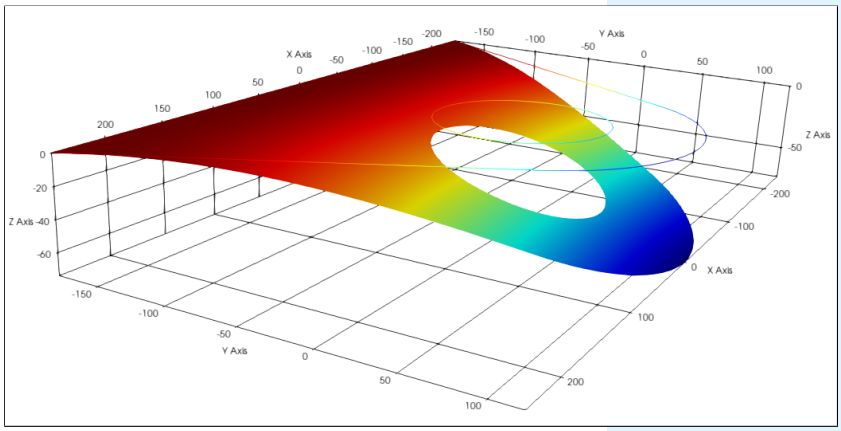

Figure 2.28: Cantilever plate with hole: deformed geometry.

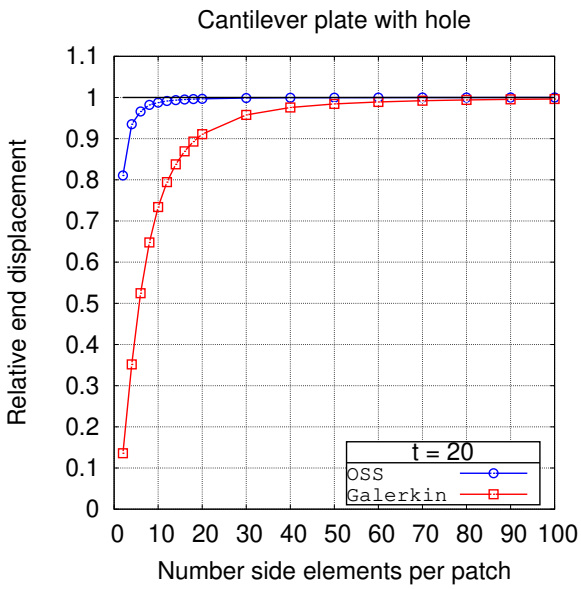

Figure 2.29: Cantilever plate with hole: relative maximum displacements for $t = 20$.

Results obtained for both thicknesses, including the comparison of the OSGS and the Galerkin formulations are shown in Figs. 2.29-2.30. Note that the converged results are used to compute the relative displacements.

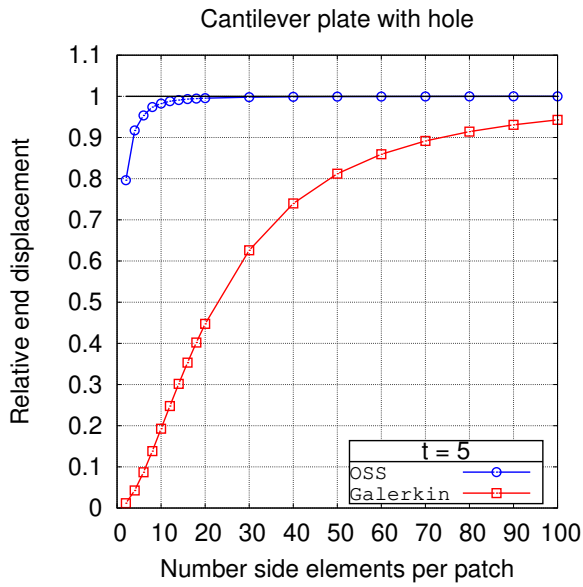

Figure 2.30: Cantilever plate with hole: relative maximum displacements for $t = 5$.

2.9 Conclusions

The numerical locking present in standard Galerkin formulations of Reissner-Mindlin plates and Timoshenko beams has been addressed using the Variational Multiscale Method. This, by itself, has the theoretical interest of developing a stable formulation for beams and plates using the same principles that have led to stable and accurate numerical formulations in many other areas of computational engineering. Two particular VMS formulations have been developed in this chapter using the ASGS and the OSGS stabilization. It has been shown that the norm in which stability can be proved for the ASGS formulation is not free of locking when $t \to 0$, whereas optimal stability and convergence has been proven for the OSGS approach for arbitrary interpolation of the variables. Nevertheless, for Timoshenko beams there exists a set of algorithmic constants for which the element stiffness matrix of the ASGS formulation coincides with that of the elastic equations, and in this case the method does converge. This, however, has to be considered a singularity rather than a general possibility.

The practical interest of the formulation developed is twofold. First, it has less degrees of freedom than than other formulations that interpolate shear and, furthermore, it can be implemented iteratively so as to use only displacements and rotations as unknowns. And, second, contrary to most locking-free methods, it is applicable to any type of elements, triangles or quads of any order and with arbitrary interpolations for displacements and rotations.

Numerical tests confirm that the theoretical predictions. In particular, the OSGS formulation provides optimally convergent rates, for both displacement and rotations. Moreover, this method is shown to be mildly sensitive to the algorithmic constants. In particular, in the numerical experiments presented it has been unnecessary to activate the stabilization terms corresponding to deflections to obtain optimally convergent results.

Acknowledgement

This work was supported by Vicerrectoría de Investigación, Desarrollo e Innovación (VRIDEI) of the Univeridad de Santiago de Chile, and the National Agency for Research and Development (ANID) Doctorado Becas Chile/2019 - 72200128 of the Government of Chile. R. Codina acknowledges the support received from the ICREA Acadèmia Research Program of the Catalan Government.

Declarations

Conflict of interest

The authors declare that they have no known competing financial interests or personal relationships that could have appeared to influence the work reported in this paper.

Replication of results

All the information required for replicating the paper results was duly presented. Data files for the results are available upon request from the authors.

Stress-displacement formulations for Solid-Shell Finite Elements

3

3.1 Abstract

This work studies the solid-shell finite element approach to approximate thin structures using a stabilized mixed two-field formulation based on the Variational Multiscale framework. The numerical locking effects inherent to the solid-shell approach are characterized using a variety of benchmark problems in the infinitesimal strain approximation. In the present work, the stabilized mixed displacement-stress formulation is proven to be adequate to deal with all kinds of numerical locking. Additionally, a more comprehensive analysis of each individual type of numerical locking, how it is triggered and how it is overcome is also provided. The numerical locking usually occurs when parasitic strains overtake the system of equations through specific components of the stress tensor. To properly analyze them, the direction of each component of the stress tensor has been defined respect to the shell directors. Therefore, it becomes necessary to formulate the solid-shell problem in curvilinear coordinates, allowing to give mechanical meaning to the stress components (shear, twisting, membrane and thickness stresses) independently of the global frame of reference. The conditions in which numerical locking is triggered as well as the stress tensor component responsible of correcting the locking behavior have been identified individually by characterizing the numerical response of a set of different benchmark problems.

3.2 Introduction

Structural elements have played an important role in the development of technology. The reason is that thin structures are the most common in nature and have proven to be essential engineering tools along history [9]. They are usually modeled as a dimensional reduction of a 3D solid where one or two of its dimensions are much thinner than the others. In this manner, beam and rod formulations have been developed to approximate thin structures with two reduced dimensions, while plate and shell formulations have been developed to model structures of a single dimension reduction [1].

In the finite element literature, shell models are usually classified into three different groups: the classical shell elements, the continuum based elements and the solid-shell elements. As the name suggest, the classical shell elements are based on conventional theories of plates and shells [53–61]; therefore, they inherently use rotational degrees of freedom to describe the kinematics with respect to the mid-surface of the shell. The continuum based shell elements, usually called degenerated elements, were first introduced by Ahmad et al. [62]. These elements are directly constructed from the continuum equations [63–65]. The derivation of these elements is straightforward, and it requires to enforce kinematic constrains to the upper and lower surfaces with respect to the shell mid-surface using rotational degrees of freedom, and thus, the enforcement of the inextensibility of the shell director. Both classical and continuum based approaches usually require to either impose the inextensibility of the director or to enforce the plane stress constraint [63, 66]; the reader can also refer to [67, 68] for a comparison between these two approaches. The solid-shell approach consists in the approximation of thin structures using 3D elements; the idea was first introduced by Hauptmann et al. [69]. In other words, this approach employs a 3D solid approximation that explicitly considers the nodes at the upper and lower surfaces of the structure and uses displacement degrees of freedom. This approach takes the advantage of not requiring additional kinematic assumptions and allows the use of three dimensional constitutive equations, at the cost of an increased size of the system of equations.

The most important difference between the approaches de-

[9]: Belytschko et al. (2014), *Nonlinear finite elements for continua and structures*

[1]: Oñate (2013), *Structural analysis with the finite element method. Linear statics: volume 2: beams, plates and shells*

[53]: Reissner (1972), *On one-dimensional finite-strain beam theory: the plane problem*

[54]: Macneal (1982), *Derivation of element stiffness matrices by assumed strain distributions*

[55]: Belytschko et al. (1986), *Efficient implementation of quadrilaterals with high coarse-mesh accuracy*

[56]: Simo et al. (1990), *On a stress resultant geometrically exact shell model. Part III: Computational aspects of the nonlinear theory*

[57]: Büchter et al. (1994), *Three-dimensional extension of non-linear shell formulation based on the enhanced assumed strain concept*

[58]: Bucalem et al. (1997), *Finite element analysis of shell structures*

[59]: Bischoff et al. (1997), *Shear deformable shell elements for large strains and rotations*

[60]: Romero (2008), *A comparison of finite elements for nonlinear beams: the absolute nodal coordinate and geometrically exact formulations*

[61]: Valle et al. (2019), *An efficient general curvilinear coordinates finite element method for the linear dynamic study of thickness-independent shells*

[62]: Ahmad et al. (1970), *Analysis of thick and thin shell structures by curved finite elements*

[63]: Kant et al. (1994), *Shell dynamics with three-dimensional degenerate finite elements*

[64]: Yang et al. (2000), *A survey of recent shell finite elements*

[65]: Marinković et al. (2008), *Degenerated shell element for geometrically nonlinear analysis of thin-walled piezoelectric active structures*

scribed comes from the treatment of the through-the-thickness integration. In regard of this, Bischoff et al. [11] made a comprehensive revision concerning the models used for finite element approximations of thin structures. This reference revises in depth the three approaches, in the linear and nonlinear cases. What all approaches share in common is the tendency to suffer numerical locking. In this context, classical shell elements are subject to shear and membrane locking. However, continuum based shell and solid-shell elements are also subject to trapezoidal and thickness locking, particularly using low order elements [70].

The present work focuses specifically in the study of thin structures using a stabilized finite element method applied to solid-shell elements. This type of elements are subject to all kinds of numerical locking when approximated using the standard irreducible Galerkin approach and low order elements. Therefore, all the locking effects have to be properly evaluated; these are:

- Shear locking is usually described in the classical shell context as the inability of a thin structure to represent zero bending strains [1]. In the context of solid-shell elements, it appears when the shell is not able to reproduce a correct coupling between the in-plane translation of its upper and lower surfaces with respect to the transverse translation of the mid-surface. For this reason, shear-locking is present in flat and curved structures subject to bending states, and the effect becomes greater as the thickness gets smaller. As a consequence of this, parasitic transverse shear strains cause an overstiffening of the structure, leading to spurious results.
- Membrane locking appears due to the inability of the shell to reproduce the coupling between the in-plane translation of its upper and lower surfaces with respect to the in-plane translation of the mid-surface. Obviously, this implies that membrane locking only appears in curved structures [71]. In this case this locking manifests itself as parasitic membrane strains when subject to inextensional bending deformations, leading to increased stiffening of the structure as well, and the locking effect intensifies as the structure gets thinner.
- Poisson thickness locking occurs when through-the-thickness displacement is approximated linearly in a bending state. The linear approximation implies that the normal transverse strains get approximated as a constant. At the

[63]: Kant et al. (1994), *Shell dynamics with three-dimensional degenerate finite elements*

[66]: Betsch et al. (1996), *A 4-node finite shell element for the implementation of general hyperelastic 3D-elasticity at finite strains*

[67]: Buechter et al. (1992), *Shell theory versus degeneration a comparison in large rotation finite element analysis*

[68]: Büchter et al. (1992), *Comparison of shell theory and degeneration*

[69]: Hauptmann et al. (1998), *A systematic development of 'solid-shell' element formulations for linear and non-linear analyses employing only displacement degrees of freedom*

[11]: Bischoff et al. (2004), *Models and finite elements for thin-walled structures*

[70]: Doll et al. (2000), *On volumetric locking of low-order solid and solid-shell elements for finite elastoviscoplastic deformations and selective reduced integration*

[1]: Oñate (2013), *Structural analysis with the finite element method. Linear statics: volume 2: beams, plates and shells*

[71]: Sze (2002), *Three-dimensional continuum finite element models for plate/shell analysis*

same time, the in-plane strains vary linearly in the thickness direction. Normal transverse and in-plane strains are coupled through Poisson's ratio. Therefore, locking arises due to the incompatibility of the approximation between the constant normal transverse strain coupled with in-plane strains which vary linearly in the transverse direction. The locking effect is only proportional to Poisson's ratio and is not affected by the thickness of the structure.

- Trapezoidal locking occurs in solid-shell elements when the shell directors defined by the element edges are not parallel [72]. It creates parasitic normal transverse strains due to the faulty coupling between the in-plane bending and the transverse extension of the element.
- Volumetric locking occurs when the material is incompressible or approaches incompressibility. The material bulk modulus increases uncontrollably and, since it scales the volumetric strains, it creates parasitic strains in the normal directions. Therefore it affects the membrane in-plane and the normal thickness strains [70].

A vast amount of research has been done with the objective of solving all kinds of numerical locking in the solid-shell context. The locking effects are mostly due to parasitic strains in a specific direction, and different approaches were focused on treating each one of them individually.

One of the most influential approaches was the Assumed Strain (AS) method, first developed by MacNeal in [73] for classic shell theory problems. It was followed by Assumed Natural Strain (ANS) methods [74]. Another important contribution to the subject was introduced by Simo and Hughes in [75] using a variational framework, which led to the Enhanced Assumed Strains (EAS) method [76]. These approaches were eventually adopted for solid-shell elements [77]. Notable developments were done by Klinkel et al [78] using ANS and EAS in linear and finite strain problems, and by Sze et al. using ANS [79, 80] to solve linear and non-linear problems, and using EAS [81] to solve hyperelastic problems. The AS, ANS and EAS approaches have endured through time, and can be found in more recent literature. Kim et al. [82] used the ANS method together with a Resultant Force formulation to solve solid-shell in finite strain problems. Hajlaoui et al. [83] developed a high order solid-shell element based on the EAS to solve buckling in solid-shell problems, and used ANS in the thickness direction to avoid locking effects.

[72]: MacNeal (1989), *Toward a defect-free four-noded membrane element*

[70]: Doll et al. (2000), *On volumetric locking of low-order solid and solid-shell elements for finite elastoviscoplastic deformations and selective reduced integration*

[73]: MacNeal (1978), *A simple quadrilateral shell element*

[74]: Park et al. (1986), *A curved C^0 shell element based on assumed natural-coordinate strains*

[75]: Simo et al. (1986), *On the variational foundations of assumed strain methods*

[76]: Simo et al. (1990), *A class of mixed assumed strain methods and the method of incompatible modes*

[77]: Belytschko et al. (1993), *Assumed strain stabilization of the eight node hexahedral element*

[78]: Klinkel et al. (1999), *A continuum based three-dimensional shell element for laminated structures*

[79]: Sze et al. (2000), *A hybrid stress ANS solid-shell element and its generalization for smart structure modelling. Part I solid shell element formulation*

[80]: Sze et al. (2000), *A hybrid stress ANS solid-shell element and its generalization for smart structure modelling. Part II smart structure modelling*

[81]: Sze et al. (2004), *A stabilized eighteen-node solid element for hyperelastic analysis of shells*

[82]: Kim et al. (2005), *A resultant 8-node solid-shell element for geometrically nonlinear analysis*

[83]: Hajlaoui et al. (2016), *An improved enhanced solid shell element for static and buckling analysis of shell structures*

Mostafa et al. [84] used a combination of ANS and EAS to deal with all types of numerical locking independently, and solved non-linear problems. Caseiro et al. [85] extended the ANS approach to NURBS based formulations to alleviate shear and membrane locking effects in linear analysis and then extended the approach to non-linear problems [86]. More recently, Huang et al. [87] developed a solid-shell element using the ANS concept in the unsymmetric finite element method.

Another common approach is the use of Reduced Integration (RI), first implemented in classical shell theory [88–90]. The method has found success over the years; however it can lead to spurious zero energy modes, known as hourglassing [91], that need to be stabilized. This is most commonly approached in the literature through assumed strain methods [71]. In this context, Schwarze and Reese used the ANS and EAS approach together with reduced integration and hourglass stabilization to solve linear [92] and finite strain [93] solid-shell problems. Reese [94] worked in a RI approach based in the EAS concept to implement a hourglass stabilization to solve large strain shell problems. Pagani et al. [95] used a RI based solid-shell formulation stabilized with ANS and EAS to solve explicit non-linear problems with selective mass scaling to achieve large critical time steps. The reduced integration approach is still being developed in the solid-shell framework. Leonetti et al. [96] proposed a model based in a combination of linear integration in the thickness direction and NURBS interpolation in the mid-plane that has been successfully used in non-linear problems. Barfusz et al. [97] used a RI based solid-shell element stabilized with ANS and EAS methods to avoid numerical locking, and solved damage plasticity problems with the resulting method.

The Mixed Interpolated Tensorial Components (MITC) method has also proven to be an effective approach to avoid numerical locking [15, 98]. The earlier contributions of this approach come from Dvokin and Bathe [99] in classical shell elements, and it has been studied further ever since [100–102]. Important contributions to the subject have been developed in solid-shell elements by Chapelle et al. [103]. The MITC approach has been one of the major approaches in the solid-shell framework. Sussman and Bathe [104] developed a MITC approach in solid-shell problems to avoid numerical locking, using nodal control vectors to describe large deformations. Recent publications show prominent results us-

[84]: Mostafa et al. (2013), *A solid-shell corotational element based on ANDES, ANS and EAS for geometrically nonlinear structural analysis*

[85]: Caseiro et al. (2014), *On the Assumed Natural Strain method to alleviate locking in solid-shell NURBS-based finite elements*

[86]: Caseiro et al. (2015), *Assumed natural strain NURBS-based solid-shell element for the analysis of large deformation elasto-plastic thin-shell structures*

[87]: Huang et al. (2018), *An unsymmetric 8-node hexahedral solid-shell element with high distortion tolerance: linear formulations*

[88]: Zienkiewicz et al. (1971), *Reduced integration technique in general analysis of plates and shells*

[89]: Naylor (1974), *Stresses in nearly incompressible materials by finite elements with application to the calculation of excess pore pressures*

[90]: Malkus et al. (1978), *Mixed finite element methods - reduced and selective integration techniques: a unification of concepts*

[91]: Belytschko et al. (1984), *Hourglass control in linear and nonlinear problems*

[71]: Sze (2002), *Three-dimensional continuum finite element models for plate/shell analysis*

[92]: Schwarze et al. (2009), *A reduced integration solid-shell finite element based on the EAS and the ANS concept—Geometrically linear problems*

[93]: Schwarze et al. (2011), *A reduced integration solid-shell finite element based on the EAS and the ANS concept—Large deformation problems*

[94]: Reese (2007), *A large deformation solid-shell concept based on reduced integration with hourglass stabilization*

ing the MITC approach in three-dimensional shell problems. Cinefra [105] solved linear solid-shell problems in curvilinear coordinates using MITC in each local strain component to solve numerical locking. Rezaiee et al. [106] used the MITC and ANS approaches together with the arc-length method to solve functionally graded shells in non-linear large deformations problems.

Many other methods have also been employed to solve locking problems, such as the B-bar method. It was first introduced by Hughes in [107] for classic shell theory using linear elements, and it was later developed in solid-shells by Simo et al. [108] using a mixed formulation for stresses formulated with a volumetric-deviatoric split. Hybrid-strain and hybrid-stress methods have also been developed for solid-shell elements in the linear [109, 110] and non-linear regimes [111, 112].

The present work deals with numerical locking in solid-shell problems *introducing additional stresses as new unknowns*, thus leading to a problem whose unknowns are stresses and displacements. The first issue to analyze is how to deal with this mixed problem, i.e., how to treat the possible compatibility conditions between the interpolation of stresses and displacements. We avoid the need to satisfy any of such conditions by using a stabilized finite element formulation based on the Variational Multiscale (VMS) framework, first introduced by Hughes [2, 3] and later developed in [43, 113]. In particular, this method allows us to use equal interpolation for stresses and displacements. Other problems that involve stresses as variables are viscoelastic flows [114, 115] or mixed formulations in solid mechanics [116, 117] (see also [118]).

The second issue to consider is *which* stresses need to be introduced as unknowns. For that, we need to have the *mechanical meaning* of the components of the stress tensor, independently of the global reference system chosen. To this end, we shall write the equilibrium equations in a curvilinear system associated to the shell, with two tangent orthogonal coordinates and a normal one. This will allow us to interpret the stress components as shear, twisting, membrane and thickness stresses. Then, a variety of benchmark cases will determine which of these stresses are required to avoid the different types of numerical locking that can appear. This systematic study is, to our knowledge, completely new. Let us anticipate that the conclusion of our analysis is that *there*

[95]: Pagani et al. (2014), *Computationally efficient explicit nonlinear analyses using reduced integration-based solid-shell finite elements*

[96]: Leonetti et al. (2018), *An efficient isogeometric solid-shell formulation for geometrically nonlinear analysis of elastic shells*

[97]: Barfusz et al. (2021), *A reduced integration-based solid-shell finite element formulation for gradient-extended damage*

[15]: Chapelle et al. (2010), *The finite element analysis of shells-fundamentals*

[98]: Bathe (2006), *Finite element procedures*

[99]: Dvorkin et al. (1984), *A continuum mechanics based four-node shell element for general nonlinear analysis*

[100]: Bathe et al. (2000), *An evaluation of the MITC shell elements*

[101]: Bathe et al. (2000), *An inf-sup test for shell finite elements*

[102]: Jeon et al. (2015), *The MITC3+ shell element in geometric nonlinear analysis*

[103]: Chapelle et al. (2004), *3D-shell elements and their underlying mathematical model*

[104]: Sussman et al. (2013), *3D-shell elements for structures in large strains*

[105]: Cinefra (2022), *Formulation of 3D finite elements using curvilinear coordinates*

[106]: Rezaiee-Pajand et al. (2022), *An evaluation of MITC and ANS elements in the nonlinear analysis of shell structures*

[107]: Hughes (1980), *Generalization of selective integration procedures to anisotropic and nonlinear media*

[108]: Simo et al. (1985), *Variational and projection methods for the volume constraint in finite deformation elasto-plasticity*

are situations in which each of the stress components is necessary to avoid locking.

In this work we will restrict ourselves to linear elasticity, under the infinitesimal strain assumption. Finite strains and hyperelastic materials will be considered in the next chapter. From the results of the present paper, all the stress components and the displacements will be considered as unknowns in this second paper.

This paper is organized as follows. First, we describe the geometrical ingredients to write the elasticity equations in curvilinear coordinates (Section 2) and later we write these equations (to fix notation), both in differential and variational forms (Section 3). The geometrical approximation of the problem is explained in Section 4, and the finite element approximation in Section 5. The numerical experimentation is presented in Section 6 and conclusions are drawn in Section 7.

3.3 Linear elasticity using curvilinear coordinates

This section collects basic results of the theory of elasticity expressed in general curvilinear coordinates (further details can be found in book by Washizu [119]). Regarding the notation employed, Greek indices will correspond to curvilinear coordinates, whereas lower case Latin indices to Cartesian coordinates.

3.3.1 Geometrical description

Let us consider a system of curvilinear coordinates $(\theta^1, \theta^2, \theta^3)$; under the infinitesimal stress assumption, the geometry of the initial and the deformed configurations will be considered equal. The position vector of any point P of curvilinear coordinates $(\theta^1, \theta^2, \theta^3)$ will be given by

$$\mathbf{x} = \mathbf{x}(\theta^1, \theta^2, \theta^3) = x^i \mathbf{e}_i,$$

where $\mathbf{e}_i$, $i = 1, 2, 3$, is the i-th vector of the Cartesian basis and $x^i = x^i(\theta^1, \theta^2, \theta^3)$, $i = 1, 2, 3$ are the functions that relate

[109]: Sze et al. (1993), *Hybrid hexahedral element for solids, plates, shells and beams by selective scaling*

[110]: Sansour et al. (2000), *Families of 4-node and 9-node finite elements for a finite deformation shell theory. An assesment of hybrid stress, hybrid strain and enhanced strain elements*

[111]: Kim et al. (1988), *A solid element formulation for large deflection analysis of composite shell structures*

[112]: Park et al. (1995), *An efficient assumed strain element model with six DOF per node for geometrically non-linear shells*

[2]: Hughes (1995), *Multiscale phenomena: Green's functions, the Dirichlet-to-Neumann formulation, subgrid scale models, bubbles and the origins of stabilized methods*

[3]: Hughes et al. (1998), *The variational multiscale method - A paradigm for computational mechanics*

[43]: Codina (2000), *Stabilization of incompressibility and convection through orthogonal sub-scales in finite element methods*

[113]: Codina (2002), *Stabilized finite element approximation of transient incompressible flows using orthogonal subscales*

[114]: Castillo et al. (2017), *Finite element approximation of the viscoelastic flow problem: A non-residual based stabilized formulation*

[115]: Moreno et al. (2019), *Logarithmic conformation reformulation in viscoelastic flow problems approximated by a VMS-type stabilized finite element formulation*

[116]: Castañar et al. (2023), *A stabilized mixed three-field formulation for stress accurate analysis including the incompressible limit in finite strain solid dynamics*

[117]: Fabra et al. (2023), *Mixed stabilized finite element methods in linear elasticity for the velocity–stress equations in the time and the frequency domains*

[118]: Codina (2009), *Finite element approximation of the three-field formulation of the Stokes problem using arbitrary interpolations*

[119]: Washizu (1968), *Variational methods in elasticity and plasticity*

the curvilinear and the Cartesian coordinates. Here and below, Einstein's summation convention is used, with repeated indexes summing from 1 to 3.

Let the notation $(\cdot)_{,\alpha}$ be the differentiation respect to θ^α, namely $(\cdot)_{,\alpha} = \partial(\cdot)/\partial\theta^\alpha$. The covariant base vectors associated to point P are defined as

$$\mathbf{g}_\alpha = \frac{\partial \mathbf{x}}{\partial \theta^\alpha} = \mathbf{x}_{,\alpha}, \quad \alpha = 1,2,3. \tag{3.1}$$

The covariant base vectors allow the definition of the covariant metric tensor $g_{\alpha\beta}$ as

$$g_{\alpha\beta} = \mathbf{g}_\alpha \cdot \mathbf{g}_\beta, \quad \alpha,\beta = 1,2,3, \tag{3.2}$$

the contravariant metric tensor $g^{\alpha\beta}$ being its inverse, i.e.,

$$g_{\alpha\gamma} g^{\gamma\beta} = \delta^\alpha_\beta, \tag{3.3}$$

where δ^α_γ is the Kronecker symbol. This allows us to define the contravariant base vectors as

$$\mathbf{g}^\alpha = g^{\alpha\beta}\mathbf{g}_\beta. \tag{3.4}$$

The derivatives of covariant vectors respect to θ^α can be obtained as

$$\mathbf{g}_{\alpha,\beta} = (\mathbf{x}_{,\alpha})_{,\beta} = \left(\mathbf{x}_{,\beta}\right)_{,\alpha} = \mathbf{g}_{\beta,\alpha}. \tag{3.5}$$

Additionally, let $\Gamma^\gamma_{\alpha\beta}$ be the three index Christoffel symbol of second kind, which provide a measure of the curvature of the coordinate axes through space, defined as

$$\Gamma^\gamma_{\alpha\beta} = \mathbf{g}_{\alpha,\beta} \cdot \mathbf{g}^\gamma = -\mathbf{g}^\gamma{}_{,\alpha} \cdot \mathbf{g}_\beta. \tag{3.6}$$

The Christoffel symbols allow us to write the derivatives of the covariant and contravariant base vectors as:

$$\mathbf{g}_{\alpha,\beta} = \Gamma^\gamma_{\alpha\beta}\mathbf{g}_\gamma, \quad \mathbf{g}^\alpha{}_{,\beta} = -\Gamma^\alpha_{\gamma\beta}\mathbf{g}^\gamma.$$

Consider next a vector field in space $\mathbf{u}\left(\theta^1,\theta^2,\theta^3\right)$. This can be written both in terms of the covariant components u_α or contravariant components u^α as

$$\mathbf{u} = u^\alpha \mathbf{g}_\alpha = u_\alpha \mathbf{g}^\alpha. \tag{3.7}$$

By using the definition in equation (3.6), the differentiation

of $\mathbf{u}$ respect to θ^β results in

$$\begin{aligned}
\mathbf{u}_{,\beta} &= (u^\alpha \mathbf{g}_\alpha)_{,\beta} && = (u_\alpha \mathbf{g}^\alpha)_{,\beta} \\
&= u^\alpha{}_{,\beta}\mathbf{g}_\alpha + u^\alpha \mathbf{g}_{\alpha,\beta} && = u_{\alpha,\beta}\mathbf{g}^\alpha + u_\alpha \mathbf{g}^\alpha{}_{,\beta} \\
&= u^\alpha{}_{,\beta}\mathbf{g}_\alpha + u^\alpha \Gamma^\gamma_{\alpha\beta}\mathbf{g}_\gamma && = u_{\alpha,\beta}\mathbf{g}^\alpha - u_\alpha \Gamma^\alpha_{\gamma\beta}\mathbf{g}^\gamma \\
&= u^\alpha{}_{|\beta}\mathbf{g}_\alpha && = u_{\alpha|\beta}\mathbf{g}^\alpha
\end{aligned} \tag{3.8}$$

where $(\cdot)_{\cdot|\beta}$ represents the covariant differentiation of the vector component. It can be obtained either for the covariant or contravariant components of a vector field, respectively as

$$u^\alpha{}_{|\beta} = u^\alpha{}_{,\beta} + u^\gamma \Gamma^\alpha_{\gamma\beta}, \qquad u_{\alpha|\beta} = u_{\alpha,\beta} - u_\gamma \Gamma^\gamma_{\alpha\beta}.$$

3.3.2 Transformation of the stress and the strain tensors

Let us obtain the transformation rule of the stress and the strain tensors between their Cartesian components written in terms of the Cartesian coordinates (x^1, x^2, x^3) and their curvilinear components written in terms of the curvilinear coordinates $(\theta^1, \theta^2, \theta^3)$. Differentiation respect to θ^α and x^i, $\alpha, i = 1, 2, 3$, can be related using the chain rule as

$$\frac{\partial(\,)}{\partial\theta^\alpha} = \frac{\partial(\,)}{\partial x^i}\frac{\partial x^i}{\partial\theta^\alpha}, \qquad \frac{\partial(\,)}{\partial x^i} = \frac{\partial(\,)}{\partial\theta^\alpha}\frac{\partial\theta^\alpha}{\partial x^i}.$$

Making use of this and equation (3.1) it becomes clear that

$$\mathbf{g}_\alpha = \frac{\partial \mathbf{x}}{\partial\theta^\alpha} = \frac{\partial \mathbf{x}}{\partial x^i}\frac{\partial x^i}{\partial\theta^\alpha} = \frac{\partial x^i}{\partial\theta^\alpha}\mathbf{e}_i, \tag{3.9}$$

and

$$\mathbf{e}_i = \frac{\partial \mathbf{x}}{\partial x^i} = \frac{\partial \mathbf{x}}{\partial\theta^\alpha}\frac{\partial\theta^\alpha}{\partial x^i} = \frac{\partial\theta^\alpha}{\partial x^i}\mathbf{g}_\alpha. \tag{3.10}$$

Scalar multiplication of equation (3.9) by $\mathbf{e}^i \equiv \mathbf{e}_i$ yields

$$\frac{\partial x^i}{\partial\theta^\alpha} = \mathbf{e}^i \cdot \mathbf{g}_\alpha, \tag{3.11}$$

and similarly, scalar multiplication of equation (3.10) by $\mathbf{g}^\alpha$ yields

$$\frac{\partial\theta^\alpha}{\partial x^i} = \mathbf{e}_i \cdot \mathbf{g}^\alpha. \tag{3.12}$$

For the variables in curvilinear coordinates, consider the displacement vector field $\mathbf{u}$, the second order stress and strain

fields $\boldsymbol{\sigma}$ and $\boldsymbol{\varepsilon}$, respectively, and the fourth order elasticity tensor $\mathbb{C}$. Let the variables in the Cartesian basis be represented as $\hat{(\cdot)}$, assumed to be expressed in terms of the Cartesian coordinates. As detailed in [119], it follows that the transformation laws between Cartesian and curvilinear coordinates are:

[119]: Washizu (1968), *Variational methods in elasticity and plasticity*

$$\hat{\sigma}^{ij} = \frac{\partial x^i}{\partial \theta^\alpha}\frac{\partial x^j}{\partial \theta^\beta}\sigma^{\alpha\beta}, \tag{3.13}$$

$$\hat{\varepsilon}_{ij} = \frac{\partial \theta^\alpha}{\partial x^i}\frac{\partial \theta^\beta}{\partial x^j}\varepsilon_{\alpha\beta}, \tag{3.14}$$

$$\hat{u}_i = \frac{\partial \theta^\alpha}{\partial x^i}u_\alpha, \tag{3.15}$$

$$\hat{\mathbb{C}}^{ijkl} = \frac{\partial x^i}{\partial \theta^\alpha}\frac{\partial x^j}{\partial \theta^\beta}\frac{\partial x^k}{\partial \theta^\gamma}\frac{\partial x^l}{\partial \theta^\delta}\mathbb{C}^{\alpha\beta\gamma\delta}. \tag{3.16}$$

The inverse transformation rules are

$$\sigma^{\alpha\beta} = \frac{\partial \theta^\beta}{\partial x^j}\frac{\partial \theta^\alpha}{\partial x^i}\hat{\sigma}^{ij}, \tag{3.17}$$

$$\varepsilon_{\alpha\beta} = \frac{\partial x^j}{\partial \theta^\beta}\frac{\partial x^i}{\partial \theta^\alpha}\hat{\varepsilon}_{ij}, \tag{3.18}$$

$$u_\alpha = \frac{\partial x^i}{\partial \theta^\alpha}\hat{u}_i, \tag{3.19}$$

$$\mathbb{C}^{\alpha\beta\gamma\delta} = \frac{\partial \theta^\delta}{\partial x^l}\frac{\partial \theta^\gamma}{\partial x^k}\frac{\partial \theta^\beta}{\partial x^j}\frac{\partial \theta^\alpha}{\partial x^i}\hat{\mathbb{C}}^{ijkl}. \tag{3.20}$$

We shall come back to some of these transformations later on.

Figure 3.1 represents the stress components in both the curvilinear and the Cartesian bases, in this case both seen from the Cartesian reference system. As usual, this representation is done on an element of solid, now considering that it is thin in one direction, namely, that of θ^3 in curvilinear coordinates (see below). The key idea is that if we consider that the solid is a shell whose mid surface is parametrized by θ^1 and θ^2, we can provide of mechanical meaning the stress components in curvilinear coordinates, but not in Cartesian coordinates. Indeed, in the situation represented in Fig. 3.1, σ^{11} and σ^{22} are the membrane stresses (the stresses tangent to the shell), $\sigma^{12} = \sigma^{21}$ are the twisting stresses (the stresses that cause rotation on the planes tangent to the shell), $\sigma^{13} = \sigma^{31}$, $\sigma^{23} = \sigma^{32}$ are the shear stresses (stresses on the faces of the solid element perpendicular to the shell and pointing in the perpendicular direction) and σ^{33} is the transverse stress (the stress

on the shell surface and normal to it). This mechanical interpretation is not possible in Cartesian coordinates.

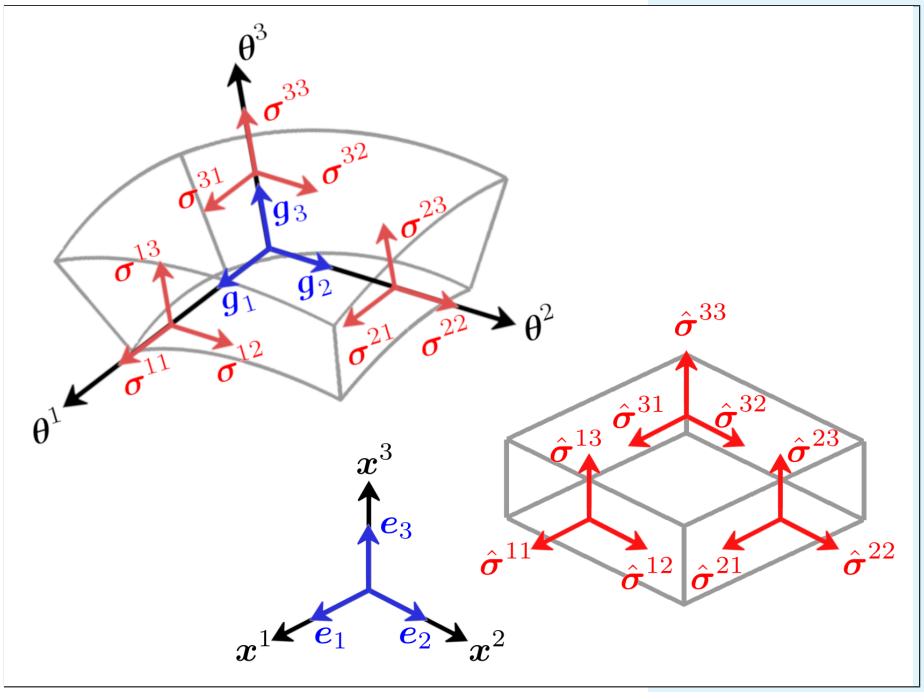

Figure 3.1: Notation for the stress components. In curvilinear coordinates, the stresses can be grouped as follows: σ^{11}, σ^{22} are the membrane stresses; $\sigma^{12} = \sigma^{21}$ are the twisting stresses; $\sigma^{13} = \sigma^{31}$, $\sigma^{23} = \sigma^{32}$ are the shear stresses; σ^{33} is the transverse stress. In Cartesian coordinates, this physical interpretation is not possible.

3.4 Governing equations

3.4.1 Differential form

Let us write the governing equations for the linear elasticity problem in a frame invariant (intrinsic) form. This will serve us to introduce the notation employed in the finite element approximation of the problem. Consider Ω to be the domain occupied by the solid in $\mathbb{R}^3$ and $\partial\Omega$ its boundary. The static equations of motion, the constitutive equations for stress, and the kinematic equations for the strain-displacement relationship are written, respectively, as

Governing equations

$$-\nabla\cdot\boldsymbol{\sigma} = \rho\mathbf{b} \quad \text{in } \Omega, \tag{3.21}$$
$$\boldsymbol{\sigma} - \mathbb{C} : \boldsymbol{\varepsilon} = \mathbf{0} \quad \text{in } \Omega, \tag{3.22}$$
$$\boldsymbol{\varepsilon} - \nabla^s\mathbf{u} = \mathbf{0} \quad \text{in } \Omega, \tag{3.23}$$

where ρ is the density, $\mathbf{b}$ are the body forces per unit of mass, and $\nabla^s\mathbf{u}$ is the symmetric gradient of the displacement.

Additional notation is necessary to build the formulations below. Let us define, in a general manner, a linear differential operator $\mathscr{L}$, the associated trace operator $\mathscr{D}$ that makes the following problem well defined, and a external force vector $\mathbf{F}$. Consider $\mathbf{U}$ to be the unknown of n components of the problem, to be defined for each specific formulation. The solid mechanics problem can be written in an abstract form as the problem of finding $\mathbf{U} : \Omega \to \mathbb{R}^n$ such that

$$\mathscr{L}\mathbf{U} = \mathbf{F} \quad \text{in } \Omega, \tag{3.24}$$
$$\mathscr{D}\mathbf{U} = \bar{\mathbf{U}} \quad \text{on } \partial\Omega. \tag{3.25}$$

We will consider $\bar{\mathbf{U}} = \mathbf{0}$ for simplicity.

Let us consider first the irreducible form of the solid problem in terms of the displacements, by replacing the strain in equation (3.23) into equation (3.22), and replacing the stress into equation (3.21). The strong form of the problem reduces to finding the unknown $\mathbf{U} = \mathbf{u}$, and now the linear operator and the external forces vector take the form $\mathscr{L} = \mathscr{L}_u$ and $\mathbf{F}_u$, respectively, where

$$\mathscr{L}_u\mathbf{u} = -\nabla\cdot\mathbb{C} : \nabla^s\mathbf{u}, \qquad \mathbf{F}_u = \rho\mathbf{b}.$$

In this case, $n = 3$ and $\mathscr{D}\mathbf{U} = \mathbf{u}$.

As for the mixed form of the problem, the two field displacement-stress approach is formulated by considering equations (3.21)-(3.23) and replacing the strains from equations (3.23) into equation (3.22). The mixed problem reduces to finding the unknown $\mathbf{U} = [\mathbf{u}, \boldsymbol{\sigma}]$, and now the linear operator and the external forces vector take the form $\mathscr{L} = \mathscr{L}_{\sigma u}$ and $\mathbf{F}_{\sigma u}$, respectively, where

$$\mathscr{L}_{\sigma u}\mathbf{U} = \begin{bmatrix} -\nabla\cdot\boldsymbol{\sigma} \\ \boldsymbol{\sigma} - \mathbb{C} : \nabla^s\mathbf{u} \end{bmatrix}, \qquad \mathbf{F}_{\sigma u} = \begin{bmatrix} \rho\mathbf{b} \\ \mathbf{0} \end{bmatrix},$$

and $D[\mathbf{u},\boldsymbol{\sigma}] = \mathbf{u}$. The problem can be symmetrized by writing the second equation as $\mathbb{C}^{-1} : \boldsymbol{\sigma} - \nabla^s\mathbf{u} = \mathbf{0}$. In this case, $n = 3 + 6 = 9$ if the symmetry of the stress tensor is taken into account in the trial and test spaces and imposed strongly, and $n = 3 + 9 = 12$ if it is not and this symmetry is a consequence of the constitutive law (which will be imposed weakly in the finite element approximation). In our implementation, we impose the symmetry of $\boldsymbol{\sigma}$ strongly.

3.4.2 Variational form

Consider $H^1(\Omega)$ to be the space of functions in $L^2(\Omega)$ whose derivatives belong to $L^2(\Omega)$. We denote as $\mathcal{U} = H^1(\Omega)^3$ the space of displacements and as $\mathcal{S} = L^2(\Omega)^{3\times3}_{sym}$ the space of stresses. As said above, the symmetry of the latter can be enforced strongly in the trial space or weakly through the weak form of the constitutive equation (see below). Let $\mathcal{X}$ be the space where the weak problem is defined, being $\mathcal{X} = \mathcal{U}$ in the case of the irreducible formulation and $\mathcal{X} = \mathcal{U} \times \mathcal{S}$ in the case of the mixed formulation; the tests functions are $\mathbf{V} = \mathbf{v} \in \mathcal{X}$ and $\mathbf{V} = [\mathbf{v},\boldsymbol{\tau}] \in \mathcal{X}$, respectively. Let us introduce the bilinear form B and the linear form L as

$$B(\mathbf{V},\mathbf{U}) = \begin{cases} (\nabla^s\mathbf{v}, \mathbb{C} : \nabla^s\mathbf{u}) & \text{in the irreducible case,} \\ (\nabla^s\mathbf{v},\boldsymbol{\sigma}) + (\boldsymbol{\tau}, \mathbb{C}^{-1} : \boldsymbol{\sigma}) - (\boldsymbol{\tau}, \nabla^s\mathbf{u}) & \text{for the stress-displacement formulation,} \end{cases}$$
$$L(\mathbf{V}) = \langle \mathbf{V}, \mathbf{F} \rangle ,$$

where $(\cdot,\cdot)$ represents the inner product in $L^2(\Omega)$ and $\langle\cdot,\cdot\rangle$ the integral of the multiplication of two functions in Ω. When there are traction boundary conditions, these should appear in the expression of the linear form L.

With all the above, the general form of the problem in equations (3.24) and (3.25) can be written in its weak form, which consists of finding $\mathbf{U} \in \mathcal{X}$ such that

$$B(\mathbf{V},\mathbf{U}) = L(\mathbf{V}), \tag{3.26}$$

for all $\mathbf{V} \in \mathcal{X}$.

3.5 Geometrical approximation using finite elements

3.5.1 Construction of the local basis

Let us consider the shell represented by a surface Ω^{2D} in $\mathbb{R}^3$, geometrically expressed by any means. Suppose that we have a finite element partition $T_h = \{K\}$ of Ω^{2D} of diameter h, so that $\bar{\Omega}^{2D} = \bigcup_{K \in T_h} K$. We will not consider the error stemming from the geometrical approximation of the shell, and thus we will consider this finite element representation as exact. Let $K \in T_h$ be an element domain of the partition, either simplicial or a quadrilateral, and consider the isoparametric mapping

$$\begin{aligned} \boldsymbol{\varphi}_K &: K_0 \longrightarrow K \\ &(\xi, \eta) \mapsto (x^1, x^2, x^3), \end{aligned}$$

that maps the reference domain $K_0 \subset \mathbb{R}^2$ to $K \subset \mathbb{R}^3$, (ξ, η) being the isoparametric coordinates. Considering a Lagrangian interpolation, if n_{nod} is the number of nodes of K and $N^A(\xi, \eta)$ are the shape functions on K_0, $A = 1, \dots, n_{nod}$, we have that

$$\boldsymbol{\varphi}_K(\xi, \eta) = \sum_{A=1}^{n_{nod}} N^A(\xi, \eta) \mathbf{x}^A,$$

where $\mathbf{x}^A$ is the position vector of node A in K, $A = 1, \dots, n_{nod}$. The collection of all mappings $\{\boldsymbol{\varphi}_K, K \in T_h\}$ provides a local parametrization of Ω^{2D}.

The vectors tangent to each $K \in T_h$ are given by

$$\mathbf{g}^*_{1,K} = \left| \frac{\partial \boldsymbol{\varphi}_K}{\partial \xi} \right|^{-1} \frac{\partial \boldsymbol{\varphi}_K}{\partial \xi}, \quad \frac{\partial \boldsymbol{\varphi}_K}{\partial \xi} = \sum_{A=1}^{n_{nod}} \frac{\partial N^A}{\partial \xi} \mathbf{x}^A,$$

$$\mathbf{g}^*_{2,K} = \left| \frac{\partial \boldsymbol{\varphi}_K}{\partial \eta} \right|^{-1} \frac{\partial \boldsymbol{\varphi}_K}{\partial \eta}, \quad \frac{\partial \boldsymbol{\varphi}_K}{\partial \eta} = \sum_{A=1}^{n_{nod}} \frac{\partial N^A}{\partial \eta} \mathbf{x}^A.$$

From them, we can compute a vector normal to $K \subset \Omega^{2D}$ as

$$\mathbf{g}^*_{3,K} = \mathbf{g}^*_{1,K} \times \mathbf{g}^*_{2,K}.$$

Note that $|\mathbf{g}^*_{3,K}| = 1$ if ξ and η are orthogonal coordinates, as it is usually the case; otherwise, we normalize $\mathbf{g}^*_{3,K}$. It is important to remark that this normalization is not necessary, although we will construct the basis vectors to be orthonormal. The implication of this is that the metric tensor will be the identity; however, we shall consider its expression in the case of arbitrary local basis, for generality.

The basis vectors constructed this way, $\{\mathbf{g}^*_{1,K}, \mathbf{g}^*_{2,K}, \mathbf{g}^*_{3,K}\}$, are discontinuous across elements. To construct a continuous basis we proceed as follows. First, the vector field $\mathbf{g}^*_{3,K}$, $K \in T_h$, is projected onto the space of continuous vector fields using a standard $L^2(\Omega^{2D})$ projection, thus obtaining the nodal vectors $\mathbf{g}^a_3$, $a = 1, \dots, n_{pts}$, n_{pts} being the nodal points of T_h, and, from them

$$\mathbf{g}_3(x^1, x^2, x^3) = G_3^{-1} \sum_{a=1}^{n_{pts}} N^a(x^1, x^2, x^3)\mathbf{g}^a_3, \qquad G_3 = |\sum_{a=1}^{n_{pts}} N^a(x^1, x^2, x^3)\mathbf{g}^a_3|,$$

N^a being the global shape function of node a. Within each element $K \in T_h$, if A is the local numbering of the global node a, we have :

$$\mathbf{g}_3|_K(\xi, \eta) = G_{3,K}^{-1} \sum_{A=1}^{n_{nod}} N^A(\xi, \eta)\mathbf{g}^A_{3,K}, \qquad G_{3,K} = |\sum_{A=1}^{n_{nod}} N^A(\xi, \eta)\mathbf{g}^A_{3,K}|. \tag{3.27}$$

Figure 3.2 shows a cut of a surface and the conceptual difference between $\mathbf{g}^*_{3,K}$ and $\mathbf{g}_3$ when linear elements are used, case in which $\mathbf{g}^*_{3,K}$ will be constant on each $K \in T_h$.

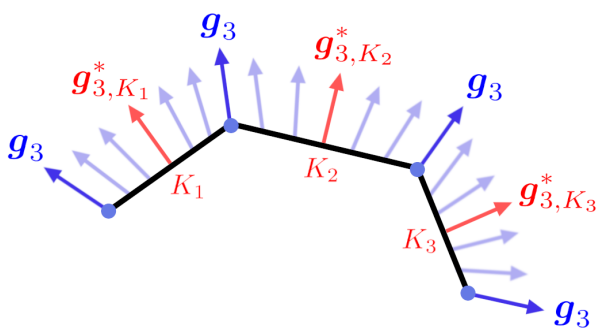

Figure 3.2: Normal vectors to the shell $\mathbf{g}^*_{3,K}$ and their smoothing $\mathbf{g}_3$.

Once the continuous global vector field $\mathbf{g}_3$ is constructed, we can build the a continuous local basis at each point $\{\mathbf{g}_1, \mathbf{g}_2, \mathbf{g}_3\}$

by defining

$$\mathbf{g}_1 = |\mathbf{g}_3 \times \mathbf{e}_3|^{-1} \mathbf{g}_3 \times \mathbf{e}_3, \quad \mathbf{g}_2 = \mathbf{g}_3 \times \mathbf{g}_1, \tag{3.28}$$

the only exception being when $\mathbf{g}_3$ aligns with $\mathbf{e}_3$, case in which we set $\mathbf{g}_1 = \mathbf{e}_1$ and $\mathbf{g}_2 = \mathbf{e}_2$ (or changing the sign if $\mathbf{g}_3$ is opposite to $\mathbf{e}_3$). The covariant basis $\{\mathbf{g}_1, \mathbf{g}_2, \mathbf{g}_3\}$ constructed this way will be such that $\{\mathbf{g}_1, \mathbf{g}_2\}$ will be *approximately* tangent to Ω^{2D} and $\mathbf{g}_3$ *approximately* normal. In fact, we can consider the shell defined by $\{\mathbf{g}_1, \mathbf{g}_2, \mathbf{g}_3\}$. The curvilinear coordinates $(\theta^1, \theta^2, \theta^3)$ are then defined as those tangent to $\{\mathbf{g}_1, \mathbf{g}_2, \mathbf{g}_3\}$ at each point.

3.5.2 Extrusion of the shell mid-surface

The domain Ω^{2D} (or, in fact, its approximation associated to $\{\mathbf{g}_1, \mathbf{g}_2, \mathbf{g}_3\}$) will be considered as the mid-surface of the shell. The solid-shell domain where the calculations will be performed is denoted as Ω^{3D}, and it is computed from the extrusion of Ω^{2D} in the normal direction. As we shall see, the construction of Ω^{3D} can be done element-wise because of the continuity of $\mathbf{g}_3$.

Suppose that the thickness of the shell is defined by its values at the nodes of T_h, denoted as t^a, $a = 1, \dots n_{pts}$. For each $K \in T_h$, the thicknesses at the nodes will be t_K^A, A being the local number of node a, and we can construct the thickness function

$$t_K(\xi, \eta) = \sum_{A=1}^{n_{nod}} N^A(\xi, \eta) t_K^A.$$

From the reference element K_0 we can construct the 3D reference element $K_0^{3D} = K_0 \times [-1, 1]$ and the mapping

$$\begin{aligned} &\boldsymbol{\psi}_K : K_0^{3D} \longrightarrow \mathbb{R}^3 \\ &\quad (\xi, \eta, \zeta) \mapsto (x^1, x^2, x^3) = \boldsymbol{\varphi}_K(\xi, \eta) + \zeta \frac{1}{2} t_K(\xi, \eta) \mathbf{g}_3|_K(\xi, \eta). \end{aligned} \tag{3.29}$$

and then set $K^{3D} = \boldsymbol{\psi}_K(K_0^{3D})$, i.e., the image of K_0^{3D} through $\boldsymbol{\psi}_K$. The solid domain where the problem is posed is then

$$\Omega^{3D} = \bigcup_{K \in T_h} K^{3D}.$$

From the continuity of $\mathbf{g}_3$ and the intrinsic continuity of the thickness function, Ω^{3D} will be a smooth extrusion of Ω^{2D}. This domain, together with the systems of coordinates and basis introduced so far, are depicted in Fig. 3.3. In the following, we will consider only one element across the thickness, but the extension to an arbitrary number of elements is straightforward, simply by fixing a partition of the thickness t_K in equations (5.10).

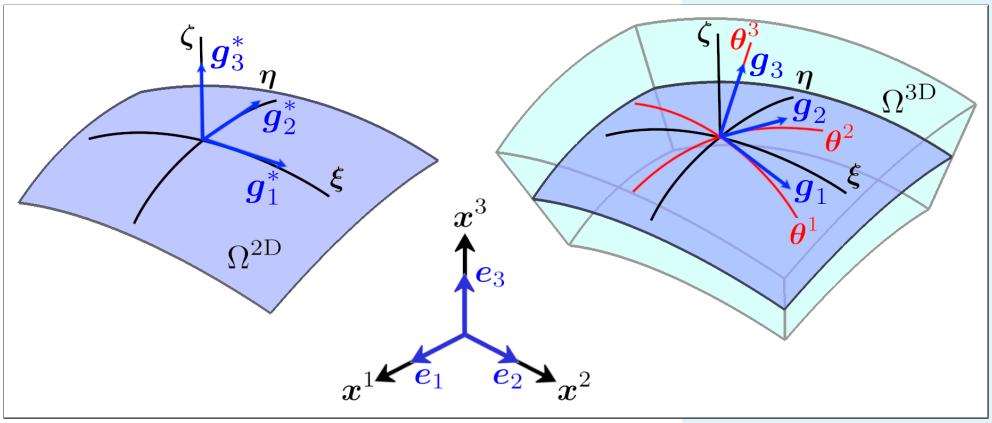

Figure 3.3: Geometry of the shell: 2D surface (left) and 3D extruded volume (right).

The construction of the local basis $\{\mathbf{g}^*_{1,K}, \mathbf{g}^*_{2,K}, \mathbf{g}^*_{3,K}\}$ can now be extended from K to K^{3D}. In general, the resulting vectors will depend on the coordinate ζ because of the dependence of t_K and $\mathbf{g}_3|_K$ on (ξ, η), which will need to be taken into account when computing $\mathbf{g}^*_{1,K}$ and $\mathbf{g}^*_{2,K}$ (see equation (5.10)). However, since we are interested in solids of small thickness, we shall take the basis $\{\mathbf{g}_1, \mathbf{g}_2, \mathbf{g}_3\}$ as constant across the thickness of the shell.

3.5.3 Interpolation across the thickness

Once the element domains $\{K^{3D}\}$ have been constructed, we need to define their degrees of freedom and a basis for the finite element space we wish to construct. As for the original partition $\{K\}$, we shall consider continuous Lagrangian interpolations, and it suffices to define them for the reference element $K_0 \times [-1, 1]$. Precisely, one of the main reasons to use 3D solid elements in the approximation of shell structures in to take advantage of the through-the-thickness interpolation of the unknowns. For this reason, it is convenient that the discretization of the mesh is performed considering an indepen-

dent discretization in the thickness direction. In other words, the number of elements, the order of interpolation, and the integration rule are set independently from the original surface mesh. Let n_s be the interpolation order of $K \in T_h$ and n_l the interpolation order of the elements in the ζ direction of the reference element. Let $N_i^{A,A'}(\xi,\eta,\zeta)$ be the shape function of a node in $K_0 \times [-1,1]$ that corresponds to node A of K_0 and node A' of the discretization of $[-1,1]$. The shape functions corresponding to the shell body $N_i^{A,A'}(\xi,\eta,\zeta)$ can now be constructed by multiplying the mid-surface shape functions $N^A(\xi,\eta)$ and the standard one dimensional Lagrangian shape functions $N^{A'}(\zeta)$ in the isoparametric space:

$$N^{A,A'}(\xi,\eta,\zeta) = N^A(\xi,\eta)\, N^{A'}(\zeta)\,. \tag{3.30}$$

Possible interpolations of hexahedral elements are shown in Table 3.4 for $n_s = 1,2$ and $n_l = 1,2$. In the following, the structure of the shape functions will be assumed and we shall simply write as $N^A(\xi,\eta,\zeta)$ the local shape function of node A, not necessarily in $K \in T_h$ but in K^{3D}; the number of nodes of K^{3D} will be again denoted as n_{nod}. Likewise, at the global level the shape functions will be written as $N^a(x^1,x^2,x^3)$, with a running again from 1 to n_{pts}. The finite element partition resulting from the extrusion of the finite element partition of the shell surface $T_h = \{K\}$ will be denoted as $T_h^{3D} = \{K^{3D}\}$.

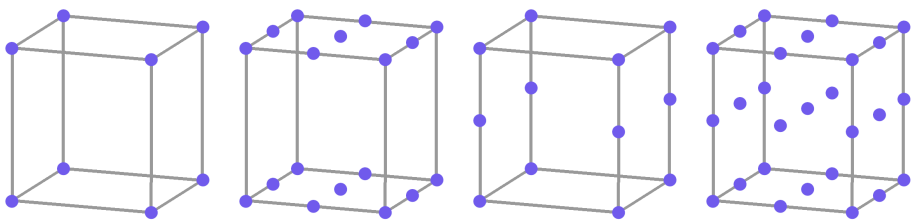

Figure 3.4: Element discretizations across the surface and through the thickness.

3.5.4 Calculation of the metric tensor and the Christoffel symbols

From the previous construction, we have the covariant basis vectors $\{\mathbf{g}_1, \mathbf{g}_2, \mathbf{g}_3\}$. From equations (3.27) and (5.8) we

have these vectors at each point of each element, i.e., we have $\mathbf{g}_\alpha|_K(\xi,\eta)$ using isoparametric coordinates, $\alpha = 1,2,3$. In what follows, we will omit the element label and the dependence on (ξ,η) to lighten the notation.

In general, from the covariant basis vectors we may compute at each point the covariant metric tensor $g_{\alpha\beta}$ given by equation (3.2), as well as its contravariant representation $g^{\alpha\beta}$ and, from this, the contravariant basis $\{\mathbf{g}^1,\mathbf{g}^2,\mathbf{g}^3\}$. However, the basis we have constructed are orthonormal, and therefore $g_{\alpha\beta} = g^{\alpha\beta} = \delta_{\alpha\beta}$ and $\mathbf{g}^\alpha = \mathbf{g}_\alpha$, $\alpha,\beta = 1,2,3$.

It only remains to compute the derivatives with respect to the curvilinear coordinates given by equation (3.5) and, from these, the Christoffel symbols given by equation (3.6). What we may compute from equations (3.27) and (5.8) are the derivatives of $\{\mathbf{g}_1,\mathbf{g}_2,\mathbf{g}_3\}$ with respect to the isoparametric coordinates (ξ,η) and, if the basis is considered variable with respect to ζ, also with respect to this coordinate. Let us call

$$\nabla_0\mathbf{g}_\alpha = \left(\frac{\partial\mathbf{g}_\alpha}{\partial\xi},\frac{\partial\mathbf{g}_\alpha}{\partial\eta},\frac{\partial\mathbf{g}_\alpha}{\partial\zeta}\right), \quad \alpha = 1,2,3.$$

Since the curvilinear coordinates $(\theta^1,\theta^2,\theta^3)$ are by construction tangent to $\{\mathbf{g}_1,\mathbf{g}_2,\mathbf{g}_3\}$, we may now compute $\mathbf{g}_{\alpha,\beta}$ as the directional derivative

$$\mathbf{g}_{\alpha,\beta} \equiv \frac{\partial\mathbf{g}_\alpha}{\partial\theta^\beta} = \mathbf{g}_\beta\cdot\nabla_0\mathbf{g}_\alpha, \quad \alpha,\beta = 1,2,3.$$

From this expression we can compute the Christoffel symbols using equation (3.6). These are needed in the general case. However, we shall see in the next section that we do not need to compute them if the unknowns of the problem are the Cartesian components of the displacement (and the stress in either reference system), despite the equilibrium equations are written in curvilinear coordinates.

This completes the geometrical approximation of the solid-shell.

3.6 Finite element approximation

3.6.1 Interpolation of displacements and stresses

[105]: Cinefra (2022), *Formulation of 3D finite elements using curvilinear coordinates*

The approach we will follow is to use the same interpolation for the displacements as for the geometry, which is also used, for example, in [105]. Therefore, these displacements will be interpolated as

$$\mathbf{u}_h(\mathbf{x}) = \sum_{a=1}^{n_{pts}} N^a(\mathbf{x})\hat{u}_i^a \mathbf{e}_i \iff \hat{u}_{hi}(\mathbf{x}) = \sum_{a=1}^{n_{pts}} N^a(\mathbf{x})\hat{u}_i^a, \tag{3.31}$$

where $\hat{u}_i^a$ is the i-th Cartesian component of the displacement at node a. Since in the Cartesian basis the covariant and contravariant components coincide, we do not need to distinguish them. Superscripts for the Cartesian components will refer to nodal values from now on.

In the finite element implementation, we shall take *the Cartesian nodal values $\hat{u}_i^a$ as the unknowns of the problem.* Therefore, we need to relate the curvilinear components of the displacement and their derivatives to these nodal values.

According to the transformation rule for displacements in equations (3.19) and (3.11), the covariant components of displacements in curvilinear coordinates can be expressed as

$$u_\alpha = g_{\alpha i}\hat{u}_i = \frac{\partial x_i}{\partial \theta^\alpha}\hat{u}_i, \tag{3.32}$$

at each point, $g_{\alpha i}$ being the i-th component of $\mathbf{g}_\alpha$ (not to be confused with the components of the metric tensor). This also follows from $\mathbf{u} = u_\beta \mathbf{g}^\beta = \hat{u}_i \mathbf{e}_i$ and taking the scalar product with $\mathbf{g}_\alpha$.

The partial derivative of u_α with respect to θ^β will be

$$\begin{aligned} u_{\alpha,\beta} &= g_{\alpha i}\hat{u}_{i,\beta} + g_{\alpha i,\beta}\hat{u}_i \\ &= g_{\alpha i}g_{\beta j}\hat{u}_{i,j} + g_{\gamma i}\Gamma^\gamma_{\alpha\beta}\hat{u}_i. \end{aligned} \tag{3.33}$$

The chain rule in the form $\hat{u}_{i,\beta} = \hat{u}_{i,j}x^j_{,\beta} = \hat{u}_{i,j}g_{\beta j}$ has been used in the first term and the definition of the Christoffel symbol in the second.

Finally, the covariant derivative of u_α with respect to θ^β will be

$$\begin{aligned} u_{\alpha|\beta} &= u_{\alpha,\beta} - \Gamma^\gamma_{\alpha\beta} u_\gamma \\ &= g_{\alpha i} g_{\beta j} \hat{u}_{i,j} + g_{\gamma i} \Gamma^\gamma_{\alpha\beta} \hat{u}_i - \Gamma^\gamma_{\alpha\beta} g_{\gamma i} \hat{u}_i \\ &= g_{\alpha i} g_{\beta j} \hat{u}_{i,j}. \end{aligned} \tag{3.34}$$

Equations (3.32)-(3.33)-(3.34) are the relationships we need to relate the curvilinear components of the displacement with the Cartesian ones. The latter will be interpolated as indicated in equation (3.31), thus providing the finite element interpolation for the curvilinear components of the displacement and their derivatives, which will be:

$$\begin{aligned} u_{h\alpha} &= g_{\alpha i} \hat{u}_{hi}, \\ u_{h\alpha,\beta} &= g_{\alpha i} g_{\beta j} \hat{u}_{hi,j} + g_{\gamma i} \Gamma^\gamma_{\alpha\beta} \hat{u}_{hi}, \\ u_{h\alpha|\beta} &= g_{\alpha i} g_{\beta j} \hat{u}_{hi,j}. \end{aligned}$$

It is understood that the basis $\{\mathbf{g}_1, \mathbf{g}_2, \mathbf{g}_3\}$ are also constructed from the finite element approximation, as explained in the previous section, although we have not introduced any symbol to distinguish this finite element approximation of the basis functions. It is observed that the Christoffel symbols are not needed to compute the covariant derivates of the covariant components of the displacement. The important expression we shall use is the last one, together with its inverse, which are the discrete counterparts of (3.14) and (3.18):

$$u_{h\alpha|\beta} = g_{\alpha i} g_{\beta j} \hat{u}_{hi,j} = \frac{\partial x_i}{\partial \theta^\alpha} \frac{\partial x_j}{\partial \theta^\beta} \hat{u}_{hi,j} \iff u_{hi,j} = g_i^\alpha g_j^\beta \hat{u}_{h\alpha|\beta} = \frac{\partial \theta^\alpha}{\partial x_i} \frac{\partial \theta^\beta}{\partial x_j} \hat{u}_{h\alpha|\beta}. \tag{3.35}$$

In the case of stresses, they are interpolated in Cartesian coordinates as

$$\boldsymbol{\sigma}_h = \sum_{a=1}^{n_{pts}} N^a(\mathbf{x}) \hat{\sigma}^a_{ij} \mathbf{e}_i \otimes \mathbf{e}_j \iff \hat{\sigma}_{hij} = \sum_{a=1}^{n_{pts}} N^a(\mathbf{x}) \hat{\sigma}^a_{ij}, \tag{3.36}$$

where $\hat{\sigma}^a_{ij}$ is the ij-th component of the stress at node a. Now we do not need derivatives of the stresses, but only the expression of their curvilinear components in terms of the Cartesian ones. This can be obtained from equation (3.17), yielding the discrete counterpart of equations (3.13) and (3.17):

$$\sigma_h{}^{\alpha\beta} = g_i^\alpha g_j^\beta \hat{\sigma}_{hij} = \frac{\partial\theta^\alpha}{\partial x_i}\frac{\partial\theta^\beta}{\partial x_j}\hat{\sigma}_{hij} \iff \hat{\sigma}_{hij} = g_{\alpha i} g_{\beta j}\sigma_h{}^{\alpha\beta} = \frac{\partial x_i}{\partial\theta^\alpha}\frac{\partial x_j}{\partial\theta^\beta}\sigma_h{}^{\alpha\beta}. \tag{3.37}$$

Again, let us point out that since the curvilinear coordinate system is orthonormal, the covariant basis coincides with the contravariant one.

3.6.2 Galerkin finite element approximation

From the partition $T_h^{3D} = \{K^{3D}\}$ of the domain Ω^{3D} we can approximate problem (3.26) using finite elements in the standard way. Let $\mathcal{X}_h \subset \mathcal{X}$ be a conforming finite element space, corresponding either to the irreducible or to the mixed form of the problem. The Galerkin approximation consists in finding $\mathbf{U}_h \in \mathcal{X}_h$ such that

$$B(\mathbf{V}_h, \mathbf{U}_h) = L(\mathbf{V}_h) \qquad \forall\, \mathbf{V}_h \in \mathcal{X}_h. \tag{3.38}$$

In the case of the irreducible formulation, this reads:

Galerkin approximation of the irreducible formulation

$$(\nabla^s \mathbf{v}_h, \mathbb{C} : \nabla^s \mathbf{u}_h) = \langle \mathbf{v}_h, \rho\mathbf{b}\rangle. \tag{3.39}$$

This equation and the following are *intrinsic*, i.e., they do not depend on the coordinate system. In the following subsection we will consider the particular cases of Cartesian and curvilinear coordinates. The standard stability estimate for the irreducible formulation can be obtained simply by taking $\mathbf{v}_h = \mathbf{u}_h$ in equation (3.39), yielding

$$(\nabla^s \mathbf{u}_h, \mathbb{C} : \nabla^s \mathbf{u}_h) = \|\mathbf{u}_h\|_E^2 \lesssim \|\mathbf{u}_h\|_E \|\rho\mathbf{b}\|_{E'} \tag{3.40}$$

where $\|\cdot\|_E$ is the energy norm, $\|\cdot\|_{E'}$ its dual and $\lesssim$ stands for $\leq$ up to positive constants. In this case, $\|\mathbf{u}_h\|_E$ corresponds to the discrete internal elastic energy (up to constants). The result $\|\mathbf{u}_h\|_E \lesssim \|\rho\mathbf{b}\|_{E'}$ implies that the irreducible formulation is numerically stable if the tensor $\mathbb{C}$ is positive definite. However, being numerically stable does not guarantee the approximation to be free of numerical locking. In fact, membrane and shear locking are anticipated when using standard low order 3D elements for the approximation of thin structures. The

Galerkin form in equation (3.38) for the mixed formulation reads:

Galerkin approximation of the mixed formulation

$$(\nabla^s \mathbf{v}_h, \boldsymbol{\sigma}_h) = \langle \mathbf{v}_h, \rho \mathbf{b} \rangle, \tag{3.41}$$

$$-(\boldsymbol{\tau}_h, \mathbb{C}^{-1} : \boldsymbol{\sigma}_h) + (\boldsymbol{\tau}_h, \nabla^s \mathbf{u}_h) = \mathbf{0}. \tag{3.42}$$

The standard Galerkin approach to this formulation using continuous interpolations for both displacements and stress fields is not stable. The stability depends on the compatibility restrictions on the finite element spaces for the displacements $\mathcal{U}_h \subset \mathcal{U}$ and for the stresses $\mathcal{S}_h \subset \mathcal{S}$ chosen, which have to fulfil the inf-sup condition. The instability due to not satisfying this condition pollutes the solution in the form of uncontrollable oscillations in the displacement field. The reader can refer to [120] for a detailed explanation regarding these conditions.

[120]: Boffi et al. (2013), *Mixed finite element methods and applications*

3.6.3 Stabilized finite element approximation

The idea of stabilized finite element methods is to overcome the instability of the Galerkin approach by modifying the variational form of the problem through the introduction of consistent terms that allow one to obtain stable solutions independently of the choice of the interpolation spaces. The stabilization employed in the present work is based on the VMS approach [2, 3, 43]. This approach has been previously discussed in [121] for the linear elastic solid problem and in [122] for solid-shell elements using Cartesian coordinates, and it is explored further in the present work by taking advantage of the local curvilinear basis which define the tangent and normal components of the stresses.

[2]: Hughes (1995), *Multiscale phenomena: Green's functions, the Dirichlet-to-Neumann formulation, subgrid scale models, bubbles and the origins of stabilized methods*

[3]: Hughes et al. (1998), *The variational multiscale method - A paradigm for computational mechanics*

[43]: Codina (2000), *Stabilization of incompressibility and convection through orthogonal sub-scales in finite element methods*

[121]: Cervera et al. (2010), *Mixed stabilized finite element methods in nonlinear solid mechanics: Part I: Formulation*

[122]: Saloustros et al. (2021), *Accurate and locking-free analysis of beams, plates and shells using solid elements*

The idea of the VMS stabilization employed in this paper consists of adding additional terms to the Galerkin formulation, that enhance stability without upsetting accuracy. It starts by splitting the space of unknowns as $\mathcal{X} = \mathcal{X}_h \oplus \mathcal{X}'$, where $\mathcal{X}_h$ is the component that can be resolved in the finite element space and $\mathcal{X}'$ is the remainder, called sub-grid scale (SGS) space. In this manner, the unknowns are split as $\mathbf{U} = \mathbf{U}_h + \mathbf{U}'$, and also the test functions as $\mathbf{V} = \mathbf{V}_h + \mathbf{V}'$.

The splitting modifies the original formulation (3.38) and the problem consists of finding $\mathbf{U}_h \in \mathcal{X}_h$ and $\mathbf{U}' \in \mathcal{X}'$ such that

$$B(\mathbf{V}_h, \mathbf{U}_h) + B(\mathbf{V}_h, \mathbf{U}') = L(\mathbf{V}_h) \qquad \forall\, \mathbf{V}_h \in \mathcal{X}_h, \tag{3.43}$$

$$B(\mathbf{V}', \mathbf{U}_h) + B(\mathbf{V}', \mathbf{U}') = L(\mathbf{V}') \qquad \forall\, \mathbf{V}' \in \mathcal{X}', \tag{3.44}$$

where (3.43) is the finite element equation and (3.44) is the SGS equation. Note that choosing $\mathcal{X}' = \{0\}$ yields the Galerkin method, making the stabilization to be consistent by construction.

Incorporating the SGSs in equation (3.43) modifies the original problem in equations (3.41)-(3.42) as follows:

$$(\nabla^s \mathbf{v}_h, \boldsymbol{\sigma}_h) + (\nabla^s \mathbf{v}_h, \boldsymbol{\sigma}') = \langle \mathbf{v}_h, \rho \mathbf{b} \rangle, \tag{3.45}$$

$$-(\boldsymbol{\tau}_h, \mathbb{C}^{-1} : \boldsymbol{\sigma}_h) + (\boldsymbol{\tau}_h, \nabla^s \mathbf{u}_h) - (\boldsymbol{\tau}_h, \mathbb{C}^{-1} : \boldsymbol{\sigma}') + (\boldsymbol{\tau}_h, \nabla^s \mathbf{u}') = \mathbf{0}. \tag{3.46}$$

Under this framework, it only remains to find an approximation of the SGSs. The objective is to express these SGSs in terms of the finite element variables, thus preserving the initial number of unknowns of the problem. The approximation needed can be achieved by working on equation (3.44), noting that

$$\begin{aligned} B(\mathbf{V}', \mathbf{U}') &= L(\mathbf{V}') - B(\mathbf{V}', \mathbf{U}_h), \\ &= L(\mathbf{V}') - \sum_K \langle \mathbf{V}', \mathscr{L}\mathbf{U}_h \rangle_K, \\ &= \sum_K \langle \mathbf{V}', \mathscr{R}\mathbf{U}_h \rangle_K, \end{aligned} \tag{3.47}$$

where $\langle \cdot, \cdot \rangle_K$ is the integral of the product of two functions over an element domain K and $\mathscr{R}\mathbf{U}_h = \mathbf{F} - \mathscr{L}\mathbf{U}_h$ is the finite element residual, defined as

$$\mathscr{R}\mathbf{U}_h = \begin{bmatrix} \mathscr{R}_u \mathbf{U}_h \\ \mathscr{R}_\sigma \mathbf{U}_h \end{bmatrix} = \begin{bmatrix} \rho \mathbf{b} + \nabla \cdot \boldsymbol{\sigma}_h \\ \mathbb{C}^{-1} : \boldsymbol{\sigma}_h - \nabla^s \mathbf{u}_h \end{bmatrix}.$$

In the second step to obtain equation (3.47) it has been considered that the SGSs vanish on the element boundaries. This approximation will also be used in the following, although it can be relaxed as explained in [45].

The specific details of how to obtain the SGSs can be reviewed in [44]. After some mathematical approximations, the SGSs

[45]: Codina et al. (2009), *Subscales on the element boundaries in the variational two-scale finite element method*

[44]: Codina et al. (2018), *Variational multiscale methods in computational fluid dynamics*

$\mathbf{U}' = [\mathbf{u}', \boldsymbol{\sigma}']^T$ can then be taken as

$$\mathbf{U}' \,|_K \approx \boldsymbol{\tau}_K P' \left(\mathscr{R}\mathbf{U}_h\right)|_K, \tag{3.48}$$

where P' is the L^2 projection onto the SGS space $\mathscr{X}'$ and the matrix of stabilization parameters $\boldsymbol{\tau}_K$, which approximates $\mathscr{L}^{-1}$ on each element K, is computed as

$$\boldsymbol{\tau}_K = \begin{bmatrix} \tau_u \mathbf{I}_3 & \mathbf{0} \\ \mathbf{0} & \tau_\sigma \mathbf{I}_6 \end{bmatrix}, \qquad \tau_u = c_u \frac{L_0 h}{C_{\text{min}}}, \qquad \tau_\sigma = c_\sigma \frac{h}{L_0},$$

where $\mathbf{I}_3$ and $\mathbf{I}_6$ are the identity on vectors and on symmetric second order tensors, respectively, c_u and c_σ are algorithmic constants, L_0 is a characteristic length of the domain, h is the element size, and C_{min} is the smallest eigenvalue of $\mathbb{C}$. As it is explained in [121], the calculation of the stabilization parameters proposed is the one that provides optimal accuracy when equal interpolation is used for the stresses and the displacements.

[121]: Cervera et al. (2010), *Mixed stabilized finite element methods in nonlinear solid mechanics: Part I: Formulation*

The SGS can then be incorporated into (3.43) by taking advantage of the additivity of the integral and the fact that, assuming $\mathbf{U}' = \mathbf{0}$ on the interelement boundaries:

$$B(\mathbf{V}, \mathbf{U}') = \sum_K \langle \mathbf{V}, \mathscr{L}\mathbf{U}' \rangle_K = \sum_K \langle \mathscr{L}^* \mathbf{V}, \mathbf{U}' \rangle_K \,, \tag{3.49}$$

where the superscript * denotes the adjoint of an operator, which comes from the integration by parts of the original operator. In this manner, using the expression for the SGSs in equation (3.48) and the property (3.49) into equation (3.43) yields the stabilized formulation

$$B(\mathbf{V}_h, \mathbf{U}_h) + \sum_K \langle \mathscr{L}^* \mathbf{V}_h, \boldsymbol{\tau}_K P' \left(\mathscr{R}\mathbf{U}_h\right) \rangle_K = L(\mathbf{V}_h). \tag{3.50}$$

It only remains to choose the space of the SGS, and thus how the projection P' is approximated.

A typical choice of the SGS space is taking it as the space of finite element residuals, leading to the Algebraic Subgrid Scale (ASGS) formulation. In this case, $P' = I$, resulting in

$$\mathbf{u}' = \tau_u(\rho \mathbf{b} + \nabla \cdot \boldsymbol{\sigma}_h), \quad \boldsymbol{\sigma}' = \tau_\sigma \left(\mathbb{C} : \nabla^s \mathbf{u}_h\right).$$

However, in this work, the SGS space is considered to be the L^2 orthogonal to the finite element space, so that $\mathscr{X} = \mathscr{X}_h \oplus \mathscr{X}_h^\perp$. Following this approach yields the Orthogonal Subgrid

Scale (OSGS) formulation, in which $P' = P_h^{\perp} = I - P_h$, P_h being the L^2 projection onto X_h. Therefore, the SGSs $\mathbf{U}'$ defined in (3.48) are computed as

Subgrid scales

$$\mathbf{u}' = \tau_u P_h^{\perp}(\rho\mathbf{b} + \nabla\cdot\boldsymbol{\sigma}_h) = \tau_u\left[\rho\mathbf{b} + \nabla\cdot\boldsymbol{\sigma}_h - P_h(\rho\mathbf{b} + \nabla\cdot\boldsymbol{\sigma}_h)\right], \tag{3.51}$$

$$\boldsymbol{\sigma}' = \tau_\sigma P_h^{\perp}(\mathbb{C} : \nabla^s\mathbf{u}_h) \;= \tau_\sigma\left[\mathbb{C} : \nabla^s\mathbf{u}_h - P_h(\mathbb{C} : \nabla^s\mathbf{u}_h)\right], \tag{3.52}$$

where the term corresponding to $P_h^{\perp}(\boldsymbol{\sigma}_h)$ vanishes because $\boldsymbol{\sigma}_h$ is in the finite element space and it is being projected onto its orthogonal counterpart.

Using the SGSs given in (3.51)-(3.52) in equations (3.45)-(3.46) yields

Orthogonal Subgrid Scales Stabilization of the mixed formulation

$$(\nabla^s\mathbf{v}_h, \boldsymbol{\sigma}_h) + \tau_\sigma(\nabla^s\mathbf{v}_h, \mathbb{C} : \nabla^s\mathbf{u}_h - P_h(\mathbb{C} : \nabla^s\mathbf{u}_h)) = (\mathbf{v}_h, \rho\mathbf{b}), \tag{3.53}$$

$$-(\boldsymbol{\tau}_h, \mathbb{C}^{-1} : \boldsymbol{\sigma}_h) + (\boldsymbol{\tau}_h, \nabla^s\mathbf{u}_h) - \tau_u(\nabla\cdot\boldsymbol{\tau}_h, \nabla\cdot\boldsymbol{\sigma}_h - P_h(\nabla\cdot\boldsymbol{\sigma}_h)) = \tau_u(\nabla\cdot\boldsymbol{\tau}_h, \rho\mathbf{b} - P_h(\rho\mathbf{b})), \tag{3.54}$$

where the term $\tau_\sigma(\boldsymbol{\tau}_h, \mathbb{C}^{-1} : \boldsymbol{\sigma}')$ vanishes due to the orthogonality condition (assuming constant physical properties).

3.6.4 Finite element formulations in Cartesian and curvilinear coordinates

The equations that need to be solved are equation (3.39) in the irreducible formulation and equations (3.53)-(3.54) in the case of the mixed stabilized formulation. The former is expected to yield locking in the case of thin structures, and it is irrelevant whether it is solved in Cartesian or curvilinear coordinates, as the degrees of freedom are the three displacement components in either system of coordinates. We shall solve them in Cartesian coordinates, i.e., we will solve the problem of finding $\hat{\mathbf{u}}_h \in U_h$ such that

$$(\hat{v}_{hi,j}, \hat{\mathbb{C}}_{ijkl}\hat{u}_{hk,l}) = \langle \hat{v}_{hi}, \rho\hat{b}_i\rangle \qquad \forall\hat{\mathbf{v}}_h \in U_h. \tag{3.55}$$

To simplify the writing, we have used the whole displacement gradient instead of its symmetric part; the contraction with the constitutive tensor, satisfying the major and minor symmetries, will produce the same result. Note also that we have considered homogeneous boundary conditions for displacements on the whole boundary; non-homogeneous displacements on part of the boundary and normal stresses on the complement could be easily acomodated.

Even if we will not used it, equation (3.55) can be transformed to curvilinear coordinates using expression (3.35) as

$$\left(\frac{\partial\theta^\alpha}{\partial x_i}\frac{\partial\theta^\beta}{\partial x_j}v_{h\alpha|\beta}, \hat{\mathbb{C}}_{ijkl}\frac{\partial\theta^\gamma}{\partial x_k}\frac{\partial\theta^\delta}{\partial x_l}u_{h\gamma|\delta}\right) = \langle v_{h\alpha}, \rho b^\alpha\rangle. \tag{3.56}$$

Let us move now to the mixed stabilized formulation. In our numerical experience, we have found that the parameter τ_u can often be set to $\tau_u = 0$ and still have a stable and accurate approximation. To simplify the writing, let us consider that this is the case. Problem (3.53)-(3.54) in Cartesian coordinates consists of finding $[\hat{\mathbf{u}}_h, \hat{\boldsymbol{\sigma}}_h] \in X_h$ such that

$$(\hat{v}_{hi,j}, \hat{\sigma}_{hij}) + \tau_\sigma(\hat{v}_{hi,j}, \hat{\mathbb{C}}_{ijkl}\hat{u}_{hk,l} - P_h(\hat{\mathbb{C}}_{ijkl}\hat{u}_{hk,l})) = \langle \hat{v}_{hi}, \rho\hat{b}_i\rangle \qquad \forall\hat{\mathbf{v}}_h \in U_h, \tag{3.57}$$

$$-(\hat{\tau}_{hij}, \hat{\mathbb{C}}^{-1}_{ijkl}\hat{\sigma}_{hkl}) + (\hat{\tau}_{hij}, \hat{u}_{hi,j}) = 0 \qquad \forall\hat{\boldsymbol{\tau}}_h \in S_h. \tag{3.58}$$

Recall that we are imposing strongly the symmetry of the stresses and the stress test functions.

We can now write problem (3.57)-(3.58) in curvilinear coordinates using the transformation rules (3.35)-(3.37), yielding:

$$\left(v_{h\alpha|\beta}, \sigma_h^{\alpha\beta}\right) + \tau_\sigma\left(\frac{\partial\theta^\alpha}{\partial x_i}\frac{\partial\theta^\beta}{\partial x_j}v_{h\alpha|\beta}, \hat{\mathbb{C}}_{ijkl}\frac{\partial\theta^\gamma}{\partial x_k}\frac{\partial\theta^\delta}{\partial x_l}u_{h\gamma|\delta} - P_h\left[\hat{\mathbb{C}}_{ijkl}\frac{\partial\theta^\gamma}{\partial x_k}\frac{\partial\theta^\delta}{\partial x_l}u_{h\gamma|\delta}\right]\right) = \langle v_{h\alpha}, \rho b^\alpha\rangle,$$

$$-\left(\frac{\partial x_i}{\partial\theta^\alpha}\frac{\partial x_j}{\partial\theta^\beta}\tau_h^{\alpha\beta}, \hat{\mathbb{C}}^{-1}_{ijkl}\frac{\partial x_k}{\partial\theta^\gamma}\frac{\partial x_l}{\partial\theta^\delta}\sigma_h^{\gamma\delta}\right) + \left(\tau_h^{\alpha\beta}, u_{h\alpha|\beta}\right) = 0.$$

Finally, we can consider a *hybrid* approach, using displacements in Cartesian coordinates and stresses in curvilinear coordinates. The convenience of this approach will be clear in the following subsection. Using again the transformation rules (3.35)-(3.37), we obtain:

$$\left(\hat{v}_{hi,j}, \frac{\partial x_i}{\partial \theta^\alpha}\frac{\partial x_j}{\partial \theta^\beta}\sigma_h^{\alpha\beta}\right) + \tau_\sigma\left(\hat{v}_{hi,j}, \hat{\mathbb{C}}_{ijkl}\hat{u}_{hk,l} - P_h(\hat{\mathbb{C}}_{ijkl}\hat{u}_{hk,l})\right) = \langle \hat{v}_i^h, \rho\hat{b}_i\rangle, \tag{3.59}$$

$$-\left(\frac{\partial x_i}{\partial \theta^\alpha}\frac{\partial x_j}{\partial \theta^\beta}\tau_h^{\alpha\beta}, \hat{\mathbb{C}}^{-1}_{ijkl}\frac{\partial x_k}{\partial \theta^\gamma}\frac{\partial x_l}{\partial \theta^\delta}\sigma_h^{\gamma\delta}\right) + \left(\frac{\partial x_i}{\partial \theta^\alpha}\frac{\partial x_j}{\partial \theta^\beta}\tau_h^{\alpha\beta}, u_{hi,j}\right) = 0. \tag{3.60}$$

Let us point out that at the continuous level $\frac{\partial x_i}{\partial \theta^\alpha} = g_{\alpha i}$, but in fact vectors $\mathbf{g}_\alpha$, $\alpha = 1, 2, 3$, are computed as described in subsection 3.5.1.

3.6.5 Deactivation of stress degrees of freedom

The convenience of equations (3.59)-(3.60) relies on the fact that, on the one hand, displacements are approximated in Cartesian coordinates, easier to handle than the curvilinear ones, and on the other hand stresses are expressed in curvilinear coordinates, thus having a mechanical meaning. In these equations, *all* the stress components are considered independent variables. However, to study which stresses need to be interpolated independently to avoid locking, we may consider a switch between their independent interpolation and their expression in terms of the (Cartesian) displacements. This switch can be constructed by redefining the stresses as

$$\sigma_h^{\alpha\beta} \leftarrow \chi^{\alpha\beta}\sigma_h^{\alpha\beta} + (1-\chi^{\alpha\beta})\frac{\partial \theta^\alpha}{\partial x_i}\frac{\partial \theta^\beta}{\partial x_j}\hat{\mathbb{C}}_{ijkl}\hat{u}_{hk,l} \quad \text{(no sum on } \alpha, \beta), \tag{3.61}$$

where $\chi^{\alpha\beta} = 1$ indicates that the stress $\sigma_h^{\alpha\beta}$ is an independent unknown, whereas if $\chi^{\alpha\beta} = 0$ this stress is computed in terms of the displacement, and likewise for the stress test function. In this last case, the corresponding equation $\alpha\beta$ in (3.60) is simply deleted. Note that if $\chi^{\alpha\beta} = 0$ for all α and β, equation (3.59) with $\tau_\sigma = 0$ reduces to equation (3.55) and equation (3.60) becomes $0 = 0$.

Equation (3.61) provides a mechanism for activating or deactivating the stress components as independent variables that will be explored in the numerical examples presented next.

3.7 Numerical results

It is known that all types of numerical locking appear in solid-shell elements when specific conditions are met. This issue has been proven to be solved by using the stabilized mixed formulation of the VMS type [122]. In this context, numerical locking is solved by using a mixed formulation where the stresses are interpolated as unknowns and are stabilized to circumvent the inf-sup condition. The shear locking problems are solved because the zero shear strain condition can be properly represented by the shear stresses. On the other hand, membrane locking is solved by obtaining control over the parasitic strains by formulating properly scaled membrane strains. Similarly, trapezoidal locking is solved by eliminating the parasitic transverse normal strains by formulating a properly scaled strain in that direction. However, identifying when is it convenient to interpolate each component of the stress tensor remains to be examined in depth. Reducing the number of unknowns to be solved can be fruitful to optimize the computational resources.

[122]: Saloustros et al. (2021), *Accurate and locking-free analysis of beams, plates and shells using solid elements*

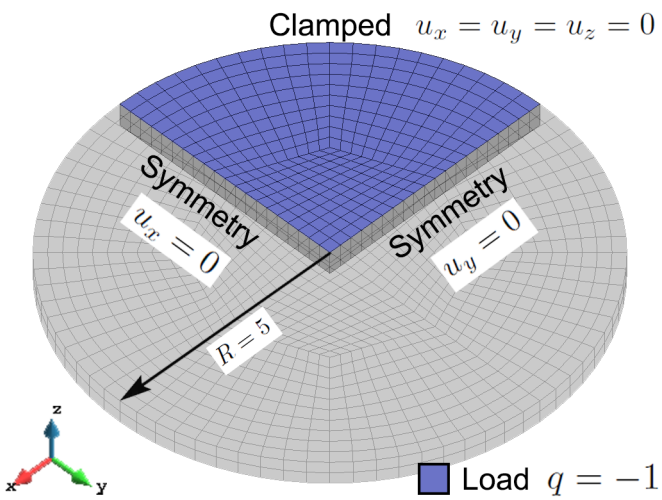

Figure 3.5: Clamped circular plate: geometry and boundary conditions.

To properly examine this possibility, the logical step is to set a list of benchmark problems and solve them interpolating as unknowns only part of the stress tensor. In this manner, the influence of each of the stresses can be described independently, and the combinations that can maintain the accuracy of the solution can be found. In the context of plate and shell structures, the stresses can be classified into four groups de-

pending on the direction they act: membrane stresses, transverse stress, twisting stresses, and shear stresses (see Fig. 3.1). Therefore the stresses are chosen considering this grouping instead of independently. Let us stress again that curvilinear coordinates are needed in the case of shells to classify the stresses.

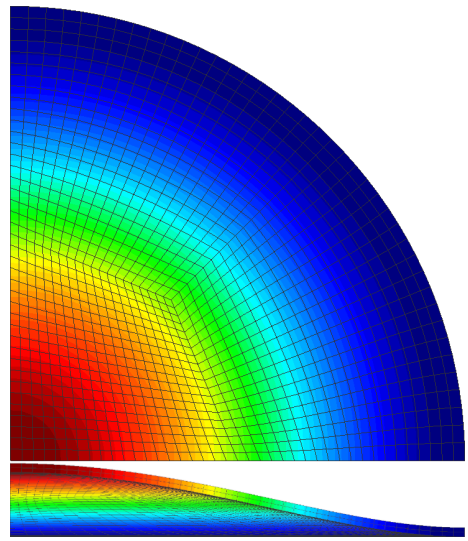

Figure 3.6: Clamped circular plate: deformed configuration.

In the following, some benchmark cases are solved to describe the numerical response of thin structures with respect to the irreducible and mixed formulations. The initial cases are flat plate benchmark problems, serving as a starting point due to their simplicity. Afterward, shell benchmark problems are solved considering the inherent complexity of curved structures. The importance of shell cases lies in the variety of mechanical responses they present when subject to different types of loads and boundary conditions. Additionally, the study takes into account the order of interpolation across the shell surface n_s and through the thickness n_l, as well as the number of elements used in the thickness direction n_{elem}, which has proven to be an important factor in the solid-shell context when dealing with Poisson thickness locking [123].

[123]: Hauptmann et al. (2000), *Extension of the 'solid-shell' concept for application to large elastic and large elastoplastic deformations*

The physical parameters used are taken from the references. Often, some unphysical values are used and also unphysical results are obtained. Nevertheless, we prefer to keep these values to compare our results with those published in the literature. No unit system is specified, understanding that all units used are consistent.

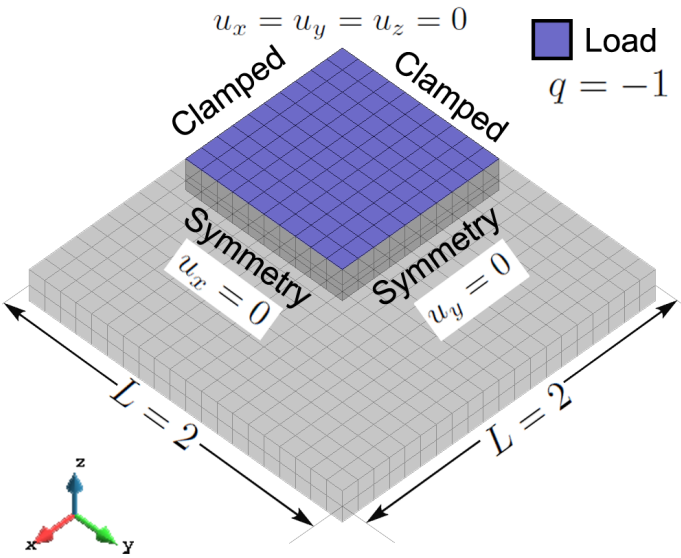

Figure 3.7: Clamped square plate: geometry and boundary conditions.

3.7.1 Analysis of plates

In this section, the performance of the stabilized mixed and the irreducible formulations presented in sections 3.6.2-3.6.3 are compared in two plate benchmark cases. The first case is the clamped circular plate under a uniformly distributed transverse load. Due to the symmetry of the geometry and the applied load, this case reduces to a one-dimensional problem, making it one of the simplest possible cases to be solved. The problem is designed in the classical manner found in the literature [81, 124, 125], by only modeling a quarter of the plate and dividing the domain into three patches with a structured mesh of bilinear elements in each, as described in Figs. 3.5-3.6. The radius of the plate is $R = 5$ and the thickness is $t = 0.1$, resulting in a slenderness ratio of $2R/t = 100$. The load is set to $q = -1$ per unit of surface across the entire surface. The material properties are $E = 10.92$ for Young's modulus and $\nu = 0.3$ for the Poisson number. The results are tracked at the center of the plate where the maximum deflection is 9778.1.

The second case is the clamped square plate under uniform distributed transverse load, a classical benchmark problem found in the literature [124]. This case is similar to the previous one; however, it does not reduce to a one-dimensional problem. Due to symmetry, only a quarter of the plate is modeled. Geometry and boundary conditions are shown in

[81]: Sze et al. (2004), *A stabilized eighteen-node solid element for hyperelastic analysis of shells*
[124]: Zhang et al. (2007), *Eight-node Reissner–Mindlin plate element based on boundary interpolation using Timoshenko beam function*
[125]: Aguirre et al. (2023), *A variational multiscale stabilized finite element formulation for Reissner–Mindlin plates and Timoshenko beams*

[124]: Zhang et al. (2007), *Eight-node Reissner–Mindlin plate element based on boundary interpolation using Timoshenko beam function*

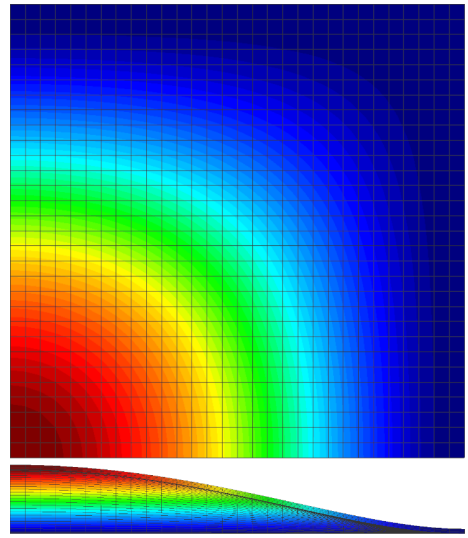

Figure 3.8: Clamped square plate: deformed configuration.

Figs. 3.7-3.8. The square has sides of length $L = 2$ and the thickness is $t = 0.01$, which yields a slenderness ratio of $L/t = 200$. The load is set to $q = -1$ per unit of surface, across the entire surface. The material properties are $E = 17.472 \cdot 10^6$ for Young's modulus and $\nu = 0.3$ for the Poisson number. Results are tracked at the center of the plate where the maximum deflection is 1.26.

Computations are first performed using the irreducible formulation to evaluate its capability to represent the bending state concerning numerical locking. Results for the circular and square plates are plotted in Figs. 3.9-3.10, solved using different combinations of n_s, n_l, and n_{elem}. As usual, relative displacement refers to the quotient between the reference solution and the solution we have computed.

The membrane and shear locking behavior is present in the cases of linear interpolation across the surface and they seem to disappear when the order is increased to quadratic. On the other hand, thickness locking is present when computed using linear through-the-thickness interpolation; therefore, a better description of the thickness strain is required. Using more linear elements in the transverse direction seems to slowly mitigate the locking behavior, but it can be solved immediately by using quadratic interpolation even with a single thickness element.

This misbehavior is examined further, considering that increasing the order of interpolation in the thickness direction

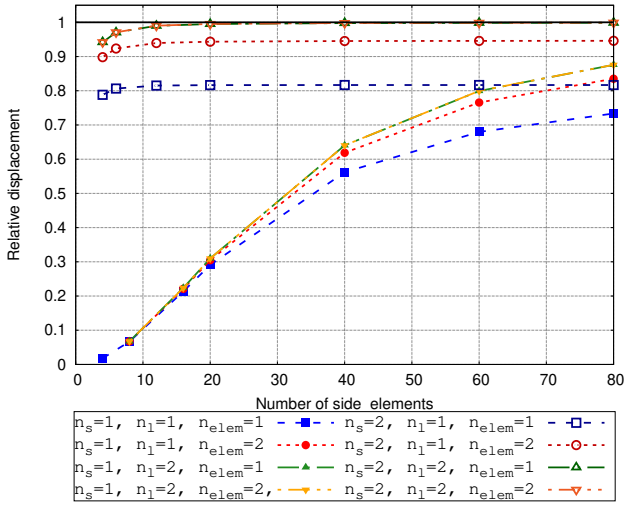

Figure 3.9: Irreducible formulation convergence for 1 and 2 elements through the thickness using linear and quadratic interpolations for circular plate.

allows for proper convergence. Fig. 3.11-3.12 shows convergence curves of cases using quadratic interpolation across the surface and up to 6 linear elements in the thickness direction. Results show that by adding more elements in the transverse direction yields little improvement in convergence. It becomes more clear that using a quadratic interpolation in the transverse direction yields better convergence and uses fewer resources compared to the option of adding more elements. These tests are useful to prove that capturing the through-the-thickness behavior is essential to have a proper approximation of the physical problem.

The same cases are solved using the stabilized mixed formulation. The interpolation order across the surface is set to $n_s = 1$, because the stabilized formulation deals with parasitic strains even when using linear elements. Therefore it should be free of membrane, shear and trapezoidal locking effects. The discretization through the thickness consists of $n_{elem} = \{1, 2\}$ elements, and interpolation orders of $n_l = \{1, 2\}$. Results are plotted in Figs. 3.13-3.14. The stabilized formulation is effective in dealing with numerical locking, except for the thickness locking. Unlike the second order irreducible approximation that needs quadratic transverse interpolation, thickness locking can be solved by using the stabilized formulation and either two elements or set quadratic interpolation through the thickness.

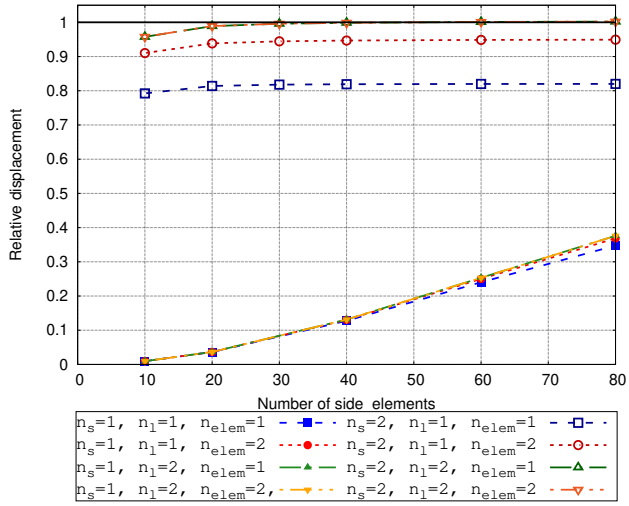

Figure 3.10: Irreducible formulation convergence for 1 and 2 elements through the thickness using linear and quadratic interpolations for square plate.

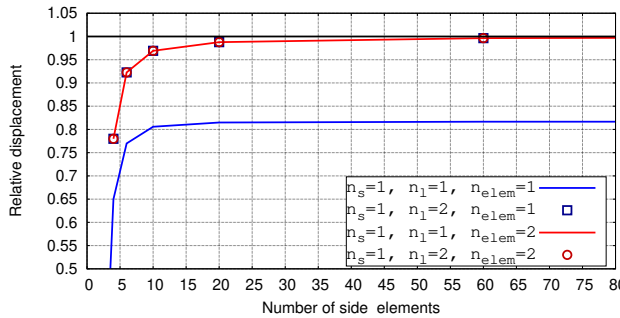

Figure 3.13: Stabilized formulation convergence for circular plate.

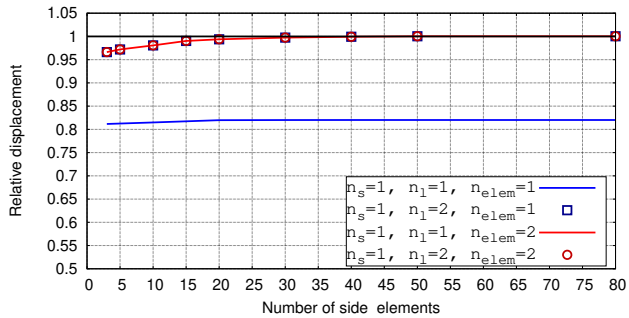

Figure 3.14: Stabilized formulation convergence for square plate.

The mechanical response of the plate problems are now checked using the mixed formulation and deactivating some of the stress degrees of freedom. However, it is tested considering that using a single linear through-the-thickness element yields thickness locking solutions. Therefore, computations are focused on either two elements or quadratic interpola-

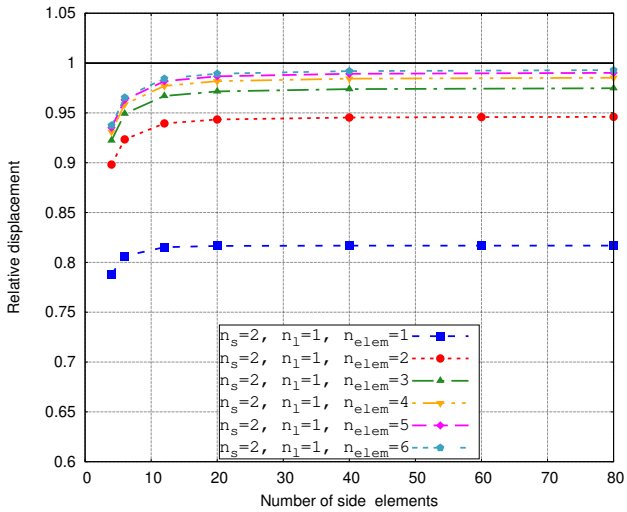

Figure 3.11: Irreducible formulation convergence curves for increasing number of linear elements through the thickness for circular plate.

tions. Results are shown in Figs. 3.15-3.16 for the circular plate case, and in Figs. 3.17-3.18 for the square plate case, where they are compared to the full mixed formulation, and to the irreducible formulation with quadratic interpolation across the surface to avoid shear and membrane locking.

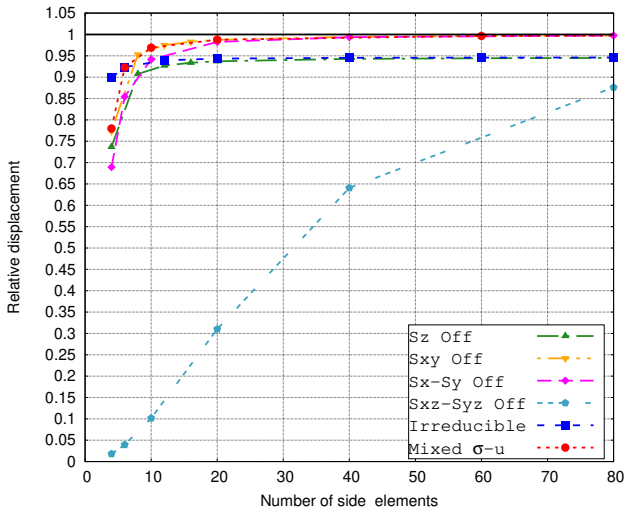

Figure 3.15: Circular plate: Stress deactivation convergence curves using $n_{nelem} = 2$.

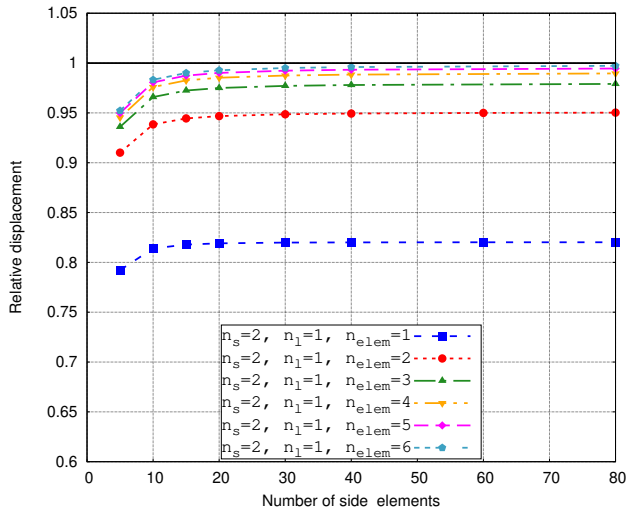

Figure 3.12: Irreducible formulation convergence curves for increasing number of linear elements through the thickness for square plate.

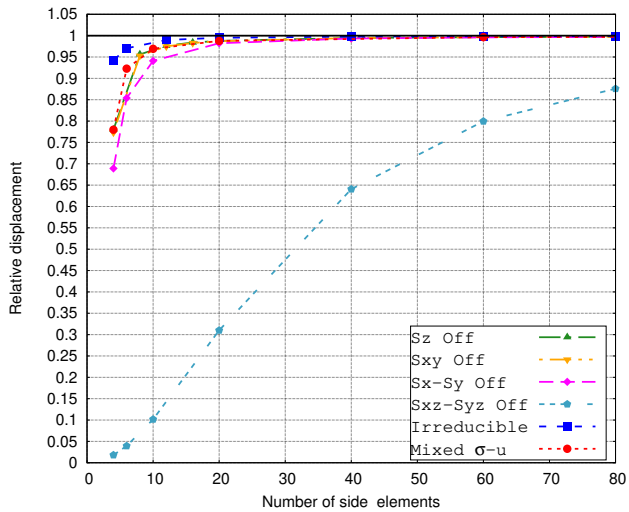

Figure 3.16: Circular plate: Stress deactivation convergence curves using $n_l = 2$.

Results confirm that the shear stress group fulfils the role of solving the shear locking in the case of plates. This result is expected and agrees with the Reissner-Mindlin plate theory, which is handled by controlling the shear strain terms [125]. Apart of the shear stress group, all other stress groups should not be necessary. However, when deactivating the thickness stress σ_z in the $n_{nelem} = 2$ approximation, it becomes clear that it is affected by thickness locking, not as in the case of $n_l = 2$. Therefore, the stabilization in the thickness direction must be activated to be effective in dealing with thickness locking.

[125]: Aguirre et al. (2023), *A variational multiscale stabilized finite element formulation for Reissner–Mindlin plates and Timoshenko beams*

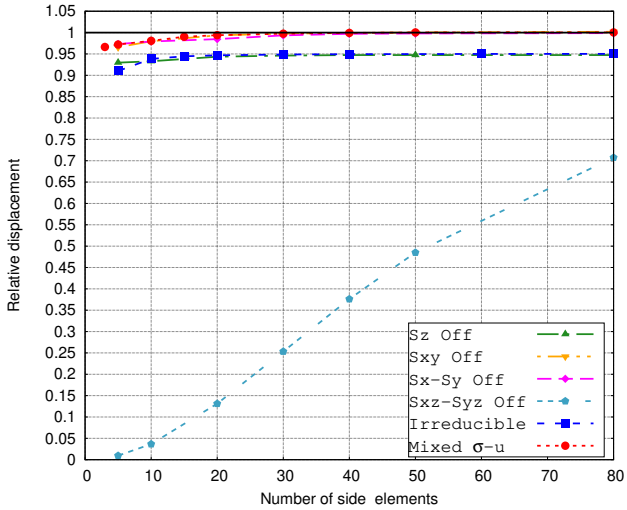

Figure 3.17: Square plate: Stress deactivation convergence curves using $n_{nelem} = 2$.

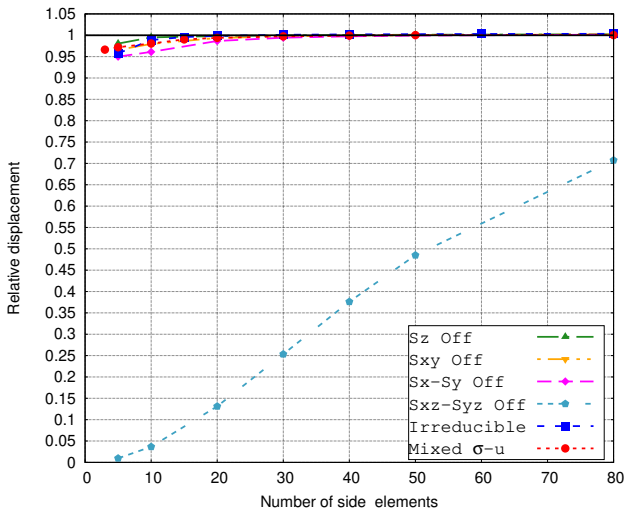

Figure 3.18: Square plate: Stress deactivation convergence curves using $n_l = 2$.

It has been confirmed that in the case of plates, the shear and thickness stresses are the only groups that matter to obtain locking-free solutions. Consequently, the total number of degrees of freedom can be reduced from 9 to 6 per node if using $n_{\text{nelem}} = 2$ (three displacements, two shear stresses and the transverse stress) or from 9 to 5 if using $n_l = 2$ (three displacements and two shear stresses). This is valid for plate structures, which do not suffer membrane or trapezoidal locking. To have a better understanding of the general behavior of thin structures, it is necessary to move from flat plates to curved shells.

3.7.2 Analysis of shells

To evaluate the mechanical response of shells it is necessary to consider curved structures, as well as specific loads that make the problem to be membrane or bending dominated. This section presents the mechanical analysis of shell structures using the irreducible and the stabilized mixed formulation. It has been proved in subsection 3.7.1 that thickness locking can be avoided either by increasing the order of interpolation or by increasing the number of elements in the thickness direction.

In the case of plates, it has also been shown in subsection 3.7.1 that the irreducible formulation suffers numerical locking when using linear interpolations across the surface and thickness directions. Because of that, computations are mainly performed using full quadratic interpolations. Nevertheless, some approximations are computed using a single linear element through the thickness to illustrate the effects of thickness locking effects.

Shell elements are usually tested using a set of tests specifically designed to evaluate the capabilities of elements to have a good performance. The tests considered in this work are taken from the literature [126, 127], and consist in subjecting shells to either inextensional bending, membrane stresses or rigid body motions. The most commonly used tests are the following:

[126]: Macneal et al. (1985), *A proposed standard set of problems to test finite element accuracy*
[127]: Belytschko et al. (1985), *Stress projection for membrane and shear locking in shell finite elements*

- The Scordelis-Lo roof and the twisted beam problems are designed to evaluate the capabilities to solve membrane strain states, whereas inextensional bending is not relevant.
- The hemispherical shell problem is used to evaluate inextensional bending modes with little membrane strain and also check if the element can reproduce rigid body rotations with respect to the shell surface normals.
- The pinched cylinder problem is a test that subjects the element to a high degree of inextensional bending modes as well as membrane strains.

In the examples below, the performance of the stabilized mixed formulation is compared with respect to the irreducible formulation. The tests are performed using different values of n_s, n_l and n_{elem} for the interpolations. Subsequently, the same tests are performed for the mixed formulation while deactivating the membrane, shear, twisting, and thickness stresses.

In that manner, the role of each one of the stresses in the stabilized formulation is put to test, and the implications of loading types and boundary conditions of each case are evaluated.

Scordelis-Lo roof

The problem consists of a single curvature cylindrical panel supported by rigid diaphragms at both ends and loaded vertically. Due to the symmetry of the problem, only a quarter of the shell is modeled using proper symmetry boundary conditions. The length of the roof is $L = 50$, the radius is $R = 25$, and the thickness is $t = 0.25$, which correspond to a slenderness ratio of $L/t = 200$. The loading is set to $q = -90$ per unit of surface across the upper surface. The geometry and boundary conditions are illustrated in Fig. 3.19-3.20.

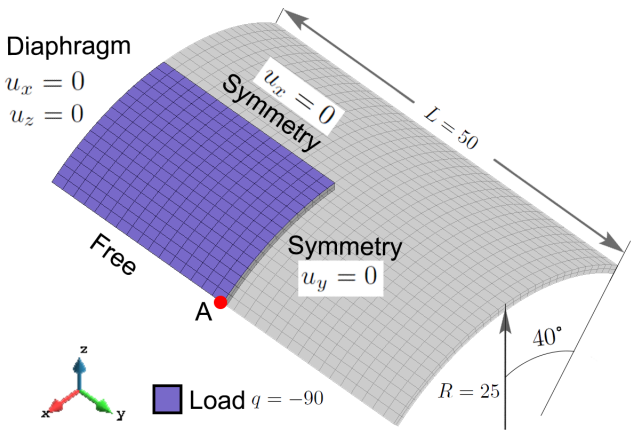

Figure 3.19: Scordelis-Lo roof: geometry and boundary conditions.

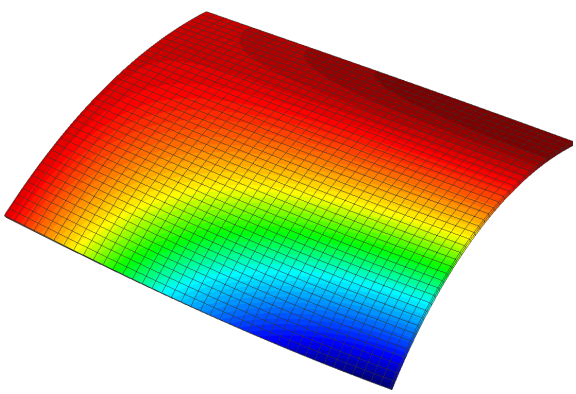

Figure 3.20: Scordelis-Lo roof: deformed configuration.

The material properties are $E = 4.32 \cdot 10^8$ for Young's modulus and $\nu = 0$ for Poisson's ratio. The solution is tracked at the mid side of the free edge, whose vertical displacement is between 0.3024 and 0.3086 according to the different authors [122, 128, 129]; however, in the present work the reference displacement is taken to be 0.3037.

[122]: Saloustros et al. (2021), *Accurate and locking-free analysis of beams, plates and shells using solid elements*
[128]: Simo et al. (1989), *On a stress resultant geometrically exact shell model. Part I: Formulation and optimal parametrization*
[129]: Belytschko et al. (1989), *Assumed strain stabilization procedure for the 9-node Lagrange shell element*

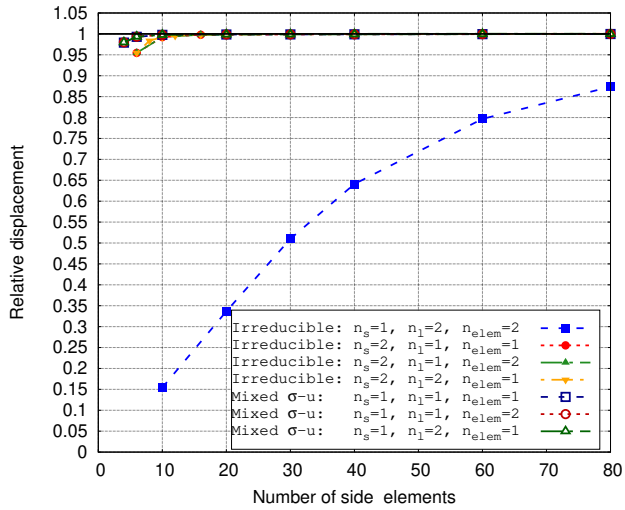

Figure 3.21: Scordelis-Lo roof: convergence curves using irreducible and mixed formulations.

Results for the irreducible and the mixed formulation are shown in Fig. 3.21, where convergence ratios of the relative displacements with respect to the number of elements are plotted. Compared to flat plate examples, which are affected only by shear and thickness locking, the present example is a curved structure and is affected by membrane and trapezoidal locking. As expected, using quadratic interpolation across the surface yields locking-free results. However, unlike the results found in the plate examples of subsection 3.7.1, this case does not present thickness locking due to the fact that it depends only on Poisson's ratio. This proves to be a good example to check that thickness locking does not depend on the formulation or the through-the-thickness interpolation choice, and since $\nu = 0$, it is natural that thickness locking disappears. Still, results prove that curvature adds an important difficulty for the problem to be solved properly.

Let us now deactivate strain groups in the mixed formulation and plot convergence curves as shown in Fig. 3.22-3.23. The notation used in this and subsequent figures is as follows: S_z stands for the thickness stress, S_{xy} for the twisting stress, S_x

and S_y for the membrane stresses and S_{xz} and S_{yz} for the membrane stresses, even if these stress components correspond to the local basis and not to the Cartesian one. In this case, shear stresses are needed to overcome shear locking, while normal thickness stress is necessary to overcome trapezoidal locking. Curiously, even though the Scordelis-Lo roof is a case to test membrane strain states, deactivating membrane stresses has no important effects in the convergence of the solution.

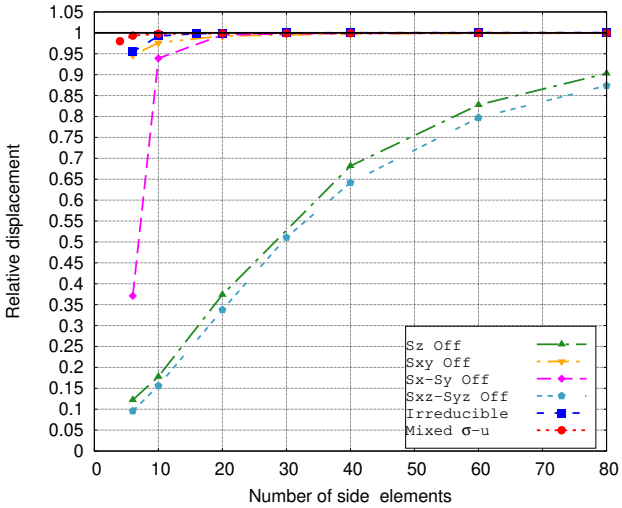

Figure 3.22: Scordelis-Lo roof: Stress deactivation convergence curves using $n_{nelem} = 2$.

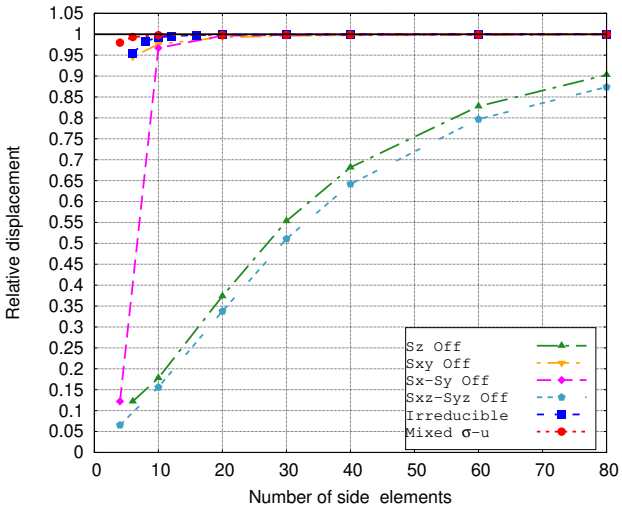

Figure 3.23: Scordelis-Lo roof: Stress deactivation convergence curves using $n_l = 2$.

Twisted beam

[126]: Macneal et al. (1985), *A proposed standard set of problems to test finite element accuracy*

This problem was initially proposed in [126] to test the wrapping effect of elements. It consists in a cantilever twisted beam with a point load at the free end, which can be directed either in or out of the plane. The geometry and boundary conditions are illustrated in Figs. 3.24-3.25. The length of the beam is $L = 12$, the width is $W = 1.1$ and the twist is 90°. This test is usually performed using a moderate thickness of $t = 0.32$; however, in the present work it is set to $t = 0.0032$, which gives a slenderness ratio of $L/t = 3750$, to have even greater locking effects. The load $P = 1$ is set outwards of the plane. As for the materials, Young's modulus is $E = 29 \cdot 10^6$ and Poisson's ratio is $\nu = 0.22$. The mesh is set using 8 elements along the width and increasing numbers of elements along the length. The solution is tracked at the center of the free end for the out-of-plane case, which has a horizontal displacement of 0.001294.

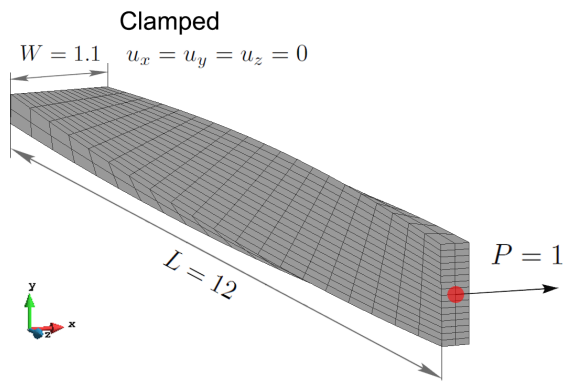

Figure 3.24: Twisted beam: geometry and boundary conditions.

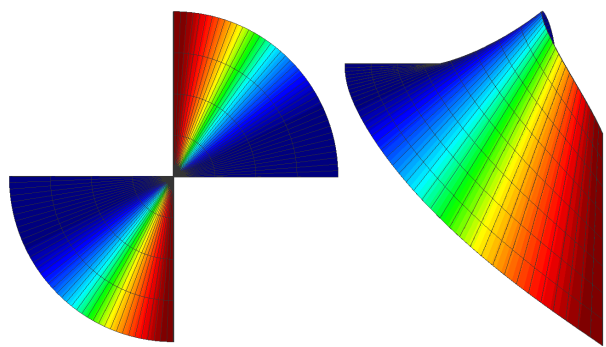

Figure 3.25: Twisted beam: deformed configuration.

Figure 3.26 shows the convergence curves of the relative dis-

placement with respect to the number of elements using the irreducible and mixed formulations. Results show that the irreducible formulation can deal with numerical locking when computing using quadratic interpolation across the surface and through the thickness, but is affected by thickness locking when using linear interpolation in the transverse direction. Due to the small thickness of the shell, the locking effects are greatly amplified, as it occurs when using linear interpolations across the surface. On the other hand, the mixed formulation is free of shear, membrane and trapezoidal locking. Results clearly show that thickness locking can be overcome either by increasing the order of interpolation or the number of elements in the thickness direction.

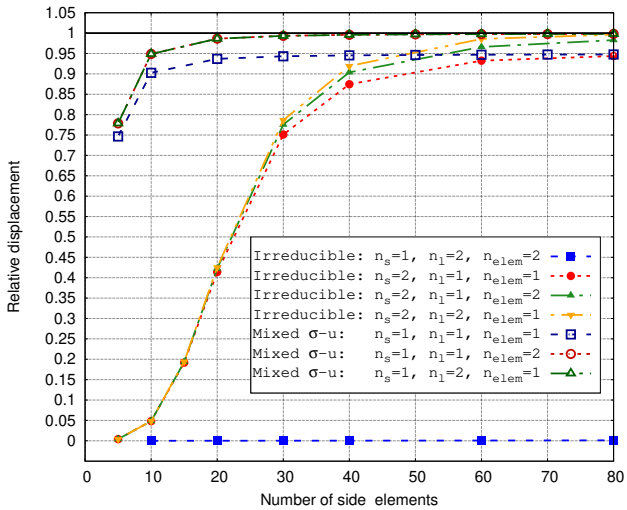

Figure 3.26: Twisted beam: convergence curves using irreducible and mixed formulations.

Even though both the twisted beam and Scordelis-Lo roof problems are membrane-dominated cases, they present different mechanical responses concerning stresses. When deactivating different stress groups, almost all stresses have to be interpolated to obtain proper convergence and avoid numerical locking, as shown in the convergence curves in Figs. 3.27-3.28. In this case, deactivating shear or twisting stresses yields locking of the solution. This is expected, considering that the problem undergoes strong shear locking effects due to the high slenderness ratio, even though it is a membrane-dominated case. This problem also undergoes a high degree of element twisting, so it expected to need twisting stresses. Being a membrane-dominated case, it is natural that deactivating membrane stresses results in membrane

locking. However, convergence curves show that membrane locking effects are much less severe compared with shear locking effects. In the case of trapezoidal locking, deactivating the thickness stress seems to have little impact on the solution, and convergence is similar to the irreducible formulation. On the other hand, thickness locking effects are mild; this becomes clear when comparing the solutions with $n_{nelem} = 2$ with $n_l = 2$, which are almost identical.

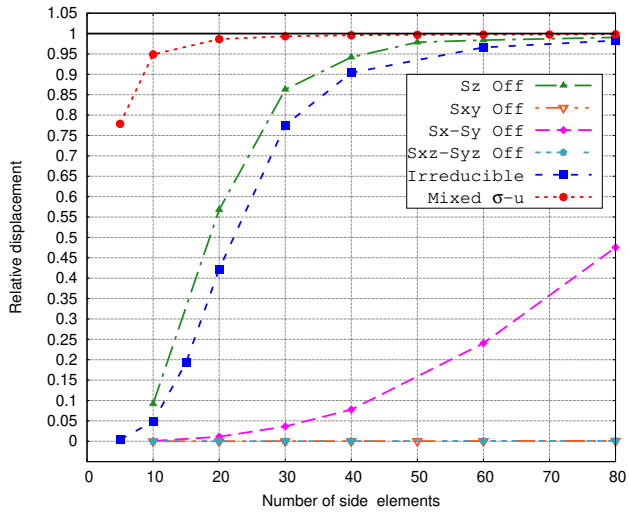

Figure 3.27: Twisted beam: Stress deactivation convergence curves using $n_{nelem} = 2$.

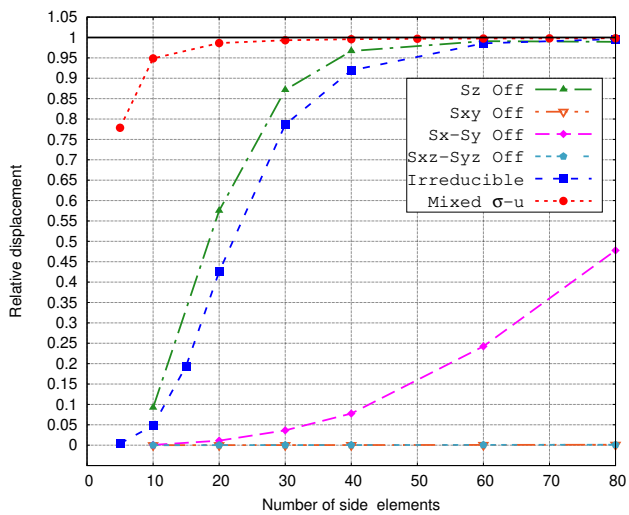

Figure 3.28: Twisted beam: Stress deactivation convergence curves using $n_l = 2$.

Hemispherical shell

This test is one step forward more challenging than the previous one because it tests both membrane and bending responses. It consists of a double curvature shell with a 18° hole, subject to point loads directed inwards and outwards of the surface. Due to the symmetry of the problem, only a quarter of the domain is modeled by using proper symmetry boundary conditions, as detailed in Figs. 3.29-3.30. The radius of the shell is $R = 10$, and the thickness is $t = 0.04$, which yields a slenderness ratio of $0.5R\pi/t = 392$. The loads are set to $P = 2$ each. The material properties are $E = 6.825 \cdot 10^7$ for Young's modulus and $\nu = 0.3$ for Poisson's ratio. Results are tracked at the points where forces are applied, where the normal displacements are 0.0940 according to the literature [126].

[126]: Macneal et al. (1985), *A proposed standard set of problems to test finite element accuracy*

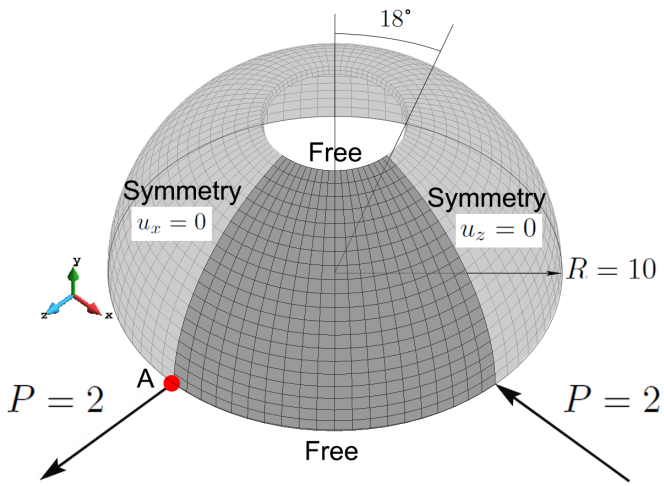

Figure 3.29: Hemispherical shell: geometry and boundary conditions.

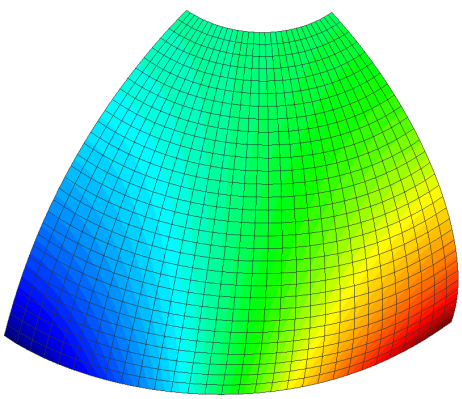

Figure 3.30: Hemispherical shell: deformed configuration.

Convergence curves for the irreducible and mixed formulations are shown in Fig. 3.31. Results show that thickness locking effects are almost negligible in all cases even though the Poisson ratio is relatively high. The stabilized mixed and the irreducible quadratic formulations are free of numerical locking independently of the interpolation chosen in the thickness direction. It appears that even though the problem is mostly bending-dominated, locking conditions are not strong enough to need a richer interpolation through the thickness.

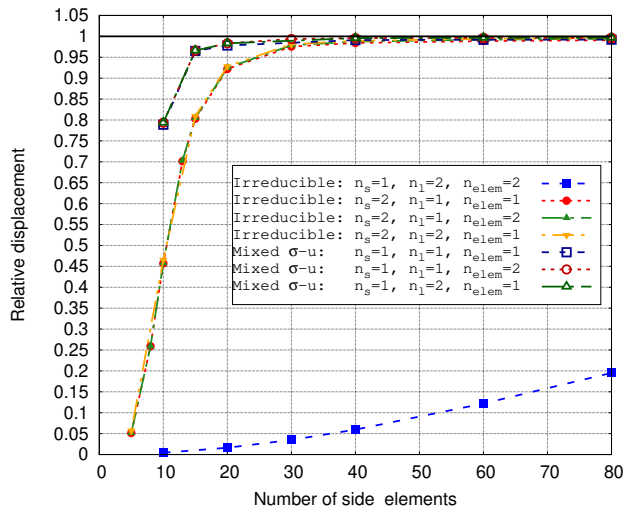

Figure 3.31: Hemispherical shell: convergence curves using irreducible and mixed formulations.

The convergence curves obtained when deactivating stress tensor components are plotted in Fig. 3.32-3.33. The curves behave in the same manner using either two elements or quadratic interpolation through the thickness. Results suggest that in this case trapezoidal locking is less relevant compared to shear and membrane locking, since the locking effect is milder when deactivating the thickness stress and stronger when deactivating the rest of the stresses. Even though the hemispherical shell problem is not designed to test element twisting, twisting stress appears to be necessary to capture the mechanical behavior of the shell.

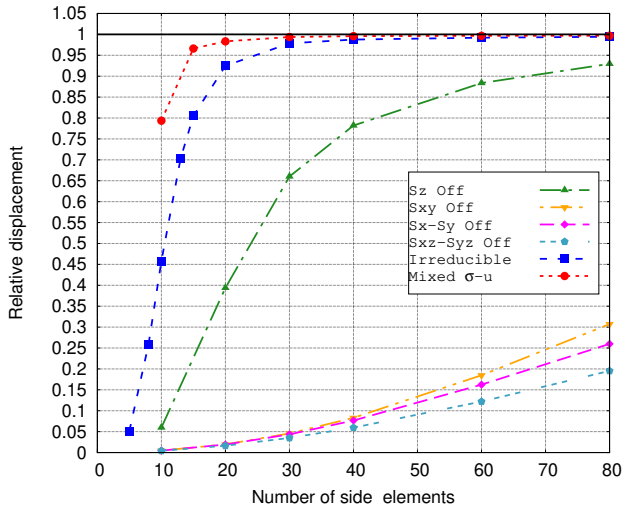

Figure 3.32: Hemispherical shell: Stress deactivation convergence curves using $n_{nelem} = 2$.

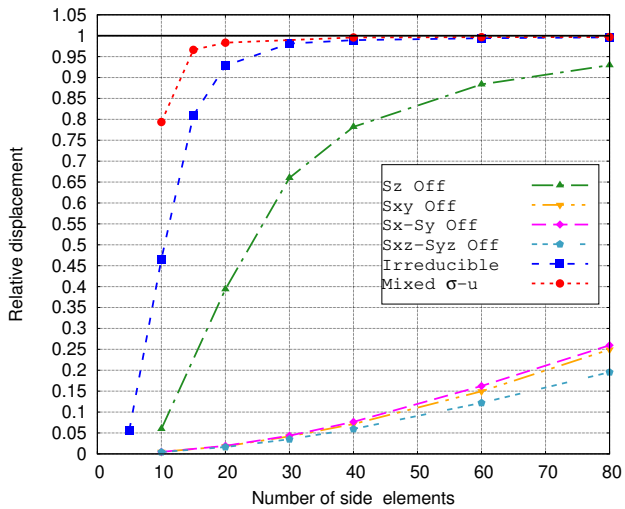

Figure 3.33: Hemispherical shell: Stress deactivation convergence curves using $n_l = 2$.

Pinched cylinder

This problem is the most demanding of the shell tests considered because it is subject to a high degree of inextensional bending. The test consists of a cylinder supported with one rigid diaphragm at each end, loaded by two radial forces at the opposite sides of the middle of the length. Because of the symmetry of the problem, only the eighth part of the cylinder is modeled using proper symmetry boundary conditions. The geometry and boundary conditions are detailed in Figs. 3.34-3.35. The geometry of the cylinder is set using

a length of $L = 600$, a radius of $R = 300$, and a thickness of $t = 3$. Therefore, the ratios of length and radius with respect to the thickness are $L/t = 200$ and $R/t = 100$, respectively. The material properties are $E = 3 \cdot 10^6$ for Young's modulus and $\nu = 0.3$ for Poisson's ratio. The loads are $P = 1$ each. The solution is tracked at the same point where the forces are applied, where the vertical displacement is $1.8384 \cdot 10^5$.

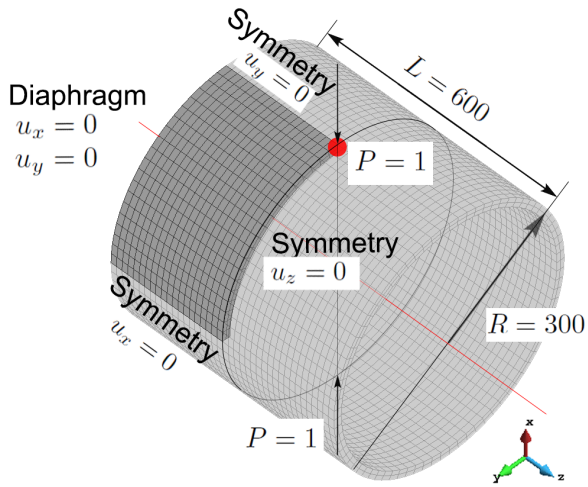

Figure 3.34: Pinched cylinder: geometry and boundary conditions.

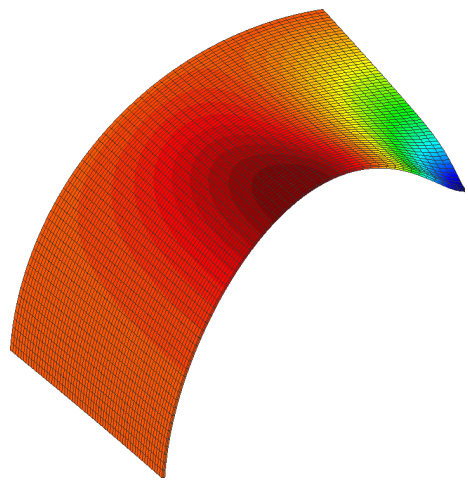

Figure 3.35: Pinched cylinder: deformed configuration.

The problem is solved for the irreducible and mixed formulations, whose convergence curves are plotted in Fig. 3.36. The thickness locking effects are stronger in this case compared with the rest of the tests. When using the irreducible formulation it becomes mandatory to use quadratic interpolation

in the thickness direction, but with the mixed formulation this can also be overcome by using two elements in the thickness direction. With respect to the other types of locking, the mixed formulation is able to deal with them using only linear elements.

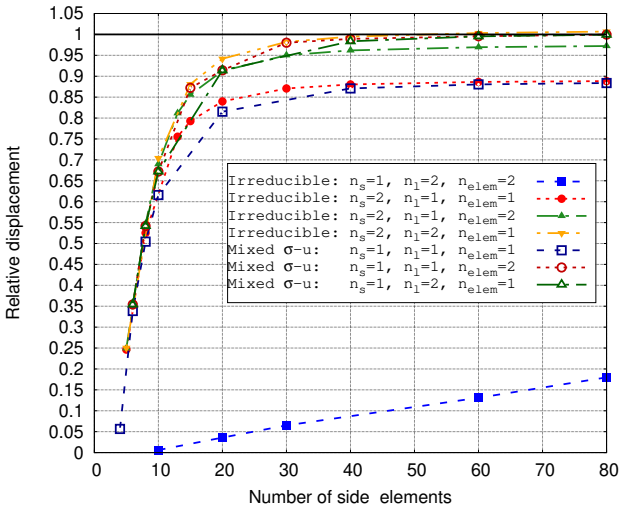

Figure 3.36: Pinched cylinder: convergence curves using irreducible and mixed formulations.

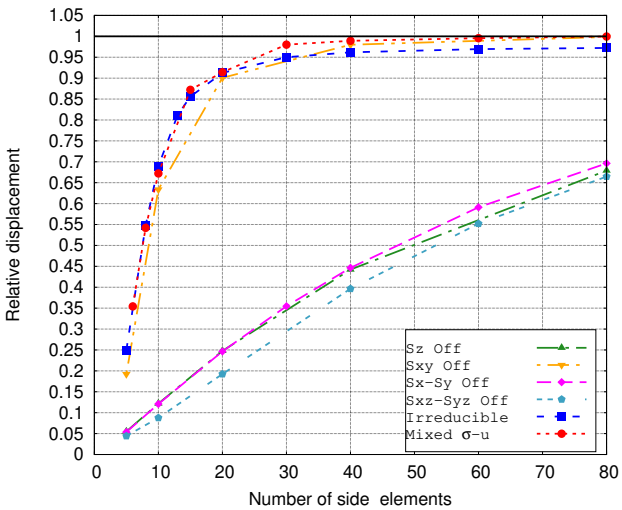

Figure 3.37: Pinched cylinder: Stress deactivation convergence curves using $n_{nelem} = 2$.

The convergence curves obtained by deactivating stress components are shown in Figs. 3.37-3.38. In this case, only the twisting stress can be turned off with no apparent locking effects. Results show that membrane, shear and trapezoidal locking are of similar intensity since the curves obtained by

neglecting the membrane, shear and thickness components of the stress, respectively, converge at a similar rate.

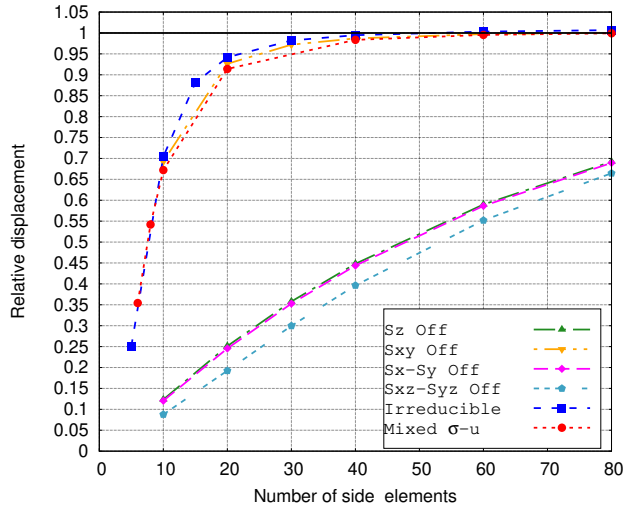

Figure 3.38: Pinched cylinder: Stress deactivation convergence curves using $n_l = 2$.

3.7.3 Result summary

The interpolation requirements and the mechanical response for plates and shells have been analyzed in subsections 3.7.1 and 3.7.2. Results show a variety of interpolation requirements to deal with numerical locking. In the irreducible formulation case, all tests have in common the need of using quadratic interpolation across the surface to deal with membrane, shear and trapezoidal locking, and quadratic interpolation in the thickness direction to deal with thickness locking. On the contrary, the mixed formulation allows to use linear elements in all directions, but it requires at least two elements in the thickness direction to deal with thickness locking. From the results it becomes clear that the bending-dominated problems are the most demanding cases in terms of interpolation, and some membrane-dominated problems can be solved using a single linear element in the thickness direction.

The stress requirements found for the mixed formulation in all numerical examples are summarized in Table 3.1. The type of locking and its intensity depend strongly on whether or not the structure is curved as well as on the bending state. Results are clear on the fact that shear locking is always present in thin structures, even in membrane-dominated states. From

the results obtained, it becomes clear that curvature dramatically increases the complexity of thin structure problems. Moreover, this confirms that all stress components are required for a robust shell mixed formulation, since all of them are important in certain scenarios.

Table 3.1: Stress tensor requirements for each benchmark test, required (×) and not-required (–).

Case	Curvature	Mechanical response	Slenderness ratio	σ_x σ_y	σ_{xy}	σ_z	σ_{xz} σ_{yz}
Circular plate	No	Bending	100	–	–	–	×
Square plate	No	Bending	200	–	–	–	×
Scordelis-Lo roof	Single	Membrane	200	–	–	×	×
Twisted beam	Double	Membrane	3750	×	×	–	×
Hemispherical shell	Double	Membrane >Bending	392	×	×	×	×
Pinched cylinder	Single	Bending >Membrane	200	×	–	×	×

3.7.4 Performance assessment

Now that it has been verified that the mixed formulation performs optimally when using the entire stress tensor, it only remains to check the performance the stabilized approach in comparison to other commonly used approaches. For this purpose, we have selected some well known references in the subject as well as some more approaches developed recently, detailed in Table 3.2. The comparisons are performed in the four shell cases presented previously, using the OSGS stabilization approach. Again we compare the convergence curves of relative displacements as presented previously in each case, as illustrated in Figs. 3.39-3.40-3.41-3.42. Results show convergence curves in agreement with those presented in the references, making the current strategy to be well suited approach to solve the shell locking problems.

Table 3.2: Reference solutions for shell analysis.

Ref.	Year	Abbreviation	Description
[58]	1997	MITC8	8-node serendipity continuum-based shell with ANS
[99]	1984	MITC4	4-node serendipity continuum-based shell with ANS
[130]	2008	MIST2	4-node MITC4 extended with a smoothing cell for membrane and bending stiffness
[85]	2014	H2ANS	ANS extended to NURBS Solid-shell element
[131]	2015	RH8s-1 RH8s-2 RH8s-4	Smoothed Finite Element Method (SFEM) Solid-shell element with ANS for transverse and trapezoidal locking.
[132]	2016	ANS-EAS-CR	ANS and EAS incorporated for different components of a Solid-shell element using a Corrotational kinematic description
[92]	2009	EAS-ANS-RI	EAS to deal with volumetric and Poisson locking, ANS for thickness and shear locking and RI for hourglass stabilization for Solid-shell element
[79]	2000	ANS$\gamma\epsilon$-HS	Hybrid-Stress formulation of Solid-shell element with ANS for shear and trapezoidal locking
[133]	2020	SBFEM	Scaled Boundary Finite Element for cubic and quadratic shell interpolations and through-the-thickness analytical integration
[134]	2018	IGA-RM	Isogremetric analysis Reisner-Mindlin continuum- based shell interpolated with cubic Lagrange polinomials (PL3) and quaratic or quintic NURBS order (PN2-PN5)

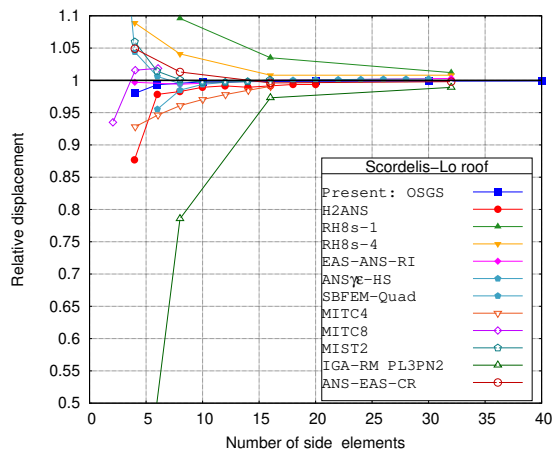

Figure 3.39: Scordelis-Lo roof: Performance of mixed $\sigma - u$ stabilized OSGS formulation respect to reference solutions.

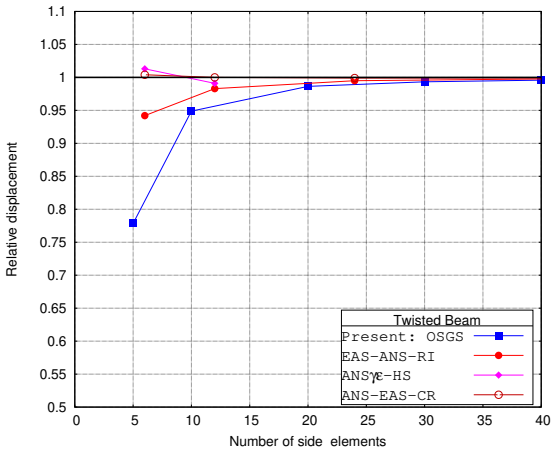

Figure 3.40: Twisted beam: Performance of mixed $\sigma - u$ stabilized OSGS formulation respect to reference solutions.

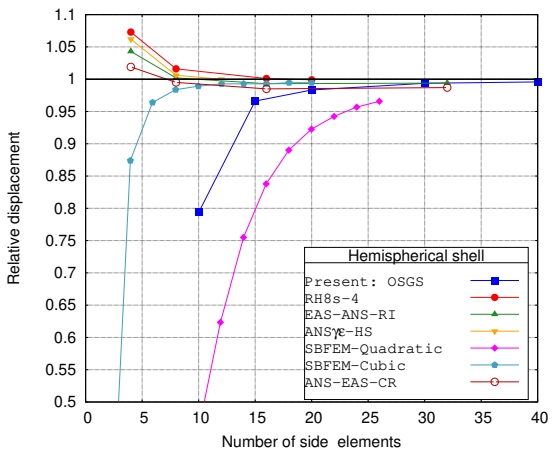

Figure 3.41: Hemispherical shell: Performance of mixed $\sigma - u$ stabilized OSGS formulation respect to reference solutions.

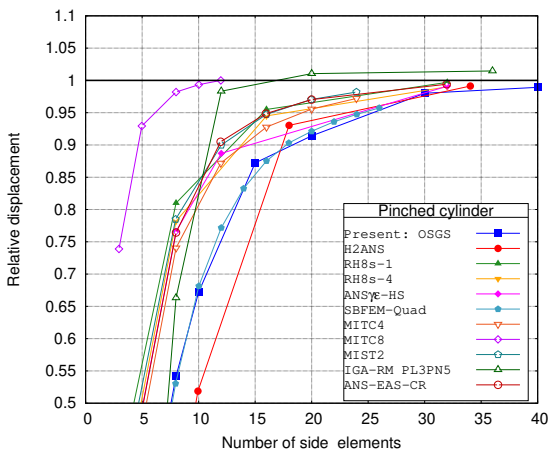

Figure 3.42: Pinched cylinder: Performance of mixed $\sigma - u$ stabilized OSGS formulation respect to reference solutions.

3.8 Conclusions

The main purpose of this work is to study numerical locking in thin structures modeled by solid-shell elements using a mixed stabilized displacement-stress formulation. The study focuses on comprehending the locking mechanism by isolating the components of the stress field with respect to the local directors. To this end, the formulation is posed using curvilinear coordinates, and the components of the stress field can be grouped with respect to the direction they act: membrane, shear, twisting and thickness stresses. Additionally, an algorithm to independently activate or deactivate the components of the stress field has been implemented, allowing to solve numerical examples by interpolating only part of the stress tensor. A set of benchmark problems have been solved interpolating all the stress tensor and deactivating a single stress group at a time. Convergence curves have been plotted in order to characterize the mechanical response of the structure with respect to numerical locking. Results show which specific stress groups have to be interpolated in curved structures in order to circumvent numerical locking; these groups depend on the geometry, type of curvature, boundary conditions and type of load. Flat structures are easier to analyze: they suffer shear locking when subject to transverse loads, and they are also affected by thickness locking if the through-the-thickness interpolation is not rich enough to capture the behavior of the solution. As a result of the present investigation, it has been proven that a robust stabilized mixed formulation that can properly handle all types of mechanical behaviors of curved shells requires interpolating all the stresses and having either a minimum of two elements or quadratic interpolation through the thickness. Obviously, if all components of the stress tensor are interpolated, there is no need to use curvilinear coordinates.

Acknowledgements

This work was supported by Vicerrectoría de Investigación, Desarrollo e Innovación (VRIDEI) of the Univeridad de Santiago de Chile, and the National Agency for Research and Development (ANID) Doctorado Becas Chile/2019 - 72200128 of the Government of Chile. R. Codina acknowledges the support received from the ICREA Acadèmia Research Program of the Catalan Government.

Declarations

Conflict of interest

The authors declare that they have no known competing financial interests or personal relationships that could have appeared to influence the work reported in this paper.

Replication of results

All the information required for replicating the paper results was duly presented. Data files for the results are available upon request from the authors.

Finite strain hyperelasticity formulations for Solid-Shell Finite Elements

4

4.1 Abstract

This chapter works as a direct continuation of the previous chapter. It is focused on modeling solid-shell elements using a stabilized two-field finite element formulation. The previous chapter introduced a stabilization technique based on the Variational Multiscale framework, which is proven to effectively adress numerical locking in infinitesimal strain problems. The primary objective of the study is to characterize the inherent numerical locking effects of solid-shell elements in order to comprehensively understand their triggers and how stabilized mixed formulations can overcome them. In this current phase of the work, the concept is extended to finite strain solid dynamics involving hyperelastic materials. The aim of introducing this method is to obtain a robust stabilized mixed formulation that enhances the accuracy of the stress field. This improved formulation holds great potential for accurately approximating shell structures undergoing finite deformations. To this end, three techniques based in the Variational Multiscale stabilization framework are presented. These stabilized formulations allow to circumvent the compatibility restriction of interpolating spaces of the unknowns inherent to mixed formulations, thus allowing any combination of them. The accuracy of the stress field is successfully enhanced while maintaining the accuracy of the displacement field. These improvements are also inherited to the solid-shell elements, providing locking-free approximation of thin structures.

4.2 Introduction

Shell structures have become an important research subject in both nature and engineering fields due to their wide ranging diversity and applicability. However, the structural element technology is a challenging topic due to the inherent unstable behavior when discretized and approximated using numerical methods [9]. In the existing literature, shell models are typically classified into three main categories: classical shell element, continuum-based element, and solid-shell elements. The main distinction among these approaches lies in the treatment of the through-the-thickness integration [11].

[9]: Belytschko et al. (2014), *Nonlinear finite elements for continua and structures*

[11]: Bischoff et al. (2004), *Models and finite elements for thin-walled structures*

The solid-shell approximation of thin structures is well known to suffer from several types of numerical locking. In the previous chapter, extensive investigations were conducted to understand the different mechanisms that trigger numerical locking, which will be briefly discussed here. Among the various types, shear-locking is the most commonly discussed form of numerical locking in the context of shell structures. Shear-locking occurs when the shell fails to accurately couple the in-plane translations of its upper and lower surfaces with the transverse translation of the mid-surface, leading to the emergence of parasitic transverse shear strains [1]. Similarly, membrane-locking arises due to the shell's inability to properly account for the coupling between the in-plane translations of its upper and lower surfaces and the in-plane translation of the mid-surface. This results in the appearance of parasitic membrane strains [71]. Geometrical approximation gives rise to trapezoidal locking, which occurs in solid-shell elements when the director vectors defining the shell's surface are not parallel, leading to the occurrence of parasitic normal transverse strains [72]. Poisson's thickness locking arises due to the incompatibility of the approximation between constant normal transverse strains and linear in-plane strains, which are coupled through Poisson's ratio. Lastly, volumetric locking occurs when the material is nearly or fully incompressible, resulting in the presence of parasitic normal strains [70].

[1]: Oñate (2013), *Structural analysis with the finite element method. Linear statics: volume 2: beams, plates and shells*

[71]: Sze (2002), *Three-dimensional continuum finite element models for plate/shell analysis*

[72]: MacNeal (1989), *Toward a defect-free four-noded membrane element*

[70]: Doll et al. (2000), *On volumetric locking of low-order solid and solid-shell elements for finite elastoviscoplastic deformations and selective reduced integration*

Reduced Integration methods are commonly employed to mitigate certain numerical instabilities by reducing undesired constraints at the quadrature points [88]. However, these approaches are prone to entail spurious zero energy modes [91]. To address this issue, Assumed Strain (AS) methods were de-

[88]: Zienkiewicz et al. (1971), *Reduced integration technique in general analysis of plates and shells*

[91]: Belytschko et al. (1984), *Hourglass control in linear and nonlinear problems*

veloped as a stabilization technique, initially implemented by MacNeal [73] in shell problems. From this point, two of the most utilized stabilization techniques were derived from AS methods: Assumed Natural Strain (ANS) [74] and Enhanced Assumed Strain (EAS) [76] methods. Even though these approaches were initially developed to deal with numerical instabilities in solid mechanic problems, they were eventually extended to classical shell theory and subsequently incorporated into solid-shell elements [77]. Another important approach consists in the Mixed Interpolated Tensorial Components (MITC) method, which has proven to be effective in mitigating numerical locking [99]. In the solid-shell framework, the MITC method has emerged as one of the primary approaches for handling instabilities [103].

There are several authors that have developed important advances based on these strategies in the context of non-linearity of solid-shells. Klinkel et al. [78] used EAS and ANS to improve the locking behavior of solid-shells with anisotropic materials. Later in [135] they used a variational principle based on the Hu-Washizu functional to decompose the strain field in two parts approximated by different function spaces. The author employs EAS to alleviate thickness locking and uses ANS interpolations for the thickness and transverse shear strains. Doll et al. [70] used a deviatoric-volumetric decoupled formulation and selective reduced reduced integration to solve finite elastoviscoplastic deformation problems. Korelc et al. [136] proposed an extension for shape functions derivatives using Taylor series to develop a locking free EAS element. Schwarze and Reese [92] developed a element based in the Hu-Washizu variational principle with only one EAS degree of freedom to treat volumetric and Poisson locking and used ANS to eliminate curvature and shear locking, and was later extended to the non-linear case in [93]. Mostafa et al. [84] used a decoupled in-plane, transverse and thickness components to approach them independently, and treated numerical lockings by using Assumed Natural Deviatoric Strain along with ANS and EAS approaches in each component. Caseiro et al. [86] presented an extension of a NURBS-based solid-shell element [85] based on ANS by using a corrotational coordinate system to integrate the constitutive law. Hajlaoui et al. [83] introduced a higher order solid shell element for static and buckling analysis of laminated composite structures based on EAS and ANS. Leonetti et al. [96] proposed an isogeometric solid-shell with linear interpola-

[73]: MacNeal (1978), *A simple quadrilateral shell element*

[74]: Park et al. (1986), *A curved C^o shell element based on assumed natural-coordinate strains*

[76]: Simo et al. (1990), *A class of mixed assumed strain methods and the method of incompatible modes*

[77]: Belytschko et al. (1993), *Assumed strain stabilization of the eight node hexahedral element*

[99]: Dvorkin et al. (1984), *A continuum mechanics based four-node shell element for general non-linear analysis*

[103]: Chapelle et al. (2004), *3D-shell elements and their underlying mathematical model*

[78]: Klinkel et al. (1999), *A continuum based three-dimensional shell element for laminated structures*

[135]: Klinkel et al. (2006), *A robust non-linear solid shell element based on a mixed variational formulation*

[70]: Doll et al. (2000), *On volumetric locking of low-order solid and solid-shell elements for finite elastoviscoplastic deformations and selective reduced integration*

[136]: Korelc et al. (2010), *An improved EAS brick element for finite deformation*

[92]: Schwarze et al. (2009), *A reduced integration solid-shell finite element based on the EAS and the ANS concept—Geometrically linear problems*

[93]: Schwarze et al. (2011), *A reduced integration solid-shell finite element based on the EAS and the ANS concept—Large deformation problems*

[84]: Mostafa et al. (2013), *A solid-shell corotational element based on ANDES, ANS and EAS for geometrically nonlinear structural analysis*

[86]: Caseiro et al. (2015), *Assumed natural strain NURBS-based solid-shell element for the analysis of large deformation elasto-plastic thin-shell structures*

[85]: Caseiro et al. (2014), *On the Assumed Natural Strain method to alleviate locking in solid-shell NURBS-based finite elements*

[83]: Hajlaoui et al. (2016), *An improved enhanced solid shell element for static and buckling analysis of shell structures*

[96]: Leonetti et al. (2018), *An efficient isogeometric solid-shell formulation for geometrically nonlinear analysis of elastic shells*

[97]: Barfusz et al. (2021), *A reduced integration-based solid-shell finite element formulation for gradient-extended damage*

[137]: Kikis et al. (2022), *Two-field formulations for isogeometric Reissner–Mindlin plates and shells with global and local condensation*

[138]: Braun et al. (1994), *Nonlinear shell formulations for complete three-dimensional constitutive laws including composites and laminates*

[59]: Bischoff et al. (1997), *Shear deformable shell elements for large strains and rotations*

[139]: Brank et al. (2002), *Nonlinear shell problem formulation accounting for through-the-thickness stretching and its finite element implementation*

[140]: Zhang et al. (2016), *Degenerated shell element with composite implicit time integration scheme for geometric nonlinear analysis*

[66]: Betsch et al. (1996), *A 4-node finite shell element for the implementation of general hyperelastic 3D-elasticity at finite strains*

[141]: Campello et al. (2011), *An exact conserving algorithm for nonlinear dynamics with rotational DOFs and general hyperelasticity. Part 2: shells*

[142]: Pimenta et al. (2004), *A fully nonlinear multi-parameter shell model with thickness variation and a triangular shell finite element*

[102]: Jeon et al. (2015), *The MITC3+ shell element in geometric nonlinear analysis*

tion through the thickness and NURBS interpolation in the mid surface, and used a reduced integration scheme to alleviate lockings. A combination of ANS and EAS methods have been employed simultaneously in a work of Barfusz et al. [97] to alleviate numerical locking in a solid-shell gradient-extended plasticity damage model of low-order isoparametric elements. More recently, in the work of Kikis and Klinkel [137] they developed a mixed formulation, with static condensation of the stress variables, based on the Hellinger-Reissner functional to alleviate membrane and shear locking.

Even through the present work is focused in solid-shell type elements, it is also worth mentioning the contributions of classical and continuum based shell elements. Braun, Bischoff and Ramm [138] proposed a 7-parameter continuum-based shell element that accounts for thickness stretching to treat thickness-locking and the EAS approach to treat the numerical lockings, and it was extended in [59] in conjunction with ANS approach. In a simmilar line, Brank et al. [139] used a another approach to reduce the formulation to a 6-parameter element. Zhang et al. [140] used a modified constitutive equation and employing MITC in the strain field to overcome shear-locking. A 4-node element with three-dimensional material laws was proposed in the work of Betsch et al. [66] using a three-field formulation and treating the strains with ANS to alleviate shear-locking. The work by Campello et a.l [141] introduced a triangular element with displacements and rotations degrees of freedom, with statically condensed finite strain equations by assuming plane stress state. The formulation was initially designed for inextensional shell director, and was later extended in [142] to account for the thickness variation by considering it as an additional degree of freedom. Jeon et al. [102] presented a MITC3 shell element for large displacements and rotations by including an assumed covariant transverse shear strain field. Gruttmann and Wagner [143] introduced a multi-field approach with statically condensed parameters to solve layered shells with geometric and material non-linearities, and dealing with shear-locking by means of the ANS approach. This approach was also extended to quadratic interpolation of strains in [144]. A more recent work by Rezaiee-Pajand and Ramezani [106] made comparative study of different MITC and ANS elements proposed in the last decade to evaluate their performance in buckling analysis.

The present work deals with the numerical locking by using a

mixed two-field approach by introducing additional stresses as new unknowns, thus leading to a problem whose unknowns are stresses and displacements. Note that even though this approach entails a considerable increase in the number of degrees of freedom per node, it also increases the accuracy of the stress and strain fields. In the previous chapter, it has been shown that having control over the stress field allows to correct the parasitic strains arising in thin structures, and also that it is necessary to take as unknowns *all* the components of the stress tensor. However, from the numerical point of view, formulating the problem using a mixed approach leads us to a saddle point problem [145]. This issue stems from the incompatibility between the interpolation spaces of the unknowns, which becomes crucial at this stage. In the context of solid and solid-shell models, utilizing the mixed stress-displacement approach does not permit the use of equal-order interpolation for the variables because it does not fulfill the inf-sup condition. Consequently, careful consideration and treatment are necessary. Hence, the need for stabilization arises. To this end, in this work a stabilized formulation based on the Variational Multiscale (VMS) framework is presented. The VMS approach was first introduced by Hugues [2, 3] and further developed in [43]. This approach was found successful in a wide variety of problems, specially in fluid mechanics [114, 115, 146] and more recently in solid mechanics [4, 116, 117, 125, 147]. By working within the VMS framework, stabilized formulations have been developed, allowing for equal-order interpolation of the unknowns.

This work is organized as follows. The geometrical approximation of the shell domain is briefly explained in Section 4.3, summarizing the geometrical construction presented in the previous chapter. In Section 4.4 the solid dynamics equations in finite strain theory are summarized, and a mixed two-field formulation of the problem is stated. The time integration scheme and the linearization method for the nonlinear problem are presented in Section 4.5. The finite element (FE) approximation is presented in Section 4.8, starting with the Galerkin FE approximation, which requires inf-sup stable interpolations, and then moving to the novel stabilized formulation we propose; as far as we are aware, this is the first work presenting a stabilized displacement-stresss formulation for the finite strain elastic problem. Several numerical examples showing the convergence and accuracy of the pro-

[143]: Gruttmann et al. (2020), *An advanced shell model for the analysis of geometrical and material nonlinear shells*

[144]: Wagner et al. (2020), *An improved quadrilateral shell element based on the Hu–Washizu functional*

[106]: Rezaiee-Pajand et al. (2022), *An evaluation of MITC and ANS elements in the nonlinear analysis of shell structures*

[145]: Boffi et al. (2013), *Mixed finite element methods and applications*

[2]: Hughes (1995), *Multiscale phenomena: Green's functions, the Dirichlet-to-Neumann formulation, subgrid scale models, bubbles and the origins of stabilized methods*

[3]: Hughes et al. (1998), *The variational multiscale method - A paradigm for computational mechanics*

[43]: Codina (2000), *Stabilization of incompressibility and convection through orthogonal sub-scales in finite element methods*

[114]: Castillo et al. (2017), *Finite element approximation of the viscoelastic flow problem: A non-residual based stabilized formulation*

[115]: Moreno et al. (2019), *Logarithmic conformation reformulation in viscoelastic flow problems approximated by a VMS-type stabilized finite element formulation*

[146]: Castillo et al. (2019), *Dynamic term-by-term stabilized finite element formulation using orthogonal subgrid-scales for the incompressible Navier–Stokes problem*

posed method are presented in Section 4.9. To end up, some conclusions are drawn in Section 4.10.

[4]: Castañar et al. (2020), *A stabilized mixed finite element approximation for incompressible finite strain solid dynamics using a total Lagrangian formulation*
[116]: Castañar et al. (2023), *A stabilized mixed three-field formulation for stress accurate analysis including the incompressible limit in finite strain solid dynamics*
[117]: Fabra et al. (2023), *Mixed stabilized finite element methods in linear elasticity for the velocity–stress equations in the time and the frequency domains*
[125]: Aguirre et al. (2023), *A variational multiscale stabilized finite element formulation for Reissner–Mindlin plates and Timoshenko beams*
[147]: Castañar et al. (2022), *Topological derivative-based topology optimization of incompressible structures using mixed formulations*

4.3 Geometrical approximation using finite elements

4.3.1 Construction of the local basis

The details of how the geometry is approximated are explained in the previous chapter; however, for the sake of completeness, they are briefly summarized here. Consider the shell surface to be represented in a general manner by Ω^{2D} in $\mathbb{R}^3$. Suppose that we have a FE partition $T_h = \{K\}$ of Ω^{2D} of diameter h, so that $\bar{\Omega}^{2D} = \bigcup_{K\in T_h} K$. Let $K \in T_h$ be an element domain of the partition and its isoparametric mapping

$$\begin{aligned} \boldsymbol{\varphi}_K \,:\, K_0 &\longrightarrow K \\ (\xi,\eta) &\mapsto (x^1, x^2, x^3), \end{aligned}$$

that maps the reference domain $K_0 \subset \mathbb{R}^2$ to $K \subset \mathbb{R}^3$, where (ξ,η) are the isoparametric coordinates. Consider a Lagrangian interpolation

$$\boldsymbol{\varphi}_K(\xi,\eta) = \sum_{A=1}^{n_{nod}} N^A(\xi,\eta)\mathbf{x}^A, \tag{4.1}$$

where n_{nod} is the number of nodes of K, $N^A(\xi,\eta)$ is the shape function of node A on K_0, $A = 1,\dots,n_{nod}$, and $\mathbf{x}^A$ is the position vector of node A in K, $A = 1,\dots,n_{nod}$. The collection of all mappings $\{\boldsymbol{\varphi}_K, K \in T_h\}$ provides a local parametrization of Ω^{2D}.

The vectors tangent to each $K \in T_h$ are given by

$$\mathbf{g}^*_{1,K} = \left|\frac{\partial\boldsymbol{\varphi}_K}{\partial\xi}\right|^{-1}\frac{\partial\boldsymbol{\varphi}_K}{\partial\xi}, \quad \frac{\partial\boldsymbol{\varphi}_K}{\partial\xi} = \sum_{A=1}^{n_{nod}}\frac{\partial N^A}{\partial\xi}\mathbf{x}^A,$$

$$\mathbf{g}^*_{2,K} = \left|\frac{\partial\boldsymbol{\varphi}_K}{\partial\eta}\right|^{-1}\frac{\partial\boldsymbol{\varphi}_K}{\partial\eta}, \quad \frac{\partial\boldsymbol{\varphi}_K}{\partial\eta} = \sum_{A=1}^{n_{nod}}\frac{\partial N^A}{\partial\eta}\mathbf{x}^A.$$

These allow us to compute vectors normal to each $K \subset \Omega^{2D}$

as

$$\mathbf{g}^*_{3,K} = \mathbf{g}^*_{1,K} \times \mathbf{g}^*_{2,K}. \tag{4.2}$$

If ξ and η are orthogonal coordinates, $|\mathbf{g}^*_{3,K}| = 1$; otherwise, $\mathbf{g}^*_{3,K}$ is normalized.

The basis vectors $\{\mathbf{g}^*_{1,K}, \mathbf{g}^*_{2,K}, \mathbf{g}^*_{3,K}\}$, are discontinuous across elements if they are only computed in this manner. To obtain a continuous basis we proceed as follows. First, we project the vector field $\mathbf{g}^*_{3,K}$, $K \in T_h$, onto the space of continuous vector fields using a standard $L^2(\Omega^{2D})$ projection, thus obtaining the nodal vectors $\mathbf{g}^a_3$, $a = 1, \dots, n_{pts}$, for the nodal points n_{pts} of T_h. Then we have that

$$\mathbf{g}_3(x^1, x^2, x^3) = G_3^{-1} \sum_{a=1}^{n_{pts}} N^a(x^1, x^2, x^3)\mathbf{g}^a_3, \quad G_3 = |\sum_{a=1}^{n_{pts}} N^a(x^1, x^2, x^3)\mathbf{g}^a_3|, \tag{4.3}$$

where N^a is the global shape function of node a. Within each element $K \in T_h$ we have

$$\mathbf{g}_3|_K(\xi, \eta) = G_{3,K}^{-1} \sum_{A=1}^{n_{nod}} N^A(\xi, \eta)\mathbf{g}^A_{3,K}, \quad G_{3,K} = |\sum_{A=1}^{n_{nod}} N^A(\xi, \eta)\mathbf{g}^A_{3,K}|, \tag{4.4}$$

where A is the local numbering of the global node a. Figure 4.1 shows a cut of a surface and the conceptual difference between $\mathbf{g}^*_{3,K}$ and $\mathbf{g}_3$. Note that for linear elements $\mathbf{g}^*_{3,K}$ will be constant on each $K \in T_h$.

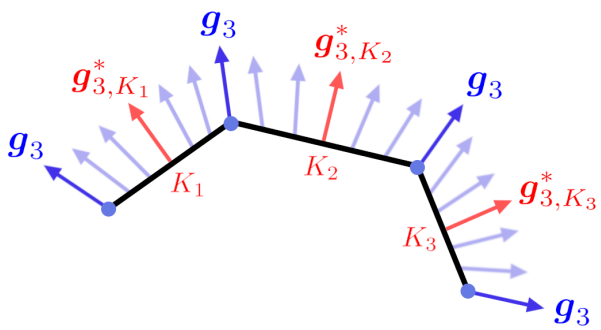

Figure 4.1: Normal vectors to the shell $\mathbf{g}^*_{3,K}$ and their smoothing $\mathbf{g}_3$.

Let $\{\mathbf{e}_1, \mathbf{e}_2, \mathbf{e}_3\}$ be the canonical basis of $\mathbb{R}^3$. Once the continuous global vector field $\mathbf{g}_3$ is constructed, we can build a

continuous local basis at each point $\{\mathbf{g}_1, \mathbf{g}_2, \mathbf{g}_3\}$ by defining

$$\mathbf{g}_1 = |\mathbf{g}_3 \times \mathbf{e}_3|^{-1} \mathbf{g}_3 \times \mathbf{e}_3, \quad \mathbf{g}_2 = \mathbf{g}_3 \times \mathbf{g}_1, \tag{4.5}$$

the only exception being when $\mathbf{g}_3$ aligns with $\mathbf{e}_3$, case in which we set $\mathbf{g}_1 = \mathbf{e}_1$ and $\mathbf{g}_2 = \mathbf{e}_2$ or $\mathbf{g}_1 = -\mathbf{e}_1$ and $\mathbf{g}_2 = -\mathbf{e}_2$ if $\mathbf{g}_3$ is opposite to $\mathbf{e}_3$. The covariant basis $\{\mathbf{g}_1, \mathbf{g}_2, \mathbf{g}_3\}$ constructed this way will be such that $\{\mathbf{g}_1, \mathbf{g}_2\}$ will be *approximately* tangent to Ω^{2D} and $\mathbf{g}_3$ *approximately* normal. The curvilinear coordinates $(\theta^1, \theta^2, \theta^3)$ are then defined as those tangent to $\{\mathbf{g}_1, \mathbf{g}_2, \mathbf{g}_3\}$ at each point.

4.3.2 Extrusion of the shell mid-surface

The domain Ω^{2D} represents the mid-surface of the shell. The solid-shell domain where the calculations are performed is denoted as Ω^{3D}, and it is computed from the extrusion of Ω^{2D} in the normal direction. The construction of Ω^{3D} can be done element-wise due to the continuity of $\mathbf{g}_3$.

Consider the thickness of the shell to be defined by its values at the nodes of T_h, denoted as t^a, $a = 1, \dots n_{pts}$. For each $K \in T_h$, the thicknesses at the nodes will be t_K^A, A being the local number of node a, and we can construct the thickness function

$$t_K(\xi, \eta) = \sum_{A=1}^{n_{nod}} N^A(\xi, \eta) t_K^A. \tag{4.6}$$

From the reference element K_0 we can construct the 3D reference element $K_0^{3D} = K_0 \times [-1, 1]$ and the mapping

$$\begin{aligned} &\boldsymbol{\psi}_K : K_0^{3D} \longrightarrow \mathbb{R}^3 \\ &\quad (\xi, \eta, \zeta) \mapsto (x^1, x^2, x^3) = \boldsymbol{\varphi}_K(\xi, \eta) + \zeta \frac{1}{2} t_K(\xi, \eta) \mathbf{g}_3|_K(\xi, \eta), \end{aligned} \tag{4.7}$$

and then set $K^{3D} = \boldsymbol{\psi}_K(K_0^{3D})$, i.e., the image of K_0^{3D} through $\boldsymbol{\psi}_K$. The solid domain where the problem is posed is then $\Omega^{3D} = \bigcup_{K \in T_h} K^{3D}$. From the continuity of $\mathbf{g}_3$ and the intrinsic continuity of the thickness function, Ω^{3D} will be a smooth extrusion of Ω^{2D}. This domain, together with the systems of coordinates and basis introduced so far, are depicted in Fig. 4.2. Since we are interested in solids of small thickness,

we shall take the basis $\{\mathbf{g}_1, \mathbf{g}_2, \mathbf{g}_3\}$ as constant across the thickness of the shell.

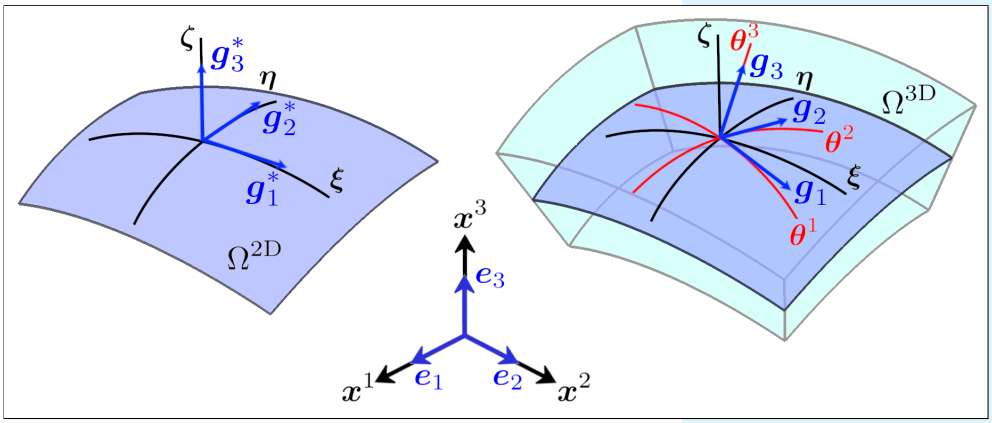

Figure 4.2: Geometry of the shell: 2D surface (left) and 3D extruded volume (right).

4.3.3 Interpolation across the thickness

Once the element domains $\{K^{3D}\}$ have been constructed, we need to define their degrees of freedom and a basis for the FE space we wish to construct. As for the original partition $\{K\}$, we shall consider continuous Lagrangian interpolations, and it suffices to define them for the reference element $K_0 \times [-1, 1]$. Let $N_i^{A,A'}(\xi, \eta, \zeta)$ be the shape function of a node in $K_0 \times [-1, 1]$ that corresponds to node A of K_0 and node A' of the discretization of $[-1, 1]$. The shape functions corresponding to the shell body $N_i^{A,A'}(\xi, \eta, \zeta)$ can now be constructed by multiplying the mid-surface shape functions $N^A(\xi, \eta)$ and the standard one dimensional Lagrangian shape functions $N^{A'}(\zeta)$ in the isoparametric space:

$$N^{A,A'}(\xi, \eta, \zeta) = N^A(\xi, \eta)\, N^{A'}(\zeta). \tag{4.8}$$

At the global level the shape functions will be written as $N^a(x^1, x^2, x^3)$, with a running again from 1 to n_{pts}. The FE partition resulting from the extrusion of the FE partition of the shell surface $T_h = \{K\}$ will be denoted as $T_h^{3D} = \{K^{3D}\}$. From this point forward, the superscript 3D will be omitted for simplicity, since the following formulations as well as the numerical experiments are presented by considering the 3D approximation of the shell.

4.4 Continuous solid dynamics problem

In the previous chapter, a comprehensive analysis of locking mechanisms in thin structures was conducted. This was achieved by formulating the linear elastic problem in curvilinear coordinates using a mixed stress-displacement approach. It was observed that interpolating specific components of the stress tensor allowed to overcome certain types of numerical locking. However, it was concluded that the most robust formulation is achieved by interpolating the entire stress tensor, as this approach is capable of addressing all types of locking in any given problem. Since the interpolation of the complete stress tensor is necessary, there is no advantage in using curvilinear coordinates. Therefore, the following problem is formulated in Cartesian coordinates. This work presents the finite strain solid dynamics problem using a total Lagrangian description in relation to a Cartesian basis. The equations are written employing index notation; therefore, repeated indexes imply summation over the spatial dimensions. Furthermore, lowercase and uppercase indices denote variables evaluated in the current and material configurations, respectively.

4.4.1 Conservation equations

Consider a solid shell occupying a domain $\Omega(t)$ of $\mathbb{R}^d$ at the current time $t \geq 0$, where $d \in \{2, 3\}$ is the number of space dimensions; $\Omega(t)$ is thus the current configuration at time t. Let $\Gamma(t) = \partial\Omega(t)$ be its boundary, whereas the counterparts of $\Omega(t)$ and $\Gamma(t)$ in the reference configuration are denoted by $\Omega_0 = \Omega(0)$ and $\Gamma_0 = \partial\Omega_0$, respectively. Let us consider the motion $\boldsymbol{\phi}$ of the deformable body through a time interval $]0, T[$, described by the mapping $\boldsymbol{\phi} : \Omega_0 \to \Omega(t)$ between the initial and current configurations, whose particles are labeled in the coordinates $\mathbf{X} \in \Omega_0$ and $\mathbf{x} \in \Omega(t)$, respectively, as follows

$$\mathbf{x} = \boldsymbol{\phi}(\mathbf{X}, t). \tag{4.9}$$

The linear momentum conservation equation in finite strain theory, in the total Lagrangian framework, reads

$$\rho_0 \frac{\partial^2 u_a}{\partial t^2} - \frac{\partial}{\partial X_A}\{F_{aB} S_{BA}\} = \rho_0 b_a \quad \text{in } \Omega_0 \times]0, T[, \tag{4.10}$$

where ρ_0 is the initial density, $\mathbf{F} = \frac{\partial \mathbf{x}}{\partial \mathbf{X}}$ is the deformation gradient, $\mathbf{S}$ is the second Piola-Kirchhoff (PK2) stress tensor and $\rho_0 \mathbf{b}$ are the body forces. Note that the angular momentum equation implies the symmetry of the PK2 stress tensor. The mass conservation equation can be written as

$$\rho J = \rho_0, \tag{4.11}$$

where ρ is the density at the current time t and $J = \det(\mathbf{F}) > 0$ is the determinant of the deformation gradient.

4.4.2 Constitutive model

Let us consider non-linear isotropic hyperelastic models, based in a strain energy function Ψ that measures the work done by stresses from the initial to the current configuration. The PK2 stress tensor can be written in terms of the strain energy function by taking derivatives with respect to the right Cauchy-Green tensor $\mathbf{C} = \mathbf{F}^T \cdot \mathbf{F}$ as

$$\mathbf{S} = 2\frac{\partial \Psi(\mathbf{C})}{\partial \mathbf{C}}. \tag{4.12}$$

This work only deals with isotropic materials; therefore the relationship between Ψ and $\mathbf{C}$ must be independent of the coordinate system chosen. For this reason, Ψ is built as a function of the invariants of $\mathbf{C}$, defined as

$$I_1 = \text{trace}(\mathbf{C}) = \mathbf{C} : \mathbf{I}, \tag{4.13}$$

$$I_2 = \text{trace}(\mathbf{C} \cdot \mathbf{C}) = \mathbf{C} : \mathbf{C}, \tag{4.14}$$

$$I_3 = \det(\mathbf{C}) = J^2. \tag{4.15}$$

The compressible Neo-Hookean material stored energy function can now be defined in terms of the invariants as

$$\Psi = \frac{\mu}{2}(I_1 - 3) - \mu \ln J + \frac{\lambda}{2}(\ln J)^2 \tag{4.16}$$

where μ and λ are Lamé material coefficients, which are related to Young modulus E and Poisson's ratio ν as follows:

$$E = \mu \frac{3\lambda + 2\mu}{\lambda + \mu}, \qquad \nu = \frac{\lambda}{2\lambda + 2\mu}.$$

Note that in a rigid body motion, or absence of deformation, the deformation gradient is the identity and the stored en-

ergy function vanishes. Note also that the present approach does not contemplate solving incompressible materials. This would require the introduction of the pressure as a variable, and to adopt a decoupled representation of the strain energy function into the deviatoric and volumetric parts. The stress-displacement formulation is expected to behave better than the irreducible one in nearly incompressible regimes [148], but nevertheless the definition of 'nearly' incompressible cases is ambiguous and the only robust way to deal with these scenarios, as well as with the fully incompressible case, is to use a mixed displacement–deviatoric stress–pressure approach, which is outside the scope of this paper but can be developed as we did in [4, 116]. Observe that volumetric locking is not due to the shell geometry, but to the material rheology.

[148]: Chiumenti et al. (2015), *A mixed three-field FE formulation for stress accurate analysis including the incompressible limit*

[4]: Castañar et al. (2020), *A stabilized mixed finite element approximation for incompressible finite strain solid dynamics using a total Lagrangian formulation*

[116]: Castañar et al. (2023), *A stabilized mixed three-field formulation for stress accurate analysis including the incompressible limit in finite strain solid dynamics*

In the particular case of compressible Neo-Hookean materials, the expression for the PK2 stress tensor can be obtained from Eq. (4.12) as

$$\mathbf{S} = \mu \left(\mathbf{I} - \mathbf{C}^{-1} \right) + \lambda \left(\ln J \right) \mathbf{C}^{-1}. \tag{4.17}$$

4.4.3 Governing equations

The solid mechanics problem is presented through a two-field formulation, using both the PK2 stresses and the displacements as unknowns; a novel FE approximation will be proposed for the resulting problem. The interpolation of $\mathbf{S}$ allows to obtain a higher accuracy in the computation of stresses in finite strain problems and, in the case of shells, it also allows to overcome numerical locking when dealing with thin structures, as it has been shown in the infinitesimal strain case [122]. For this purpose, let us construct the mathematical framework for the present formulation. Consider the space-time domain $\mathscr{D} = \{(\mathbf{X}, t) \,|\, \mathbf{X} \in \Omega_0, t \in]0, T[\}$ where the problem is defined. This problem consists of finding a displacement field $\mathbf{u} : \mathscr{D} \to \mathbb{R}^d$ and a PK2 stress tensor field $\mathbf{S} : \mathscr{D} \to \mathbb{R}^d \otimes \mathbb{R}^d$ such that

[122]: Saloustros et al. (2021), *Accurate and locking-free analysis of beams, plates and shells using solid elements*

Governing equations

$$\rho_0 \frac{\partial^2 u_a}{\partial t^2} - \frac{\partial}{\partial X_A}\{F_{aB} S_{BA}\} = \rho_0 b_a \quad \text{in } \Omega_0 \times]0,T[\,, \quad a = 1,\dots,d, \tag{4.18}$$

$$S_{AB} - 2\frac{\partial \Psi}{\partial C_{AB}} = 0 \qquad \text{in } \Omega_0 \times]0,T[\,, \quad A,B = 1,\dots,d, \tag{4.19}$$

where initial conditions for displacements $\mathbf{u}|_{t=0} = \mathbf{u}_0$ and velocities $\frac{\partial \mathbf{u}}{\partial t}\big|_{t=0} = \dot{\mathbf{u}}_0$ in Ω_0 must be prescribed along with proper boundary conditions:

$$\mathbf{u} = \mathbf{u}_D \quad \text{on } \Gamma_{0,D}, \tag{4.20}$$

$$\mathbf{n}_0 \cdot (\mathbf{F} \cdot \mathbf{S}) = \mathbf{t}_N \quad \text{on } \Gamma_{0,N}, \tag{4.21}$$

for the reference configuration Dirichlet $\Gamma_{0,D}$ and Neumann $\Gamma_{0,N}$ boundaries, where prescribed displacements $\mathbf{u}_D$ and prescribed tractions $\mathbf{t}_N$ are imposed, considering the outward unit vector $\mathbf{n}_0$ normal to the reference configuration boundary.

4.4.4 Variational form of the problem

Let $H^1(\Omega)$ be the space of functions in $L^2(\Omega)$ whose derivatives belong to $L^2(\Omega)$. Consider the field spaces $\mathbb{V} \subset H^1(\Omega)^d$ and $\mathbb{T} \subset L^2(\Omega)^{d\times d}$ where the displacements and the PK2 stresses are well-defined, respectively, for all time $t \in]0,T[$. The subspace $\mathbb{V}_0$ of $\mathbb{V}$ consists of functions $\mathbb{V}$ that vanish on the Dirichlet boundary $\Gamma_{0,D}$. Let $\mathbb{W} = \mathbb{V} \times \mathbb{T}$ and $\mathbb{W}_0 = \mathbb{V}_0 \times \mathbb{T}$ be the spaces where the weak form of the problem is defined, so that the spaces of unknowns $\mathbf{U} = [\mathbf{u}, \mathbf{S}]^T$ and test functions $\mathbf{V} = [\mathbf{v}, \mathbf{T}]^T$ correspond to $\mathbf{U} \in \mathbb{W}$ and $\mathbf{V} \in \mathbb{W}_0$, respectively.

Let us denote by $\langle \cdot, \cdot \rangle$ the integral of the product of two functions in Ω_0. The variational form of the problem is constructed by testing the system (4.18)-(4.19) against arbitrary test functions $\mathbf{V}$. Consequently, the weak form of the problem consists of finding $\mathbf{U} :]0,T[\to \mathbb{W}$ such that the initial and boundary conditions are satisfied and

$$\left\langle v_a, \rho_0 \frac{\partial^2 u_a}{\partial t^2} \right\rangle + \mathscr{A}(\mathbf{V}, \mathbf{U}) = \mathscr{F}(\mathbf{V}) \quad \forall \mathbf{V} \in \mathbb{W}_0, \tag{4.22}$$

where $\mathscr{A}(\mathbf{V},\mathbf{U})$ is a semilinear form defined on $\mathbb{W}_0 \times \mathbb{W}$ as

$$\mathscr{A}(\mathbf{V},\mathbf{U}) := \left\langle \frac{\partial v_a}{\partial X_A}, F_{aB} S_{AB} \right\rangle + \langle T_{AB}, S_{AB} \rangle - \left\langle T_{AB}, 2\frac{\partial \Psi}{\partial C_{AB}} \right\rangle, \tag{4.23}$$

and $\mathscr{F}(\mathbf{V})$ is a linear form on $\mathbb{W}_0$ defined by

$$\mathscr{F}(\mathbf{V}) := \langle v_a, \rho_0 b_a \rangle + \left\langle v_a, t_{N_a} \right\rangle_{\Gamma_{0,N}}. \tag{4.24}$$

4.5 Time integration

Terms involving time derivatives can be approximated using different approaches, being the finite difference method the most commonly used. In the present work, only implicit time integration is considered because an explicit scheme would require extremely small time steps to fulfil the stability conditions. In the current problem, the second time derivative of the displacement $\frac{\partial^2 \mathbf{u}}{\partial t^2} =: \mathbf{a}$ has to be approximated at a given time step $t^{n+1} = t^n + \delta t$, where n is the time step counter and δt is the time step size of the uniform partition of the time interval $]0, T[$. In what follows, only Backward Differentiation Formula (BDF) time integration schemes are considered, and depending on the desired accuracy, the following can be selected:

$$\text{BDF1}: \quad \mathbf{a}^{n+1} = \frac{1}{\delta t^2}\left[\mathbf{u}^{n+1} - 2\mathbf{u}^n + \mathbf{u}^{n-1}\right] + \mathcal{O}(\delta t), \tag{4.25}$$

$$\text{BDF2}: \quad \mathbf{a}^{n+1} = \frac{1}{\delta t^2}\left[2\mathbf{u}^{n+1} - 5\mathbf{u}^n + 4\mathbf{u}^{n-1} - \mathbf{u}^{n-1}\right] + \mathcal{O}(\delta t^2), \tag{4.26}$$

where $\mathcal{O}(\cdot)$ is the approximation order of the scheme depending on the time step size.

4.6 Linearization

The finite strain solid mechanics problem is inherently nonlinear, hence it must be linearized in order to solve the system. The idea is to obtain a bilinear operator that allows to compute a correction $\delta\mathbf{U} := [\delta\mathbf{u}, \delta\mathbf{S}]^T$ of the guessed solution $\mathbf{U}^{n+1}$ at a time t^{n+1}. The linearization is performed using a Newton-Raphson scheme on the formulation presented in Eq. (4.22), and the unknown becomes the correction of the

displacement. Therefore the new problem consists in finding $\delta\mathbf{U} \in \mathbb{W}_0$ such that

Linearized formulation

$$\left\langle \mathbf{v}, \rho_0 \frac{C}{\delta t^2}\delta\mathbf{u} \right\rangle + \mathscr{B}(\mathbf{V}, \delta\mathbf{U}) = \mathscr{F}(\mathbf{V}) - \mathscr{A}\left(\mathbf{V}, \mathbf{U}^{n+1}\right) - \left\langle \mathbf{v}, \rho_0 \mathbf{a}^{n+1} \right\rangle \quad \forall \mathbf{V} \in \mathbb{W}_0, \tag{4.27}$$

where $\mathscr{B}(\mathbf{V}, \delta\mathbf{U})$ defined on $\mathbb{W}_0 \times \mathbb{W}_0$ is the bilinear form obtained through the linearization of $\mathscr{A}(\mathbf{V}, \mathbf{U})$, and it is defined as

$$\mathscr{B}(\mathbf{V}, \delta\mathbf{U}) = \left\langle \frac{\partial v_a}{\partial X_A}, \frac{\partial \delta u_a}{\partial X_B} S_{BA} \right\rangle + \left\langle \frac{\partial v_a}{\partial X_A}, F_{aB}\delta S_{BA} \right\rangle + \langle T_{AB}, \delta S_{AB} \rangle - \left\langle T_{AB}, \mathbb{C}_{ABCD} F_{aC} \frac{\partial \delta u_a}{\partial X_D} \right\rangle, \tag{4.28}$$

where $\mathbb{C}_{ABCD} = 4\frac{\partial^2 \Psi}{\partial C_{AB} \partial C_{CD}}$ is the constitutive tangent matrix which relates variations of the PK2 stress tensor $\delta\mathbf{S}$ and the Right Cauchy tensor $\delta\mathbf{C}$. In the same manner, the time derivative term has been linearized as

$$\left.\frac{\partial^2 \mathbf{u}}{\partial t^2}\right|_{t^{n+1}} = \frac{C}{\delta t^2}\delta\mathbf{u} + \mathbf{a}^{n+1}, \tag{4.29}$$

where C is a coefficient that depends on the integration scheme; precisely $C = 1$ for BDF1 and $C = 2$ for BDF2, and $\mathbf{a}^{n+1}$ is the acceleration obtained in the previous iteration, computed as stated in Eqs. (4.25) and (4.26).

Note that the bilinear formm $\mathscr{B}$ depends on the unknown of the previous iteration $\mathbf{U}^{n+1}$ through the evaluation of the different tensor functions that depend on it, even though this dependence has not been explicitly displayed.

4.7 Symmetrization

The symmetric form of the problem can be obtained from Eq. (4.27) by multiplying the linearized terms of the constitutive equation by $-\mathbb{C}^{-1}$, resulting in

$$\left\langle \mathbf{v}, \rho_0 \frac{C}{\delta t^2} \delta \mathbf{u} \right\rangle + \mathscr{B}^{\mathrm{s}}(\mathbf{V}, \delta \mathbf{U}) = \mathscr{F}(\mathbf{V}) - \mathscr{A}^{\mathrm{s}}\left(\mathbf{V}, \mathbf{U}^{n+1}\right) - \left\langle \mathbf{v}, \rho_0 \mathbf{a}^{n+1} \right\rangle \quad \forall \mathbf{V} \in \mathbb{W}_0, \tag{4.30}$$

where

$$\mathscr{B}^{\mathrm{s}}(\mathbf{V}, \delta \mathbf{U}) = \left\langle \frac{\partial v_a}{\partial X_A}, \frac{\partial \delta u_a}{\partial X_B} S_{BA} \right\rangle + \left\langle \frac{\partial v_a}{\partial X_A}, F_{aB} \delta S_{BA} \right\rangle - \left\langle T_{AB}, \mathbb{C}^{-1}_{ABCD} \delta S_{CD} \right\rangle + \left\langle T_{AB}, F_{aA} \frac{\partial \delta u_a}{\partial X_B} \right\rangle, \tag{4.31}$$

$$\mathscr{A}^{\mathrm{s}}(\mathbf{V}, \mathbf{U}) = \left\langle \frac{\partial v_a}{\partial X_A}, F_{aB} S_{AB} \right\rangle - \left\langle T_{AB}, \mathbb{C}^{-1}_{ABCD} S_{CD} \right\rangle + \left\langle T_{AB}, 2\mathbb{C}^{-1}_{ABCD} \frac{\partial \Psi}{\partial C_{CD}} \right\rangle. \tag{4.32}$$

By utilizing the symmetric form of the problem, we tackle an energy minimization problem, employing stresses as test functions instead of strains found in the non-symmetric form. This approach offers computational advantages, allowing to use solvers particularly adapted to symmetric systems of equations. However, to simplify the exposition we will consider next the FE approximation to Eq. (4.27).

4.8 Finite element approximation

4.8.1 Galerkin finite element formulation

The standard Galerkin approximation of the variational problem defined in Eq. (4.27) can be constructed by taking a FE partition $\mathscr{P}_h$ of the domain Ω_0 corresponding to the solid-shell and constructed using the extrusion described in Section 4.3. The diameter of an element domain $K \in \mathscr{T}_h$ is denoted by h_K, and the diameter of the element partition is defined as $h = \max\{h_K | K \in \mathscr{P}_h\}$. Under the considerations above, the conforming FE spaces are constructed in the usual manner $\mathbb{V}_h \subset \mathbb{V}$ and $\mathbb{T}_h \subset \mathbb{T}$; therefore $\mathbb{W}_h = \mathbb{V}_h \times \mathbb{T}_h$. The subspace of $\mathbb{V}_h$ of vectors that vanish on the Dirichlet boundary is denoted as $\mathbb{V}_{h,0} \subset \mathbb{V}_0$, and $\mathbb{W}_{h,0} = \mathbb{V}_{h,0} \times \mathbb{T}_h$.

The Galerkin FE approximation consists of finding $\delta \mathbf{U}_h = [\delta \mathbf{u}_h, \delta \mathbf{S}_h]^T \in \mathbb{W}_{h,0}$ for a time t^{n+1} in a given iteration, such that

Galerkin formulation

$$\left\langle \mathbf{v}_h, \rho_0 \frac{C}{\delta t^2} \delta \mathbf{u}_h \right\rangle + \mathscr{B}\left(\mathbf{V}_h, \delta \mathbf{U}_h\right) = \mathscr{F}\left(\mathbf{V}_h\right) - \mathscr{A}\left(\mathbf{V}_h, \mathbf{U}_h^{n+1}\right) - \left\langle \mathbf{v}_h, \rho_0 \mathbf{a}_h^{n+1} \right\rangle \quad \forall \mathbf{V}_h \in \mathbb{W}_{h,0}. \tag{4.33}$$

The Galerkin FE approximation lacks of stability unless particular interpolations are used to interpolate the displacement and PK2 stress fields, requiring to satisfy appropriate inf-sup conditions [145]. Let us consider now the symmetrized problem (4.30) and discuss the stability of this linearized problem, although the discussion could be extended to the original nonlinear problem. Taking $\mathbf{v}_h = \delta \mathbf{u}_h$ (assuming homogeneous Dirichlet boundary conditions) and $\mathbf{T}_h = -\delta \mathbf{S}_h$ it is found that

[145]: Boffi et al. (2013), *Mixed finite element methods and applications*

$$\mathscr{B}^{\mathrm{s}}\left(\mathbf{V}_h, \delta \mathbf{U}_h\right) = \left\langle \frac{\partial \delta u_{h_a}}{\partial X_A}, \frac{\partial \delta u_{h_a}}{\partial X_B} S_{BA} \right\rangle + \left\langle \delta S_{h_{AB}}, \mathbb{C}^{-1}_{ABCD} \delta S_{h_{CD}} \right\rangle. \tag{4.34}$$

Suppose that the given guess is away from buckling, so that the solution of the continuous problem exists and is unique. Since, for thermodynamical reasons, $\mathbb{C}^{-1}$ is known to be a positive-definite tensor, the second term defines a norm of tensor $\delta \mathbf{S}_h$ and thus one can have control on this norm. However, it is obvious that $\mathbf{S}_h$ is not positive-definite, and therefore the first term can be either positive or negative. The only possibility to have control on the displacement gradients is to satisfy the inf-sup condition

$$\inf_{\mathbf{v}_h \in \mathbb{V}_{0,h}} \sup_{\mathbf{T}_h \in \mathbb{T}_h} \frac{\langle \nabla \mathbf{v}_h, \mathbf{T}_h \rangle}{\|\mathbf{v}_h\|_{\mathbb{W}} \|\mathbf{T}_h\|_{\mathbb{T}}} \geq \beta_1, \tag{4.35}$$

for a constant $\beta_1 > 0$. This, in turn, guarantees that the global inf-sup condition of the problem, which can be written as

$$\inf_{\delta \mathbf{U}_h \in \mathbb{W}_{0,h}} \sup_{\mathbf{V}_h \in \mathbb{W}_h} \frac{\mathscr{B}^{\mathrm{s}}\left(\mathbf{V}_h, \delta \mathbf{U}_h\right)}{\|\mathbf{V}_h\|_{\mathbb{W}} \|\delta \mathbf{U}_h\|_{\mathbb{W}}} \geq \beta_2, \tag{4.36}$$

will be satisfied for a constant $\beta_2 > 0$. However, FE element interpolations satisfying the compatibility condition (4.35) are rare and difficult to implement. In particular, it is not satisfied by the convenient equal interpolation for displacements and stresses. However, the need to satisfy condition (4.35) to

obtain a stable formulation is circumvented if stabilized FE formulations are used. We present one of these formulations in the next subsection.

4.8.2 Stabilized finite element formulation

[3]: Hughes et al. (1998), *The variational multiscale method - A paradigm for computational mechanics*

The stabilized formulation employed in the present work follows the VMS framework, first proposed by Hughes et al. [3]. The idea is to add additional consistent terms to the original Galerkin FE formulation that enhance the stability without upsetting the accuracy. In this case, this is achieved by adding a finer resolution space $\bar{\mathbb{W}}$, called sub-grid scale (SGS) space, to the FE space $\mathbb{W}_h$. Therefore, the space in which the problem is defined is split into two parts, $\mathbb{W} = \mathbb{W}_h \oplus \bar{\mathbb{W}}$, implying that $\mathbb{V} = \mathbb{V}_h \oplus \bar{\mathbb{V}}$ and $\mathbb{T} = \mathbb{T}_h \oplus \bar{\mathbb{T}}$. In the same manner, the space $\mathbb{W}_0$ is split as $\mathbb{W}_0 = \mathbb{W}_{h,0} \oplus \bar{\mathbb{W}}_0$. As a consequence the unknowns are split into $\mathbf{U} = \mathbf{U}_h + \bar{\mathbf{U}}$, where $\bar{\mathbf{U}} = \left[\bar{\mathbf{u}}, \bar{\mathbf{S}}\right]^T \in \bar{\mathbb{W}}_0$ is the SGS. The same split applies to the iterative increments, $\delta\mathbf{U} = \delta\mathbf{U}_h + \delta\bar{\mathbf{U}}$.

With the splitting introduced, problem in (4.33) turns into: find $\delta\mathbf{U} \in \mathbb{W}_{h,0}$ and $\bar{\mathbf{U}} \in \bar{\mathbb{W}}_0$ such that

$$\left\langle \mathbf{v}_h, \rho_0 \frac{C}{\delta t^2} \delta\mathbf{u}_h \right\rangle + \left\langle \mathbf{v}_h, \rho_0 \bar{\mathbf{a}}^{n+1} \right\rangle + \mathscr{B}\left(\mathbf{V}_h, \delta\mathbf{U}_h\right) + \mathscr{B}\left(\mathbf{V}_h, \delta\bar{\mathbf{U}}\right) = \mathscr{F}\left(\mathbf{V}_h\right) - \left\langle \mathbf{v}_h, \rho_0 \mathbf{a}_h^{n+1} \right\rangle - \mathscr{A}\left(\mathbf{V}_h, \mathbf{U}_h^{n+1} + \bar{\mathbf{U}}^{n+1}\right), \tag{4.37}$$

$$\left\langle \bar{\mathbf{v}}, \rho_0 \frac{C}{\delta t^2} \delta\mathbf{u}_h \right\rangle + \left\langle \bar{\mathbf{v}}, \rho_0 \bar{\mathbf{a}}^{n+1} \right\rangle + \mathscr{B}\left(\bar{\mathbf{V}}, \delta\mathbf{U}_h\right) + \mathscr{B}\left(\bar{\mathbf{V}}, \delta\bar{\mathbf{U}}\right) = \mathscr{F}\left(\bar{\mathbf{V}}\right) - \left\langle \bar{\mathbf{v}}, \rho_0 \mathbf{a}_h^{n+1} \right\rangle - \mathscr{A}\left(\bar{\mathbf{V}}, \mathbf{U}_h^{n+1} + \bar{\mathbf{U}}^{n+1}\right), \tag{4.38}$$

for all $\mathbf{V}_h \in \mathbb{W}_{h,0}$ and $\bar{\mathbf{V}} \in \bar{\mathbb{W}}_0$. Since $\bar{\mathbf{U}}^{n+1}$ is expected to be small, we may approximate

$$\mathscr{A}\left(\bar{\mathbf{V}}, \mathbf{U}_h^{n+1} + \bar{\mathbf{U}}^{n+1}\right) \approx \mathscr{A}\left(\bar{\mathbf{V}}, \mathbf{U}_h^{n+1}\right) + \mathscr{B}\left(\bar{\mathbf{V}}, \bar{\mathbf{U}}\right),$$

and arrive to the problem:

$$\left\langle \mathbf{v}_h, \rho_0 \frac{C}{\delta t^2} \delta \mathbf{u}_h \right\rangle + \left\langle \mathbf{v}_h, \rho_0 \bar{\mathbf{a}}^{n+1} \right\rangle + \mathscr{B}\left(\mathbf{V}_h, \delta \mathbf{U}_h\right) + \mathscr{B}\left(\mathbf{V}_h, \bar{\mathbf{U}}\right) = \mathscr{F}\left(\mathbf{V}_h\right) - \left\langle \mathbf{v}_h, \rho_0 \mathbf{a}_h^{n+1} \right\rangle - \mathscr{A}\left(\mathbf{V}_h, \mathbf{U}_h^{n+1}\right), \quad (4.39)$$

$$\left\langle \bar{\mathbf{v}}, \rho_0 \frac{C}{\delta t^2} \delta \mathbf{u}_h \right\rangle + \left\langle \bar{\mathbf{v}}, \rho_0 \bar{\mathbf{a}}^{n+1} \right\rangle + \mathscr{B}\left(\bar{\mathbf{V}}, \delta \mathbf{U}_h\right) + \mathscr{B}\left(\bar{\mathbf{V}}, \bar{\mathbf{U}}\right) = \mathscr{F}\left(\bar{\mathbf{V}}\right) - \left\langle \bar{\mathbf{v}}, \rho_0 \mathbf{a}_h^{n+1} \right\rangle - \mathscr{A}\left(\bar{\mathbf{V}}, \mathbf{U}_h^{n+1}\right). \quad (4.40)$$

Here, Eq. (4.39) is called FE equation and Eq. (4.40) is called SGS equation. Note that we need to approximate for the SGS, not only for its iterative increment.

The main idea to derive the stabilized FE formulation is to obtain an expression for the SGS $\bar{\mathbf{U}}$ in terms of the FE variables from the SGS equation [45]. For this matter, consider that the SGSs behave as bubble functions, whose velocity components vanish at the inter-element boundaries, although this assumption can be relaxed. Therefore, Eq. (4.40) can be integrated by parts within each element to obtain

[45]: Codina et al. (2009), *Subscales on the element boundaries in the variational two-scale finite element method*

Stabilized formulation

$$\sum_K \left\langle \bar{\mathbf{v}}_h, \rho_0 \frac{C}{\delta t^2} \delta \mathbf{u}_h \right\rangle_K + \sum_K \left\langle \bar{\mathbf{v}}, \rho_0 \bar{\mathbf{a}}^{n+1} \right\rangle_K + \sum_K \left\langle \bar{\mathbf{V}}, \mathrm{B}\left(\delta \mathbf{U}_h\right) \right\rangle_K + \sum_K \left\langle \bar{\mathbf{V}}, \mathrm{B}\left(\bar{\mathbf{U}}\right) \right\rangle_K = \sum_K \left\langle \bar{\mathbf{V}}, \mathrm{F} \right\rangle_K - \sum_K \left\langle \bar{\mathbf{V}}, \mathrm{A}\left(\mathbf{U}_h^{n+1}\right) \right\rangle_K - \sum_K \left\langle \bar{\mathbf{v}}, \rho_0 \mathbf{a}_h^{n+1} \right\rangle_K, \quad (4.41)$$

for all $\bar{\mathbf{V}} \in \bar{\mathbb{W}}$, where the operators $\mathrm{B} = [\mathrm{B}_u, \mathrm{B}_S]^T$ and $\mathrm{A} = [\mathrm{A}_u, \mathrm{A}_S]^T$ which come from integration by parts $\mathscr{B}\left(\bar{\mathbf{V}}, \delta \mathbf{U}_h\right) = \sum_K \left\langle \bar{\mathbf{V}}, \mathrm{B}\left(\delta \mathbf{U}_h\right) \right\rangle_K$ and $\mathscr{A}\left(\bar{\mathbf{V}}, \delta \mathbf{U}_h\right) = \sum_K \left\langle \bar{\mathbf{V}}, \mathrm{A}\left(\delta \mathbf{U}_h\right) \right\rangle_K$, respectively, and $\mathrm{F} = [\mathrm{F}_u, \mathrm{F}_S]^T$ are defined by

$$\mathrm{B}_u\left(\delta \mathbf{U}_h\right)_a = -\frac{\partial}{\partial X_A}\left\{\frac{\delta u_{h_a}}{\partial X_B} S_{AB}\right\} - \frac{\partial}{\partial X_A}\left\{F_{aB} \delta S_{h_{AB}}\right\}, \quad (4.42)$$

$$\mathrm{B}_S\left(\delta \mathbf{U}_h\right)_{AB} = \delta S_{h_{AB}} - \mathbb{C}_{ABCD} F_{aC} \frac{\partial \delta u_{h_a}}{\partial X_D}, \quad (4.43)$$

$$\mathrm{A}_u\left(\mathbf{U}_h^{n+1}\right)_a = -\frac{\partial}{\partial X_A}\left\{F_{aB} S_{BA}\right\}, \quad (4.44)$$

$$\mathrm{A}_S\left(\mathbf{U}_h^{n+1}\right)_{AB} = S_{AB} - 2\frac{\partial \Psi}{\partial C_{AB}}, \quad (4.45)$$

$$\mathrm{F}_u = \rho_0 b_a, \quad (4.46)$$

$$\mathrm{F}_S = 0. \quad (4.47)$$

Let us consider the SGSs to be quasi-static, implying that the time derivative terms of the SGS are neglected. Then, Eq. (4.41) enforces that

$$\bar{\Pi}\left(\mathrm{B}\left(\delta\mathbf{U}_h\right)+\mathrm{B}\left(\bar{\mathbf{U}}\right)\right)=\bar{\Pi}\left(\mathrm{F}-\mathrm{A}\left(\mathbf{U}_h^{n+1}\right)\right), \tag{4.48}$$

where $\bar{\Pi}$ is the $L^2\left(\Omega_0\right)$ projection into the SGS space. Let us define the following residual operators

$$\begin{aligned}\mathrm{R}_{\delta\mathrm{U}}\left(\delta\mathbf{U}_h\right) &= -\mathrm{B}\left(\delta\mathbf{U}_h\right),\\ \mathrm{R}_{\mathrm{U}}\left(\mathbf{U}_h^{n+1}\right) &= \mathrm{F}-\mathrm{A}\left(\mathbf{U}_h^{n+1}\right).\end{aligned}$$

An expression for the SGS can be obtained from Eq. (4.40) in the form of

$$\bar{\Pi}\left(\boldsymbol{\tau}_K^{-1}\bar{\mathbf{U}}\right)=\bar{\Pi}\left(\mathrm{R}_{\delta\mathrm{U}}\left(\delta\mathbf{U}_h\right)+\mathrm{R}_{\mathrm{U}}\left(\mathbf{U}_h^{n+1}\right)\right), \tag{4.49}$$

where the matrix $\boldsymbol{\tau}_K^{-1}$ is an approximation of the operator B withing each element K. The details on how to design $\boldsymbol{\tau}_K$ are not discussed in the present work, but can be reviewed in [118, 149]. In this case, $\boldsymbol{\tau}_K$ is taken as a diagonal matrix where the stabilization parameters are taken from [121, 148] as the following

$$\boldsymbol{\tau}_K=\begin{bmatrix}\tau_u\mathbf{I}_d & \mathbf{0}\\ \mathbf{0} & \tau_S\mathbf{I}\end{bmatrix},\qquad \tau_u=c_u\frac{h_K^2}{2\mu},\qquad \tau_S=c_S,$$

where c_u and c_S are algorithmic parameters to be chosen. Considering that $\boldsymbol{\tau}_K^{-1}\bar{\mathbf{U}}$ belongs to the SGS space, the projection results in the identity $\bar{\Pi}\left(\boldsymbol{\tau}_K^{-1}\bar{\mathbf{U}}\right)=\boldsymbol{\tau}_K^{-1}\bar{\mathbf{U}}$. Therefore, an expression of the SGS can be obtained in terms of the FE variables from Eq. (4.49) as

$$\bar{\mathbf{U}}\approx\boldsymbol{\tau}_K\bar{\Pi}\left(\mathrm{R}_{\delta\mathrm{U}}\left(\delta\mathbf{U}_h\right)+\mathrm{R}_{\mathrm{U}}\left(\mathbf{U}_h^{n+1}\right)\right)\qquad \text{in } K\in\mathscr{P}_h.$$

The SGS can now be introduced in Eq. (4.39), and the new stabilized form of the problem reads

$$\begin{aligned}\left\langle\mathbf{v}_h,\rho_0\frac{C}{\delta t^2}\delta\mathbf{u}_h\right\rangle+\left\langle\mathbf{v}_h,\rho_0\bar{\mathbf{a}}^{n+1}\right\rangle+\mathscr{B}\left(\mathbf{V}_h,\delta\mathbf{U}_h\right)+\sum_K\boldsymbol{\tau}_K\left\langle\mathrm{L}\left(\mathbf{V}_h\right),\bar{\Pi}\left(\mathrm{R}_{\delta\mathrm{U}}\left(\delta\mathbf{U}_h\right)\right)\right\rangle_K\\ =\mathscr{F}\left(\mathbf{V}_h\right)-\mathscr{A}\left(\mathbf{V}_h,\mathbf{U}_h^{n+1}\right)-\left\langle\mathbf{v}_h,\rho_0\mathbf{a}_h^{n+1}\right\rangle-\sum_K\boldsymbol{\tau}_K\left\langle\mathrm{L}\left(\mathbf{V}_h\right),\bar{\Pi}\left(\mathrm{R}_{\mathrm{U}}\left(\mathbf{U}_h^{n+1}\right)\right)\right\rangle_K,\end{aligned} \tag{4.50}$$

[118]: Codina (2009), *Finite element approximation of the three-field formulation of the Stokes problem using arbitrary interpolations*
[149]: Roa et al. (2016), *Variational multi-scale finite element approximation of the compressible Navier-Stokes equations*
[121]: Cervera et al. (2010), *Mixed stabilized finite element methods in nonlinear solid mechanics: Part I: Formulation*
[148]: Chiumenti et al. (2015), *A mixed three-field FE formulation for stress accurate analysis including the incompressible limit*

where $\mathrm{L}(\mathbf{V}_h) = [\mathrm{L}_u(\mathbf{V}_h), \mathrm{L}_S(\mathbf{V}_h)]^T$ comes from the integration by parts $\mathscr{B}(\mathbf{V}_h, \tilde{\mathbf{U}}) = \sum_K \langle \mathrm{L}(\mathbf{V}_h), \tilde{\mathbf{U}} \rangle_K$, whose components are defined by

$$\mathrm{L}_u(\mathbf{V}_h)_a = -\frac{\partial}{\partial X_B}\left\{\frac{\partial v_{h_a}}{\partial X_A} S_{BA}\right\} + \frac{\partial}{\partial X_D}\left\{T_{h_{AB}} \mathbb{C}_{ABCD} F_{aC}\right\} \quad (4.51)$$

$$\mathrm{L}_S(\mathbf{V}_h)_{AB} = \frac{\partial v_a}{\partial X_A} F_{aB} + T_{h_{AB}} \quad (4.52)$$

From this point, it only remains to choose to which space the SGSs belong. In the VMS framework, there are several possibilities, which can be revised in a general extent in [46, 113–115]. In a practical sense, it determines the type of projection performed by $\tilde{\Pi}$. In what follows, three possibilities are presented.

[46]: Codina (2000), *On stabilized finite element methods for linear systems of convection–diffusion-reaction equations*
[113]: Codina (2002), *Stabilized finite element approximation of transient incompressible flows using orthogonal subscales*
[114]: Castillo et al. (2017), *Finite element approximation of the viscoelastic flow problem: A non-residual based stabilized formulation*
[115]: Moreno et al. (2019), *Logarithmic conformation reformulation in viscoelastic flow problems approximated by a VMS-type stabi-*

Algebraic Sub-Grid Scales (ASGS)

The simplest choice is to consider the projection as the identity on the residuals as $\tilde{\Pi} = I$ in each element K. Thus, we have that

$$\tilde{\Pi}\left(\mathrm{R}_{\delta \mathrm{U}}(\delta \mathbf{U}_h) + \mathrm{R}_{\mathrm{U}}\left(\mathbf{U}_h^{n+1}\right)\right) = \mathrm{R}_{\delta \mathrm{U}}(\delta \mathbf{U}_h) + \mathrm{R}_{\mathrm{U}}\left(\mathbf{U}_h^{n+1}\right), \quad (4.53)$$

and the stabilized formulation (4.50) becomes

$$\begin{aligned}\left\langle \mathbf{v}_h, \rho_0 \frac{C}{\delta t^2} \delta \mathbf{u}_h \right\rangle + \left\langle \mathbf{v}_h, \rho_0 \tilde{\mathbf{a}}^{n+1} \right\rangle + \mathscr{B}(\mathbf{V}_h, \delta \mathbf{U}_h) + \sum_K \boldsymbol{\tau}_K \langle \mathrm{L}(\mathbf{V}_h), \mathrm{R}_{\delta \mathrm{U}}(\delta \mathbf{U}_h) \rangle_K \\ = \mathscr{F}(\mathbf{V}_h) - \mathscr{A}\left(\mathbf{V}_h, \mathbf{U}_h^{n+1}\right) - \left\langle \mathbf{v}_h, \rho_0 \mathbf{a}_h^{n+1} \right\rangle - \sum_K \boldsymbol{\tau}_K \left\langle \mathrm{L}(\mathbf{V}_h), \mathrm{R}_{\mathrm{U}}\left(\mathbf{U}_h^{n+1}\right) \right\rangle_K .\end{aligned} \quad (4.54)$$

Orthogonal Sub-Grid Scales (OSGS)

The most natural approach would be to choose the SGS space to be the orthogonal complement to the FE space. Therefore the projection can be computed as the identity minus the FE part of the residual as $\tilde{\Pi} = I - \Pi^h$, where Π^h is the $L^2(\Omega_0)$ projection into the FE space.

Thus, in this case we have:

$$\bar{\Pi}\left(\mathrm{R}_{\delta\mathrm{U}}\left(\delta\mathbf{U}_h\right)+\mathrm{R}_{\mathrm{U}}\left(\mathbf{U}_h^{n+1}\right)\right)=\mathrm{R}_{\delta\mathrm{U}}\left(\delta\mathbf{U}_h\right)+\mathrm{R}_{\mathrm{U}}\left(\mathbf{U}_h^{n+1}\right)-\Pi^h\left(\mathrm{R}_{\mathrm{U}}\left(\mathbf{U}_h^{n+1}\right)\right), \tag{4.55}$$

and the stabilized formulation (4.50) becomes

$$\begin{aligned}\left\langle\mathbf{v}_h,\rho_0\frac{C}{\delta t^2}\delta\mathbf{u}_h\right\rangle+\left\langle\mathbf{v}_h,\rho_0\bar{\mathbf{a}}^{n+1}\right\rangle+\mathscr{B}\left(\mathbf{V}_h,\delta\mathbf{U}_h\right)+\sum_K\boldsymbol{\tau}_K\left\langle\mathrm{L}\left(\mathbf{V}_h\right),\mathrm{R}_{\delta\mathrm{U}}\left(\delta\mathbf{U}_h\right)\right\rangle_K\\ =\mathscr{F}\left(\mathbf{V}_h\right)-\mathscr{A}\left(\mathbf{V}_h,\mathbf{U}_h^{n+1}\right)-\left\langle\mathbf{v}_h,\rho_0\mathbf{a}_h^{n+1}\right\rangle\\ -\sum_K\boldsymbol{\tau}_K\left\langle\mathrm{L}\left(\mathbf{V}_h\right),\mathrm{R}_{\mathrm{U}}\left(\mathbf{U}_h^{n+1}\right)-\Pi^h\left(\mathrm{R}_{\mathrm{U}}\left(\mathbf{U}_h^{n+1}\right)\right)\right\rangle_K.\end{aligned} \tag{4.56}$$

Split-Orthogonal Sub-Grid Scales (S-OSGS)

Another possibility is to formulate the OSGS stabilization using the minimum number of terms to stabilize the problem. To achieve this, components of $\mathrm{B}\left(\delta\mathbf{U}_h\right)$, $\mathrm{A}\left(\mathbf{U}_h^{n+1}\right)$ and $\mathrm{L}\left(\mathbf{V}_h\right)$ presented in equations (4.42)-(4.47) and (4.51)-(4.52) are split into $\mathrm{B}^*=\left[\mathrm{B}_u^*,\mathrm{B}_S^*\right]^T$, $\mathrm{A}^*=\left[\mathrm{A}_u^*,\mathrm{A}_S^*\right]^T$ and $\mathrm{L}=\left[\mathrm{L}_u^*,\mathrm{L}_S^*\right]^T$ defined as

$$\begin{aligned}\mathrm{B}_u^*\left(\delta\mathbf{U}_h\right)_a&=0,\\ \mathrm{B}_S^*\left(\delta\mathbf{U}_h\right)_{AB}&=-\mathbb{C}_{ABCD}F_{aC}\frac{\partial\delta u_{h_a}}{\partial X_D},\\ \mathrm{A}_u^*\left(\mathbf{U}_h^{n+1}\right)_a&=0,\\ \mathrm{A}_S^*\left(\mathbf{U}_h^{n+1}\right)_{AB}&=-2\frac{\partial\Psi}{\partial C_{AB}},\\ \mathrm{L}_u^*\left(\mathbf{V}_h\right)_a&=0,\\ \mathrm{L}_S^*\left(\mathbf{V}_h\right)_{AB}&=\frac{\partial v_{h_a}}{\partial X_A}F_{aB}.\end{aligned}$$

The residual operators are modified accordingly to $\mathrm{R}_{\delta\mathrm{U}}^*\left(\delta\mathbf{U}_h\right)=-\mathrm{B}^*\left(\delta\mathbf{U}_h\right)$ and $\mathrm{R}_{\mathrm{U}}^*\left(\mathbf{U}_h^{n+1}\right)=\mathrm{F}-\mathrm{A}^*\left(\mathbf{U}_h^{n+1}\right)$, and the stabilized S-OSGS formulation results in

$$\left\langle \mathbf{v}_h, \rho_0 \frac{C}{\delta t^2} \delta \mathbf{u}_h \right\rangle + \left\langle \mathbf{v}_h, \rho_0 \bar{\mathbf{a}}^{n+1} \right\rangle + \mathscr{B}\left(\mathbf{V}_h, \delta \mathbf{U}_h\right) + \sum_K \boldsymbol{\tau}_K \left\langle \mathrm{L}^*\left(\mathbf{V}_h\right), \mathrm{R}^*_{\delta \mathbf{U}}\left(\delta \mathbf{U}_h\right) \right\rangle_K$$
$$= \mathscr{F}\left(\mathbf{V}_h\right) - \mathscr{A}\left(\mathbf{V}_h, \mathbf{U}_h^{n+1}\right) - \left\langle \mathbf{v}_h, \rho_0 \mathbf{a}_h^{n+1} \right\rangle$$
$$- \sum_K \boldsymbol{\tau}_K \left\langle \mathrm{L}^*\left(\mathbf{V}_h\right), \mathrm{R}^*_{\mathbf{U}}\left(\mathbf{U}_h^{n+1}\right) - \Pi^h\left(\mathrm{R}^*_{\mathbf{U}}\left(\mathbf{U}_h^{n+1}\right)\right) \right\rangle_K . \tag{4.57}$$

This variation of the OSGS approach is not merely a simplification, since it retains the optimal L^2-convergence rate respect to the element size, but also has improved capabilities in problems with high gradients of the solution.

4.9 Numerical examples

This section presents a set of numerical examples designed to evaluate the performance of the stabilized FE formulation, considering that it is suitable for both regular solid elements and thin solid-shell elements. In a first instance the order of convergence and accuracy of the solution are assessed using solid elements in 2D and 3D cases, as the stabilized displacement-stress formulation presented has not been proposed before. Subsequently, three shell benchmark problems of different initial curvatures are solved for the numerical locking assessment. In these three shell examples, we have compared two approaches, namely, the irreducible formulation with quadratic elements and the mixed formulation with linear elements across the thickness of the shell. None of them locks, but we have checked that the irreducible formulation with linear elements locks in all cases, and thus results are not included.

4.9.1 Manufactured solution

The first numerical example is designed to test the proposed formulation to check its order of convergence with respect to the element size h. The case consists of a 2D solid body subjected to a load whose analytical solution is known. To do this, the analytical solution is substituted in the continuum equations to obtain the forcing terms that lead to the deformation state. In this manner, they can be introduced in the

discretized FE computations with the corresponding boundary conditions. All the quantities are assumed dimensionless for this example.

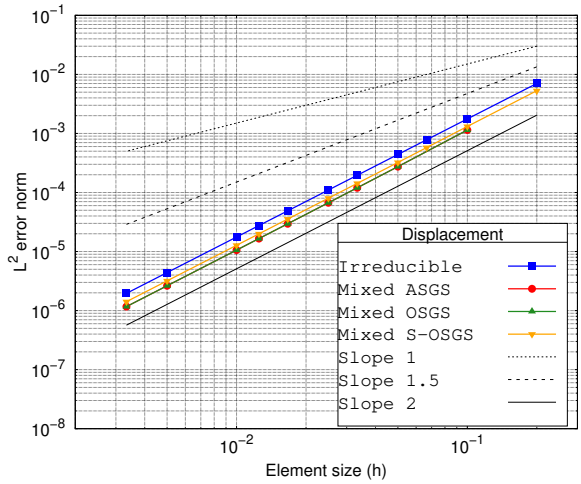

Figure 4.3: Displacement convergence curves upon mesh refinement.

The problem consists of a 2D solid under plane strain assumption, the domain is a square $\Omega_0 = (0,1)\times(0,1)$ whose imposed manufactured displacement field is

$$\mathbf{u}(X,Y) = 0.001\left[\exp(X+Y), \exp(X+Y)\right], \tag{4.58}$$

for the Cartesian coordinates X and Y in the reference configuration. The material is set as Neo-Hookean with shear modulus $\mu = 1375000$ and Poisson's ratio $\nu = 0.2$. The PK2 stress tensor field is computed with respect to the manufactured solution as

$$\mathbf{S} = \mu\left(\mathbf{I} - \mathbf{C}^{-1}\right) + \lambda(\ln J)\,\mathbf{C}^{-1}. \tag{4.59}$$

The case is computed for different meshes of square bilinear elements, increasing the number of elements per side progressively, and computing the error in the $L^2(\Omega_0)$ error norm. Convergence curves for displacements and PK2 stresses for the ASGS, OSGS and S-OSGS mixed formulations upon mesh refinement are plotted in Figs. 4.3-4.4, and with respect to the total number of degrees of freedom in Fig. 4.5-4.6. Note that the irreducible formulation locally computes the stresses at the integration points, while the mixed formulation adopts a continuous stress field. To compare stress accuracy, a local smoothing technique has been applied to the original discontinuous stress fields of the mixed irreducible formulation.

Therefore, Figs. 4.4-4.6 present the continuous values obtained after the smoothing operation.

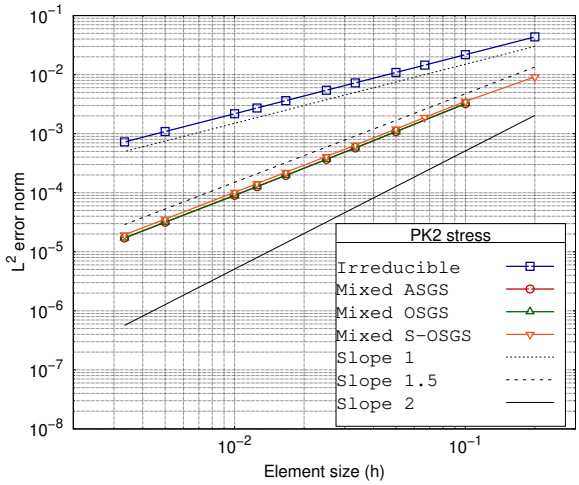

Figure 4.4: PK2 stress convergence curves upon mesh refinement.

Results in Figs. 4.3-4.4 show that the slope of convergence for displacements are of order 2 in the irreducible and the stabilized mixed formulations, which is theoretically correct. However, PK2 stresses in the stabilized mixed formulation cases show a super-convergence rate of slope 1.5 instead of the theoretical rate of 1, which is the expected for linear interpolation elements. Furthermore, the accuracy of the PK2 stress upon mesh refinement is also greatly increased in the stabilized mixed formulations when compared to the irreducible one since the later requires a mesh nearly 10 times finer to achieve the same degree of error. The increased accuracy can be verified from the results in Fig. 4.6, where accuracy vs the number of degrees of freedom is compared; this number is what defines the size of the problem. Let us compare the results for an error threshold of 10^{-3}, portrayed with a horizontal line in the plot. In the displacement curves it is clear that the mixed formulation has slight loss in accuracy that does not surpass an order of magnitude. In contrast, for the PK2 stress field, the quadratic irreducible formulation requires approximately 10^5 degrees of freedom to reach the error threshold, whereas the mixed formulation requires only about $3.5 \cdot 10^3$. This equivalent to roughly 3.5% of the costs of the quadratic irreducible to achieve the same result in the stress field, which is, a huge improvement. Considering all the above, it becomes clear that the accuracy of the PK2 stress field is highly enhanced in the stabilized mixed formulations,

at the cost of a slightly diminished accuracy of the displacement field.

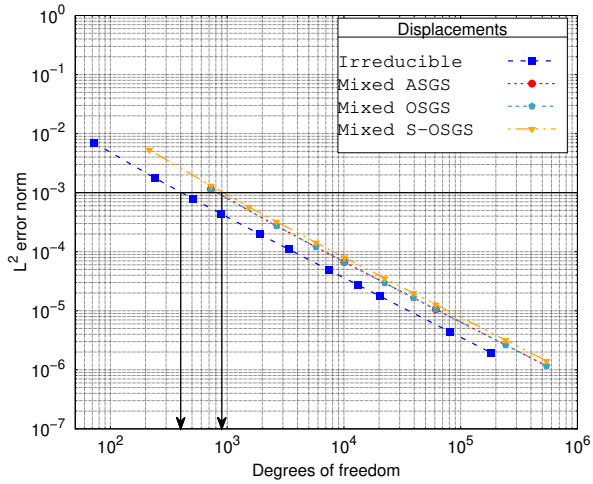

Figure 4.5: Displacement convergence curves with respect to the total number of degrees of freedom.

From the results we can deduce that all of the three stabilization approaches give almost identical results. However, in the later examples we employ only the S-OSGS approach. This is justified by a number of reasons. Firstly, we prefer the OSGS over the ASGS approach because the orthogonal projection results in a weakly consistent formulation that makes the residual go to zero for smaller element sizes, which is not fulfilled by the algebraic approach. Secondly, the S-OSGS is preferred over the OSGS simply because we avoid adding extra terms that do not contribute to the stabilization.

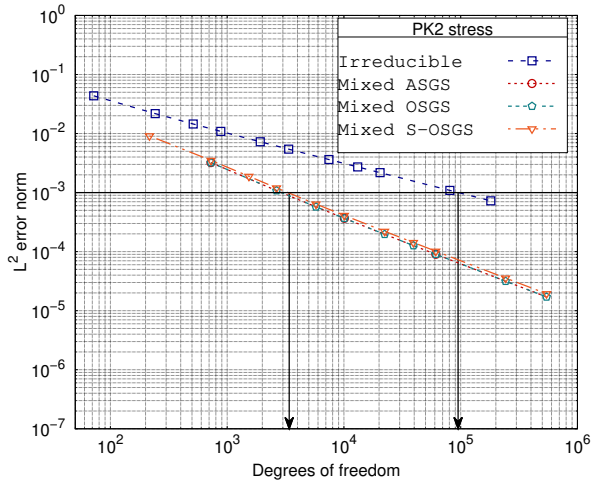

Figure 4.6: PK2 stress convergence curves with respect to the total number of degrees of freedom.

4.9.2 Twisting column

The twisting column is a classical test to assess the robustness of a FE formulation in extreme non-linear deformations [150, 151]. The problem consists of a column of length $L = 6$ m and square transverse shape of side $a = 1$ m whose center aligns with the origin, clamped on the bottom face and subject to an initial velocity defined as

$$\mathbf{v}_0(X,Y,Z) = \omega \sin\left(\frac{\pi Z}{2L}\right)(Y,-X,0)^T \qquad \left[\frac{\mathrm{m}}{\mathrm{s}}\right], \tag{4.60}$$

for the angular velocity $\omega = 100$ rad/s and Cartesian coordinates X, Y, Z. The geometry, mesh and boundary conditions are illustrated in Fig. 4.7. The material is defined as Neo-Hookean, with a Young modulus $E = 1.7 \cdot 10^7$ Pa, a Poisson's ratio $\nu = 0.3$ and an initial density $\rho_0 = 1100$ kg/m^3. Three different meshes are used: Mesh 1 with $10 \times 10 \times 60$, Mesh 2 with $15 \times 15 \times 80$ and Mesh 3 with $20 \times 20 \times 100$ structured trilinear hexahedral elements.

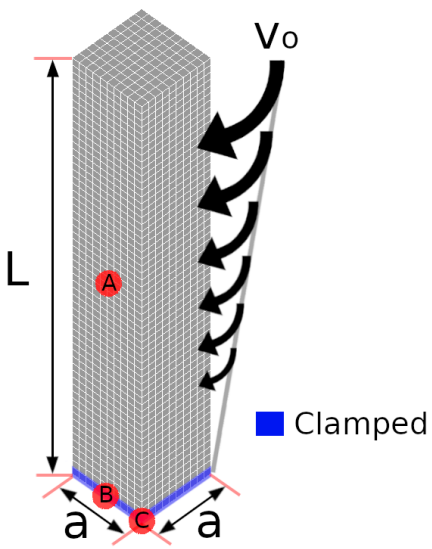

Figure 4.7: Twisting column: geometry, mesh and boundary conditions.

The problem is run with a BDF2 time integration scheme because it is second order accurate in time and it is also able to dissipate non-physical mode oscillations. It has also been proven in [116] that a Newmark scheme, even though it is second order accurate in time, it is not able to mitigate the

[150]: Bonet et al. (2015), *A first order hyperbolic framework for large strain computational solid dynamics. Part I: Total Lagrangian isothermal elasticity*
[151]: Gil et al. (2016), *A first order hyperbolic framework for large strain computational solid dynamics. Part II: Total Lagrangian compressible, nearly incompressible and truly incompressible elasticity*

[116]: Castañar et al. (2023), *A stabilized mixed three-field formulation for stress accurate analysis including the incompressible limit in finite strain solid dynamics*

non-physical modes, while a first order BDF1 scheme is too dissipative and can mask physical oscillations. It is important to remark that BDF2 can also dissipate physical oscillations, but to a much lesser extend, since it is a second order algorithm. Therefore, in this case a time step size of $\delta t = 0.002$ s has been chosen to retain the physical oscillations. The cases are run for the irreducible and the stabilized S-OSGS mixed formulation. A graphical description of the deformation and the PK2 stress field for the irreducible and S-OSGS formulations are shown in Figs. 4.8 and 4.9, respectively, using Mesh 2 for eight different time frames. The mixed formulation approach provides smoother stress fields and is able to capture stress concentration with increased precision near the clamped base of the column.

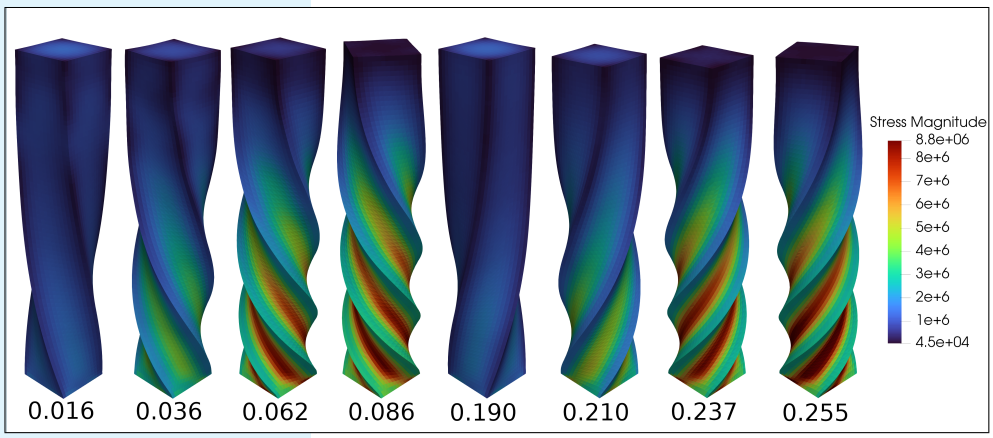

Figure 4.8: Twisting column: deformation and PK2 stress field in the irreducible formulation, at different times.

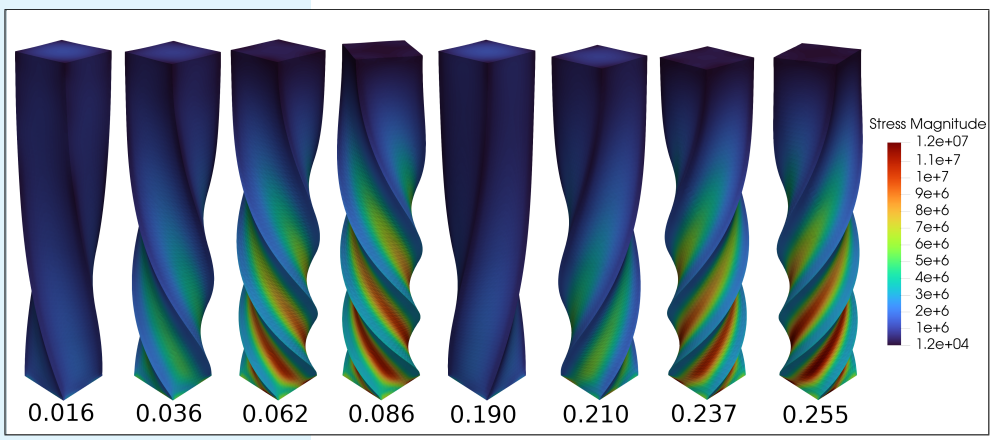

Figure 4.9: Twisting column: deformation and PK2 stress field in the S-OSGS mixed formulation, at different times.

The time evolution of both displacement and PK2 stress at point A, of coordinates $[0.5, 0, 3]$ m are shown in Figs. 4.10-4.11. Displacements converge in a similar manner upon mesh refinement using any formulation. With regards to the PK2 stresses, the irreducible formulation shows an unstable behavior at the beginning of the computation that dissipates as it advances through time, a behavior that is not present when using the S-OSGS stabilization. Stresses can be subject to concentration or singularities, so in order to assess this issue they are analyzed using Mesh 2. Stresses are plotted at points B and C of coordinates $[0.5, 0, 0]$ m and $[0.5, 0.5, 0]$ m, respectively, in Figs. 4.12-4.13. The behavior is much more unstable in the irreducible formulation, although it follows a similar trend as the stresses obtained with the S-OSGS formulation.

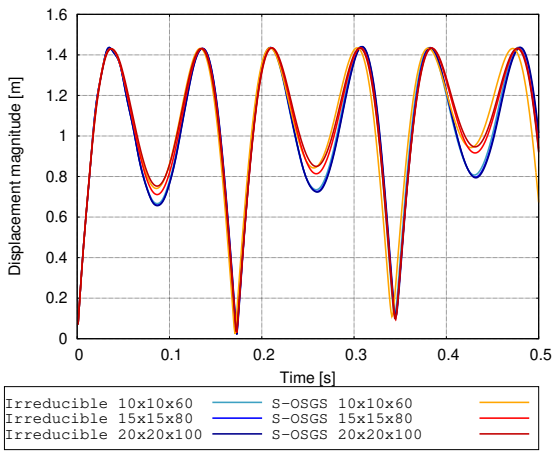

Figure 4.10: Twisting column: displacement time evolution at point A.

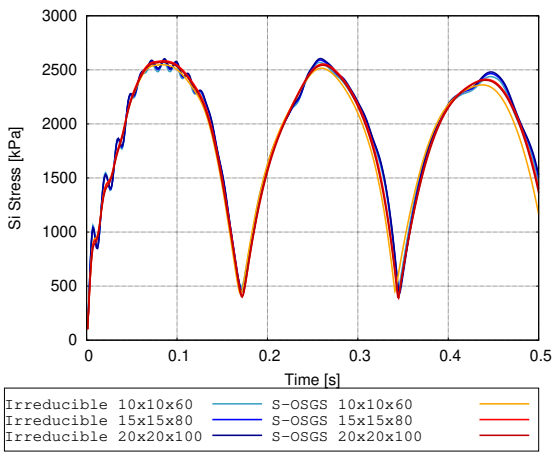

Figure 4.11: Twisting column: PK2 stress time evolution at point A.

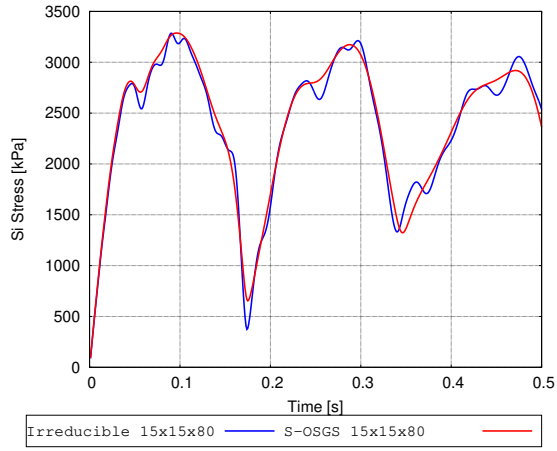

Figure 4.12: Twisting column: Time evolution of PK2 stress at point B.

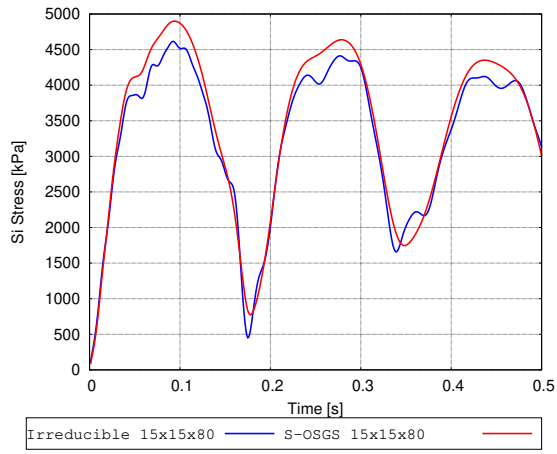

Figure 4.13: Twisting column: Time evolution of PK2 stress at point C.

4.9.3 No-curvature case: Slit annular plate subject to lifting force

This is a classical benchmark to assess the performance of thin shell formulations in finite strain regimes. The problem was first proposed by Başar and Ding [152]. It consists of an annular plate slit radially, clamped in one end and subject to a lifting line force at the opposite end. The problem is set using inner and outer radius $R_i = 6\,\text{mm}$ and $R_o = 10\,\text{mm}$, respectively, and the thickness is $t = 0.03\,\text{mm}$. The material properties are $E = 2.1 \cdot 10^4\,\text{kN/mm}^2$ for the Young modulus and $\nu = 0$ for the Poisson ratio. The line force is set upwards in the transverse direction with a value of $q = 0.8\,\text{N/mm}$,

[152]: Başar et al. (1990), *Finite-rotation elements for the non-linear analysis of thin shell structures*

and the deformation is tracked in every load increment at the points A and B, as portrayed in Figs.4.14-4.15.

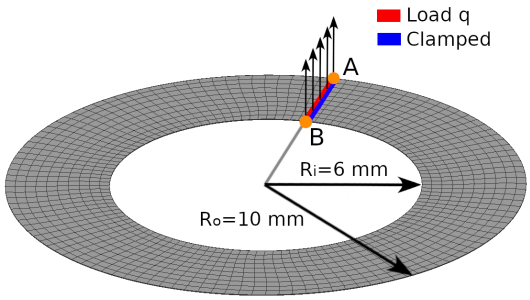

Figure 4.14: Slit annular plate: geometry, mesh and boundary conditions.

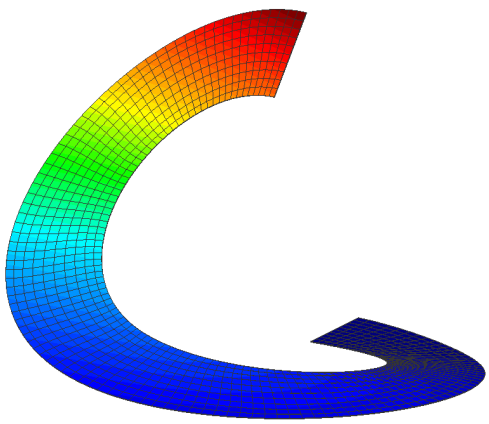

Figure 4.15: Slit annular plate: deformed configuration.

The problem is solved using the stabilized S-OSGS and the irreducible formulations with linear elements and quadratic hexahedral elements, respectively. The mesh is built using 10 radial elements and an increasing number of elements along the perimeter, resulting in four different meshes of 10×20, 10×40, 10×80 and 10×120 elements, with two elements in the thickness direction. Computations are performed using load factor increments of size 0.02 from 0 to 1 to track the evolution of the deformed configuration, portrayed in Figs. 4.16-4.17.

Results are similar for both formulations, with displacements of 17.201 and 13.594 at points A and B, respectively, which show good agreement with the literature [84, 96, 153, 154]. It is important to remark the fact that the mixed formulation

[84]: Mostafa et al. (2013), *A solid-shell corotational element based on ANDES, ANS and EAS for geometrically nonlinear structural analysis*
[96]: Leonetti et al. (2018), *An efficient isogeometric solid-shell formulation for geometrically nonlinear analysis of elastic shells*
[153]: Li et al. (2019), *An unsymmetric 8-node hexahedral solid-shell element with high distortion tolerance: Geometric nonlinear formulations*
[154]: Sze et al. (2002), *An eight-node hybrid-stress solid-shell element for geometric non-linear analysis of elastic shells*

converges at a similar rate compared to the irreducible formulation even though they use different orders of interpolation.

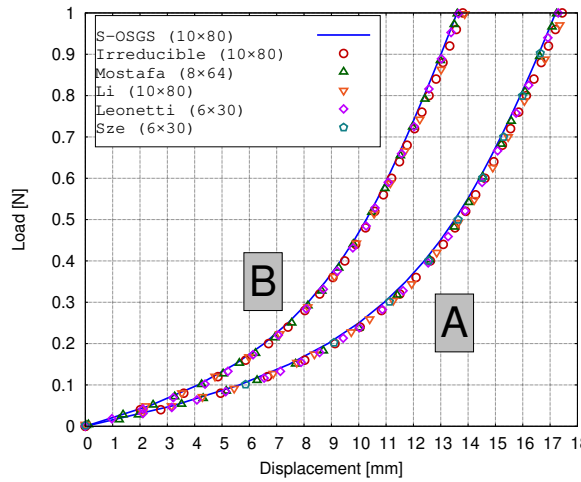

Figure 4.16: Slit annular plate: displacements with respect to the number of elements. References: Mostafa et al. [84], Li et al. [153] Leonetti et al. [96] Sze et al.[154].

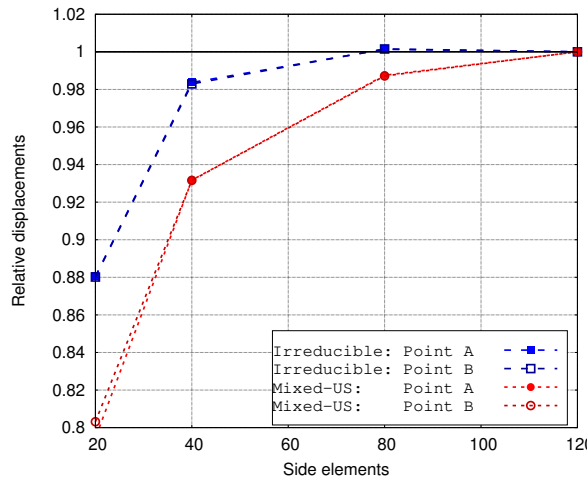

Figure 4.17: Slit annular plate: convergence with respect to the number of elements.

4.9.4 Single-curvature case: Hyperelastic cylinder

This benchmark problem was originally proposed by Büchter et al. [57] and since then became a standard case to test shell formulations in finite strain shells. The problem consists of an open-ended cylinder of length $L = 30\,\text{cm}$ and radius $R = 9\,\text{cm}$ and thickness $t = 0.2\,\text{cm}$, resting in a rigid support, and subjected to a line force q kN/m from above in a closing

[57]: Büchter et al. (1994), *Three-dimensional extension of non-linear shell formulation based on the enhanced assumed strain concept*

direction. The geometry, mesh and boundary conditions are illustrated in Fig. 4.18-4.19. Due to symmetry, only the half of the cylinder is modeled using appropriate symmetry boundary conditions. The material is defined as Neo-Hookean with $\mu = 60\,\text{kN/mm}^2$ and $\lambda = 240\,\text{kN/mm}^2$, which correspond to a Young modulus of $E = 168\,\text{kN/mm}^2$ and a Poisson's ratio of $\nu = 0.4$.

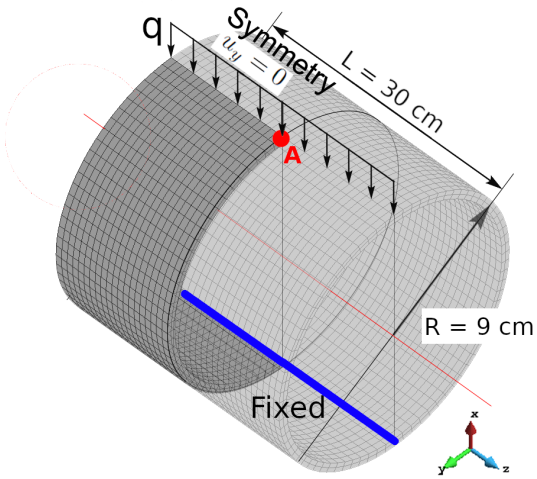

Figure 4.18: Hyperelastic cylinder: geometry, mesh and boundary conditions.

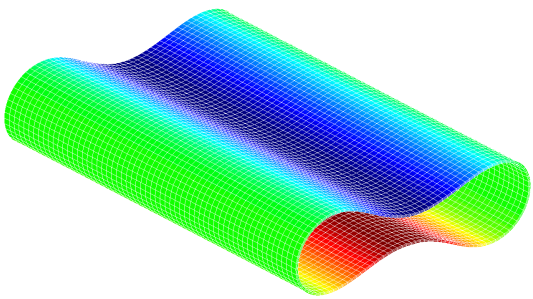

Figure 4.19: Hyperelastic cylinder: deformed configuration.

The problem is solved using the stabilized S-OSGS and the irreducible formulations with linear elements and quadratic hexahedral elements, respectively. The domain is discretized using meshes of 80×80 structured quadrilateral (extruded to hexahedral) elements and 3000 unstructured triangular (extruded to prismatic) elements with two elements in the thickness direction. Results are compared using the vertical displacement tracked at point A with respect to the total load $P = qL$ as the deformation advances through small increment

factors of 0.05 from 0 to 1 to have a good resolution of the evolution, as portrayed in Figs. 4.20-4.21. In this case, the stabilized formulation also shows a slightly faster convergence compared to the quadratic irreducible formulation. The stabilized formulation is designed in a general manner, so it is not limited to any specific type of element or mesh structure. As it can be seen in Fig. 4.20-4.21, it behaves properly regardless the type of mesh, resulting in a robust shell formulation.

Table 4.1: Reference solutions for Hyperelastic cylinder.

Reference	Result [kN]
Present: S-OSGS	35.12
Present: S-OSGS (Unstructured)	35.9
Present: Irreducible	34.80
Butcher et al. [57]	34.7
Brank et al. [139]	35.1
Sze et al. [81]	34 (15.6[cm])
Schwarze et al [93]	34.66
Kiendl et al [155]	34.86

In the literature, it is usual to measure the total load necessary to obtain a displacement of 16 cm. In this case, it is achieved at $P = 34.80$ kN and $P = 35.12$ kN in the irreducible and stabilized mixed formulation, respectively. This corresponds with the values reported in the literature, we summarize them in table 4.1 because the references do not report the load vs displacement curve.

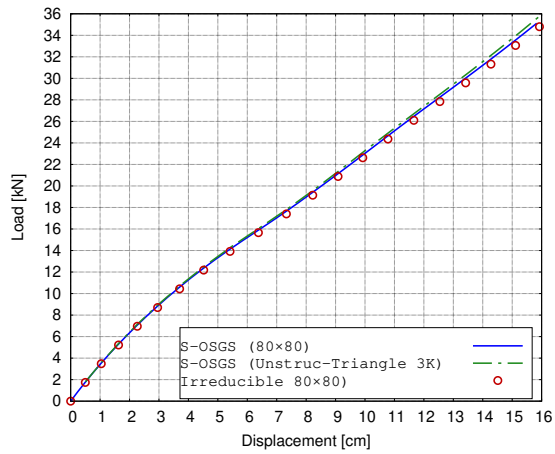

Figure 4.20: Hyperelastic cylinder: displacements with respect to number of elements.

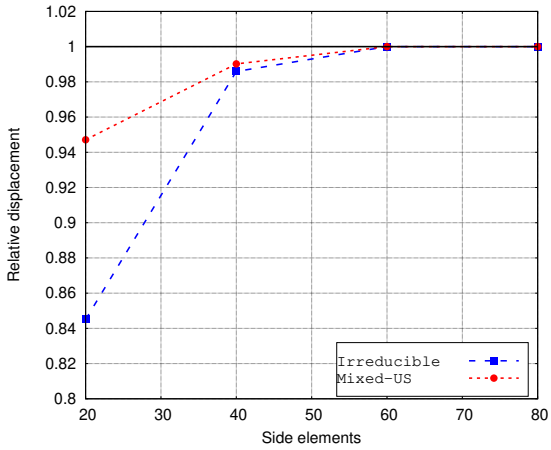

Figure 4.21: Hyperelastic cylinder: convergence with respect to number of elements.

4.9.5 Double-curvature case: Hemispherical shell

This benchmark problem is usually used to test inextensible membrane and bending modes in shell elements [112, 156]. It consists of a hemisphere of radius $R = 10$mm and thickness $t = 0.04$mm with a 18° hole with respect to the Z-axis at the top. The structure is subject to two pairs of diametrical opposite forces $P = 1\,\mathrm{N}$ along the X and Y axes. The geometry, mesh and boundary conditions are depicted in Figs. 4.22-4.23. Due to the symmetry of the problem, only a quarter of the hemisphere is modelled with appropriate symmetry boundary conditions. The material is set as Neo-Hookean with $\lambda = 0.039375\,\mathrm{kN/mm^2}$ and $\mu = 0.02625\,\mathrm{kN/mm^2}$, which correspond to a Young modulus $E = 0.06825\,\mathrm{kN/mm^2}$ and a Poisson's ratio $\nu = 0.3$.

[112]: Park et al. (1995), *An efficient assumed strain element model with six DOF per node for geometrically non-linear shells*
[156]: Stander et al. (1989), *An assessment of assumed strain methods in finite rotation shell analysis*

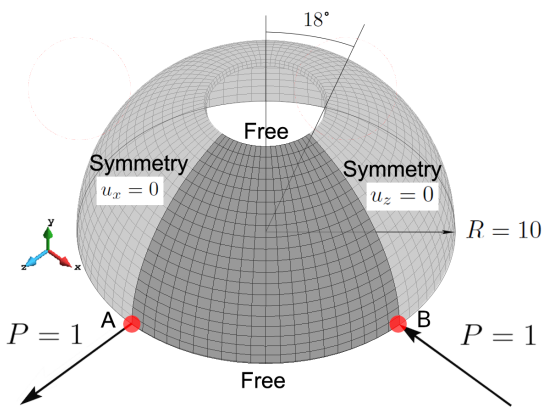

Figure 4.22: Hemispherical shell: geometry, mesh and boundary conditions.

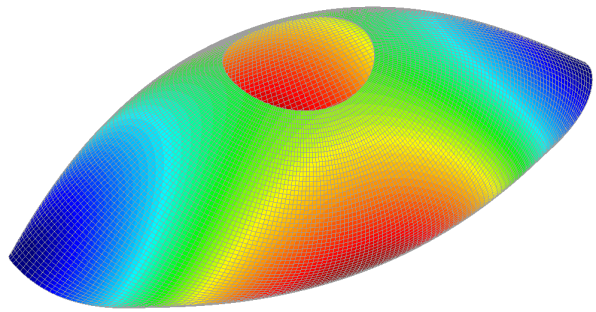

Figure 4.23: Hemispherical shell: deformed configuration.

The problem is solved using the stabilized S-OSGS and the irreducible formulations with linear elements and quadratic hexahedral elements, respectively. The domain is discretized using meshes of 20×20, 40×40, 60×60 and 80×80 elements with two elements along the thickness direction. The horizontal displacements are tracked at points A and B located at the points where the loads are applied, as indicated in Fig. 4.22. The load increases by increments of 5 from 0 to 400 to have a detailed description of the evolution. Results show good agreement with the literature [102, 143, 144, 154] as the displacements converge to 4.059 cm and 8.155 cm at points A and B, respectively.

[102]: Jeon et al. (2015), *The MITC3+ shell element in geometric nonlinear analysis*
[143]: Gruttmann et al. (2020), *An advanced shell model for the analysis of geometrical and material nonlinear shells*
[144]: Wagner et al. (2020), *An improved quadrilateral shell element based on the Hu–Washizu functional*
[154]: Sze et al. (2002), *An eight-node hybrid-stress solid-shell element for geometric non-linear analysis of elastic shells*

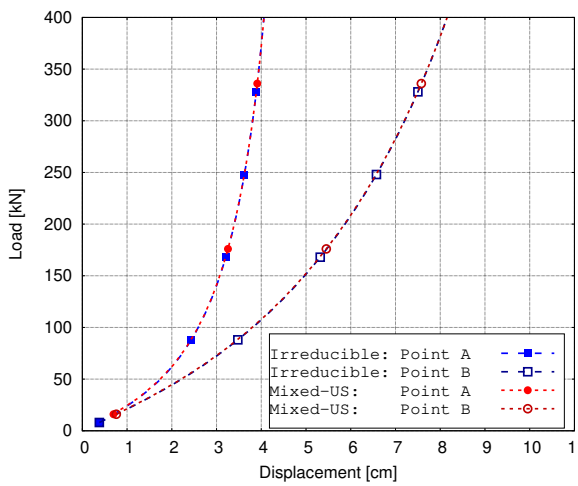

Figure 4.24: Hemispherical shell: displacements with respect to number of elements. References: Sze et al. [154], Wagner et al. [144], Gruttmann et al. [143], Jeon et al. [102].

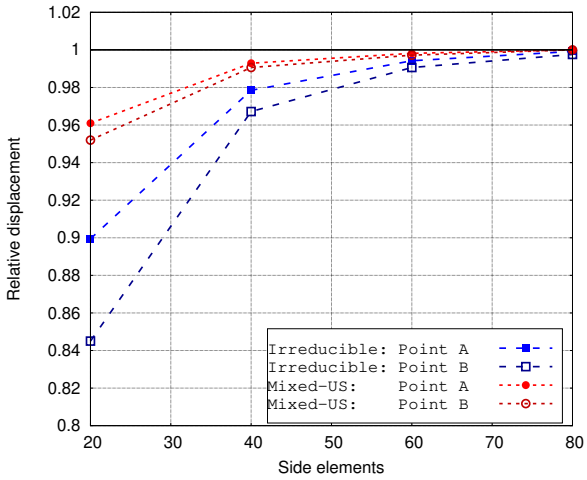

Figure 4.25: Hemispherical shell: convergence with respect to number of elements.

4.10 Conclusions

A stabilized FE formulation based on the Variational Multiscale framework is proposed for dealing with solid compressible materials and thin solid-shell structures in the finite strain regime. The two-field formulation is approached using two different residual-based stabilization techniques: the Algebraic and Orthogonal Sub-Grid Scales and the term-by-term Split-Orthogonal Sub-Grid Scales. These stabilized formulations offer several advantages over the displacement-based formulation. Firstly, they overcome the space compatibility restrictions associated with the interpolation of the unknowns, providing the freedom to choose any combination of interpolating spaces. Additionally, they enable the retention of quadratic order convergence in the displacement field and increase the convergence rate from 1 to 1.5 in the PK2 stress field. This results in a significantly enhanced accuracy of the PK2 stress field, albeit with a slightly reduced accuracy of the displacement field. Furthermore, the stabilized formulations have demonstrated greater robustness, even in coarse meshes. Moreover, these formulations are quasi-static in nature but can accurately represent dynamic behavior, surpassing the capabilities of irreducible formulations. However, when much smaller time steps are required, the inclusion of dynamic SGSs may become necessary to ensure accuracy.

In the context of shells, it is well-known that thin structures approximated using solid-shell elements are prone to various types of numerical locking. However, even in the case of extremely thin structures in the finite strain regime, the stabilized formulation effectively addresses numerical locking issues and enables a more accurate representation of the deformation state compared to a quadratic element irreducible formulation. The significant advantage of utilizing the stabilized two-field formulation in solid-shell elements for shell problems is that it preserves all the enhancements provided for solid elements, while eliminating the need for additional constraints typically present in classical shell formulations.

Acknowledgements

This work was supported by Vicerrectoría de Investigación, Desarrollo e Innovación (VRIDEI) of the Univeridad de Santiago de Chile, and the National Agency for Research and Development (ANID) Doctorado Becas Chile/2019 - 72200128 of the Government of Chile. I. Castañar gratefully acknowledges the support received from the Agència de Gestió d'Ajut i de Recerca through the predoctoral FI grant 2019-FI-B-00649. R. Codina gratefully acknowledges the support received through the ICREA Acadèmia Research Program of the Catalan Government. This work was partially funded through the TOPFSI-APP: Ref. PDC2022-133581-I00 MICINN of the Spanish Government. CIMNE is a recipient of a "Severo Ochoa Programme for Centers of Excellence in R&D" grant (CEX2018-000797-S) by the Spanish Ministry of Economy and Competitiveness.

Declarations

Conflict of interest

The authors declare that they have no known competing financial interests or personal relationships that could have appeared to influence the work reported in this paper.

Replication of results

All the information required for replicating the paper results was duly presented. Data files for the results are available upon request from the authors.

Fluid-Structure Interaction for hyperelastic solid-shells using Embedded Mesh

5

5.1 Abstract

This work introduces a numerical framework for addressing Fluid-Structure Interaction problems involving thin structures subject to finite strain deformations. The proposed approach utilizes an embedded mesh method to establish a coupling interface between the fluid and structural domains. The novelty of the work is the incorporation of a recently developed locking-free stabilized formulation of solid-shell elements to handle the structural domain. The framework employs established techniques to handle pressure jumps in the fluid domain across the embedding interface and enforce boundary conditions, such as discontinuous shape functions for the pressure unknowns designed to segregate nodal contributions of the cut elements, and Nitsche's method for the weak imposition of transmission conditions in the fluid. The present approach is validated through a series of benchmark cases in both 2D and 3D environments, progressively increasing in complexity. The results demonstrate good agreement with existing literature, establishing the presented framework as a viable method for addressing Fluid-Structure Interaction problems involving thin structures subject to large strains.

5.2 Introduction

The Fluid-Structure Interaction (FSI) problem is commonly formulated by solving the partial differential equations governing the fluid, structure, and the coupling conditions at the boundaries where the domains interact. Several families of numerical techniques exist to deal with this complex phenomenon, which need to define the strategy used to solve each of the components of the problem: the equations of fluid mechanics, the equations of solid mechanics, and the algorithmic approach for the coupling between both of them. This kind of problem can be approached by using either a monolithic or a partitioned scheme. The monolithic approach involves solving the fluid, structure, and interface equations as a unified system. Consequently, both domains advance simultaneously, requiring the solution of a large system of equations. On the other hand, the partitioned scheme employs separate solvers for each domain. Here, smaller independent systems of equations are solved separately, and the solution is obtained iteratively in a staggered manner. While the monolithic scheme results in a larger system of equations due to its simultaneous treatment of fluid, structure, and coupling equations, the partitioned approach involves solving smaller systems independently, coupling them iteratively. This efficiency makes the partitioned approach the preferred choice in many computational mechanics codes.

However, the partitioned scheme has its drawbacks. Firstly, the coupling algorithm is not guaranteed to converge consistently [157]. Secondly, the added-mass instability arises when the density of the structure is comparable to or lower than that of the fluid. As implied by its name, this instability results in an added-mass effect or increased inertia of the structure due to the surrounding fluid not being able to occupy the same physical space simultaneously [158]. While the stability and convergence of the coupling process primarily depends on the ratio of the apparent added mass to the structural mass [159], the elasticity coefficients and time steps have to be taken into account to obtain stable solutions [160]. It is important to remark that the added-mass instability is not an inherent concern for all FSI problems. It rather becomes important in applications such as hemodynamics, where the blood as well as other biological tissues have similar densities [161–164], but is does not appear in cases where the density of the solid is greater than that of the fluid, such

[157]: Causin et al. (2005), *Added-mass effect in the design of partitioned algorithms for fluid–structure problems*

[158]: Yu et al. (2013), *Generalized fictitious methods for fluid–structure interactions: Analysis and simulations*

[159]: Brummelen (2009), *Added mass effects of compressible and incompressible flows in fluid-structure interaction*

[160]: Idelsohn et al. (2009), *Fluid–structure interaction problems with strong added-mass effect*

[161]: Nobile (2001), *Numerical approximation of fluid-structure interaction problems with application to haemodynamics*

[162]: Le Tallec et al. (2001), *Fluid structure interaction with large structural displacements*

[163]: Hirschhorn et al. (2020), *Fluid–structure interaction modeling in cardiovascular medicine–A systematic review 2017–2019*

[164]: Sacks et al. (2009), *On the biomechanics of heart valve function*

as in aeroelasticity problems [165–167]. Lastly, it is important to emphasize that the added-mass effect is not present in the monolithic approach, because the energy balance between fluid and structure is automatically satisfied [158].

In the context of partitioned schemes, coupling can be implemented using either a strong or a weak approach. Strong coupling schemes necessitate a sub-iteration algorithm involving both domains for each time step. Although this type of coupling is computationally expensive, it yields the same solution as the monolithic scheme after the iterative process. In contrast, weakly coupled schemes use the solution from one domain for each time step to subsequently solve the other domain in a staggered manner. However, this approach can introduce instabilities associated with the coupling procedure [168], including the added mass effect.

The numerical techniques to approach FSI problems can also be classified depending on whether or not fluid the mesh conforms to an interface between fluid and structure [169] and therefore, on how to communicate the information between the fluid, the solid and the mesh [166]. On the one hand, there are methods where the fluid mesh conforms to an interface; the most common approaches of this type are Arbitrary Lagrangian-Eulerian (ALE) methods [170] and deforming-spatial-domain or space-time procedures [171]. On the other hand, there are methods where the fluid and structure meshes do not conform; methods that follow this approach are the Embedded Mesh (EM) methods [172], where the embedded interface is implicitly represented by tools such as in cut-cell methods [173] and level-set methods [174]. It is important to note that, regardless of whether the mesh conforms to an interface, every FSI formulation requires the governing equations of both fields to satisfy the wall boundary conditions.

The ALE method considers a reference coordinate system for the fluid that moves accommodating the motion of the solid. While this method excels at accurately depicting sharp interfaces, it comes with the disadvantage of requiring adaptive meshes or re-meshing processes, which can be computationally expensive [175], depending on the interface and the meshing algorithm [176].

Concerning EM methods, the solid and the fluid are discretized separately, and their meshes do not need to coincide at an interface. This flexibility allows the solid, described in a Lagrangian way, to move through the Eulerian-described fluid.

[165]: Farhat et al. (2006), *Provably second-order time-accurate loosely-coupled solution algorithms for transient nonlinear computational aeroelasticity*

[166]: Kamakoti et al. (2004), *Fluid–structure interaction for aeroelastic applications*

[167]: Guruswamy (2002), *A review of numerical fluids/structures interface methods for computations using high-fidelity equations*

[158]: Yu et al. (2013), *Generalized fictitious methods for fluid–structure interactions: Analysis and simulations*

[168]: Loehner et al. (1998), *Fluid-structure-thermal interaction using a loose coupling algorithm and adaptive unstructured grids*

[169]: Kim et al. (2019), *Immersed boundary methods for fluid-structure interaction: A review*

[166]: Kamakoti et al. (2004), *Fluid–structure interaction for aeroelastic applications*

[170]: Hirt et al. (1974), *An arbitrary Lagrangian-Eulerian computing method for all flow speeds*

[171]: Tezduyar et al. (1992), *A new strategy for finite element computations involving moving boundaries and interfaces-the deforming-spatial-domain/space-time procedure: II. Computation of free-surface flows, two-liquid flows, and flows with drifting cylinders*

[172]: Peskin (1973), *Flow patterns around heart valves: a digital computer method for solving the equations of motion*

[173]: Udaykumar et al. (1996), *Elafint: a mixed Eulerian–Lagrangian method for fluid flows with complex and moving boundaries*

[174]: Dunne (2006), *An Eulerian approach to fluid–structure interaction and goal-oriented mesh adaptation*

Generally, EM methods can be classified into two types: Diffused Boundary Methods and Sharp Interface Methods [177]. In the former, the embedded boundaries are smeared by distributing the singular forces to the surrounding background mesh nodes. This family includes the classic Immersed Boundary (IB) method, first proposed by Peskin in [172], the Direct Forcing IB method [178], and the Penalization method [179]. The latter consist of methods that eliminate the smearing feature, such as Cut-Cell methods [180], Immersed Interface methods [181], Hybrid Cartesian-IB methods, and Curvilinear IB methods [182]. All these methods require imposing the boundary conditions in an unfitted manner. This is typically addressed by enforcing them in a weak sense. Techniques such as the penalty method [183], the Lagrange multipliers method [184], or the Nitsche method [185, 186] are commonly utilized to handle this issue.

The approach used in this work correspond to a EM method of the Cut Finite Element Method (Cut-FEM) type [187, 188]. This family of methods allows to signal the exact position of the embedded interface by defining a iso-surface function to pinpoint its location. We prefer to adhere to Cut-FEM type approaches as they enable the attainment of accurate solutions through purely local boundary condition imposition [189]. A particular feature of our approach is that in elements intersected by the embedded interface, the conventional FE space is replaced by a discontinuous one. This substitution facilitates the disconnection of velocity and pressure fields in both sides of an intersected element, enabling the representation of solution discontinuities arising from the immersion of a thin body.

This study is a direct continuation of two previous works. The first one is dedicated to the analysis of numerical locking solid-shell elements and how to overcome it by using stabilized formulations [190], and the second one is dedicated to the extension of the stabilized formulation to finite strain theory [191]. The present work is dedicated to extend the concepts developed previously to the FSI problem by using an EM approach, wherein the solid mesh is embedded inside the fluid mesh. The main contribution of this work consists in the employment of the stabilized mixed displacement-stress formulations developed for solid-shell elements to handle FSI problems. For the present study, both domains are approached by using mixed formulations: in the fluid domain a velocity-pressure formulation, whereas in the solid

[175]: Baiges et al. (2017), *Refficientlib: an efficient load-rebalanced adaptive mesh refinement algorithm for high-performance computational physics meshes*

[176]: Han et al. (2019), *An Eulerian–Lagrangian–Lagrangian method for solving thin moving rigid body immersed in the fluid*

[177]: Sotiropoulos et al. (2014), *Immersed boundary methods for simulating fluid–structure interaction*

[172]: Peskin (1973), *Flow patterns around heart valves: a digital computer method for solving the equations of motion*

[178]: Fadlun et al. (2000), *Combined immersed-boundary finite-difference methods for three-dimensional complex flow simulations*

[179]: Kevlahan et al. (2001), *Computation of turbulent flow past an array of cylinders using a spectral method with Brinkman penalization*

[180]: Kirkpatrick et al. (2003), *A representation of curved boundaries for the solution of the Navier–Stokes equations on a staggered three-dimensional Cartesian grid*

[181]: Leveque et al. (1994), *The immersed interface method for elliptic equations with discontinuous coefficients and singular sources*

[182]: Ge et al. (2007), *A numerical method for solving the 3D unsteady incompressible Navier–Stokes equations in curvilinear domains with complex immersed boundaries*

[183]: Babuška (1973), *The finite element method with penalty*

[184]: Ito et al. (2008), *Lagrange Multiplier Approach to Variational Problems and Applications*

domain a displacement-stress formulation. The use of mixed formulations is usually associated to an incompatibility in the space of the unknowns if not interpolated properly [145]. For that reason, the problem is approached by means of stabilized formulations. The stabilization techniques are based on the VMS framework, which enables the use of equal-order interpolation for unknowns and, in the case of the solid-shell elements, it also ensures that the formulation is free from the numerical locking that is inherent to them.

In addition to the stabilized Finite Element (FE) formulations utilized for solving each individual problem, the present FSI approach requires several essential components to be achieved properly. Firstly, it is necessary to implement a search algorithm to find the intersection of the solid interface inside the fluid elements, ensuring the accurate definition of the intersection and the new integration points. This task is nontrivial, as search algorithms can be computationally costly if not implemented efficiently. Secondly, there is a need to define shape functions capable of handling pressure-segregated domains. Thirdly, a proper strategy must be chosen to impose the transmission conditions at the interfaces of the solid and the fluid. Lastly, in strongly coupled schemes, it is crucial to ensure the convergence of the transmission conditions. Therefore, a coupling strategy is required to minimize the interface residuals. All of these challenges are thoroughly addressed in the present work.

This work is organized as follows: the geometrical approximation of the shell domain is briefly explained in Section 5.3. It is followed by the introduction of the governing equations of the fluid and solid problems in Section 5.4, where the solid dynamics equations in finite strain theory and Navier-Stokes continuum equations are summarized, starting with the differential form of the corresponding boundary value problems in Subsection 5.4.1. The variational form of the solid and fluid problems are explained in Subection 5.4.2, presented in their mixed displacement-stress and velocity-pressure formulations, respectively. The time integration and linearization are described in Section 5.5. Consecutively, the stabilization techniques are briefly summarized in Section 5.6. Then, a brief summary of the construction of discontinuous shape functions is presented in Section 5.7. Details regarding the FSI problem, including the transmission conditions and the coupling strategy, are explained in Section 5.8. The strategy utilized to construct the embedded interface from the meshes

[185]: Nitsche (1971), *Über ein Variationsprinzip zur Lösung von Dirichlet-Problemen bei Verwendung von Teilräumen, die keinen Randbedingungen unterworfen sind*

[186]: Hansbo (2005), *Nitsche's method for interface problems in computa-tional mechanics*

[187]: Hansbo et al. (2004), *A finite element method for the simulation of strong and weak discontinuities in solid mechanics*

[188]: Burman et al. (2015), *CutFEM: Discretizing geometry and partial differential equations*

[189]: Burman et al. (2012), *Fictitious domain finite element methods using cut elements: II. A stabilized Nitsche method*

[190]: Aguirre et al. (2023), *Stress-displacement stabilized finite element analysis of thin structures using solid-shell elements - Part I: On the need of interpolating the stresses*

[191]: Aguirre et al. (2023), *Stress-displacement stabilized finite element analysis of thin structures using Solid-Shell elements - Part II: Finite strain hyperelasticity*

[145]: Boffi et al. (2013), *Mixed finite element methods and applications*

is explained in Section 5.9. Some numerical examples are portrayed in Section 5.10. Lastly, the final remarks and conclusions are presented in Section 5.11.

5.3 Geometrical approximation of solid-shells using finite elements

5.3.1 Construction of the local basis

[190]: Aguirre et al. (2023), *Stress-displacement stabilized finite element analysis of thin structures using solid-shell elements - Part I: On the need of interpolating the stresses*

Let us summarize the construction of the geometrical approximation to solid-shells presented in [190]. Let us first consider the shell as a surface, represented by Ω_s^{2D} in $\mathbb{R}^3$. Suppose that we have a FE partition $T_h = \{K\}$ of Ω_s^{2D} of diameter h, so that $\bar{\Omega}^{2D} = \bigcup_{K\in T_h} K$. Let $K \in T_h$ be an element domain of the partition with isoparametric coordinates (ξ, η), its mapping from the reference domain $K_0 \subset \mathbb{R}^2$ to $K \subset \mathbb{R}^3$ defined as

$$\begin{aligned} \boldsymbol{\varphi}_K &: K_0 \longrightarrow K \\ &(\xi, \eta) \mapsto (x^1, x^2, x^3). \end{aligned} \tag{5.1}$$

Consider n_{nod} as the number of nodes of K, and a Lagrangian interpolation

$$\boldsymbol{\varphi}_K(\xi, \eta) = \sum_{A=1}^{n_{nod}} N^A(\xi, \eta)\mathbf{x}^A, \tag{5.2}$$

where $N^A(\xi, \eta)$ is the shape function of node A on K_0, and $\mathbf{x}^A$ is the position vector of node A in K, $A = 1, \dots, n_{nod}$. The collection of all mappings $\{\boldsymbol{\varphi}_K, K \in T_h\}$ provides a local parametrization of Ω_s^{2D}. The vectors tangent to each $K \in T_h$ can be constructed as

$$\mathbf{g}_{1,K}^* = \left|\frac{\partial \boldsymbol{\varphi}_K}{\partial \xi}\right|^{-1} \frac{\partial \boldsymbol{\varphi}_K}{\partial \xi}, \quad \frac{\partial \boldsymbol{\varphi}_K}{\partial \xi} = \sum_{A=1}^{n_{nod}} \frac{\partial N^A}{\partial \xi}\mathbf{x}^A, \tag{5.3}$$

$$\mathbf{g}_{2,K}^* = \left|\frac{\partial \boldsymbol{\varphi}_K}{\partial \eta}\right|^{-1} \frac{\partial \boldsymbol{\varphi}_K}{\partial \eta}, \quad \frac{\partial \boldsymbol{\varphi}_K}{\partial \eta} = \sum_{A=1}^{n_{nod}} \frac{\partial N^A}{\partial \eta}\mathbf{x}^A, \tag{5.4}$$

which allow us to compute vectors normal to each $K \subset \Omega_s^{2D}$ as

$$\mathbf{g}_{3,K}^* = \mathbf{g}_{1,K}^* \times \mathbf{g}_{2,K}^*. \tag{5.5}$$

If ξ and η are orthogonal coordinates, $|\mathbf{g}^*_{3,K}| = 1$; otherwise, $\mathbf{g}^*_{3,K}$ is normalized.

The basis vectors $\{\mathbf{g}^*_{1,K}, \mathbf{g}^*_{2,K}, \mathbf{g}^*_{3,K}\}$, are discontinuous across elements if they are computed in this manner. However, they can be used to obtain a continuous basis. First, we project the vector field $\mathbf{g}^*_{3,K}$, $K \in T_h$, onto the space of continuous vector fields using a standard $L^2(\Omega_s^{2D})$ projection, thus obtaining the nodal vectors $\mathbf{g}^a_3$, $a = 1, \dots, n_{pts}$, for the nodal points n_{pts} of T_h. Then it follows that

$$\mathbf{g}_3(x^1, x^2, x^3) = \frac{\sum_{a=1}^{n_{pts}} N^a(x^1, x^2, x^3)\mathbf{g}^a_3}{\left|\sum_{a=1}^{n_{pts}} N^a(x^1, x^2, x^3)\mathbf{g}^a_3\right|},$$

where N^a is the global shape function of node a. Within each element $K \in T_h$ we have

$$\mathbf{g}_3|_K(\xi, \eta) = \frac{\sum_{A=1}^{n_{nod}} N^A(\xi, \eta)\mathbf{g}^A_{3,K}}{\left|\sum_{A=1}^{n_{nod}} N^A(\xi, \eta)\mathbf{g}^A_{3,K}\right|} \tag{5.6}$$

where A is the local numbering of the global node a. Figure 5.1 shows a cut of a surface and the conceptual difference between $\mathbf{g}^*_{3,K}$ and $\mathbf{g}_3$. Note that for linear elements $\mathbf{g}^*_{3,K}$ will be constant on each $K \in T_h$.

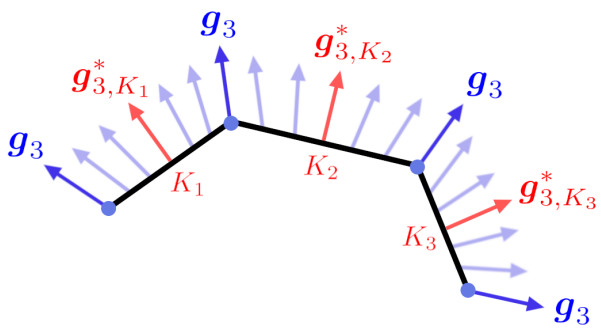

Figure 5.1: Normal vectors to the shell $\mathbf{g}^*_{3,K}$ and their smoothing $\mathbf{g}_3$.

Let $\{\mathbf{e}_1, \mathbf{e}_2, \mathbf{e}_3\}$ be the canonical basis of $\mathbb{R}^3$. Once the continuous global vector field $\mathbf{g}_3$ is constructed, a continuous local basis can be built at each point $\{\mathbf{g}_1, \mathbf{g}_2, \mathbf{g}_3\}$ by defining

$$\mathbf{g}_1 = \frac{\mathbf{g}_3 \times \mathbf{e}_3}{|\mathbf{g}_3 \times \mathbf{e}_3|} \tag{5.7}$$

$$\mathbf{g}_2 = \mathbf{g}_3 \times \mathbf{g}_1, \tag{5.8}$$

the only exception being when $\mathbf{g}_3$ aligns with $\mathbf{e}_3$, case in

which we set $\mathbf{g}_1 = \mathbf{e}_1$ and $\mathbf{g}_2 = \mathbf{e}_2$ or $\mathbf{g}_1 = -\mathbf{e}_1$ and $\mathbf{g}_2 = -\mathbf{e}_2$ if $\mathbf{g}_3$ is opposite to $\mathbf{e}_3$. The covariant basis $\{\mathbf{g}_1, \mathbf{g}_2, \mathbf{g}_3\}$ constructed this way will be such that $\{\mathbf{g}_1, \mathbf{g}_2\}$ will be *approximately* tangent to Ω_s^{2D} and $\mathbf{g}_3$ *approximately* normal.

5.3.2 Extrusion of the shell mid-surface

The solid-shell domain where the calculations are performed is denoted as Ω_s^{3D}, and it is computed from the normal direction extrusion of Ω_s^{2D}, which also represents the mid-surface of the shell. The construction of Ω_s^{3D} can be done elementwise due to the continuity of $\mathbf{g}_3$.

Consider the thickness of the shell to be defined by its values at the nodes of T_h, denoted as t^a, $a = 1, \dots n_{pts}$. For each $K \in T_h$, the thicknesses at the nodes will be t_K^A, A being the local number of node a, and the thickness function can be constructed as

$$t_K(\xi, \eta) = \sum_{A=1}^{n_{nod}} N^A(\xi, \eta) t_K^A. \tag{5.9}$$

The 3D element $K_0^{3D} = K_0 \times [-1, 1]$ can be constructed from the reference element K_0, and the mapping

$$\begin{aligned} \boldsymbol{\psi}_K &: K_0^{3D} \longrightarrow \mathbb{R}^3 \\ (\xi, \eta, \zeta) &\mapsto (x^1, x^2, x^3) = \boldsymbol{\varphi}_K(\xi, \eta) + \zeta \frac{1}{2} t_K(\xi, \eta) \mathbf{g}_3|_K(\xi, \eta), \end{aligned} \tag{5.10}$$

and then set $K^{3D} = \boldsymbol{\psi}_K(K_0^{3D})$, i.e., the image of K_0^{3D} through $\boldsymbol{\psi}_K$. The solid domain where the problem is posed is then $\Omega_s^{3D} = \bigcup_{K \in T_h} K^{3D}$. From the continuity of $\mathbf{g}_3$ and the intrinsic continuity of the thickness function, Ω_s^{3D} will be a smooth extrusion of Ω_s^{2D}. This domain is depicted in Fig. 5.2.

5.3.3 Interpolation across the thickness

After constructing the element domain $\{K^{3D}\}$, it only remains to define their degrees of freedom and basis for the FE space. Let us consider continuous Lagrangian interpolations for the original partition $\{K\}$ to define them for the reference element $K_0 \times [-1, 1]$. Let $N_i^{A,A'}(\xi, \eta, \zeta)$ be the shape function of a node in $K_0 \times [-1, 1]$ that corresponds to node A of K_0

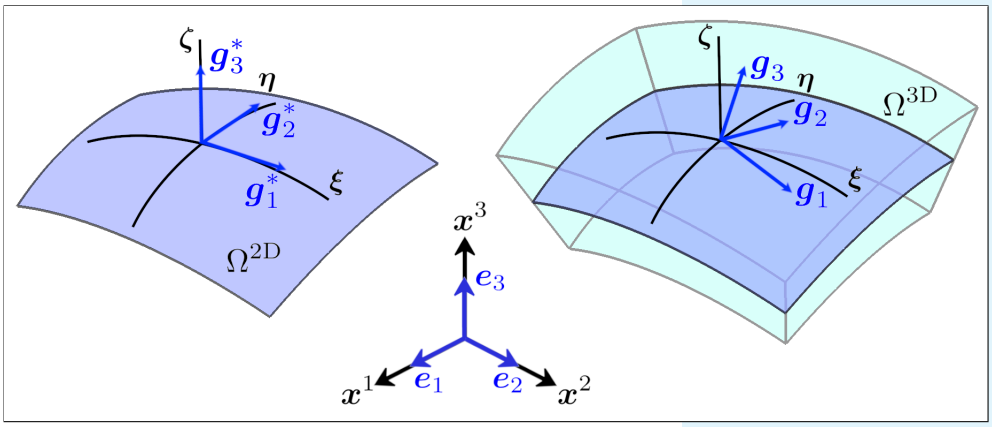

Figure 5.2: Geometry of the shell: 2D surface (left) and 3D extruded volume (right).

and node A' of the discretization of $[-1, 1]$. The shape functions corresponding to the solid-shell body $N_i^{A,A'}(\xi, \eta, \zeta)$ are constructed by multiplying the mid-surface shape functions $N^A(\xi, \eta)$ and the standard one dimensional Lagrangian shape functions $N^{A'}(\zeta)$ in the isoparametric space as

$$N^{A,A'}(\xi, \eta, \zeta) = N^A(\xi, \eta) N^{A'}(\zeta). \tag{5.11}$$

At the global level the shape functions will be written as $N^a(x^1, x^2, x^3)$, with a running again from 1 to n_{pts}. The FE partition resulting from the extrusion of the FE partition of the shell surface $T_h = \{K\}$ will be denoted as $T_h^{3D} = \{K^{3D}\}$. From this point forward, the superscript 3D will be omitted for simplicity, since the following formulations as well as the numerical experiments are presented by considering the 3D approximation of the shell.

5.4 Governing equations

5.4.1 Boundary value problems

Finite strain solid continuum equations

Consider the solid domain to be $\Omega_s(t)$ of $\mathbb{R}^d$ at the current time $t \geq 0$, where $d \in \{2, 3\}$ is the number of space dimensions; consequently $\Omega_s(t)$ is the current configuration and $\Gamma_s(t) = \partial\Omega_s(t)$ is the domain boundary at time t. The domain and its boundary defined in the reference configuration are denoted

by $\Omega_s^0 = \Omega_s(0)$ and $\Gamma_s^0 = \partial\Omega_s^0$, respectively. Let us consider the motion $\boldsymbol{\phi}$ of the deformable solid through a time interval $]0,T[$, whose mapping is described by $\boldsymbol{\phi} : \Omega_s^0 \to \Omega_s(t)$. The solid particles are labeled $\mathbf{X} \in \Omega_s^0$ and $\mathbf{x} \in \Omega_s(t)$ for the initial and current configurations, respectively, and the motion is defined as

$$\mathbf{x} = \boldsymbol{\phi}(\mathbf{X}, t). \tag{5.12}$$

Consider the space-time domain $\mathscr{D} = \{(\mathbf{X}, t) \,|\, \mathbf{X} \in \Omega_0, t \in]0,T[\}$ where the problem is defined. This problem consists of finding a displacement field $\mathbf{u}_s : \mathscr{D} \to \mathbb{R}^d$ and a second Piola-Kirchhoff (PK2) stress tensor field $\mathbf{S}_s : \mathscr{D} \to \mathbb{R}^d \otimes \mathbb{R}^d$ such that

Finite Strain solid governing equations

$$\rho_s^0 \frac{\partial^2 u_{s_a}}{\partial t^2} - \frac{\partial}{\partial X_A}\{F_{s_{aB}} S_{s_{BA}}\} = \rho_s^0 b_{s_a} \qquad \text{in } \Omega_s^0, t \in]0,T[, \tag{5.13}$$

$$S_{s_{AB}} - 2\frac{\partial \Psi_s}{\partial C_{s_{AB}}} = 0 \qquad \text{in } \Omega_s^0, t \in]0,T[, \tag{5.14}$$

$$\rho_s J_s = \rho_s^0 \qquad \text{in } \Omega_s^0, t \in]0,T[, \tag{5.15}$$

$$\mathbf{u}_s = \mathbf{u}_{s,D} \qquad \text{on } \Gamma_{s,D}^0, t \in]0,T[, \tag{5.16}$$

$$\mathbf{n}_s \cdot (\mathbf{F}_s \cdot \mathbf{S}_s) = \mathbf{t}_{s,N} \qquad \text{on } \Gamma_{s,N}^0, t \in]0,T[, \tag{5.17}$$

$$\mathbf{u}_s = \mathbf{u}_s^0 \qquad \text{in } \Omega_s^0, t = 0, \tag{5.18}$$

$$\dot{\mathbf{u}}_s = \dot{\mathbf{u}}_s^0 \qquad \text{in } \Omega_s^0, t = 0. \tag{5.19}$$

For clarity, we have used index notation in (5.13)-(5.14), with index a (in the deformed configuration) and A, B, C, D (in the reference configuration) running from 1 to d, and using the summation convention.

Let us briefly discuss the above equations. Eq. (5.13) is the balance of linear momentum equation in a total Lagrangian framework, where $\mathbf{F}_s = \frac{\partial \mathbf{x}}{\partial \mathbf{X}}$ is the deformation gradient, ρ_s is the density at time t, ρ_s^0 is the initial density, $J_s = \det(\mathbf{F}_s) > 0$ is the determinant of the deformation gradient, $\mathbf{S}_s$ is the second Piola-Kirchhoff (PK2) stress tensor whose symmetry is implied by the angular momentum equations, and $\rho_s^0 \mathbf{b}$ are the body forces. Eq. (5.14) correspond to the constitutive equation, where the PK2 stress tensor is written in terms of the strain energy function Ψ_s by taking derivatives with respect to the right Cauchy-Green tensor $\mathbf{C}_s = \mathbf{F}_s^T \cdot \mathbf{F}_s$. Eq. (5.15) is

the mass conservation equation, Eq. (5.16) is the imposition of displacement boundary conditions $\mathbf{u}_{s,D}$ on the Dirichlet boundaries, Eq. (5.17) is the imposition of prescribed tractions $\mathbf{t}_N$ on the Neumann boundaries $\Gamma^0_{s,N}$ considering the outward unit vector $\mathbf{n}_s$ normal to the reference configuration boundary, and Eqs.(5.18)-(5.19) are the imposition of initial displacements $\mathbf{u}^0_s$ and velocities $\dot{\mathbf{u}}_{s,0} = \frac{\partial \mathbf{u}_s}{\partial t}\Big|_{t=0}$, respectively.

The material is considered as a non-linear isotropic hyperelastic model. Therefore, Ψ_s is built as a function of the invariants of $\mathbf{C}_s$, defined as

$$
\begin{aligned}
I_1 &= \text{trace}(\mathbf{C}_s) = \mathbf{C}_s : \mathbf{I}, \\
I_2 &= \text{trace}(\mathbf{C}_s \cdot \mathbf{C}_s) = \mathbf{C}_s : \mathbf{C}_s, \\
I_3 &= \det(\mathbf{C}_s) = J_s^2.
\end{aligned}
$$

The compressible Neo-Hookean material stored energy function is defined in terms of the invariants as

$$
\Psi_s = \frac{\mu_s}{2}(I_1 - 3) - \mu_s \ln J_s + \frac{\lambda_s}{2}(\ln J_s)^2 \tag{5.20}
$$

where μ_s and λ_s are Lamé material coefficients. Therefore, Ψ_s measures the work done by stresses from the initial to the current configuration, making the relationship between Ψ_s and $\mathbf{C}_s$ to be independent of the coordinate system chosen. Note that in a rigid body motion, or absence of deformation, the deformation gradient is the identity and the stored energy function vanishes. For this specific material, an expression for the PK2 stress tensor can be obtained from Eq. (5.14), resulting in

$$
\mathbf{S}_s = \mu_s \left(\mathbf{I} - \mathbf{C}_s^{-1}\right) + \lambda_s (\ln J_s)\, \mathbf{C}_s^{-1}. \tag{5.21}
$$

The solid mechanics problem is presented through a mixed displacement-PK2 stress formulation. The reason lies in the fact that the interpolation of $\mathbf{S}_s$ allows to overcome numerical locking inherent to shell problems, as has been proven in previous works [190, 191]. The finite strain formulation has already been developed in [190], and therefore in the present work it is only briefly recalled for completeness. It is also worth mentioning that the extension to incompressible materials can be achieved by adopting a decoupled representation of the strain energy function which divides it into the deviatoric and volumetric parts [4, 116].

[190]: Aguirre et al. (2023), *Stress-displacement stabilized finite element analysis of thin structures using solid-shell elements - Part I: On the need of interpolating the stresses*

[191]: Aguirre et al. (2023), *Stress-displacement stabilized finite element analysis of thin structures using Solid-Shell elements - Part II: Finite strain hyperelasticity*

[190]: Aguirre et al. (2023), *Stress-displacement stabilized finite element analysis of thin structures using solid-shell elements - Part I: On the need of interpolating the stresses*

[4]: Castañar et al. (2020), *A stabilized mixed finite element approximation for incompressible finite strain solid dynamics using a total Lagrangian formulation*

[116]: Castañar et al. (2023), *A stabilized mixed three-field formulation for stress accurate analysis including the incompressible limit in finite strain solid dynamics*

Navier-Stokes continuum equations

Let us consider a computational domain Ω_f of $\mathbb{R}^d$ for dimensions $d \in \{2, 3\}$, with boundaries Γ_f, in a time interval $]0, T[$. The standard two-field Navier-Stokes problem for incompressible fluid consist in finding the velocity $\mathbf{u}_f$ and pressure p_f such that

Fluid governing equations

$$\rho_f \frac{\partial \mathbf{u}_f}{\partial t} + \rho_f \mathbf{u}_f \cdot \nabla \mathbf{u}_f - \nabla \cdot \left(2\mu_f \nabla^s \mathbf{u}_f\right) + \nabla p_f = \mathbf{f}_f \qquad \text{in } \Omega_f(t), t \in]0, T[\,, \tag{5.22}$$

$$\nabla \cdot \mathbf{u}_f = 0 \qquad \text{in } \Omega_f(t), t \in]0, T[\,, \tag{5.23}$$

$$\mathbf{u}_f = \mathbf{u}_{f,D} \qquad \text{on } \Gamma_{f,D}(t), t \in]0, T[\,, \tag{5.24}$$

$$\mathbf{n}_f \cdot \boldsymbol{\sigma}_f = \mathbf{t}_{f,N} \qquad \text{on } \Gamma_{f,N}(t), t \in]0, T[\,, \tag{5.25}$$

$$\mathbf{u}_f = \mathbf{u}_{f,0} \qquad \text{in } \Omega_f(t), t = 0, \tag{5.26}$$

where Eqs. (5.22)-(5.23) are the balance of linear momentum and the incompressibility restraint, respectively, Eqs. (5.24)-(5.25) are the Dirichlet and Neumann boundary conditions, and Eq. (5.26) is the velocity initial condition. In the balance of linear momentum equation, ρ_f is the fluid density, μ_f is the dynamic Newtonian viscosity, $\nabla^s \mathbf{u}_f = \frac{1}{2}\left(\nabla \mathbf{u}_f + \left(\nabla \mathbf{u}_f\right)^T\right)$ is the symmetrical gradient of the velocity vector, and $\mathbf{f}_f$ is the body forces vector. In the boundary condition equations, $\mathbf{u}_{f,D}$ is the prescribed velocity in the Dirichlet boundary, $\mathbf{n}_f$ is the unit normal pointing outwards from the fluid in the interface, $\boldsymbol{\sigma}_f = -p\mathbf{I} + 2\mu_f \nabla^s \mathbf{u}_f$ is the Cauchy stress tensor, and $\mathbf{t}_{f,N}$ is the prescribed fluid traction on the Neumann boundaries. Lastly, the initial velocity condition $\mathbf{u}_{f,0}$ is given to supply the governing equations.

5.4.2 Variational form

Let us consider $H^1(\Omega)$ to be the space of $L^2(\Omega)$ functions whose derivatives belong to $L^2(\Omega)$, for a domain Ω. In a general manner, the integral of the product of two functions in a domain ω is denoted by $\langle \cdot, \cdot \rangle_\omega$, omitting the subscript when ω is either Ω_s^0 or Ω_f depending on the problem being referred to. The variational form of the solid or fluid flow problems are defined in the following.

Variational form for the solid problem

For the solid problem the spaces are defined as $\mathbb{U} \subset H^1(\Omega_s)^d$ and $\mathbb{T} \subset L^2(\Omega_s)^{d\times d}$ for the displacements and the PK2 stresses, respectively, for all time $t \in]0,T[$. Functions in $\mathbb{U}$ satisfy the Dirichlet boundary conditions, whereas we denote as $\mathbb{U}_0$ the space of functions that vanish on the Dirichlet boundary of the solid domain $\Gamma^0_{s,D}$. Let $\mathbb{W} = \mathbb{U}\times\mathbb{T}$ and $\mathbb{W}_0 = \mathbb{U}_0\times\mathbb{T}$ be the spaces where the weak form of the solid problem is defined, so that the unknowns $\mathbf{U}_s = [\mathbf{u}_s, \mathbf{S}_s]^T$ and test functions $\mathbf{V}_s = [\mathbf{v}_s, \mathbf{T}_s]^T$ are such that $\mathbf{U}_s \in \mathbb{W}$ for each time t and $\mathbf{V}_s \in \mathbb{W}_0$, respectively. By testing system (5.13)-(5.14) against arbitrary test functions $\mathbf{V}_s$, the weak form of the problem consists of finding $\mathbf{U}_s :]0,T[\to \mathbb{W}$ such that the initial conditions are satisfied and

$$\left\langle \mathbf{v}_s, \rho^0_s \frac{\partial^2 \mathbf{u}_s}{\partial t^2} \right\rangle + \mathscr{A}_s(\mathbf{V}_s, \mathbf{U}_s) = \mathscr{F}_s(\mathbf{V}_s) \quad \forall \mathbf{V}_s \in \mathbb{W}_0, \tag{5.27}$$

where $\mathscr{A}_s(\mathbf{V}_s, \mathbf{U}_s)$ is a semilinear form defined on $\mathbb{W}_0 \times \mathbb{W}$ as

$$\mathscr{A}_s(\mathbf{V}_s, \mathbf{U}_s) := \left\langle \frac{\partial v_{s_a}}{\partial X_A}, F_{s_{aB}} S_{s_{AB}} \right\rangle + \left\langle T_{s_{AB}}, S_{s_{AB}} \right\rangle - \left\langle T_{s_{AB}}, 2\frac{\partial \Psi_s}{\partial C_{s_{AB}}} \right\rangle, \tag{5.28}$$

and $\mathscr{F}_s(\mathbf{V}_s)$ is a linear form on $\mathbb{W}_0$ defined by

$$\mathscr{F}_s(\mathbf{V}_s) := \left\langle \mathbf{v}_s, \rho^0_s \mathbf{b} \right\rangle + \left\langle \mathbf{v}_s, \mathbf{t}_{s,N} \right\rangle_{\Gamma^0_{s,N}}. \tag{5.29}$$

Variational form for the fluid problem

For the fluid flow problem, the velocity and pressure spaces are defined as $\mathbb{V} \subset H^1\left(\Omega_f\right)^d$ satisfying the Dirichlet conditions and $\mathbb{Q} = L^2\left(\Omega_f\right)$, respectively. Let also $\mathbb{V}_0 \subset H^1\left(\Omega_f\right)^d$ be the space of functions that vanish on the Dirichlet boundary of the fluid domain $\Gamma^0_{f,D}$. Let $\mathbb{X} := \mathbb{V}\times\mathbb{Q}$ and $\mathbb{X}_0 := \mathbb{V}_0\times\mathbb{Q}$, so that the unknowns $\mathbf{U}_f = \left[\mathbf{u}_f, p_f\right]^T \in \mathbb{X}$ for each time t and the test functions $\mathbf{V}_f = \left[\mathbf{v}_f, q_f\right]^T \in \mathbb{X}_0$. By testing Eqs.(5.22)-(5.23) against arbitrary test functions $\mathbf{V}_f$, the weak form of the problem consists of finding $\mathbf{U}_f :]0,t_f[\to \mathbb{X}$ such that

the initial conditions are satisfied and

$$\left\langle \mathbf{v}_f, \rho_f \frac{\partial \mathbf{u}_f}{\partial t} \right\rangle + \mathscr{A}_f\left(\mathbf{V}_f, \mathbf{U}_f\right) = \mathscr{F}_f\left(\mathbf{V}_f\right) \quad \forall \mathbf{V}_f \in \mathbb{X}_0, \quad (5.30)$$

where $\mathscr{A}_f\left(\mathbf{V}_f, \mathbf{U}_f\right)$ is a semilinear form defined on $\mathbb{X} \times \mathbb{X}_0$ as

$$\mathscr{A}_f\left(\mathbf{V}_f, \mathbf{U}_f\right) = \left\langle \mathbf{v}_f, \rho_f \mathbf{u}_f \cdot \nabla \mathbf{u}_f \right\rangle + \left\langle \nabla^s \mathbf{v}_f, 2\mu_f \nabla^s \mathbf{u}_f \right\rangle - \left\langle \nabla \cdot \mathbf{v}_f, p_f \right\rangle + \langle q, \nabla \cdot \mathbf{u} \rangle \quad (5.31)$$

and $\mathscr{F}_f\left(\mathbf{V}_f\right)$ is a linear form on $\mathbb{X}_0$ defined by

$$\mathscr{F}_f\left(\mathbf{V}_f\right) = \left\langle \mathbf{v}_f, \mathbf{f}_f \right\rangle + \left\langle \mathbf{v}_f, \mathbf{t}_{f,N} \right\rangle_{\Gamma_{f,N}}. \quad (5.32)$$

5.5 Time integration and linearization

In order to create a proper linear system of equations once discretized in space, the variational forms defined in Eqs. (5.27) and (5.30) need further treatment. In both cases the time derivative term has to be properly approximated using a time integration scheme. In the solid case, the geometric and material stiffness terms have to be linearized (first and third terms of Eq. (5.28)), while in the fluid case, only the convective term has to be linearized (first term in Eq. (5.31)). The time integration and linearization of each individual problem is described below.

5.5.1 Time integration

The time integration is performed by using an implicit scheme of the Backward Differentiation Formula (BDF) type for both solid and fluid problems. As usual, first order time integration (BDF1) is used to initialize computations, and it is followed by a second order time integration (BDF2) for the rest of the problem.

For this purpose, consider n as the time step counter and δt is the time step size of the uniform partition of the time interval $]0, T[$, and $\mathcal{O}(\cdot)$ is the approximation order of the scheme depending on the time step size. For the solid part, the second

time derivative of the displacement $\frac{\partial^2 \mathbf{u}_s}{\partial t^2} =: \mathbf{a}_s$ is approximated at a given time step $t^{n+1} = t^n + \delta t$ as

$$\text{BDF1}: \quad \mathbf{a}_s^{n+1} = \frac{1}{\delta t^2}\left[\mathbf{u}_s^{n+1} - 2\mathbf{u}_s^n + \mathbf{u}_s^{n-1}\right] + \mathcal{O}(\delta t), \tag{5.33}$$

$$\text{BDF2}: \quad \mathbf{a}_s^{n+1} = \frac{1}{\delta t^2}\left[2\mathbf{u}_s^{n+1} - 5\mathbf{u}_s^n + 4\mathbf{u}_s^{n-1} - \mathbf{u}_s^{n-2}\right] + \mathcal{O}(\delta t^2). \tag{5.34}$$

Similarly for the fluid part, the first time derivative of the velocity $\frac{\partial \mathbf{u}_f}{\partial t} =: \mathbf{a}_f$ is computed as

$$\text{BDF1}: \quad \mathbf{a}_f^{n+1} = \frac{1}{\delta t}\left[\mathbf{u}_f^{n+1} - \mathbf{u}_f^n\right] + \mathcal{O}(\delta t), \tag{5.35}$$

$$\text{BDF2}: \quad \mathbf{a}_f^{n+1} = \frac{1}{2\delta t}\left[3\mathbf{u}_f^{n+1} - 4\mathbf{u}_f^n + \mathbf{u}_f^{n-1}\right] + \mathcal{O}\left(\delta t^2\right). \tag{5.36}$$

5.5.2 Linearization

The finite strain solid mechanics equations yield a non-linear system that must be linearized in order to be solved. The idea is to obtain a bilinear operator that allows to compute a correction $\delta \mathbf{U}_s := [\delta \mathbf{u}_s, \delta \mathbf{S}_s]^T$ of the guessed solution $\mathbf{U}_s^{n+1}$ at a time t^{n+1}. The linearization is performed by using a Newton-Raphson scheme on the formulation presented in Eq. (5.27), meaning that the unknown for which we solve becomes the correction of the solution. Therefore the new problem consists in finding $\delta \mathbf{U}_s \in \mathbb{W}_0$ such that

$$\left\langle \mathbf{v}_s, \rho_s^0 \frac{c_s}{\delta t^2} \delta \mathbf{u}_s \right\rangle + \mathscr{B}_s(\mathbf{V}_s, \delta \mathbf{U}_s) = \mathscr{F}_s(\mathbf{V}_s) - \mathscr{A}_s\left(\mathbf{V}_s, \mathbf{U}_s^{n+1}\right) - \left\langle \mathbf{v}_s, \rho_s^0 \mathbf{a}_s^{n+1} \right\rangle \quad \forall \mathbf{V}_s \in \mathbb{W}_0, \tag{5.37}$$

where $\mathscr{B}_s(\mathbf{V}_s, \delta \mathbf{U}_s)$ defined on $\mathbb{W}_0 \times \mathbb{W}_0$ is the bilinear form obtained through the linearization of $\mathscr{A}_s(\mathbf{V}_s, \mathbf{U}_s)$, and it is defined as

$$\mathscr{B}_s(\mathbf{V}_s, \delta \mathbf{U}_s) = \left\langle \frac{\partial v_{s_a}}{\partial X_A}, \frac{\partial \delta u_{s_a}}{\partial X_B} S_{s_{BA}} \right\rangle + \left\langle \frac{\partial v_{s_a}}{\partial X_A}, F_{s_{aB}} \delta S_{s_{BA}} \right\rangle + \left\langle T_{s_{AB}}, \delta S_{s_{AB}} \right\rangle - \left\langle T_{s_{AB}}, \mathbb{C}_{s_{ABCD}} F_{s_{aC}} \frac{\partial \delta u_{s_a}}{\partial X_D} \right\rangle, \tag{5.38}$$

where $\mathbb{C}_s = 4\frac{\partial^2 \Psi_s}{\partial \mathbf{C}_s \partial \mathbf{C}_s}$ is the constitutive tangent matrix which relates variations of the PK2 stress tensor $\delta \mathbf{S}_s$ and the right

Cauchy tensor $\delta \mathbf{C}_s$. In the same manner, the time derivative term is linearized as

$$\left.\frac{\partial^2 \mathbf{u}}{\partial t^2}\right|_{t^{n+1}} = \frac{c_s}{\delta t^2}\delta \mathbf{u} + \mathbf{a}^{n+1}, \tag{5.39}$$

where c_s is a coefficient that depends on the integration scheme ($c_s = 1$ for BDF1 and $c_s = 2$ for BDF2), and $\mathbf{a}_s^{n+1}$ is the acceleration obtained in the previous iteration, computed as stated in Eqs. (5.33) and (5.34). The bilinear form $\mathscr{B}_s$ relies on the previous iteration values of the unknown $\mathbf{U}_s^{n+1}$ through the evaluation of various tensor functions, although this dependence has not been explicitly presented.

The Navier-Stokes equations have a non-linearity in the convective term presented in Eq. (5.27), that can be linearized using a proper scheme. In this work, both fixed point and Newton-Raphson schemes are considered. Let us consider $\hat{\mathbf{u}}_f$ to be the previous iteration velocity in a given time step and c_l a constant that determines the type of linearization. The linearized problem consists in finding $\mathbf{U}_f \in \mathbb{X}$ such that

$$\left\langle \mathbf{v}_f, \rho_f \mathbf{a}_f \right\rangle + \mathscr{B}_f\left(\mathbf{V}_f, \mathbf{U}_f\right) = \mathscr{F}_f\left(\mathbf{V}_f\right) - c_l \left\langle \mathbf{v}_f, \rho_f \hat{\mathbf{u}}_f \cdot \nabla \hat{\mathbf{u}}_f \right\rangle \quad \forall \mathbf{V}_f \in \mathbb{X}_0, \tag{5.40}$$

where $\mathscr{B}_f$ is a bilinear form defined as

$$\begin{aligned}\mathscr{B}_f\left(\mathbf{V}_f, \mathbf{U}_f\right) = &\left\langle \mathbf{v}_f, \rho_f \hat{\mathbf{u}}_f \cdot \nabla \mathbf{u}_f \right\rangle + c_l \left\langle \mathbf{v}_f, \rho_f \mathbf{u}_f \cdot \nabla \hat{\mathbf{u}}_f \right\rangle \\ &+ \left\langle \nabla^s \mathbf{v}_f, 2\mu_f \nabla^s \mathbf{u}_f \right\rangle - \left\langle \nabla \cdot \mathbf{v}_f, p_f \right\rangle + \left\langle q, \nabla \cdot \mathbf{u} \right\rangle,\end{aligned} \tag{5.41}$$

and the values $c_l = 0$ and $c_l = 1$ set the linearization as fixed point and Newton-Raphson schemes, respectively.

5.6 Stabilized Finite Element formulation

Given that the primary objective of this work is not to introduce the already established stabilized formulation that we use, the details regarding the mathematical foundations are omitted. The stabilized formulation adopted here follows the Variational Multiscale (VMS) framework, initially proposed

by Hughes et al. [3] and further developed in [43]. The fundamental concept within this framework is incorporating additional consistent terms into the original Galerkin FE formulation, enhancing its stability without compromising accuracy. This enhancement is achieved by introducing a finer resolution space, known as the sub-grid scale (SGS) space.

[3]: Hughes et al. (1998), *The variational multiscale method - A paradigm for computational mechanics*

[43]: Codina (2000), *Stabilization of incompressibility and convection through orthogonal sub-scales in finite element methods*

Let us start with the standard Galerkin FE approximation of the variational problem defined in Eqs. (5.37) for the solid and in Eq. (5.40) for the fluid. In a general manner, if we consider a FE partition $\mathscr{P}_h$ of a domain Ω, the diameter of an element domain $K \in \mathscr{P}_h$ is denoted by h_K, and the diameter of the element partition is defined as $h = \max\{h_K | K \in \mathscr{P}_h\}$. Under this definition, the FE partitions of the solid and fluid domains will be denoted as $\mathscr{P}_h^s$ and $\mathscr{P}_h^f$, respectively.

5.6.1 Finite Strain stabilized formulation

The conforming FE spaces of the solid domain are constructed in the usual manner $\mathbb{U}_h \subset \mathbb{U}$ and $\mathbb{T}_h \subset \mathbb{T}$; therefore $\mathbb{W}_h = \mathbb{U}_h \times \mathbb{T}_h$. The subspace of $\mathbb{U}_h$ of vectors that vanish on the Dirichlet boundary is denoted as $\mathbb{U}_{h,0} \subset \mathbb{U}_0$, and $\mathbb{W}_{h,0} = \mathbb{U}_{h,0} \times \mathbb{T}_h$. Therefore, the Galerkin FE approximation consists of finding $\delta \mathbf{U}_{s,h} = \left[\delta \mathbf{u}_{s,h}, \delta \mathbf{S}_{s,h}\right]^T \in \mathbb{W}_{h,0}$ for a time t^{n+1}, such that

$$\begin{aligned}\left\langle \mathbf{v}_{s,h}, \rho_s^0 \frac{c_s}{\delta t^2} \delta \mathbf{u}_{s,h} \right\rangle + \mathscr{B}_s\left(\mathbf{V}_{s,h}, \delta \mathbf{U}_{s,h}\right) =& \mathscr{F}_s\left(\mathbf{V}_{s,h}\right) \\ &- \mathscr{A}_s\left(\mathbf{V}_{s,h}, \mathbf{U}_{s,h}^{n+1}\right) - \left\langle \mathbf{v}_{s,h}, \rho_s^0 \mathbf{a}_{s,h}^{n+1} \right\rangle \quad \forall \mathbf{U}_{s,h} \in \mathbb{W}_{h,0}.\end{aligned} \tag{5.42}$$

The Galerkin FE approximation lacks of stability unless particular interpolations are used to interpolate the displacement and PK2 stress fields, requiring to satisfy appropriate inf-sup conditions which can be achieved by means of stabilization [145]. The stabilized formulation using the VMS approach for the solid mechanics problem has been initially developed for the finite strain solids for the three-field formulations to obtain enhanced precision in the stress field and to circumvent the numerical locking due to incompressibility [116]. It has also been extended to solid-shell elements in order to formulate a locking-free approach in the approximation of thin structures [190].

[145]: Boffi et al. (2013), *Mixed finite element methods and applications*

[116]: Castañar et al. (2023), *A stabilized mixed three-field formulation for stress accurate analysis including the incompressible limit in finite strain solid dynamics*

[190]: Aguirre et al. (2023), *Stress-displacement stabilized finite element analysis of thin structures using solid-shell elements - Part I: On the need of interpolating the stresses*

For the mixed finite strain solid formulation we choose the SGS space to be the orthogonal complement to the FE space, namely, we use the Orthogonal Subgrid Scale formulation (OSGS), which yields

Finite Strain solid stabilized formulation

$$\begin{aligned}\left\langle \mathbf{v}_{s,h}, \rho_s^0 \frac{c_s}{\delta t^2}\delta\mathbf{u}_{s,h}\right\rangle + \mathscr{B}_s\left(\mathbf{V}_{s,h}, \delta\mathbf{U}_{s,h}\right) + \sum_K \left\langle \mathrm{L}^s\left(\mathbf{V}_{s,h}\right), \boldsymbol{\tau}_K \mathrm{R}^s_{\delta\mathbf{U}}\left(\delta\mathbf{U}_{s,h}\right)\right\rangle_K \\ = \mathscr{F}_s\left(\mathbf{V}_{s,h}\right) - \mathscr{A}_s\left(\mathbf{V}_{s,h}, \mathbf{U}^{n+1}_{s,h}\right) - \left\langle \mathbf{v}_{s,h}, \rho_s^0 \mathbf{a}^{n+1}_{s,h}\right\rangle \\ - \sum_K \left\langle \mathrm{L}^s\left(\mathbf{V}_{s,h}\right), \boldsymbol{\tau}_K \left[\mathrm{R}^s_{\mathbf{U}}\left(\mathbf{U}^{n+1}_{s,h}\right) - \Pi^h\left(\mathrm{R}^s_{\mathbf{U}}\left(\mathbf{U}^{n+1}_{s,h}\right)\right)\right]\right\rangle_K, \end{aligned} \tag{5.43}$$

where Π^h is the L^2 projection onto the FE space and $\mathrm{L}^s = \left[\mathrm{L}^s_u, \mathrm{L}^s_S\right]^T$ is the adjoint operator that comes from the integration by parts of $\mathscr{B}_s$, defined by components as

$$\begin{aligned}\mathrm{L}^s_u\left(\mathbf{V}_{s,h}\right)_a &= -\frac{\partial}{\partial X_B}\left\{\frac{\partial v_{s,h_a}}{\partial X_A} S_{s,h_{BA}}\right\} + \frac{\partial}{\partial X_D}\left\{T_{s_{AB}} \mathbb{C}_{s_{ABCD}} F_{s_{aC}}\right\}, \\ \mathrm{L}^s_S\left(\mathbf{V}_{s,h}\right)_{AB} &= \frac{\partial v_{s,h_a}}{\partial X_A} F_{s_{aB}} + T_{s_{AB}},\end{aligned}$$

The residual operators $\mathrm{R}^s_{\delta\mathbf{U}}$ and $\mathrm{R}^s_{\mathbf{U}}$ are defined as

$$\begin{aligned}\mathrm{R}^s_{\delta\mathbf{U}}\left(\delta\mathbf{U}_{s,h}\right) &= -\mathrm{B}^s\left(\delta\mathbf{U}_{s,h}\right), \\ \mathrm{R}^s_{\mathbf{U}}\left(\mathbf{U}^{n+1}_{s,h}\right) &= \mathrm{F}^s - \mathrm{A}^s\left(\mathbf{U}^{n+1}_{s,h}\right),\end{aligned}$$

where the components of $\mathrm{B}^s = \left[\mathrm{B}^s_u, \mathrm{B}^s_S\right]^T$, $\mathrm{A}^s = \left[\mathrm{A}^s_u, \mathrm{A}^s_S\right]^T$, and $\mathrm{F}^s = \left[\mathrm{F}^s_u, \mathrm{F}^s_S\right]^T$ are defined as

$$\begin{aligned}\mathrm{B}^s_u\left(\delta\mathbf{U}_{s,h}\right)_a &= -\frac{\partial}{\partial X_A}\left\{\frac{\delta u_{s,h_a}}{\partial X_B} S_{s,h_{AB}}\right\} - \frac{\partial}{\partial X_A}\left\{F_{s_{aB}} \delta S_{s,h_{AB}}\right\}, \\ \mathrm{B}^s_S\left(\delta\mathbf{U}_h\right)_{AB} &= \delta S_{s,h_{AB}} - \mathbb{C}_{s_{ABCD}} F_{s_{aC}} \frac{\partial \delta u_{s,h_a}}{\partial X_D}, \\ \mathrm{A}^s_u\left(\mathbf{U}^{n+1}_h\right)_a &= -\frac{\partial}{\partial X_A}\left\{F_{s_{aB}} S_{s,h_{BA}}\right\}, \\ \mathrm{A}^s_S\left(\mathbf{U}^{n+1}_{s,h}\right)_{AB} &= S_{s,h_{AB}} - 2\frac{\partial \Psi}{\partial C_{s,AB}}, \\ \mathrm{F}^s_{ua} &= \rho_s^0 b_{s_a}, \\ \mathrm{F}^s_S &= 0.\end{aligned}$$

It is understood that $\mathbf{F}_s$ and $\mathbf{C}_s$ are computed with $\mathbf{u}_{s,h}$. Tensor $\mathbb{C}_s$ is the fourth order tangent constitutive tensor.

The matrix $\boldsymbol{\tau}_K^{-1}$ is an approximation of the operator B^s withing each element K. The details on how to design $\boldsymbol{\tau}_K$ can be reviewed in [118]. In this case, $\boldsymbol{\tau}_K$ is taken as a diagonal matrix where the stabilization parameters are

[118]: Codina (2009), *Finite element approximation of the three-field formulation of the Stokes problem using arbitrary interpolations*

$$\boldsymbol{\tau}_K = \begin{bmatrix} \tau_u \mathbf{I}_d & \mathbf{0} \\ \mathbf{0} & \tau_S \mathbf{I} \end{bmatrix}, \qquad \tau_u = c_u \frac{h_K^2}{2\mu_s}, \qquad \tau_S = c_S,$$

where c_u and c_S are algorithmic parameters to be chosen. In the examples below they are set as $c_u = 0$ and $c_S = 0.1$, although it has been proven that the formulation is very insensitive to them, and they can be set in a wide range of values. It has to be noted that this expression of the stabilization parameters mimics the classical primal formulation of the mixed problem in the linear (infinitesimal strain) case [192]. The possibility of using other expressions with better convergence behavior in finite strain problems needs to be explored.

[192]: Badia et al. (2009), *Unified Stabilized Finite Element Formulations for the Stokes and the Darcy Problems*

5.6.2 Navier-Stokes stabilized formulation

The standard Galerkin approximation of the Navier-Stokes can be constructed using conforming FE spaces for the velocity $\mathbb{V}_h \subset \mathbb{V}$, the velocity test functions $\mathbb{V}_{h,0} \subset \mathbb{V}_0$ and the pressure $\mathbb{Q}_h \subset \mathbb{Q}$, in the usual manner. If $\mathbb{X}_h := \mathbb{V}_h \times \mathbb{Q}_h$ and $\mathbb{X}_{h,0} := \mathbb{V}_{h,0} \times \mathbb{Q}_h$, the Galerkin FE approximation consists of finding $U_{f,h} = \left[\mathbf{u}_{f,h}, p_{f,h}\right]^T$ for a time t^{n+1} such that

Navier-Stokes stabilized formulation

$$\left\langle \mathbf{v}_{f,h}, \rho_f \mathbf{a}_{f,h} \right\rangle + \mathscr{B}_f\left(\mathbf{V}_{f,h}, \mathbf{U}_{f,h}\right) = \mathscr{F}_f\left(\mathbf{V}_{f,h}\right) - c_l \left\langle \mathbf{v}_{f,h}, \rho_f \hat{\mathbf{u}}_{f,h} \cdot \nabla \hat{\mathbf{u}}_{f,h} \right\rangle \quad \forall \mathbf{V}_{f,h} \in \mathbb{X}_{h,0}. \tag{5.44}$$

It is well known that the approximation in Eq. (5.44) has numerical instabilities that need to be addressed. The first one arises when the nonlinear convective term dominates the viscous term, giving place to spurious boundary layers. The second one is the incompatibility of $\mathbb{V}_h \times \mathbb{Q}_h$ which arises when using equal order interpolation, and therefore the discrete compatibility or inf-sup condition is not satisfied. However,

these can be overcome by using the VMS approach presented below. This kind of stabilized formulations have been long established for the Navier-Stokes problem, including compressible [113] and incompressible flows [193], as well as viscoelastic fluids [114, 115]. A complete review on this approach can be found in [194].

[113]: Codina (2002), *Stabilized finite element approximation of transient incompressible flows using orthogonal subscales*

[193]: Parada et al. (2020), *A fractional step method for computational aeroacoustics using weak imposition of Dirichlet boundary conditions*

[114]: Castillo et al. (2017), *Finite element approximation of the viscoelastic flow problem: A non-residual based stabilized formulation*

[115]: Moreno et al. (2019), *Logarithmic conformation reformulation in viscoelastic flow problems approximated by a VMS-type stabilized finite element formulation*

[194]: Codina et al. (2017), *Variational Multiscale Methods in Computational Fluid Dynamics*

For the stabilized Navier-Stokes formulation we choose the projection of the SGS to be the identity on the space of FE residuals, resulting in the Algebraic Subgrid Scale formulation (ASGS), which yields

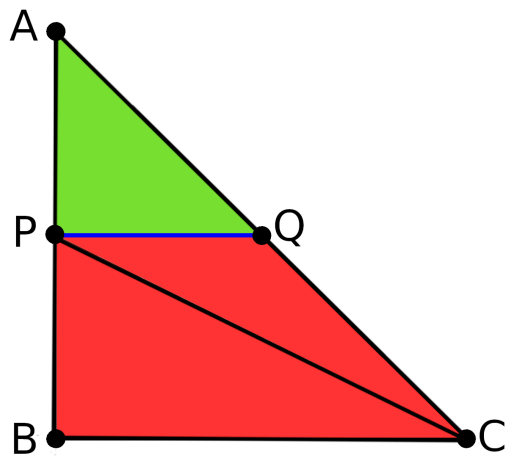

Figure 5.3: Partition of a triangle element into sub-elements following the interface.

$$\left\langle \mathbf{v}_{f,h}, \rho_f \mathbf{a}_{f,h} \right\rangle + \mathscr{B}_f\left(\mathbf{V}_{f,h}, \mathbf{U}_{f,h}\right) - \sum_K \left\langle \mathrm{L}^f\left(\mathbf{V}_{f,h}\right), \boldsymbol{\alpha}_K \mathrm{R}^f\left(\mathbf{U}_{f,h}\right)\right\rangle_K$$
$$= \mathscr{F}_f\left(\mathbf{V}_{f,h}\right) - c_l \left\langle \mathbf{v}_{f,h}, \rho_f \hat{\mathbf{u}}_{f,h} \cdot \nabla \hat{\mathbf{u}}_{f,h} \right\rangle \quad \forall \mathbf{V}_{f,h} \in \mathbb{X}_{h,0}, \tag{5.45}$$

where $\mathrm{L}^f = \left[\mathrm{L}^f_u, \mathrm{L}^f_p\right]^T$ is the adjoint operator that comes from the integration by parts of $\mathscr{B}_f$ defined as

$$\mathrm{L}^f_u\left(\mathbf{V}_{f,h}\right) = -\rho_f \hat{\mathbf{u}}_{f,h} \cdot \nabla \mathbf{v}_{f,h} - \nabla \cdot \left(2\mu_f \nabla^s \mathbf{v}_{f,h}\right) - \nabla q_{f,h},$$
$$\mathrm{L}^f_p\left(\mathbf{V}_{f,h}\right) = \nabla \cdot \mathbf{v}_{f,h},$$

and the residual R^f is defined as

$$\mathrm{R}^f\left(\mathbf{U}_{f,h}\right) = \mathrm{F}^f - \mathrm{B}^f\left(\mathbf{U}_{f,h}\right),$$

where the components of $\mathrm{B}^f = \left[\mathrm{B}_u^f, \mathrm{B}_p^f\right]^T$ and $\mathrm{F}^f = \left[\mathrm{F}_u^f, \mathrm{F}_p^f\right]^T$ are defined as

$$\begin{aligned}
\mathrm{B}_u^f\left(\mathbf{U}_{f,h}\right) &= \rho_f \hat{\mathbf{u}}_f \cdot \nabla \mathbf{u}_{f,h} - \nabla \cdot \left(2\mu_f \nabla^s \mathbf{u}_{f,h}\right) + \nabla p_{f,h}, \\
\mathrm{B}_p^f\left(\mathbf{U}_{f,h}\right) &= -\nabla \cdot \mathbf{u}_{f,h}, \\
\mathrm{F}_u^f &= \mathbf{f}_f, \\
\mathrm{F}_p^f &= 0,
\end{aligned}$$

and the matrix $\boldsymbol{\alpha}_K$ of stabilization parameters is computed as

$$\boldsymbol{\alpha}_K = \begin{bmatrix} \alpha_u \mathbf{I}_d & \mathbf{0} \\ \mathbf{0} & \alpha_p \end{bmatrix}, \quad \alpha_u = \left[c_1 \frac{\mu_f}{h_K^2} + c_2 \frac{\rho_f \left|\hat{u}_f\right|}{h_K} \right]^{-1}, \quad \alpha_p = \frac{h_K^2}{\alpha_u},$$

where $\left|\hat{u}_f\right|$ is the Euclidean norm of the velocity guess, and the algorithmic parameters are chosen as $c_1 = 4$ and $c_2 = 2$ for linear elements.

5.7 Discontinuous shape functions

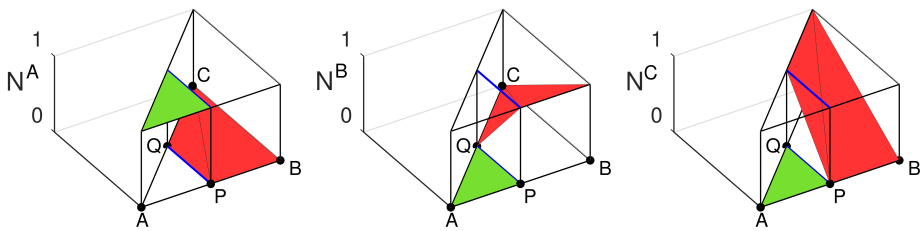

Figure 5.4: Discontinuous shape functions for cut elements.

5.7.1 Ausas et al. shape functions

The pressure discontinuities in the fluid domain arising due to the presence of a solid interface embedded in it are addressed by using the discontinuous shape functions presented by Ausas et al. in [195]. These shape functions facilitate the segregation of degrees of freedom within an element into two entirely independent parts, with no additional treatment required for neighboring elements. This local implementation

[195]: Ausas et al. (2010), *An improved finite element space for discontinuous pressures*

simplifies the construction of discontinuous shape functions, applying the same principles to both triangles and tetrahedral elements. This approach is convenient at the computational level, because it does not require to add additional degrees of freedom, which avoids the need of recomputing the domain's graph at each time step. For simplicity, only a brief summary of the implementation for triangular elements is provided.

Consider a triangle ABC, whose edges $\bar{AB}$ and $\bar{AC}$ are cut by the interface at points P and Q respectively. We wish to construct a FE basis that is discontinuous across PQ. As illustrated in Fig. 5.3, the element is divided into a positive (green) and a negative (red) side. At the same time, the element is divided into sub-elements that follow the interface: in this case the sub-triangles are arbitrarily created as APQ, CQP and BCP. To achieve a discontinuous approximation, the shape functions on the green side must exclusively depend on the nodes belonging to the green side, while the shape functions on the red side must solely depend on the nodes that belong to the red side. This explanation may seem redundant, but it is crucial to the construction of discontinuous functions. Let N^A, N^B and N^C be the shape functions of nodes A, B and C of a triangular element. The basic idea is to "carry" the values of N^A, N^B and N^C through their adjacent edges in their respective sides. By this logic, the discontinuous shape functions take the form illustrated in Fig. 5.4, constructed as follows: point A is the only point available at the green side; therefore, the value of the shape function N^A at point A is carried to points P and Q, and it is zero along the red side. The red side has points B and C; therefore, N^B carries its value from B to P and N^C carries its value from C to Q, and are zero along the green side.

Let P^+ and P^- be the coordinates of point P reached from the green and the red sides of the triangle, respectively, and likewise for Q^+ and Q^-. With the above modifications, the discontinuous shape functions take the following values at the nodes:

$$
\begin{aligned}
&N^A(A) = 1, && N^B(A) = 0, && N^C(A) = 0,\\
&N^A(B) = 0, && N^B(B) = 1, && N^C(B) = 0,\\
&N^A(C) = 0, && N^B(C) = 0, && N^C(C) = 1,\\
&N^A(P^+) = 1, && N^B(P^+) = 0, && N^C(P^+) = 0,\\
&N^A(P^-) = 0, && N^B(P^-) = 1, && N^C(P^-) = 0,
\end{aligned}
$$

$$N^A(Q^+) = 1, \qquad N^B(Q^+) = 0, \qquad N^C(Q^+) = 0,$$
$$N^A(Q^-) = 0, \qquad N^B(Q^-) = 0, \qquad N^C(Q^-) = 1.$$

It is important to remark that these discontinuous shape functions fulfill important properties:

- They form a nodal basis, their values are one at their respective nodes and zero at the other nodes.
- Their sum equals a constant function equal to one along the element.
- Their extreme values are one and zero, and take place at the nodes.

It is worth mentioning that derivatives are zero in certain parts of the element, as the shape functions remain constant on sides where the cut leaves only one node. This fact leads to an expected convergence rate of $\mathcal{O}\left(h^{3/2}\right)$ [195].

[195]: Ausas et al. (2010), *An improved finite element space for discontinuous pressures*

5.7.2 Code implementation

Utilizing the fact that discontinuous shape functions operate locally, a systematic procedure is implemented to modify the regular shape function arrays $[N_{shape}]$ when needed. The concept is to acquire the shape functions of each sub-element by creating two modifier arrays whose values depend on: (i) the side where the sub-element is located, and (ii) which edge has been intersected in the original element. To achieve this, the shape functions are organized as an array, storing values at each integration point in columns.

Let us consider the triangle numeration depicted in Fig. 5.5, where edge nodes n_4, n_5 and n_6 are created at the intersection points if the corresponding edge is intersected, or at its midpoint if it is not intersected.

The positive (M^+) and negative (M^-) modifier arrays are rectangular arrays whose number of columns is equal to the number of shape functions, and a number of rows equal to the sum of the number of original nodes and edge nodes. For the present example the cut goes through nodes n_5 and n_6, called *active edge nodes*, creating the sub-element $n_3n_6n_5$ in the positive side and the sub-elements $n_1n_2n_6$ and $n_2n_5n_6$ in the negative side.

The modifier arrays are constructed as follows:

1. Initialize M^+ and M^- to 0.
2. For each column: set to 1 the row of the corresponding to the shape function. In this case N^3 is the only shape function active in the positive (green) side, whereas N^1 and N^2 are active in the negative (red) side. Therefore:

$$[M^+] = \begin{array}{c} \begin{matrix} N^1 & N^2 & N^3 \end{matrix} \\ \begin{bmatrix} 0 & 0 & 0 \\ 0 & 0 & 0 \\ 0 & 0 & 1 \\ 0 & 0 & 0 \\ 0 & 0 & 0 \\ 0 & 0 & 0 \end{bmatrix} \end{array} \begin{matrix} n_1 \\ n_2 \\ n_3 \\ n_4 \\ n_5 \\ n_6 \end{matrix} \quad ; \quad [M^-] = \begin{array}{c} \begin{matrix} N^1 & N^2 & N^3 \end{matrix} \\ \begin{bmatrix} 1 & 0 & 0 \\ 0 & 1 & 0 \\ 0 & 0 & 0 \\ 0 & 0 & 0 \\ 0 & 0 & 0 \\ 0 & 0 & 0 \end{bmatrix} \end{array} \begin{matrix} n_1 \\ n_2 \\ n_3 \\ n_4 \\ n_5 \\ n_6 \end{matrix}$$

3. For each column: set to 1 the rows of active edge nodes that are adjacent to the node corresponding to the shape function. In this case, the active nodes n_5 and n_6. In the positive (green) side, both of them are adjacent to n_3, whereas in the negative side (red), n_5 is adjacent to n_2 and n_6 is adjacent to n_1. Therefore:

$$[M^+] = \begin{array}{c} \begin{matrix} N^1 & N^2 & N^3 \end{matrix} \\ \begin{bmatrix} 0 & 0 & 0 \\ 0 & 0 & 0 \\ 0 & 0 & 1 \\ 0 & 0 & 0 \\ 0 & 0 & 1 \\ 0 & 0 & 1 \end{bmatrix} \end{array} \begin{matrix} n_1 \\ n_2 \\ n_3 \\ n_4 \\ n_5 \\ n_6 \end{matrix} \quad ; \quad [M^-] = \begin{array}{c} \begin{matrix} N^1 & N^2 & N^3 \end{matrix} \\ \begin{bmatrix} 1 & 0 & 0 \\ 0 & 1 & 0 \\ 0 & 0 & 0 \\ 0 & 0 & 0 \\ 0 & 1 & 0 \\ 1 & 0 & 0 \end{bmatrix} \end{array} \begin{matrix} n_1 \\ n_2 \\ n_3 \\ n_4 \\ n_5 \\ n_6 \end{matrix}$$

4. For every sub-element with a set of local nodes $[n_{local}]$, multiply the rows of the modifiers corresponding to $[n_{local}]$ with the regular shape function arrays. This gives the positive (green) and negative (red) discontinuous shape functions arrays:

$$[N^+] = [M^+]^T_{[n_{local}]}[N_{shape}]$$
$$[N^-] = [M^-]^T_{[n_{local}]}[N_{shape}]$$

These arrays contain the values of the discontinuous shape functions at the nodes of a sub-element, including the edge nodes. This procedure is applicable to tetrahedral elements as well, the only difference being the size of the modifier arrays. For example, consider the case of a tetrahedral elements being cut as depicted in Fig. 5.5; the modified arrays are:

$$[M^+] = \begin{array}{c} \begin{matrix} N^1 & N^2 & N^3 & N^4 \end{matrix} \\ \begin{bmatrix} 0 & 0 & 0 & 0 \\ 0 & 0 & 0 & 0 \\ 0 & 0 & 0 & 0 \\ 0 & 0 & 0 & 1 \\ 0 & 0 & 0 & 0 \\ 0 & 0 & 0 & 0 \\ 0 & 0 & 0 & 1 \\ 0 & 0 & 0 & 0 \\ 0 & 0 & 0 & 1 \\ 0 & 0 & 0 & 1 \end{bmatrix} \end{array} \begin{matrix} n_1 \\ n_2 \\ n_3 \\ n_4 \\ n_5 \\ n_6 \\ n_7 \\ n_8 \\ n_9 \\ n_{10} \end{matrix} \quad ; \quad [M^-] = \begin{array}{c} \begin{matrix} N^1 & N^2 & N^3 & N^4 \end{matrix} \\ \begin{bmatrix} 1 & 0 & 0 & 0 \\ 0 & 1 & 0 & 0 \\ 0 & 0 & 1 & 0 \\ 0 & 0 & 0 & 0 \\ 0 & 0 & 0 & 0 \\ 0 & 0 & 0 & 0 \\ 1 & 0 & 0 & 0 \\ 0 & 0 & 0 & 0 \\ 0 & 1 & 0 & 0 \\ 0 & 0 & 1 & 0 \end{bmatrix} \end{array} \begin{matrix} n_1 \\ n_2 \\ n_3 \\ n_4 \\ n_5 \\ n_6 \\ n_7 \\ n_8 \\ n_9 \\ n_{10} \end{matrix}$$

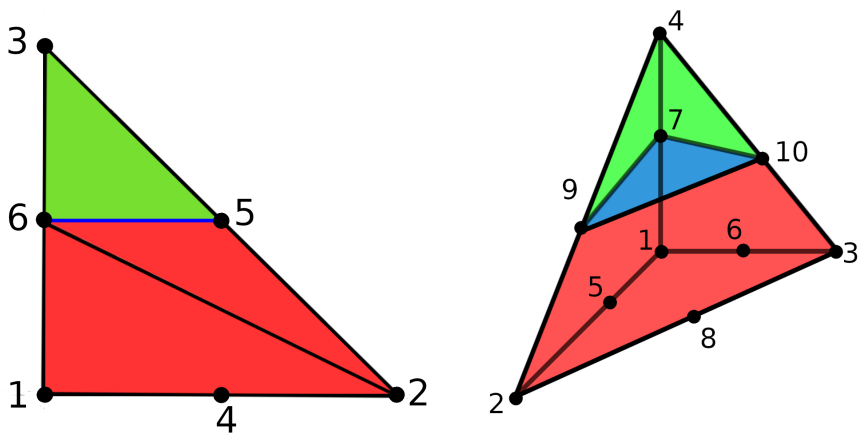

Figure 5.5: Triangular (a) and tetrahedral (b) element numerations of regular nodes and edge nodes. Active edge nodes are connected by a blue line or surface.

5.8 Fluid-Structure interaction

5.8.1 Transmission conditions

The FSI problem addressed in this study employs a partitioned scheme, where the fluid and the solid are solved independently and coupled at the embedded interface. The solid domain is embedded within the fluid domain with non-matching interfaces. It is crucial to note that, from the fluid's perspective, the embedded interface is perceived as a surface in 3D and, by extension, as a line in 2D cases. In the construction of the solid domain, as detailed in Section 5.3, we use a volumeless surface of the solid domain Ω_s^{2D} as a reference to extrude a volumetric body for the solid-shell. For the transmission conditions, the same volumeless surface as the embedding interface is used. Therefore, the coupling interface is defined as $\Gamma_{cut}(t) = \Omega_f(t) \bigcap \Omega_s^{2D}(t)$, where the Dirichlet-Neumann coupling conditions must be satisfied. The fluid is solved considering the position, displacement, and velocity of the solid-shell mid-surface, while the tractions acting on the solid are computed from the fluid. This is achieved through a block-iterative scheme, where the solid and the fluid are sequentially solved with strong coupling.

The coupling consists of kinematic and dynamic conditions to be fulfilled. Firstly, the kinematic transmission of no-slip wall condition is:

$$\mathbf{u}_f = \frac{\partial \mathbf{u}_s}{\partial t} \quad \text{on } \Gamma_{cut}(t), \tag{5.46}$$

which ensures the continuity of the velocity in $\Omega_f(t)$ across $\Gamma_{cut}(t)$. In other words, the fluid adjacent to the interface conducts the same movement as the solid. Secondly, the dynamic boundary condition of the equilibrium of surface tractions along the interface is:

$$\mathbf{n}_f \cdot \boldsymbol{\sigma}_f = \mathbf{n}_s \cdot \boldsymbol{\sigma}_s \qquad \text{on } \Gamma_{cut}(t). \tag{5.47}$$

A crucial aspect of our approach is that the coupling interface corresponds to the mid-surface of the solid-shell. By using this approximation, the process of transferring the shell velocity to the fluid is trivial because it only requires to pass the shell's mid-surface velocity. However, tractions require an special treatment due to the discontinuity of pressures and the limitations of the discontinuous shape functions. Firstly,

as has already been explained in Section 5.7, due to the construction process of the discontinuous shape functions, its derivatives can be zero in one of the sides of the element. In fact, in the case of triangular elements there is always a zero-derivative in one of the sides. Consequently, computing the fluid tractions as $\mathbf{t}_f = \mathbf{n}_f \cdot \left(-p\mathbf{I} + 2\mu_f \nabla^s \mathbf{u}_f\right)$ is not consistent because the velocity gradient cannot be captured at both sides of the embedded interface at the same time. For this reason, the approximation is performed by using only the pressure as

$$\mathbf{t}_f = -\mathbf{n}_f p_f \qquad \text{on } \Gamma_{cut}(t). \tag{5.48}$$

Note that this limitation can be overcome by using enriched spaces for shape function derivatives in cut elements, as the one introduced in [196]. Likewise, velocity non-conformity can be dealt with using classical discontinuous Galerkin (DG) techniques (see below). Secondly, tractions have to be integrated independently at both sides of the embedded interface because they are physically independent of each other, and that is exactly what the discontinuous shape functions are trying to convey. Lastly, the traction integration is only performed at the mid-surface's normal direction and not in its transverse direction, as would occur at one of the ends of a cantilever bar. This approximation is justified because the effect of tractions in the transverse direction of the shell should be small for thin structures. However, as shown below in Section 5.10, the consequences of not including this contribution becomes apparent when the embedded structure is relatively thick.

[196]: Coppola-Owen et al. (2005), *Improving Eulerian two-phase flow finite element approximation with discontinuous gradient pressure shape functions*

5.8.2 Weak imposition of velocities

To enforce the velocity transmission condition described in Eq. (5.46) on the fluid, several options are available. One option involves creating new nodes in the element cuts, requiting a local re-meshing of the fluid mesh. However, this approach requires the activation and deactivation of new nodes whenever the mesh cutting process is performed. The mesh cutting process is performed on every coupling iteration, which is very expensive from the computational standpoint. In this work, the chosen option involves the use of discontinuous shape functions configured at element level, which allows the use of the same degrees of freedom already present in

the fluid element. Considering that the discontinuous shape functions already take into account the embedded interface, the prescription of weak Dirichlet boundary conditions can be easily imposed by means of Nitsche's method.

Let E^h_{cut} be the edges of $\mathscr{P}^f_h$ created by the intersections of Γ_{cut}, there is a contribution of boundary terms that appear when the differential equations are integrated by parts that vanish on regular boundaries. However, test functions $\mathbf{v}_{f,h}$ do not vanish in E_{cut} and must be considered. Nitsche's method consists in adding to the discrete variational form of the problem in Eq. (5.45) the following terms:

Nitsche's method for weak imposition of velocities

$$\sum_{E_{cut}} \left\langle \mathbf{v}_{f,h} \,,\, p_{f,h}\mathbf{n}_f - 2\mu_f \mathbf{n}_f \cdot \nabla^s \mathbf{u}_{f,h} \right\rangle + \sum_{E_{cut}} \left\langle -q_{f,h}\mathbf{n}_f - 2\mu_f \mathbf{n}_f \cdot \nabla^s \mathbf{v}_{f,h} \,,\, \mathbf{u}_{f,h} - \dot{\mathbf{u}}_{s,h} \right\rangle + \sum_{E_{cut}} \frac{\mu_N}{h_E} \left\langle \mathbf{v}_{f,h} \,,\, \mathbf{u}_{f,h} - \dot{\mathbf{u}}_s \right\rangle, \tag{5.49}$$

where $\dot{\mathbf{u}}_s$ is the velocity of the solid in the coupling interface. In Eq.(5.49), the first term comes precisely from the integration by parts, the second term is the adjoint consistency term, and the third term is the stabilization term. The adjoint consistency term is designed according to [45, 197, 198]. The stabilization term penalizes the restriction given by the boundary condition in Eq. (5.46) and is scaled by the characteristic length h_E of E_{cut} and the algorithmic parameter μ_N, which has units of viscosity, defined as

$$\mu_N = \mu_f + \rho_f h_E |\bar{\mathbf{u}}_f|, \tag{5.50}$$

where $\bar{\mathbf{u}}_f$ is the maximum velocity of the fluid domain computed in the previous iteration.

It is crucial to emphasize that integrating Nitsche's terms on both sides of the embedded interface is essential because the modified shape functions render them entirely independent of each other. Therefore, the interface where weak boundary conditions are imposed actually consists of two distinct decoupled overlapping interfaces.

In the present embedded approach, there are pressure discontinuities due to the embedded interface dividing the fluid domain, which are captured by using discontinuous shape

[45]: Codina et al. (2009), *Subscales on the element boundaries in the variational two-scale finite element method*
[197]: Codina et al. (2013), *On the design of discontinuous Galerkin methods for elliptic problems based on hybrid formulations*
[198]: Badia et al. (2014), *Error analysis of discontinuous Galerkin methods for the Stokes problem under minimal regularity*

functions in the elements cut by the interface. Furthermore, the velocity field is approximated by these functions in the cut elements, even if the velocity field is continuous. This approach opens up the possibility to impose other boundary conditions where the velocity field is not completely continuous, such as slip wall or wall law, where only the normal component of the velocity is continuous [199]. This approach is useful because by having locally segregated velocities allows to avoid the instabilities associated to badly cut elements. However, the use of these functions in the velocity field, whose space is a subspace $H^1\left(\Omega_f\right)^d$, makes the formulation to be non-conforming. The way to deal with this non-conformity is the same as in DG techniques. The classical symmetric interior penalty method amounts to add a term similar to (5.49) but summing for all edges (faces, in 3D) of elements in which the discontinuous interpolation has been used, and replacing $\mathbf{u}_{f,h} - \dot{\mathbf{u}}_s$ by the jump in velocities and the flux operators by the mean of the flux operators between adjacent elements [197]. However, being the non-conformity restricted to the band of elements crossed by the solid, we have numerically verified that it is not necessary to introduce the terms described.

[199]: Zorrilla et al. (2019), *A modified finite element formulation for the imposition of the slip boundary condition over embedded volumeless geometries*

[197]: Codina et al. (2013), *On the design of discontinuous Galerkin methods for elliptic problems based on hybrid formulations*

5.8.3 Coupling strategy

Strongly coupled strategies require to ensure the convergence of the transmission conditions. This is typically achieved through Newton-Raphson iterative procedures known for their efficiency [200]. However, in this work, an Aitken relaxation scheme is implemented for simplicity, although it can be extended to more efficient methods [201]. Within each time step, this approach allows the application of dynamic relaxation to transmission conditions in each coupling iteration, thereby enhancing the convergence rate. The Aitken relaxation procedure computes an optimal relaxation parameter ω_{i+1} for each iteration $i+1$, such that coupling displacements are:

$$\mathbf{u}_{s,h}^{i+1} \leftarrow (1-\omega_{i+1})\mathbf{u}_{s,h}^{i+1} + \omega_{i+1}\mathbf{u}_{s,h}^{i}, \tag{5.51}$$

where ω_{i+1} is computed as follows:

[200]: Zorrilla et al. (2020), *An embedded Finite Element framework for the resolution of strongly coupled Fluid–Structure Interaction problems. Application to volumetric and membrane-like structures*

[201]: Delaissé et al. (2023), *Quasi-Newton Methods for Partitioned Simulation of Fluid–Structure Interaction Reviewed in the Generalized Broyden Framework*

1. At the beginning of a time step, set the initial relaxation parameter ω_0 and initialize Aitken's factor γ_i:
   $\omega_i = \omega_0$.
   $\gamma_i = 0$.
2. Compute the difference between the actual and previous iteration solutions:
   $\Delta \mathbf{u}_{s,h}^{i+1} = \mathbf{u}_{s,h}^{i+1} - \mathbf{u}_{s,h}^{i}$.
3. Compute Aitken's factor:
   $\gamma_{i+1} = \gamma_i + (\gamma_i - 1)\frac{\left(\Delta \mathbf{u}_{s,h}^{i} - \Delta \mathbf{u}_{s,h}^{i+1}\right)^T \Delta \mathbf{u}_{s,h}^{i+1}}{\left|\Delta \mathbf{u}_{s,h}^{i} - \Delta \mathbf{u}_{s,h}^{i+1}\right|^2}$.
4. Compute Aitken's optimal relaxation parameter:
   $\omega_{i+1} = 1 - \gamma_{i+1}$.
5. Update the iteration counter and all the arrays that depend on the iteration.

After the coupling strategy is performed, it is imperative to compute the coupling velocities based on the relaxed displacements. This approach enables the fluid to update the solution of a time step in a staggered manner, mitigating pressure spikes resulting from the movement of the embedding interface.

5.9 Discontinuous level-set calculation

The embedded FSI approach employed in this study utilizes the solid mesh to establish a discontinuous level-set interface embedded within the fluid mesh. Consequently, it becomes necessary to determine which fluid elements are intersected and the location of these intersection points. In this section, a brief overview of the process of selecting and cutting elements is provided. This is a generic procedure applicable not only to the FSI problem discussed in this work but also to other physical problems. When referring to meshes and elements, the terms 'background' for the fluid and 'foreground' for the solid are used for solid and fluid, respectively. The entire process is divided into two parts: (i) identifying candidates to check for intersections and (ii) performing intersection checks and determining the cut locations.

5.9.1 Element selection tool: octree and quadtree based search

Efficiently cutting background elements using foreground elements requires minimizing the number of intersection checks. To achieve this, octree and quadtree data structures are employed in 3D and 2D cases, respectively. In both instances, these structures are referred to as 'tree' as the same concepts apply to both 2D and 3D cases.

The tree structure works as follows:

1. Create the tree structure containing:
   - Tree coordinate bounding box that defines the space it occupies.
   - List of foreground elements that belong to the tree.
   - List of background elements that belong to the tree.
   - Children objects that have the same structure as the parent tree, recursively.
2. Create initial bounding boxes:
   - Compute the tree bounding box by comparing the maximum and minimum coordinates of all the listed foreground elements.
   - Compute the bounding box of all background and foreground elements based on their coordinates.
3. Store initial element information:
   - If a foreground element bounding box intersects with the initial tree bounding box: add it to the initial tree foreground element list. Note that due to the nature of this structure, all foreground elements will be stored.
   - If a background element bounding box intersects with the initial tree bounding box: add it to the initial tree background element list.
4. Create children trees: the bounding box is divided by half in all dimensions, each new bounding box will define the location of a child tree (4 children in quadtree and 8 children in octree).
5. Loop on child trees:
   - Check the tree bounding box range of all listed foreground elements; if they intersect: move it from the parent tree to the current child tree list of foreground elements.

- Check the tree bounding box range of all listed background elements; if they intersect: move it from the parent tree to the current child tree list of background elements.
- If the threshold of the number of foreground element is met: repeat from item 4.

The result is a tree structure, as depicted in Fig. 5.6 in a 2D case. In this illustration, the stored foreground elements are blue, while the stored background elements are represented in various shades of orange, where lighter colors correspond to higher-order tree children. Note that there are background elements that belong to more than a single order tree and they are colored with intermediate colors.

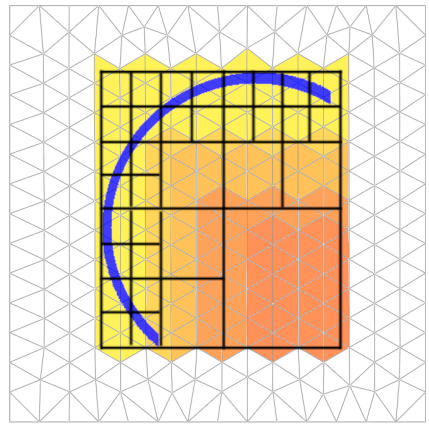

Figure 5.6: Quadtree stored elements based on foreground elements (blue). Stored background elements (orange scale) with lighter colors correspond to higher order tree child.

It is crucial to establish thresholds for both the maximum number of elements a list can store to ensure the creation of new tree children, thereby enhancing the resolution of the mapping.

5.9.2 Element intersection algorithm

Once the initial tree data structure is established, identifying candidates for intersection checks becomes straightforward. It involves looping over all the tree children containing at least one element in the foreground element list. This approach significantly reduces the number of candidates to test for intersections compared to the initial selection. The procedure is simple and capitalizes on the tree structure used for selecting background candidates. As depicted in the flowchart in Fig. 5.7, the first part consists in finding the candidates for performing the intersection check.

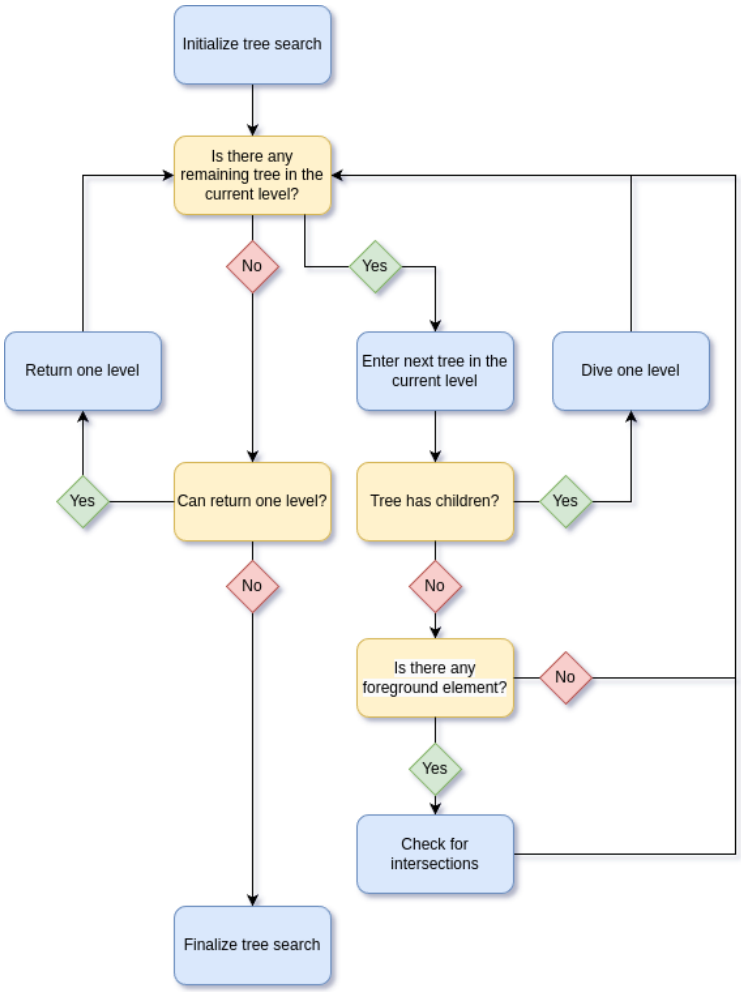

Figure 5.7: Element search algorithm flowchart: using tree structure to test element intersection candidates.

A visual representation of the final selection is illustrated in Fig. 5.8, where the intersection candidates are highlighted in green. This approach significantly reduces the amount of testing by considering only the candidates rather than all the initially stored background elements. The significance of minimizing the number of operations performed to find the mesh intersection is crucial, particularly in time-dependent coupled computations that necessitate checking for intersections after every coupling iteration.

The intersections are determined by executing a ray-tracing

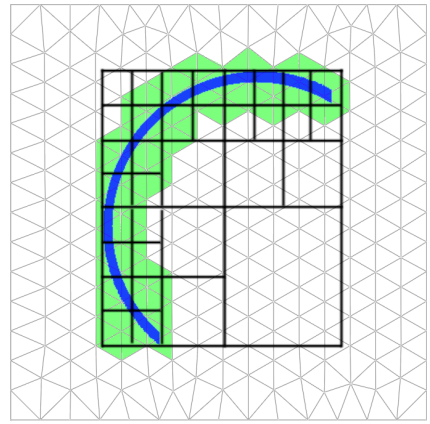

Figure 5.8: Quadtree selection of background element candidates (green) based on foreground elements (blue).

process, utilizing the background element edges as rays and the foreground elements as surfaces, as detailed in the flowchart in Fig. 5.9. It is essential to recognize that ray-tracing considers the ray to be indefinitely long, and the surface to be infinitely wide. Therefore, complementing the ray-tracing algorithm with a barycentric coordinate check of the intersection point on the surface of the foreground element becomes necessary. This check verifies whether the intersection point is contained in the edge of the background element.

In this manner, background element that are cut in two parts are obtained, as illustrated in Fig. 5.10, which are called *regular cuts*. However, it is possible that the embedded interface cuts a background element poorly, leaving one of the sides with zero volume or not completely defined. Those cases are referred to as *degenerated cuts*. There are several ways for this to happen, as portrayed in Fig. 5.11 for triangular elements and in Fig.5.12 for tetrahedral elements. Considering that elements connect to their neighboring elements at nodes, edges, and faces, a degenerated cut makes it impossible to determine which of the neighboring elements is cut. For this reason, it is necessary to establish a consistent procedure to handle degenerated cuts.

Several approaches can be employed to address degenerated cuts. In this work, this issue is solved by locally performing a slight translation of the interface along its normal direction. The translation distance is determined by a tolerance proportional to the element size. This procedure results in scenarios where, depending on the direction of the normal of the surface, the interface can be moved *inside* or *outside* of the element. This approach maintains consistency among neigh-

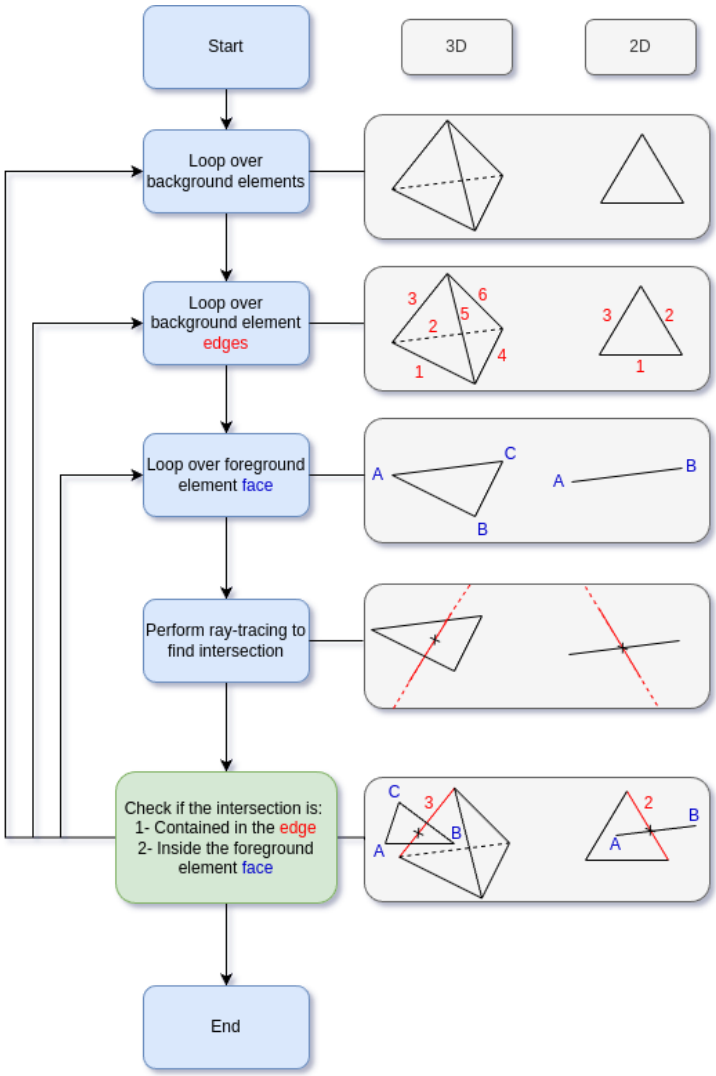

Figure 5.9: Element intersection flowchart. Intersections are found by a ray-tracing algorithm.

boring elements because the normal direction of the interface is independent of them. Therefore, if the interface is not captured by one element, it will be captured by its neighboring element. The underlying concept of this procedure is to assign a small volume to the side of the cut element that has zero volume. This allows for numerical integration during the FE approximation. Approaching the treatment of degenerated cuts in this manner is not a novelty, it has been tested

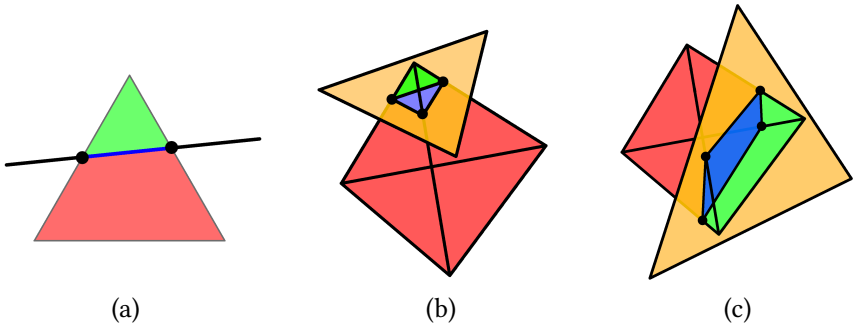

Figure 5.10: Regular cuts of triangles (a) and tetrahedra with 3 (b) and 4 (c) intersections.

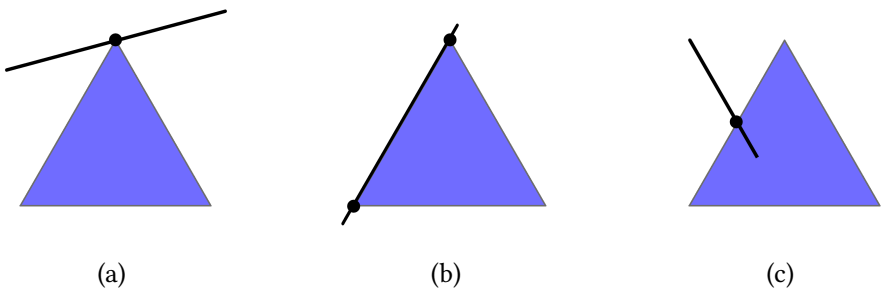

Figure 5.11: Degenerated triangle: (a) one intersection at a node, (b) edge overlapping cut, and (c) one intersection at one edge.

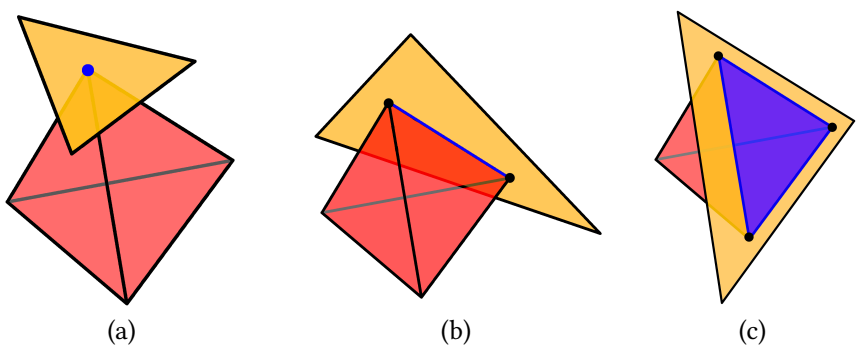

Figure 5.12: Degenerated tetrahedra cuts: (a) one intersection at a node, (b) edge overlapping cut, (c) face overlapping cut.

before in previous works [199, 200, 202], and has proved to not have a measurable effect the solution. The procedure is exemplified in Fig. 5.13 for triangular elements, which directly translates to tetrahedral elements. In this example, the direction of the outside correction is indicated by a red arrow, while the direction of the inside correction is depicted with a green arrow. It is important to note that there are instances where the interface cuts a background element edge without passing through the whole element. In such cases, a projection of the interface is considered to ensure the element is completely cut.

[199]: Zorrilla et al. (2019), *A modified finite element formulation for the imposition of the slip boundary condition over embedded volumeless geometries*
[200]: Zorrilla et al. (2020), *An embedded Finite Element framework for the resolution of strongly coupled Fluid–Structure Interaction problems. Application to volumetric and membrane-like structures*
[202]: Zorrilla et al. (2021), *A discontinuous Nitsche-based finite element formulation for the imposition of the Navier-slip condition over embedded volumeless geometries*

In certain cases, the interface is referred to as *over-defined*, indicating that it is defined with more points than necessary to define a plane. Specifically, this occurs when there are more than two intersection points in 2D or three in 3D. Such situations often occur in regular cuts of tetrahedral elements, as illustrated in the four-point intersection of Fig. 5.10. However, over-defined cuts can also occur when the size of the background mesh is not fine enough to accurately describe the interface. In such cases, the interface is approximated as the best-fitting plane of the intersection points using a least squares approximation. To accurately denote the position

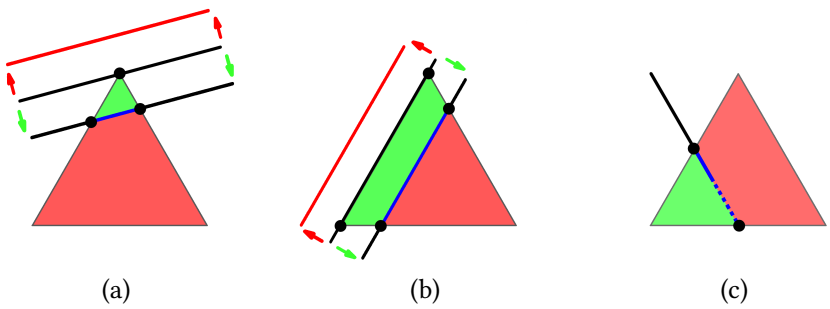

Figure 5.13: Degenerated triangle: inside and outside corrections for (a) one intersection at a node, (b) edge overlapping cut, and (c) inside projection correction.

of the embedded interface, the level set is computed as the perpendicular distance between the element nodes and the cut plane. This ensures that the embedded interface can be retrieved at each element as the zero iso-surface of the level-set field. Consequently, the level-set is locally stored for each cut element. This approach is justified by the fact that the interface may be locally over-defined or its position may need correction to account for degenerated intersections. In ei-

ther case, the level-set will exhibit discontinuities between elements.

5.10 Numerical results

In this section, the embedded FSI approach is applied to classical benchmark problems commonly used in the literature. The summarized ingredients described throughout the work include: (i) the use of a locking-free formulation of solid-shell elements based on a mixed displacement-PK2 stress stabilization for finite strains, (ii) capturing the discontinuities of the fluid domain using discontinuous shape functions, (iii) weak imposition of boundary conditions at cut elements through Nitsche's method, and (iv) coupling the fluid and solid domains using Dirichlet-Neumann transmission conditions. However, to address them properly, they are tested in a staggered manner of increasing difficulty. Initially, the embedding technique and the weak imposition of boundary conditions are tested by solving fluid dynamic problems with a rigid stationary solid in a one-way coupling fashion. Using this approach, the coupling interface transmits zero velocity to the fluid, while tractions are not transmitted to the solid. First a stationary problem is solved and then a time-dependent one. Following this, a fully coupled FSI problems is solved with a deformable solid and complete transmission conditions. Using the same methodology, a dynamic problem that converges to a stationary solution is solved first, subsequently followed by a dynamic problem that exhibits a periodic solution.

5.10.1 Elbow pipe with internal wall

The initial example involves a 90°-curved elbow pipe with an internal zero-thickness rigid wall embedded inside the fluid domain, dividing the flow into two independent ducts. The internal wall is positioned such that the upper duct maintains a constant cross-section, while the lower duct contracts by half after the curvature. This contraction induces an acceleration of the flow, maintaining a constant total flow rate. This problem was initially proposed by Idelsohn et al. [203] using a slip interface as internal wall. However, as summarized in Fig.5.14, here the no-slip interface version of the problem

[203]: Idelsohn et al. (2018), *Multifluid flows with weak and strong discontinuous interfaces using an elemental enriched space*

[202]: Zorrilla et al. (2021), *A discontinuous Nitsche-based finite element formulation for the imposition of the Navier-slip condition over embedded volumeless geometries*

portrayed in [202] is solved, which is later extended the to its 3D version.

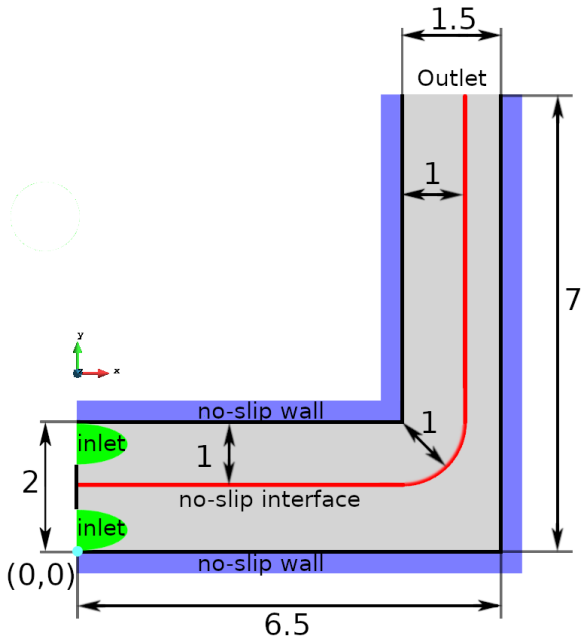

Figure 5.14: 2D and 3D elbow with internal wall: geometry and boundary conditions

The boundary conditions of the 2D case consist in no-slip conditions at the upper and lower walls, and the following velocities at the inlet:

$$u_x(y) = \begin{cases} u_x^{top}(y) & \text{if } 1.25 < y < 2 \\ 0 & \text{if } 0.75 < y < 1.25 \\ u_x^{bot}(y) & \text{if } 0 < y < 0.75 \end{cases} \tag{5.52}$$

where u_x^{top} and u_x^{bot} are the parabolic velocities for the upper and lower inlets, defined as

$$u_x^{top}(y) = -12.642y^2 + 41.0864y - 31.6049, \tag{5.53}$$

$$u_x^{bot}(y) = -12.642y^2 + 9.4812y. \tag{5.54}$$

Note that only 75% of the width of the channel is set as inlet so it is not influenced by the discontinuous interpolation at the interface. For the 3D extension, slip lateral walls are used, so the solution is equivalent to the 2D counterpart. The problem is solved for Re = 1 using meshes of 122k unstructured triangular elements and 164k structured tetrahedral elements in the 2D and 3D cases, respectively. Note that the 3D mesh is much coarser than the 2D counterpart because of its addi-

tional dimension. Results are illustrated in Figs. 5.15-5.16 for the 2D case and in Figs.5.17-5.18 for the 3D case.

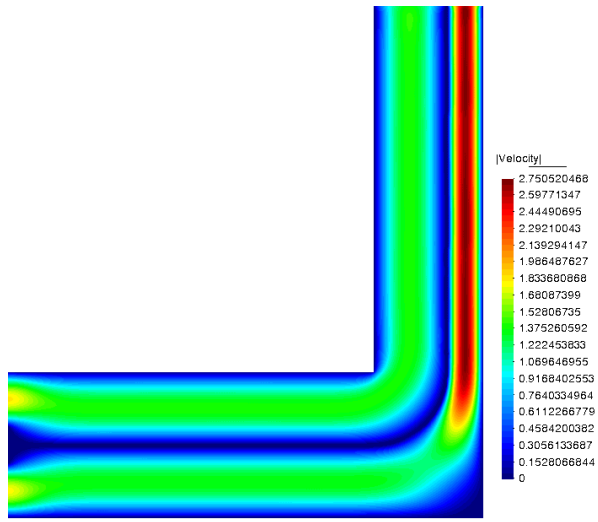

Figure 5.15: 2D elbow with internal wall: velocity magnitude.

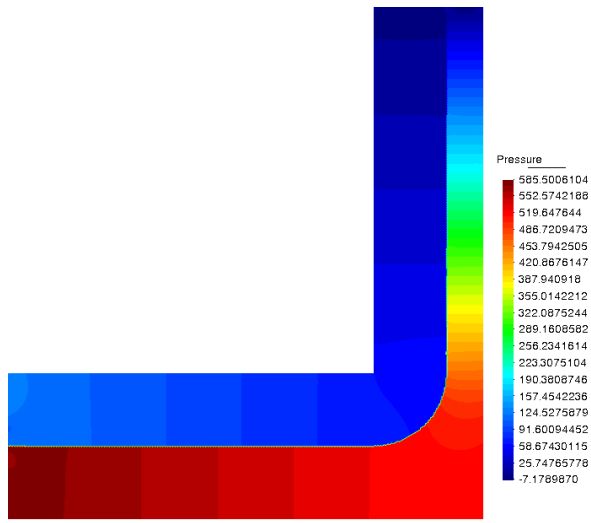

Figure 5.16: 2D elbow with internal wall: pressure.

The purpose of these examples is to illustrate how the pressure can be computed in a discontinuous manner through an interface. To show the the discontinuity, in Fig. 5.19-5.20 the pressure along a transverse line located near the outlet is plotted, between coordinates $(5, 6)$-$(6.5, 6)$, where the different pressures of each side of the duct can be clearly identified. The pressure jump in the 2D case is sharper when compared to the 3D case because of the better resolution provided by

the mesh. In order to make more comprehensive comparisons, the velocity profiles are plotted at the outlet. Results show good agreement between the 2D and 3D versions and with respect to the reference solutions shown in [202].

[202]: Zorrilla et al. (2021), *A discontinuous Nitsche-based finite element formulation for the imposition of the Navier-slip condition over embedded volumeless geometries*

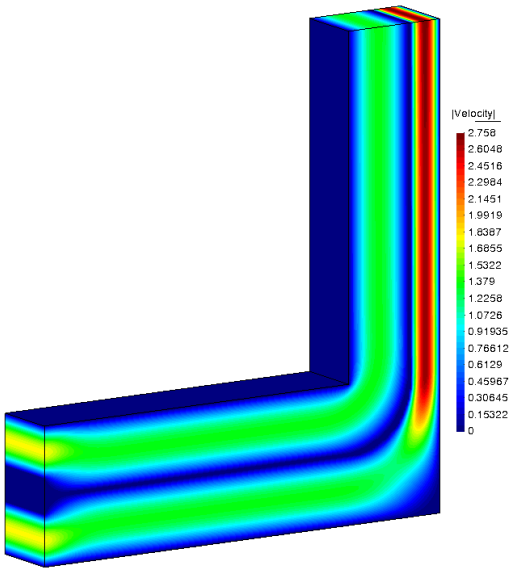

Figure 5.17: 3D elbow with internal wall: (a) velocity and (b) pressure.

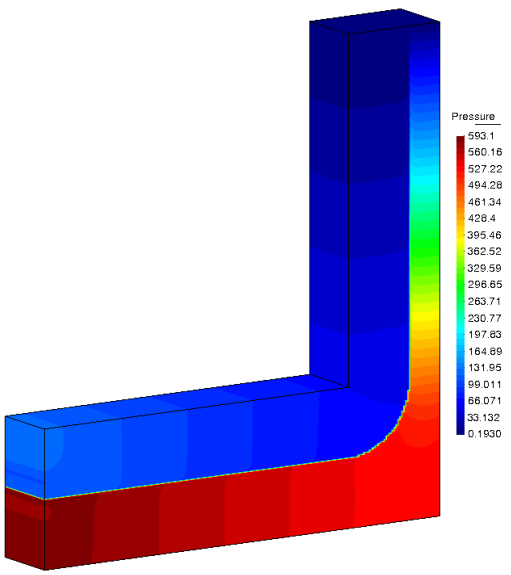

Figure 5.18: 3D elbow with internal wall: (a) velocity and (b) pressure.

An important aspect of the current embedded approach must be considered. Firstly, by weakly enforcing the velocity in

the cut elements using Nitsche's method, the kinematic constraint is transferred to the nodes through the intersected edges. Secondly, the discontinuous shape functions of Ausas et al. have zero derivatives on one side of the cut, making this element unable to properly capture velocity gradients. Consequently, when enforcing a zero velocity constraint, as in this case, the condition is applied to the entire element, resulting in an artificial shrinkage of the duct [200]. A possible remedy is to use regular shape functions for the velocity space, though it comes with the hurdle of dealing with ill-conditioned elements when they are poorly cut. Nevertheless, the embedded approach is expected to converge to the solution obtained with a body-fitted approach with mesh refinement. Recall also the DG-like terms could be added, but we have found them unnecessary.

[200]: Zorrilla et al. (2020), *An embedded Finite Element framework for the resolution of strongly coupled Fluid–Structure Interaction problems. Application to volumetric and membrane-like structures*

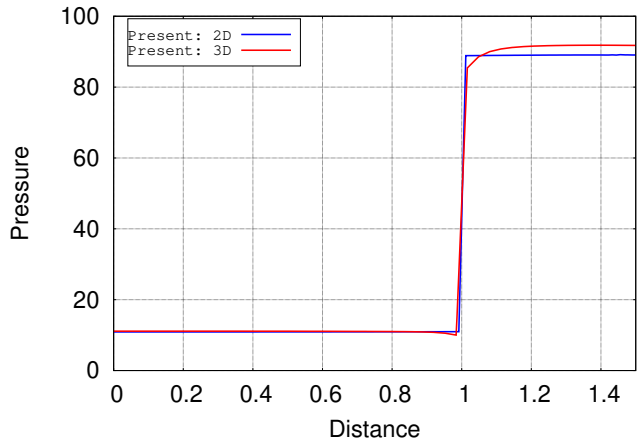

Figure 5.19: Elbow pipe with internal wall: 2D and 3D elbow pressure through the coordinates (5, 6)-(6.5, 6).

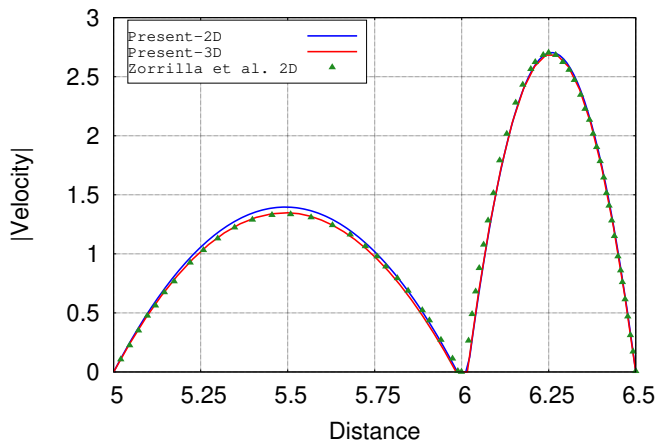

Figure 5.20: Elbow pipe with internal wall: 2D and 3D elbow velocity magnitude at the outlet. References: Zorrilla et al. [202]

5.10.2 Flow over a cylinder

The second example consists in the classical benchmark problem of flow over a cylinder. The setup and boundary conditions are detailed in Fig. 5.21. Regarding boundary conditions, the characteristic length is set to $D = 1$, the inlet is configured with a constant velocity profile, and the upper and lower walls are set with a slip boundary condition. The cylinder is modeled as a rigid solid embedded inside the fluid domain. For comparison purposes, the problem is also solved using the standard approach where the cylinder boundary matches the mesh. The domains consist of 75k and 65k unstructured triangular elements for the embedded and standard approaches, respectively. Although the mesh is similar in both approaches, with smaller elements around the cylinder area, the embedded case mesh has more elements to compensate for those located inside the cylinder.

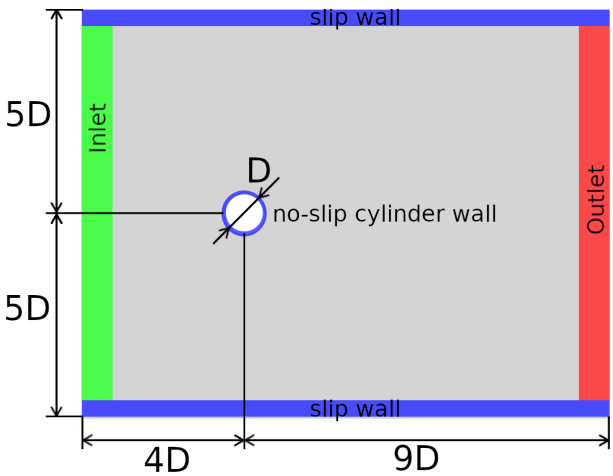

Figure 5.21: Flow over a cylinder: geometry and boundary conditions.

This benchmark problem is widely known for having a stationary solution for low Reynolds numbers; however, the solution encounters a bifurcation when it is increased near $Re = 40$, where the flow starts an oscillatory behavior. The problem is solved for a time step of $\delta t = 0.01$ in both cases, which is enough to properly capture the oscillations. Pressure and velocity contours for $Re = 70$ are illustrated in Fig. 5.22-5.23 to portray the oscillating flow. A zoom view around the cylinder is also presented to show how the elements are cut. The cuts are not sharp because the sub-elements created by the cut interface are not post-processed; therefore, it is limited

to show a gradient generated by the nodal values of the elements.

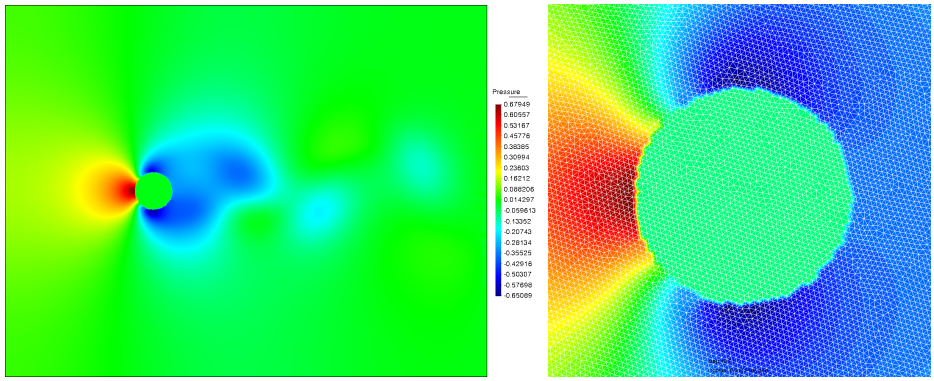

Figure 5.22: Flow over a cylinder: pressure for $Re = 70$, complete view and zoom view.

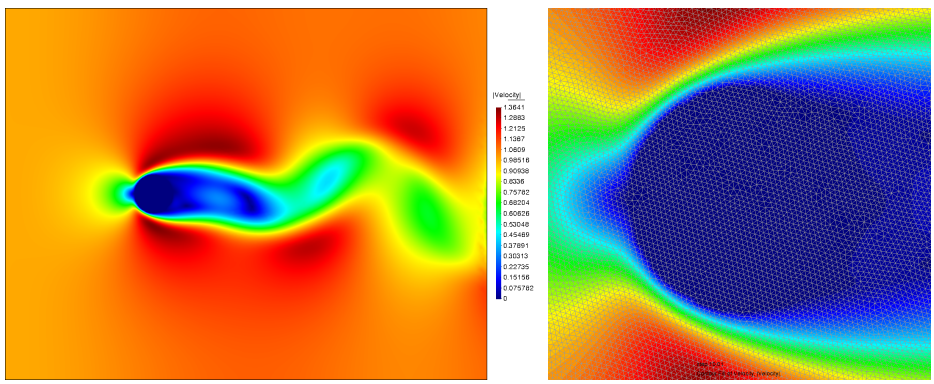

Figure 5.23: Flow over a cylinder: velocity magnitude for $Re = 70$, complete view and zoom view.

In order to make a more comprehensive assessment of the embedded approach performance, cases are solved for increasing Reynolds numbers and compared with the standard approach. The time evolution for pressures and velocities are summarized in Fig. 5.24 for $Re = 30, 40, 50, 60, 70, 80$ at a point of coordinates $(2, 0)$. The same range of values are purposely used in every type of plot to illustrate the increment of amplitude of the oscillation as the Reynolds number increases. From the results displayed for $Re = 30, 40$, it can be seen that using the embedded approach the instability is triggered at a slightly lower Reynolds number. However, by looking at the oscillations of the more convective cases, it becomes clear

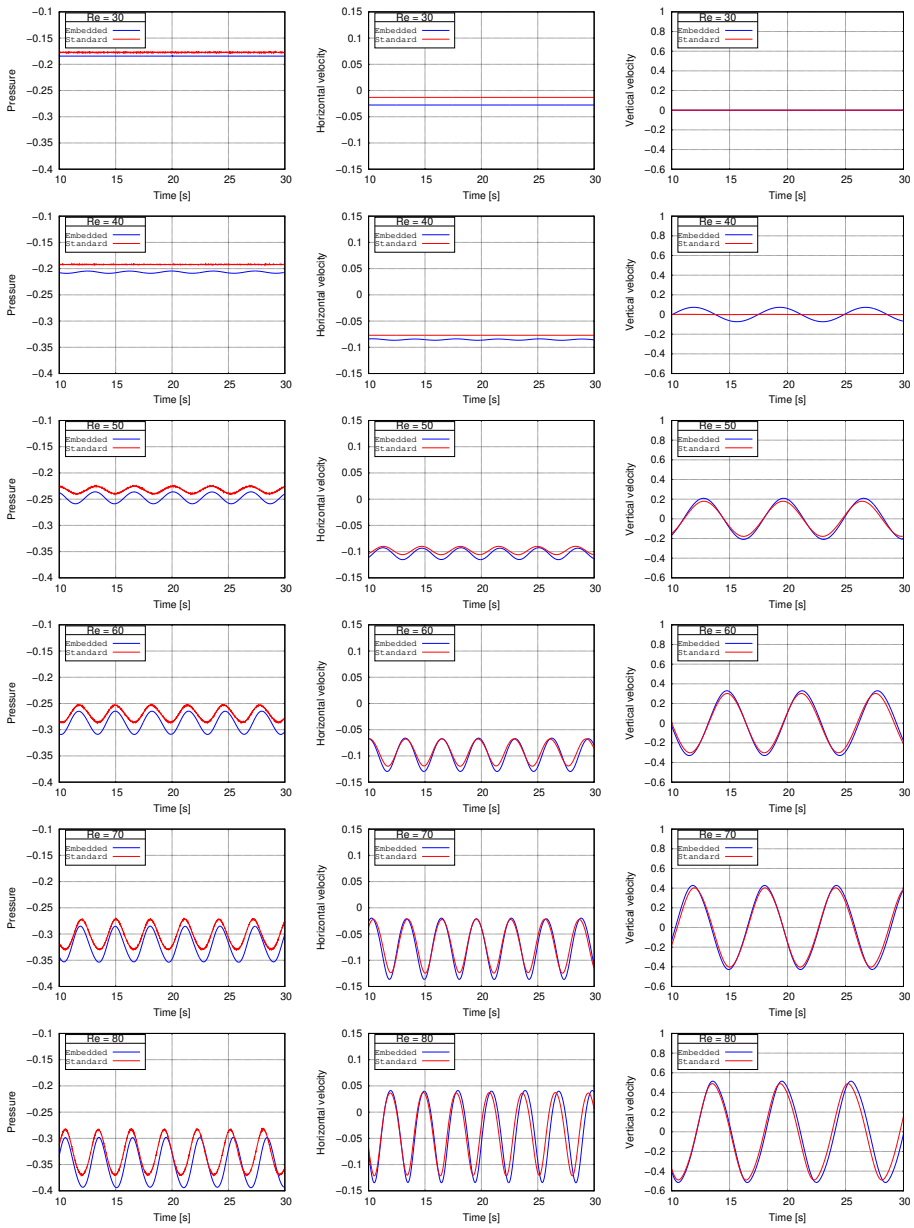

Figure 5.24: Flow over a cylinder: pressure, horizontal and vertical velocity for $Re = 30, 40, 50, 60, 70, 80$.

that the current approach is able to capture the dynamics of the problem accurately.

5.10.3 Vertical plate in a fluid tunnel

The third example consists in a fluid flowing through a tunnel with a vertical hyperelastic plate partially blocking the flow. The solid is increasingly deformed by the fluid during the initial transient until it reaches a stationary solution. This case has been previously studied by Zhang et al. [204] and Hang et al. [205] in 2D and 3D environments, respectively. The geometry and boundary conditions are summarized in Fig. 5.25. For the present example, the reference values of $H = 1$, $L = 1$, $b = 0.8$ and the plate thickness $t_p = 0.04$ are used. The geometry is extended to 3D using a width of 0.5 for the tunnel and the plate.

[204]: Zhang et al. (2012), *Immersed smoothed finite element method for two dimensional fluid–structure interaction problems*

[205]: Han et al. (2021), *ELL for 3D FSI problems with thin flexible structures based on the continuum-based shell element*

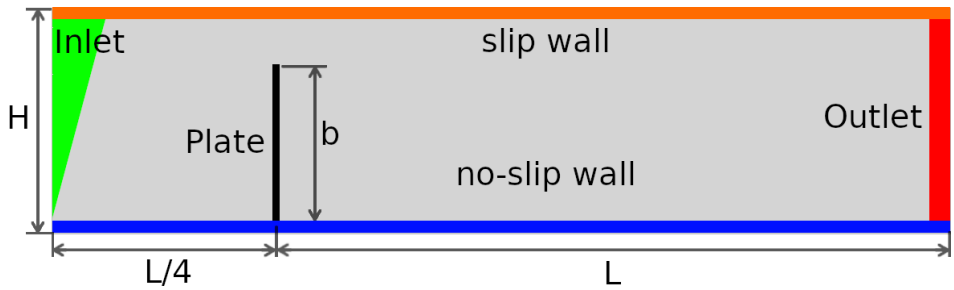

Figure 5.25: 2D Vertical plate in a fluid tunnel - Geometry and boundary conditions.

The fluid domain boundary conditions consist in slip and no-slip walls for the top and bottom walls, respectively. The inlet velocity is set as a parabolic profile that increases along the y-axis using the following function:

$$u_f(0,y,0,t) = \begin{cases} \hat{u}_f(0,y,0)\frac{1-\cos\left(\frac{\pi}{2}t\right)}{2} & \text{if } t < t_{init} \\ \hat{u}_f(0,y,0) & \text{otherwise} \end{cases} \quad ; \quad \hat{u}_f(0,y,0) = 1.5\left(-y^2+2y\right),$$

considering the bottom left corner of the domain as the origin of the Cartesian coordinate system. Note that in order to have a smoother initial transient, a cosine time function is used to slowly increase the inlet velocity to reach its maximum using $t_{init} = 0.1$ for the 2D case and $t_{init} = 0.5$ for the 3D case. For the 3D extension of the problem, no-slip boundary conditions are used at the lateral walls of the tunnel. The problem is solved using a time step of $\delta t = 0.01$ in

both cases. The domain of the 2D case is meshed with 35k linear triangular elements in the fluid and 300 line elements on the solid, which are extruded to 600 bilinear quadrilateral elements. Similarly, the domain of the 3D case is meshed with 235k linear tetrahedral elements in the fluid and 200 triangular elements on the solid, which are extruded to 1k linear prismatic elements. The solid boundary conditions consist in simply fixing the lower end of the plate, and fixing the plate displacements in the z-axis direction for the 3D case. The Dirichlet transmission conditions are set on the fluid by imposing the solid velocity on the elements cut by the interface, while the Neumann transmission conditions are set by imposing the fluid tractions on the whole plate. The properties of the fluid are $\rho_f = 1$ and $\mu_f = 0.1$, whereas the solid is configured as a compressible Neo-Hookean material with $\rho = 7.8$, $E = 10^5$ and $\nu = 0.3$.

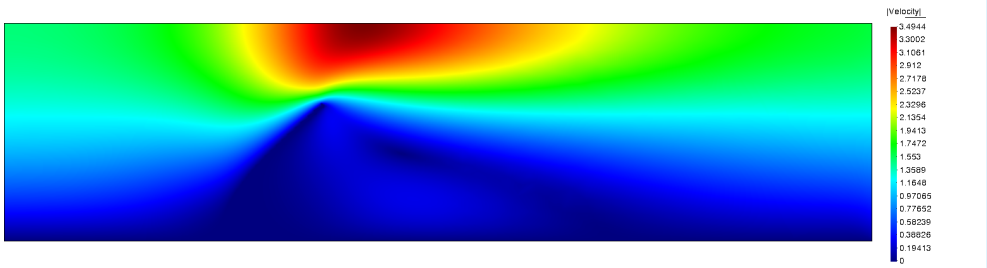

Figure 5.26: 2D Vertical plate in a fluid tunnel - Stationary velocity magnitude.

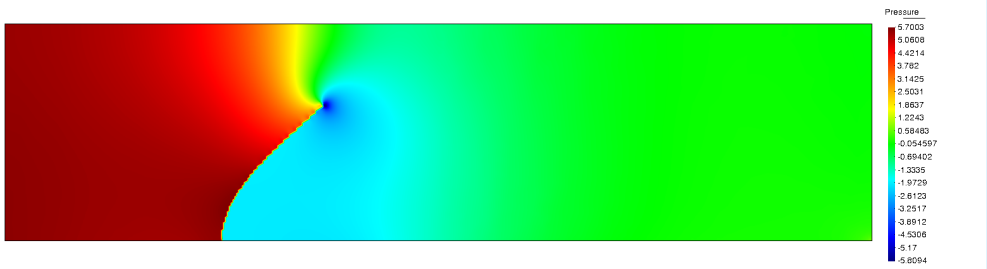

Figure 5.27: 2D Vertical plate in a fluid tunnel - Stationary pressure.

The fluid velocity and pressure fields are displayed in Figs.5.26-5.27 for the 2D case, and in Figs.5.28-5.29 for the 3D case. For the solid domain, the vertical and horizontal displacement of the plate at its upper end is followed, as shown in Fig. 5.32 for

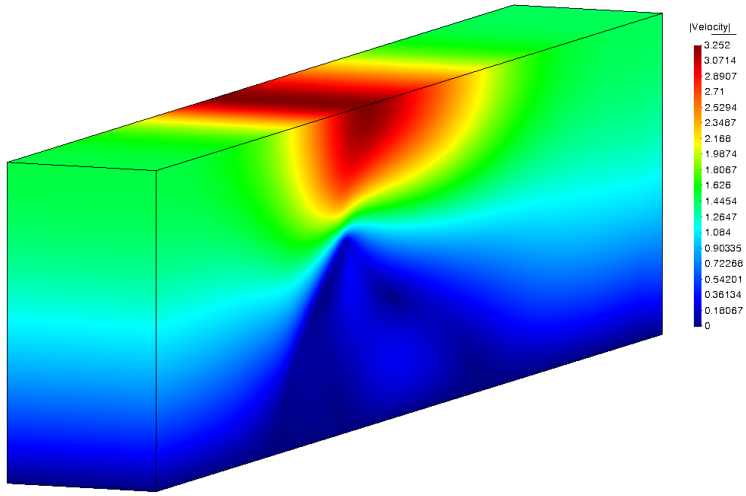

Figure 5.28: 3D Vertical plate in a fluid tunnel - Stationary velocity magnitude.

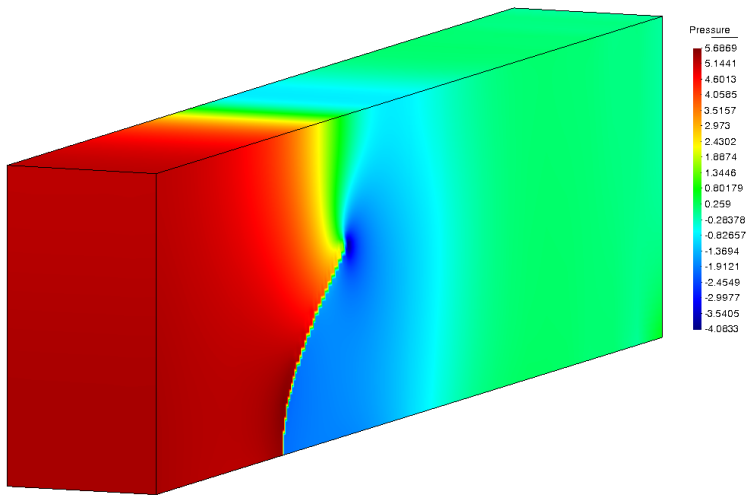

Figure 5.29: 3D Vertical plate in a fluid tunnel - Stationary pressure.

the 2D and 3D cases. Considering that our shell formulation follows a mixed approach that uses displacements and the PK2 stress as unknowns, they are shown at the converged configuration in Figs. 5.30-5.31. Although there is no data to compare the displacements in the y-axis, there are some authors that have reported them in the x-axis [204–206]. Due to the different time functions used in the initial

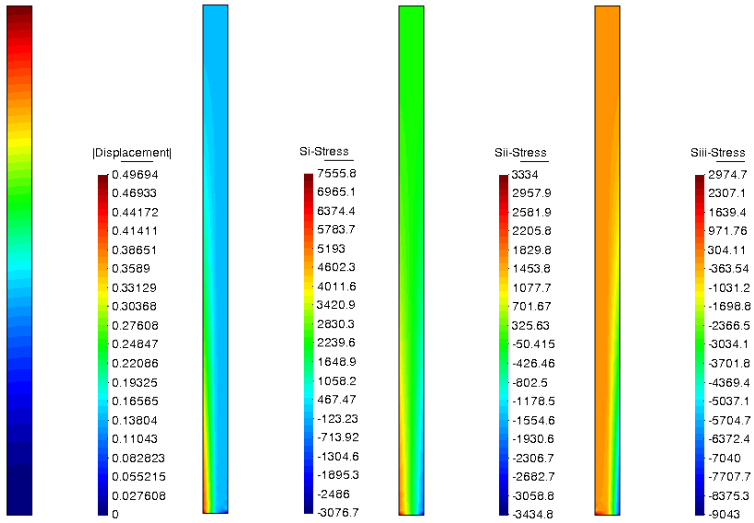

Figure 5.30: 2D Vertical plate in a fluid tunnel - Displacement and principal PK2 stress fields.

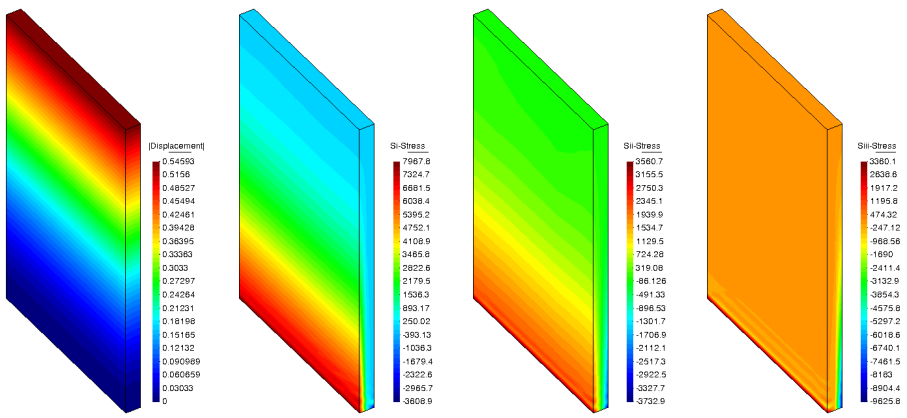

Figure 5.31: 3D Vertical plate in a fluid tunnel - Displacement and PK2 principal stress fields.

transient, there are slight differences in the time evolution results between the 3D and the 2D cases. There is a difference in the final stationary result, which can be attributed to the mesh refinement, which is much coarser than the one used in the 2D case.

[204]: Zhang et al. (2012), *Immersed smoothed finite element method for two dimensional fluid–structure interaction problems*
[205]: Han et al. (2021), *ELL for 3D FSI problems with thin flexible structures based on the continuum-based shell element*
[206]: Han et al. (2020), *An Eulerian-Lagrangian-Lagrangian method for 2D fluid-structure interaction problem with a thin flexible structure immersed in fluids*

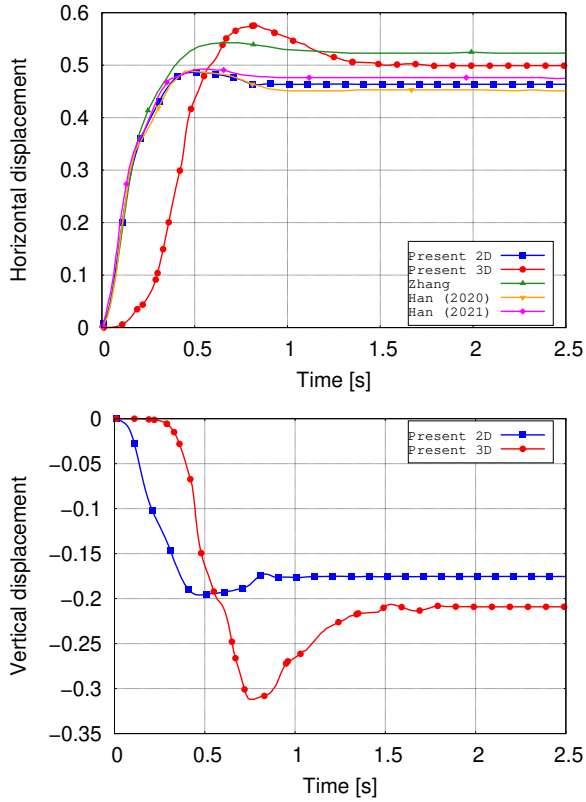

Figure 5.32: Vertical plate in a fluid tunnel - Horizontal and vertical displacement at the upper end. References: Zhang et al. [204], Han et al. (2020) [206], Han et al. (2021) [205].

5.10.4 Turek and Hron benchmark

[207]: Turek et al. (2006), *Proposal for Numerical Benchmarking of Fluid-Structure Interaction between an Elastic Object and Laminar Incompressible Flow*

The last example consists in one of the most widely used benchmark tests in the FSI context. It was designed by Turek and Hron in [207], with three different variants referred as FSI1, FSI2 and FSI3. In this example, the FSI2 variant is used as a reference. The case consists in a channel flow around an elastic bar attached to a rigid cylinder, which results in a self-induced oscillation. The domain and boundary conditions are summarized in Fig.5.33. The domain dimensions for the fluid are set as $H = 0.41$, $L = 2.5$, $a = 0.2$, $b = 0.2$ and $D = 0.1$. The boundary conditions consists of no-slip conditions at the cylinder and the upper and lower walls, and the inlet velocity is prescribed with a parabolic profile given by

$$u_f(0,y,t) = \begin{cases} \hat{u}_f(0,y)\frac{1-\cos\left(\frac{\pi}{2}t\right)}{2} & \text{if } t < 2.0 \\ \hat{u}_f(0,y) & \text{otherwise} \end{cases} \quad ; \qquad \hat{u}_f(0,y) = 1.5\hat{u}_{in}\frac{y\,(H-y)}{\left(\frac{H}{2}\right)^2}$$

where $\hat{u}_{in} = 1$ is the average inflow velocity. For the solid domain, the bar of length 0.35 and thickness 0.02 is aligned to the center of the cylinder. The domain is meshed with 45k linear triangular elements in the fluid and 100 line elements on the solid, which are extruded to 200 bilinear quadrilateral elements. The problem is solved with a time step of $\delta t = 0.005$. As for the boundary conditions, the bar is simply fixed at its left end. The Dirichlet transmission conditions are set on the fluid by imposing the solid velocity on the elements cut by the interface, while the Neumann transmission conditions are set by imposing the fluid tractions on the whole bar. The fluid density and viscosity are $\rho_f = 1000$ and $\mu_f = 1$, respectively, whereas the solid density, Young's modulus and Poisson's ratio are $\rho_s = 10^4$ $E_s = 1.4 \cdot 10^6$ and $\nu_s = 0.4$, respectively.

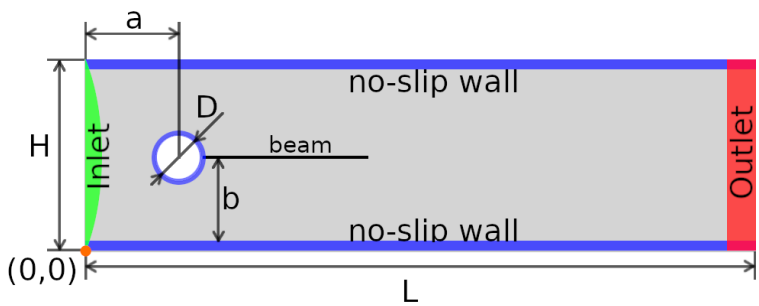

Figure 5.33: Turek benchmark - Geometry and boundary conditions.

The results of the fluid domain are shown in Figs. 5.34 and 5.35 for velocity and pressure fields. For the solid domain, the original paper reports the time evolution of the displacement at the right end of the beam. At the fully developed state, when the oscillation's amplitude and frequency stabilize, the authors report displacements of -0.01458 ± 0.01244 and 0.00123 ± 0.0806, in the x-axis and y-axis, respectively. They also provide a one second time span of the oscillations, which is used to compare our results in Figs. 5.36-5.37.

The results obtained with our approach show good agree-

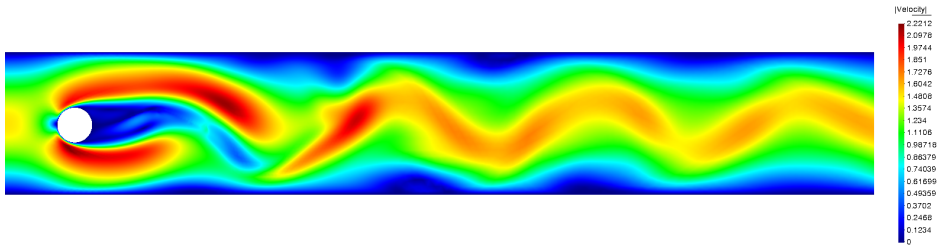

Figure 5.34: Turek benchmark - velocity norm at time $t = 7.61$.

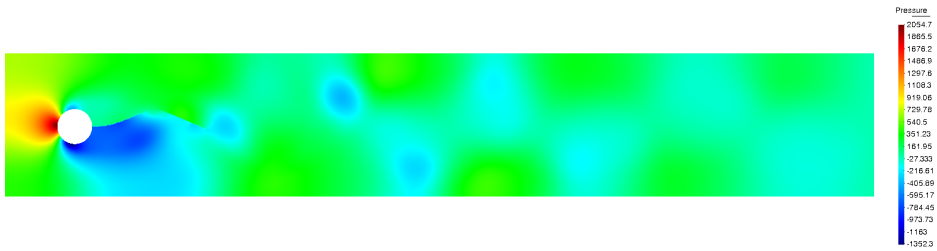

Figure 5.35: Turek benchmark - pressure at time $t = 7.61$.

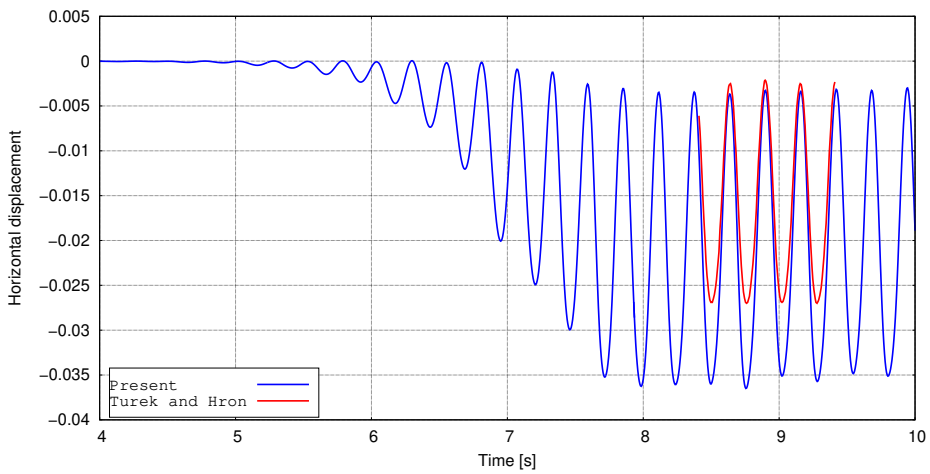

Figure 5.36: Turek benchmark - Horizontal displacement at the right end of the bar. Reference: Turek and Hron [207].

[207]: Turek et al. (2006), *Proposal for Numerical Benchmarking of Fluid-Structure Interaction between an Elastic Object and Laminar Incompressible Flow*

ment when comparing the oscillation frequencies with respect to those in reference [207]. However, the amplitudes we have obtained are slightly larger, specially in the x-axis

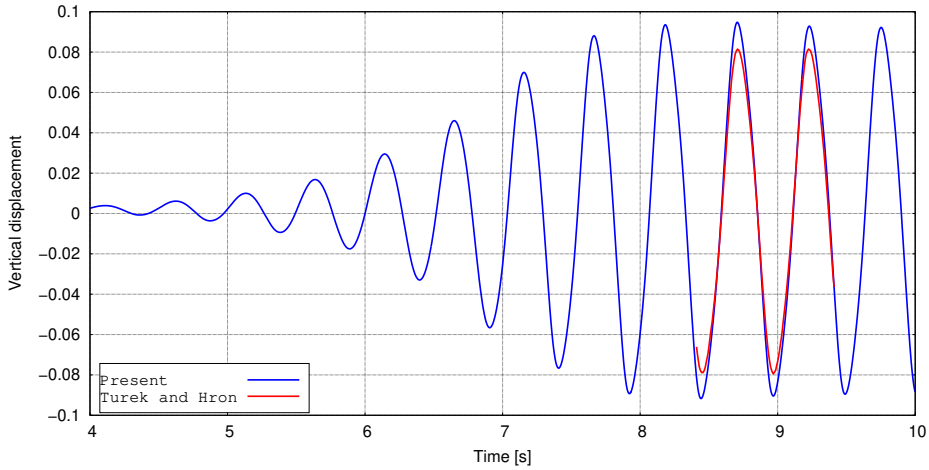

Figure 5.37: Turek benchmark - Vertical displacement at the right end of the bar. Reference: Turek and Hron [207].

direction. As explained in Section 5.8, this can be attributed to several causes. Firstly, the material used in this work is a Neo-Hookean instead of the Saint-Venant–Kirchhoff material law used in the original paper. Secondly, the time step differs from those used in the original paper ($\delta t = 0.001, 0.002$). Lastly, and perhaps the most significant difference, in our approach the solid 'sees' the beam as a line, not as a rectangle. This in particular means that tractions are not integrated at the free end of the beam in the transverse direction, and they may be large enough to affect the physics of the solution.

5.11 Conclusions

In this work, a numerical framework for the approximation of FSI problems involving hyperelastic thin structures using an embedded approach is presented. The main novelty of this approach consists in approximating the solid domain by using a recently developed locking-free stabilized formulation for solid-shell elements [190, 191]. The embedding of the solid mesh into the fluid mesh is not straightforward because solid-shell elements are thin volumetric bodies, which are not eligible to act as a embedding interface. For this reason, the issue is solved by using the solid-shell mid-surface as the interface to perform the embedding into the fluid domain. As a consequence, the transmission conditions of the Dirichlet-Neumann type require a special treatment.

[190]: Aguirre et al. (2023), *Stress-displacement stabilized finite element analysis of thin structures using solid-shell elements - Part I: On the need of interpolating the stresses*
[191]: Aguirre et al. (2023), *Stress-displacement stabilized finite element analysis of thin structures using Solid-Shell elements - Part II: Finite strain hyperelasticity*

This approach requires several key elements to function effectively. Firstly, from a computational standpoint, it is essential to implement a search algorithm to identify the background elements cut by the interface and an intersection algorithm to locate the intersections. This is achieved by utilizing a tree data structure that divides the domain into smaller sub-domains for the search and a ray-tracing algorithm to pinpoint the intersection points in each element. Secondly, from the fluid perspective, the embedded interface motivates the use of discontinuous shape functions to disconnect the pressures on each side of the interface. The fluid pressures are locally segregated at the element level, avoiding an increase in the computational overhead. The discontinuous shape functions are also suitable for weakly prescribing the Dirichlet transmission conditions using Nitsche's method, as they are imposed using the velocity of the embedded interface. Lastly, the Neumann transmission conditions are imposed by computing the fluid tractions at the embedded interface. Therefore, they need to be transferred to the solid-shell external surfaces.

The approach has undergone testing across various benchmark cases in both 2D and 3D environments, progressively increasing the difficulty in a staggered manner. Initially, one-way coupling cases have been addressed, testing the element-embedded interface and the weak imposition of boundary conditions on the fluid side. The evaluation has begun with a stationary problem, followed by a time-dependent problem featuring a periodic solution. Subsequently, a deformable

solid has been introduced, and dynamic problems have been solved to assess the entire coupling scheme. The results have demonstrated good agreement with existing literature, establishing the presented framework as a viable method for approaching FSI problems with thin structures.

Acknowledgements

This work was supported by Vicerrectoría de Investigación, Desarrollo e Innovación (VRIDEI) of the Univeridad de Santiago de Chile, and the National Agency for Research and Development (ANID) Doctorado Becas Chile/2019 - 72200128 of the Government of Chile. A. Aguirre gratefully acknowledges the support received by Computational Heat and Fluid Flow Lab from Universidad de Santiago de Chile. R. Codina gratefully acknowledges the support received through the ICREA Acadèmia Research Program of the Catalan Government. This work was partially funded through the TOPFSI-APP: Ref. PDC2022-133581-I00 MICINN of the Spanish Government. CIMNE is a recipient of a "Severo Ochoa Programme for Centers of Excellence in R&D" grant (CEX2018-000797-S) by the Spanish Ministry of Economy and Competitiveness.

Declarations

Conflict of interest

The authors declare that they have no known competing financial interests or personal relationships that could have appeared to influence the work reported in this paper.

Replication of results

All the information required for replicating the paper results was duly presented. Data files for the results are available upon request from the authors.

Conclusions 6

6.1 Achievements

The primary objective of this study has been to establish the foundations for a comprehensive computational framework capable of modeling thin structures without encountering numerical locking issues. This framework aims to address both infinitesimal and finite strain deformations of flat and curved structures, as well as the interaction with a surrounding fluid.

- In **Chapter** 2, the Finite Element approximations of Timoshenko beams and Reissner-Mindlin plates, which are susceptible to shear-locking issues, have been comprehensively investigated. The instabilities were approached by means of the Variational Multiscale framework. While the Algebraic Subgrid Scale approach was previously utilized to address this problem, this work has extended it through extensive numerical analysis and testing. However, the numerical analysis demonstrated that the Algebraic Subgrid Scale approach was not able solve the locking problem, which was later proven by numerical approximations. Consequently, the Orthogonal Subgrid Scale method has been employed as a improved alternative. This approach has been studied by means of numerical analysis and it is able to properly handle the issues that lead to instability. Furthermore, numerous numerical tests have confirmed its locking-free behavior and demonstrated its proper stability properties, improved accuracy, and optimal convergence ratios, making it a highly robust approach.

- In **Chapter** 3, the approximation of infinitesimal deformations of thin structures using solid-shell elements has been explored. These elements are vulnerable to various types of numerical locking, primarily due to their poor aspect ratio, curvature, and potential deformation modes. Consequently, the focus of this work was on investigating the mechanisms that trigger each type of numerical locking. This investigation have been

undertaken through the application of stabilization techniques based on the Variational Multiscale framework in the displacement-stress mixed form of the problem. The problem has been formulated in a curvilinear coordinate system, enabling the selection of stress tensor components to be included in the approximation. Extensive testing was conducted using various benchmark problems to determine the minimum stress components required in the approximation. Ultimately, it was found that the most robust approach to shell problems involves considering all of their components. Nonetheless, the stabilized formulation have proven to be highly robust and competitive with frequently used approaches in the literature.

- In **Chapter** 4, the approximation of thin structures using solid-shell elements has been extended to finite strain deformations employing hyperelastic materials. The mixed formulation considers displacements and the second Piola-Kirchhoff stress tensor as the unknowns. Various stabilization techniques of the Variational Multiscale framework were employed, with all of them yielding similar results. The obtained results demonstrate a significantly improved convergence ratio and accuracy in the stress field, albeit at the cost of slightly reduced accuracy in the displacement field. Nonetheless, even in the case of extremely thin structures in the finite strain regime, the stabilized formulation effectively addresses numerical locking issues and enables a more accurate representation of the deformation state compared to a quadratic element irreducible formulation. Furthermore, the approach presented in this chapter have provided robust results that are competitive with traditional and more recently developed methods.

- In **Chapter** 5, the mixed displacement-stress formulation for solid-shell elements of finite strain deformations was extended to Fluid-Structure Interaction problems. This approach involves employing an Embedded Mesh approach of the Cut-Fem type, wherein a discontinuous level-set function is set within the fluid elements to represent the embedded interface. The implementation of this approach necessitates the utilization of quadtree and octree data structures, along with a ray-tracing algorithm, to precisely determine the po-

sition of the intersection points between both meshes. The pressure discontinuities in the fluid, caused by the presence of a solid interface, have been captured using discontinuous shape functions that allows the segregation of node contributions. These functions are defined element-wise, ensuring that the implementation remains entirely local without the need for additional degrees of freedom. Furthermore, the discontinuous shape functions enable the weak imposition of velocity transmission conditions through Nitsche's method. The novelty of this work lied in presenting a new framework for approaching Fluid-Structure Interaction problems using the Variational Multiscale framework. This was achieved by combining the advancements in hyperelastic solid-shell elements with the already established stabilized approach for fluid mechanics, through various techniques available in the literature.

6.2 Future work

All the formulations, methodologies, and applications presented in this thesis represent significant contributions. However, there are still areas that warrant further investigation. This section will discuss potential future work that could build upon the findings presented thus far. Some possible directions for future research include:

- **Addressing volumetric locking**.
  While the thesis extensively addresses numerical locking of thin structures, it has not delved into numerical locking arising from incompressibility. This omission is due to the fact that this issue has been handled in the context of the Variational Multiscale framework for regular solids [4] by using a deviatoric/volumetric decomposition of the strain energy function. However, for the sake of completeness in this research line, it is important to explicitly address it in the context of solid-shell elements. This would ensure a comprehensive understanding of numerical locking issues inherent to this type of elements.

[4]: Castañar et al. (2020), *A stabilized mixed finite element approximation for incompressible finite strain solid dynamics using a total Lagrangian formulation*

- **Exploring other shell models**.
  Classical shell models are modeled by considering displacements and rotation degrees of freedom to represent the deformation and the transverse director vector. These type of formulations are another alternative to those studied in the thesis, with their own advantages and drawbacks. For example, classical formulations allow to perform a dimensional reduction of the element thus they work as a volumeless body which reduces number of degrees of freedom with respect to volumetric element. However, it would require to address the modifications of the constitutive tensor that are usually required to approximate the shell behaviour [11], and the small thickness limitations of such theories.

[11]: Bischoff et al. (2004), *Models and finite elements for thin-walled structures*

- **Topology Optimization of shell structures**.
  Shell structures are known for their high load-bearing capabilities achieved with relatively low material usage. Consequently, a logical next step would be to enhance the structural design further by determining the optimal material layout to meet specific performance targets. This objective can be achieved through the application of Topology Optimization techniques [147].

[147]: Castañar et al. (2022), *Topological derivative-based topology optimization of incompressible structures using mixed formulations*

- **Fractional-step schemes**
  In this thesis, shell problems are mostly approached by using solid-shell elements by using stabilized forms of the mixed formulations. As consequence the number of degrees of freedom of the problem are increased considerably with respect to the irreducible approach. Nevertheless, the additional cost proves to be worth because of the increased accuracy of the solution. However, the overall cost can be drastically reduced by incorporating a fractional-step approach that segregates the computation of each field [208].

[208]: Castillo et al. (2015), *First, second and third order fractional step methods for the three-field viscoelastic flow problem*

- **Material non-linearity**
  The thesis presented a framework to deal with geometrical non-linearity of shells through stabilized formulations, which proved to be robust and accurate. These developments can be followed by considering material non-linearity, such as plasticity or viscoelasticity, by taking advantage of the mixed displacement-stress formulation and implementing stress-based formulations [209].

[209]: Ambati et al. (2018), *Isogeometric Kirchhoff–Love shell formulation for elasto-plasticity*

- **Composite structures**
  The developments accomplished in this thesis allow for robust computations and reliable results of the behavior of thin shells. However, it is still limited to the use of a single material in the thickness direction. In contrast, engineering applications aim for lighter and stronger structures through the development of advanced materials [210, 211]. For this reason, it is reasonable to extend the shell formulation to consider anisotropic composite and laminated materials by taking advantage of the curvilinear coordinate system and the layered extrusion used to build solid-shell elements.

[210]: Qatu et al. (2010), *Recent research advances on the dynamic analysis of composite shells: 2000–2009*
[211]: Stegmann et al. (2005), *Discrete material optimization of general composite shell structures*

Bibliography

Here are the references in citation order.

[1] Eugenio Oñate. *Structural analysis with the finite element method. Linear statics: volume 2: beams, plates and shells*. Springer Science & Business Media, 2013 (cited on pages 7, 8, 17, 64, 65, 120).

[2] Thomas JR Hughes. "Multiscale phenomena: Green's functions, the Dirichlet-to-Neumann formulation, subgrid scale models, bubbles and the origins of stabilized methods." In: *Computer methods in applied mechanics and engineering* 127.1-4 (1995). Publisher: Citeseer, pp. 387–401. DOI: https://doi.org/10.1016/0045-7825(95)00844-9 (cited on pages 8, 18, 19, 68, 69, 85, 123).

[3] Thomas JR Hughes et al. "The variational multiscale method - A paradigm for computational mechanics." In: *Computer methods in applied mechanics and engineering* 166.1-2 (1998). Publisher: Elsevier, pp. 3–24. DOI: https://doi.org/10.1016/S0045-7825(98)00079-6 (cited on pages 8, 18, 19, 68, 69, 85, 123, 136, 175).

[4] Inocencio Castañar, Joan Baiges, and Ramon Codina. "A stabilized mixed finite element approximation for incompressible finite strain solid dynamics using a total Lagrangian formulation." In: *Computer Methods in Applied Mechanics and Engineering* 368 (Aug. 2020), p. 113164. DOI: 10.1016/j.cma.2020.113164. (Visited on 03/11/2024) (cited on pages 8, 123, 124, 130, 169, 217).

[5] Jesús Gerardo Valdés Vázquez. "Nonlinear Analysis of Orthotropic Membrane and Shell Structures Including Fluid-Structure Interaction." es. http://purl.org/dc/dcmitype/Text. Universitat Politècnica de Catalunya (UPC), 2007. (Visited on 01/28/2024) (cited on page 8).

[6] EARL H. DOWELL. "Nonlinear oscillations of a fluttering plate." In: *AIAA Journal* 4.7 (1966). Publisher: American Institute of Aeronautics and Astronautics _eprint: https://doi.org/10.2514/3.3658, pp. 1267–1275. DOI: 10.2514/3.3658. (Visited on 03/12/2024) (cited on page 9).

[7] J. M. McCarthy et al. "Fluttering energy harvesters in the wind: A review." In: *Journal of Sound and Vibration* 361 (Jan. 2016), pp. 355–377. DOI: 10.1016/j.jsv.2015.09.043. (Visited on 03/12/2024) (cited on page 9).

[8] Douglas D. Bueno, Luiz C. S. Góes, and Paulo J. P. Gonçalves. "Flutter analysis including structural uncertainties." en. In: *Meccanica* 50.8 (Aug. 2015), pp. 2093–2101. DOI: 10.1007/s11012-015-0138-8. (Visited on 03/12/2024) (cited on page 9).

[9] Ted Belytschko et al. *Nonlinear finite elements for continua and structures*. John wiley & sons, 2014 (cited on pages 9, 64, 120).

[10] Javier Bonet and Richard D Wood. *Nonlinear continuum mechanics for finite element analysis*. Cambridge university press, 1997 (cited on page 9).

[11] Manfred Bischoff et al. “Models and finite elements for thin-walled structures.” In: *Encyclopedia of computational mechanics* (2004). Publisher: Wiley Online Library (cited on pages 9, 65, 120, 218).

[12] A. Melendo et al. *www.gidhome.com*. 2018. URL: url%7Bwww.gidsimulation.com%7D (cited on page 14).

[13] J Rakowski. “The interpretation of the shear locking in beam elements.” In: *Computers & Structures* 37.5 (1990). Publisher: Elsevier, pp. 769–776. DOI: https://doi.org/10.1016/0045-7949(90)90106-C (cited on page 16).

[14] Klaus-Jürgen Bathe. “The inf–sup condition and its evaluation for mixed finite element methods.” In: *Computers & Structures* 79.2 (2001). Publisher: Elsevier, pp. 243–252. DOI: https://doi.org/10.1016/S0045-7949(00)00123-1 (cited on page 17).

[15] Dominique Chapelle and Klaus-Jurgen Bathe. *The finite element analysis of shells-fundamentals*. Springer Science & Business Media, 2010 (cited on pages 17, 18, 30, 67, 68).

[16] Ricardo Durán and Elsa Liberman. “On mixed finite element methods for the Reissner-Mindlin plate model.” In: *Mathematics of Computation* 58.198 (1992), pp. 561–573. DOI: https://doi.org/10.1090/S0025-5718-1992-1106965-0 (cited on page 17).

[17] C Lovadina. “Analysis of a mixed finite element method for the Reissner-Mindlin plate problems.” In: *Computer Methods in Applied Mechanics and Engineering* 163.1-4 (1998). Publisher: Elsevier, pp. 71–85. DOI: https://doi.org/10.1016/S0045-7825(98)00003-6 (cited on page 17).

[18] Richard Falk and Tong Tu. “Locking-free finite elements for the Reissner-Mindlin plate.” In: *Mathematics of Computation* 69.231 (2000), pp. 911–928. DOI: https://doi.org/10.1090/S0025-5718-99-01165-5 (cited on pages 17, 18, 30).

[19] Franco Brezzi, Klaus-Jürgen Bathe, and Michel Fortin. “Mixed-interpolated elements for Reissner–Mindlin plates.” In: *International Journal for Numerical Methods in Engineering* 28.8 (1989). Publisher: Wiley Online Library, pp. 1787–1801. DOI: https://doi.org/10.1002/nme.1620280806 (cited on page 17).

[20] Thomas JR Hughes and Leopoldo P Franca. “Convergence of transverse shear stresses in the finite element analysis of plates.” In: *Communications in Applied Numerical Methods* 4.2 (1988). Publisher: Wiley Online Library, pp. 185–187. DOI: https://doi.org/10.1002/cnm.1630040208 (cited on page 17).

[21] Thomas JR Hughes and Leopoldo P Franca. “A mixed finite element formulation for Reissner-Mindlin plate theory: Uniform convergence of all higher-order spaces.” In: *Computer Methods in Applied Mechanics and Engineering* 67.2 (1988). Publisher: Elsevier, pp. 223–240. DOI: https://doi.org/10.1016/0045-7825(88)90127-2 (cited on pages 17, 18, 30).

[22] Rolf Stenberg. “A new finite element formulation for the plate bending problem.” In: *Asymptotic methods for elastic structures* (1995). Publisher: de Gruyter, pp. 209–221. DOI: https://doi.org/10.1515/9783110873726.209 (cited on pages 17, 18, 30).

[23] Phill-Seung Lee and Klaus-Jürgen Bathe. "Development of MITC isotropic triangular shell finite elements." In: *Computers & Structures* 82.11-12 (2004). Publisher: Elsevier, pp. 945–962 (cited on page 17).

[24] L Beirao da Veiga, Dominique Chapelle, and I Paris Suarez. "Towards improving the MITC6 triangular shell element." In: *Computers & structures* 85.21-22 (2007). Publisher: Elsevier, pp. 1589–1610. DOI: https://doi.org/10.1016/j.compstruc.2007.03.003 (cited on page 17).

[25] Felipe Lepe, David Mora, and Rodolfo Rodríguez. "Locking-free finite element method for a bending moment formulation of Timoshenko beams." In: *Computers & Mathematics with Applications* 68.3 (2014). Publisher: Elsevier, pp. 118–131 (cited on page 18).

[26] M Toolabi et al. "Enhanced mixed interpolation XFEM formulations for discontinuous Timoshenko beam and Mindlin-Reissner plate." In: *International Journal for Numerical Methods in Engineering* 115.6 (2018). Publisher: Wiley Online Library, pp. 714–737 (cited on page 18).

[27] Bradley T Darrall, Gary F Dargush, and Ali R Hadjesfandiari. "Finite element Lagrange multiplier formulation for size-dependent skew-symmetric couple-stress planar elasticity." In: *Acta Mechanica* 225.1 (2014). Publisher: Springer, pp. 195–212. DOI: https://doi.org/10.1007/s00707-013-0944-9 (cited on page 18).

[28] Lourenço Beirão da Veiga, David Mora, and Rodolfo Rodríguez. "Numerical analysis of a locking-free mixed finite element method for a bending moment formulation of Reissner-Mindlin plate model." In: *Numerical Methods for Partial Differential Equations* 29.1 (2013). Publisher: Wiley Online Library, pp. 40–63. DOI: https://doi.org/10.1002/num.21698 (cited on page 18).

[29] F Brezzi and L Donatella Marini. "A nonconforming element for the Reissner–Mindlin plate." In: *Computers & Structures* 81.8-11 (2003). Publisher: Elsevier, pp. 515–522. DOI: https://doi.org/10.1016/S0045-7949(02)00418-2 (cited on page 18).

[30] C Chinosi, C Lovadina, and LD Marini. "Nonconforming locking-free finite elements for Reissner–Mindlin plates." In: *Computer Methods in Applied Mechanics and Engineering* 195.25-28 (2006). Publisher: Elsevier, pp. 3448–3460. DOI: https://doi.org/10.1016/j.cma.2005.06.025 (cited on pages 18, 48).

[31] Victor M Calo, Nathaniel O Collier, and Antti H Niemi. "Analysis of the discontinuous Petrov–Galerkin method with optimal test functions for the Reissner–Mindlin plate bending model." In: *Computers & Mathematics with Applications* 66.12 (2014). Publisher: Elsevier, pp. 2570–2586 (cited on page 18).

[32] Thomas Führer, Carlos García Vera, and Norbert Heuer. "A locking-free DPG scheme for Timoshenko beams." In: *Computational Methods in Applied Mathematics* 21.2 (2021). Publisher: De Gruyter, pp. 373–383 (cited on page 18).

[33] Gabriel R Barrenechea, Tomás P Barrios, and Andreas Wachtel. "Stabilised finite element methods for a bending moment formulation of the Reissner-Mindlin plate model." In: *Calcolo. A Quarterly on Numerical Analysis and Theory of Computation* 52.3 (2015). Publisher: Springer, pp. 343–369. DOI: https://doi.org/10.1007/s10092-014-0120-1 (cited on page 18).

[34] Javier Videla, Sundararajan Natarajan, and Stéphane PA Bordas. "A new locking-free polygonal plate element for thin and thick plates based on Reissner-Mindlin plate theory and assumed shear strain fields." In: *Computers & Structures* 220 (2019). Publisher: Elsevier, pp. 32–42. DOI: https://doi.org/10.1016/j.compstruc.2019.04.009 (cited on page 18).

[35] Petra Peisker. "A multigrid method for Reissner-Mindlin plates." In: *Numerische Mathematik* 59.1 (1991). Publisher: Springer, pp. 511–528. DOI: https://doi.org/10.1007/BF01385793 (cited on page 18).

[36] Reijo Kouhia. "On stabilized finite element methods for the Reissner–Mindlin plate model." In: *International Journal for Numerical Methods in Engineering* 74.8 (2008). Publisher: Wiley Online Library, pp. 1314–1328. DOI: https://doi.org/10.1002/nme.2211 (cited on page 18).

[37] Joachim Schöberl and Rolf Stenberg. "Multigrid methods for a stabilized Reissner–Mindlin plate formulation." In: *SIAM Journal on Numerical Analysis* 47.4 (2009). Publisher: SIAM, pp. 2735–2751. DOI: https://doi.org/10.1137/060672182 (cited on page 18).

[38] P Peisker, W Rust, and E Stein. "Iterative solution methods for plate bending problems: multigrid and preconditioned cg algorithm." In: *SIAM Journal on Numerical Analysis* 27.6 (1990). Publisher: SIAM, pp. 1450–1465. DOI: https://doi.org/10.1137/0727084 (cited on pages 18, 19).

[39] Klaus-Jürgen Bathe and Eduardo N Dvorkin. "A four-node plate bending element based on Mindlin/Reissner plate theory and a mixed interpolation." In: *International Journal for Numerical Methods in Engineering* 21.2 (1985). Publisher: Wiley Online Library, pp. 367–383. DOI: https://doi.org/10.1002/nme.1620210213 (cited on pages 18, 19).

[40] Dominique Chapelle and Rolf Stenberg. "An optimal low-order locking-free finite element method for Reissner–Mindlin plates." In: *Mathematical Models and Methods in Applied Sciences* 8.03 (1998). Publisher: World Scientific, pp. 407–430. DOI: https://doi.org/10.1142/S0218202598000172 (cited on pages 18, 19).

[41] Douglas N Arnold and Franco Brezzi. "Some new elements for the Reissner-Mindlin plate model." In: *Boundary Value Problems for Partial Differential Equations and Applications* (1993). Publisher: Citeseer, pp. 287–292 (cited on pages 18, 19).

[42] M. Bischoff and K.-U. Bletzinger. "Improving stability and accuracy of Reissner–Mindlin plate finite elements via algebraic subgrid scale stabilization." In: *Computer Methods in Applied Mechanics and Engineering* 193 (2004). Publisher: Elsevier, pp. 1517–1528. DOI: https://doi.org/10.1016/j.cma.2003.12.036 (cited on pages 18, 19, 32).

[43] Ramon Codina. "Stabilization of incompressibility and convection through orthogonal sub-scales in finite element methods." In: *Computer methods in applied mechanics and engineering* 190.13-14 (2000). Publisher: Elsevier, pp. 1579–1599. DOI: https://doi.org/10.1016/S0045-7825(00)00254-1 (cited on pages 19, 68, 69, 85, 123, 175).

[44] Ramon Codina et al. “Variational multiscale methods in computational fluid dynamics.” In: *Encyclopedia of Computational Mechanics, Second Edition* (2018). Publisher: Wiley Online Library, pp. 1–28. DOI: https://doi.org/10.1002/9781119176817.ecm2117 (cited on pages 25, 86).

[45] Ramon Codina, Javier Principe, and Joan Baiges. “Subscales on the element boundaries in the variational two-scale finite element method.” In: *Computer Methods in Applied Mechanics and Engineering* 198.5-8 (2009). Publisher: Elsevier, pp. 838–852. DOI: https://doi.org/10.1016/j.cma.2008.10.020 (cited on pages 26, 86, 137, 186).

[46] Ramon Codina. “On stabilized finite element methods for linear systems of convection–diffusion-reaction equations.” In: *Computer Methods in Applied Mechanics and Engineering* 188.1-3 (2000). Publisher: Elsevier, pp. 61–82. DOI: https://doi.org/10.1016/S0045-7825(00)00177-8 (cited on pages 31, 32, 34, 35, 139).

[47] Yan Shang et al. “Two generalized conforming quadrilateral Mindlin–Reissner plate elements based on the displacement function.” In: *Finite Elements in Analysis and Design* 99 (2015). Publisher: Elsevier, pp. 24–38 (cited on page 54).

[48] Luo Yunhua and Anders Eriksson. “An alternative assumed strain method.” In: *Computer Methods in Applied Mechanics and Engineering* 178.1-2 (1999). Publisher: Elsevier, pp. 23–37 (cited on page 54).

[49] Dragan Ribarić and Gordan Jelenić. “Higher-order linked interpolation in quadrilateral thick plate finite elements.” In: *Finite Elements in Analysis and Design* 51 (2012). Publisher: Elsevier, pp. 67–80 (cited on page 54).

[50] Song Cen et al. “Hybrid displacement function element method: a simple hybrid-Trefftz stress element method for analysis of Mindlin–Reissner plate.” In: *International Journal for Numerical Methods in Engineering* 98.3 (2014). Publisher: Wiley Online Library, pp. 203–234 (cited on page 54).

[51] Warren C Young, Richard G Budynas, and Ali M Sadegh. *Roark’s formulas for stress and strain*. McGraw-Hill Education, 2012 (cited on pages 54, 56).

[52] Xiaoxiao Du, Gang Zhao, and Wei Wang. “Nitsche method for isogeometric analysis of Reissner–Mindlin plate with non-conforming multi-patches.” In: *Computer Aided Geometric Design* 35 (2015). Publisher: Elsevier, pp. 121–136 (cited on page 59).

[53] Eric Reissner. “On one-dimensional finite-strain beam theory: the plane problem.” In: *Zeitschrift für angewandte Mathematik und Physik ZAMP* 23.5 (1972). Publisher: Springer, pp. 795–804 (cited on page 64).

[54] Richard H Macneal. “Derivation of element stiffness matrices by assumed strain distributions.” In: *Nuclear Engineering and Design* 70.1 (1982). Publisher: Elsevier, pp. 3–12 (cited on page 64).

[55] Ted Belytschko and William E Bachrach. “Efficient implementation of quadrilaterals with high coarse-mesh accuracy.” In: *Computer Methods in Applied Mechanics and Engineering* 54.3 (1986). Publisher: Elsevier, pp. 279–301 (cited on page 64).

[56] Juan C Simo, David D Fox, and Mustapha S Rifai. "On a stress resultant geometrically exact shell model. Part III: Computational aspects of the nonlinear theory." In: *Computer Methods in Applied Mechanics and Engineering* 79.1 (1990). Publisher: Elsevier, pp. 21–70 (cited on page 64).

[57] Norbert Büchter, Ekkehard Ramm, and Deane Roehl. "Three-dimensional extension of non-linear shell formulation based on the enhanced assumed strain concept." In: *International Journal for Numerical Methods in Engineering* 37.15 (1994). Publisher: Wiley Online Library, pp. 2551–2568 (cited on pages 64, 150, 152).

[58] ML Bucalem and Klaus-Jurgen Bathe. "Finite element analysis of shell structures." In: *Archives of Computational Methods in Engineering* 4.1 (1997). Publisher: Springer, pp. 3–61 (cited on pages 64, 114).

[59] M Bischoff and E Ramm. "Shear deformable shell elements for large strains and rotations." In: *International Journal for Numerical Methods in Engineering* 40.23 (1997). Publisher: Wiley Online Library, pp. 4427–4449 (cited on pages 64, 122).

[60] Ignacio Romero. "A comparison of finite elements for nonlinear beams: the absolute nodal coordinate and geometrically exact formulations." In: *Multibody System Dynamics* 20.1 (2008). Publisher: Springer, pp. 51–68 (cited on page 64).

[61] JM Valle, ALEJANDRO Albanesi, and V Fachinotti. "An efficient general curvilinear coordinates finite element method for the linear dynamic study of thickness-independent shells." In: *Latin American Journal of Solids and Structures* 16 (2019). Publisher: SciELO Brasil (cited on page 64).

[62] Sohrabuddin Ahmad, Bruce M Irons, and OC Zienkiewicz. "Analysis of thick and thin shell structures by curved finite elements." In: *International Journal for Numerical Methods in Engineering* 2.3 (1970). Publisher: Wiley Online Library, pp. 419–451 (cited on page 64).

[63] T Kant, S Kumar, and UP Singh. "Shell dynamics with three-dimensional degenerate finite elements." In: *Computers & structures* 50.1 (1994). Publisher: Elsevier, pp. 135–146 (cited on pages 64, 65).

[64] Henry TY Yang et al. "A survey of recent shell finite elements." In: *International Journal for Numerical Methods in Engineering* 47.1-3 (2000). Publisher: Wiley Online Library, pp. 101–127 (cited on page 64).

[65] D Marinković, H Köppe, and U Gabbert. "Degenerated shell element for geometrically nonlinear analysis of thin-walled piezoelectric active structures." In: *Smart Materials and Structures* 17.1 (2008). Publisher: IOP Publishing, p. 015030 (cited on page 64).

[66] P Betsch, F Gruttmann, and E13908390861 Stein. "A 4-node finite shell element for the implementation of general hyperelastic 3D-elasticity at finite strains." In: *Computer Methods in Applied Mechanics and Engineering* 130.1-2 (1996). Publisher: Elsevier, pp. 57–79 (cited on pages 64, 65, 122).

[67] Norbert Buechter and Ekkehard Ramm. "Shell theory versus degeneration a comparison in large rotation finite element analysis." In: *International Journal for Numerical Methods in Engineering* 34.1 (1992). Publisher: Wiley Online Library, pp. 39–59 (cited on pages 64, 65).

[68] N Büchter and E Ramm. "Comparison of shell theory and degeneration." In: *Nonlinear analysis of shells by finite elements*. Springer, 1992, pp. 15–30 (cited on pages 64, 65).

[69] R Hauptmann and K Schweizerhof. "A systematic development of 'solid-shell' element formulations for linear and non-linear analyses employing only displacement degrees of freedom." In: *International Journal for Numerical Methods in Engineering* 42.1 (1998). Publisher: Wiley Online Library, pp. 49–69 (cited on pages 64, 65).

[70] Stefan Doll et al. "On volumetric locking of low-order solid and solid-shell elements for finite elastoviscoplastic deformations and selective reduced integration." In: *Engineering Computations* 17.7 (2000). Publisher: MCB UP Ltd, pp. 874–902 (cited on pages 65, 66, 120, 121).

[71] KY Sze. "Three-dimensional continuum finite element models for plate/shell analysis." In: *Progress in Structural Engineering and Materials* 4.4 (2002). Publisher: Wiley Online Library, pp. 400–407 (cited on pages 65, 67, 120).

[72] Richard H MacNeal. "Toward a defect-free four-noded membrane element." In: *Finite elements in analysis and design* 5.1 (1989). Publisher: Elsevier, pp. 31–37 (cited on pages 66, 120).

[73] Richard H MacNeal. "A simple quadrilateral shell element." In: *Computers & Structures* 8.2 (1978). Publisher: Elsevier, pp. 175–183 (cited on pages 66, 121).

[74] KC Park and GM Stanley. "A curved C^0 shell element based on assumed natural-coordinate strains." In: *Journal of Applied Mechanics* 53.2 (1986), pp. 278–290 (cited on pages 66, 121).

[75] JC Simo and Hughes. "On the variational foundations of assumed strain methods." In: *Journal of Applied Mechanics* 53.1 (1986), pp. 51–54 (cited on page 66).

[76] Juan C Simo and MS1058742 Rifai. "A class of mixed assumed strain methods and the method of incompatible modes." In: *International Journal for Numerical Methods in Engineering* 29.8 (1990). Publisher: Wiley Online Library, pp. 1595–1638 (cited on pages 66, 121).

[77] Ted Belytschko and Lee P Bindeman. "Assumed strain stabilization of the eight node hexahedral element." In: *Computer Methods in Applied Mechanics and Engineering* 105.2 (1993). Publisher: Elsevier, pp. 225–260 (cited on pages 66, 121).

[78] S Klinkel, F Gruttmann, and W Wagner. "A continuum based three-dimensional shell element for laminated structures." In: *Computers & Structures* 71.1 (1999). Publisher: Elsevier, pp. 43–62 (cited on pages 66, 121).

[79] KY Sze and LQ0990 Yao. "A hybrid stress ANS solid-shell element and its generalization for smart structure modelling. Part I solid shell element formulation." In: *International Journal for Numerical Methods in Engineering* 48.4 (2000). Publisher: Wiley Online Library, pp. 545–564 (cited on pages 66, 114).

[80] KY Sze, LQ Yao, and Sung Yi. "A hybrid stress ANS solid-shell element and its generalization for smart structure modelling. Part II smart structure modelling." In: *International Journal for Numerical Methods in Engineering* 48.4 (2000). Publisher: Wiley Online Library, pp. 565–582 (cited on page 66).

[81] KY Sze, S-J Zheng, and SH Lo. "A stabilized eighteen-node solid element for hyperelastic analysis of shells." In: *Finite Elements in Analysis and Design* 40.3 (2004). Publisher: Elsevier, pp. 319–340 (cited on pages 66, 93, 152).

[82] KD Kim, GZ Liu, and SC1109 Han. "A resultant 8-node solid-shell element for geometrically nonlinear analysis." In: *Computational Mechanics* 35 (2005). Publisher: Springer, pp. 315–331 (cited on page 66).

[83] A Hajlaoui et al. "An improved enhanced solid shell element for static and buckling analysis of shell structures." In: *Mechanics & Industry* 17.5 (2016). Publisher: EDP Sciences, p. 510 (cited on pages 66, 121, 122).

[84] M Mostafa, MV Sivaselvan, and CA3072432 Felippa. "A solid-shell corotational element based on ANDES, ANS and EAS for geometrically nonlinear structural analysis." In: *International Journal for Numerical Methods in Engineering* 95.2 (2013). Publisher: Wiley Online Library, pp. 145–180 (cited on pages 67, 121, 149, 150).

[85] JF Caseiro et al. "On the Assumed Natural Strain method to alleviate locking in solid-shell NURBS-based finite elements." In: *Computational Mechanics* 53 (2014). Publisher: Springer, pp. 1341–1353 (cited on pages 67, 114, 121, 122).

[86] JF Caseiro et al. "Assumed natural strain NURBS-based solid-shell element for the analysis of large deformation elasto-plastic thin-shell structures." In: *Computer Methods in Applied Mechanics and Engineering* 284 (2015). Publisher: Elsevier, pp. 861–880 (cited on pages 67, 121).

[87] Junbin Huang et al. "An unsymmetric 8-node hexahedral solid-shell element with high distortion tolerance: linear formulations." In: *International Journal for Numerical Methods in Engineering* 116.12-13 (2018). Publisher: Wiley Online Library, pp. 759–783 (cited on page 67).

[88] OC Zienkiewicz, RL Taylor, and JM0253 Too. "Reduced integration technique in general analysis of plates and shells." In: *International Journal for Numerical Methods in Engineering* 3.2 (1971). Publisher: Wiley Online Library, pp. 275–290 (cited on pages 67, 120).

[89] DJ438051 Naylor. "Stresses in nearly incompressible materials by finite elements with application to the calculation of excess pore pressures." In: *International Journal for Numerical Methods in Engineering* 8.3 (1974). Publisher: Wiley Online Library, pp. 443–460 (cited on page 67).

[90] David S Malkus and Thomas JR Hughes. "Mixed finite element methods - reduced and selective integration techniques: a unification of concepts." In: *Computer Methods in Applied Mechanics and Engineering* 15.1 (1978). Publisher: Elsevier, pp. 63–81 (cited on page 67).

[91] Ted Belytschko et al. “Hourglass control in linear and nonlinear problems.” In: *Computer Methods in Applied Mechanics and Engineering* 43.3 (1984). Publisher: Elsevier, pp. 251–276 (cited on pages 67, 120).

[92] Marco Schwarze and Stefanie Reese. “A reduced integration solid-shell finite element based on the EAS and the ANS concept—Geometrically linear problems.” In: *International Journal for Numerical Methods in Engineering* 80.10 (2009). Publisher: Wiley Online Library, pp. 1322–1355 (cited on pages 67, 114, 121).

[93] Marco Schwarze and Stefanie Reese. “A reduced integration solid-shell finite element based on the EAS and the ANS concept—Large deformation problems.” In: *International Journal for Numerical Methods in Engineering* 85.3 (2011). Publisher: Wiley Online Library, pp. 289–329 (cited on pages 67, 121, 152).

[94] Stefanie Reese. “A large deformation solid-shell concept based on reduced integration with hourglass stabilization.” In: *International Journal for Numerical Methods in Engineering* 69.8 (2007). Publisher: Wiley Online Library, pp. 1671–1716 (cited on page 67).

[95] Mara Pagani, S Reese, and Umberto Perego. “Computationally efficient explicit nonlinear analyses using reduced integration-based solid-shell finite elements.” In: *Computer Methods in Applied Mechanics and Engineering* 268 (2014). Publisher: Elsevier, pp. 141–159 (cited on pages 67, 68).

[96] Leonardo Leonetti et al. “An efficient isogeometric solid-shell formulation for geometrically nonlinear analysis of elastic shells.” In: *Computer Methods in Applied Mechanics and Engineering* 331 (2018). Publisher: Elsevier, pp. 159–183 (cited on pages 67, 68, 121, 122, 149, 150).

[97] Oliver Barfusz et al. “A reduced integration-based solid-shell finite element formulation for gradient-extended damage.” In: *Computer Methods in Applied Mechanics and Engineering* 382 (2021). Publisher: Elsevier, p. 113884 (cited on pages 67, 68, 122).

[98] Klaus-Jürgen Bathe. *Finite element procedures*. Klaus-Jurgen Bathe, 2006 (cited on pages 67, 68).

[99] Eduardo N Dvorkin and Klaus-Jürgen Bathe. “A continuum mechanics based four-node shell element for general non-linear analysis.” In: *Engineering computations* 1.1 (1984). Publisher: MCB UP Ltd, pp. 77–88 (cited on pages 67, 68, 114, 121).

[100] Klaus-Jürgen Bathe, Alexander Iosilevich, and Dominique Chapelle. “An evaluation of the MITC shell elements.” In: *Computers & Structures* 75.1 (2000). Publisher: Elsevier, pp. 1–30 (cited on pages 67, 68).

[101] Klaus-Jürgen Bathe, Alexander Iosilevich, and Dominique Chapelle. “An inf-sup test for shell finite elements.” In: *Computers & Structures* 75.5 (2000). Publisher: Elsevier, pp. 439–456 (cited on pages 67, 68).

[102] Hyeong-Min Jeon et al. “The MITC3+ shell element in geometric nonlinear analysis.” In: *Computers & Structures* 146 (2015). Publisher: Elsevier, pp. 91–104 (cited on pages 67, 68, 122, 154).

[103] Dominique Chapelle, Anca Ferent, and KJ2037782 Bathe. "3D-shell elements and their underlying mathematical model." In: *Mathematical Models and Methods in Applied Sciences* 14.01 (2004). Publisher: World Scientific, pp. 105–142 (cited on pages 67, 68, 121).

[104] Theodore Sussman and Klaus-Jürgen Bathe. "3D-shell elements for structures in large strains." In: *Computers & structures* 122 (2013). Publisher: Elsevier, pp. 2–12 (cited on pages 67, 68).

[105] Maria Cinefra. "Formulation of 3D finite elements using curvilinear coordinates." In: *Mechanics of Advanced Materials and Structures* 29.6 (2022). Publisher: Taylor & Francis, pp. 879–888 (cited on pages 68, 82).

[106] Mohammad Rezaiee-Pajand and Mohammadreza Ramezani. "An evaluation of MITC and ANS elements in the nonlinear analysis of shell structures." In: *Mechanics of Advanced Materials and Structures* 29.26 (2022). Publisher: Taylor & Francis, pp. 4677–4697 (cited on pages 68, 122, 123).

[107] Thomas JR Hughes. "Generalization of selective integration procedures to anisotropic and nonlinear media." In: *International Journal for Numerical Methods in Engineering* 15.9 (1980). Publisher: Wiley Online Library, pp. 1413–1418 (cited on page 68).

[108] JC Simo, Robert L Taylor, and KS822744 Pister. "Variational and projection methods for the volume constraint in finite deformation elasto-plasticity." In: *Computer methods in applied mechanics and engineering* 51.1-3 (1985). Publisher: Elsevier, pp. 177–208 (cited on page 68).

[109] KY Sze and A Ghali. "Hybrid hexahedral element for solids, plates, shells and beams by selective scaling." In: *International Journal for Numerical Methods in Engineering* 36.9 (1993). Publisher: Wiley Online Library, pp. 1519–1540 (cited on pages 68, 69).

[110] C Sansour and FG Kollmann. "Families of 4-node and 9-node finite elements for a finite deformation shell theory. An assesment of hybrid stress, hybrid strain and enhanced strain elements." In: *Computational Mechanics* 24 (2000). Publisher: Springer, pp. 435–447 (cited on pages 68, 69).

[111] YH Kim and SW Lee. "A solid element formulation for large deflection analysis of composite shell structures." In: *Computational structural mechanics & fluid dynamics*. Elsevier, 1988, pp. 269–274 (cited on pages 68, 69).

[112] Hoon C Park, Chahngmin Cho, and Sung W Lee. "An efficient assumed strain element model with six DOF per node for geometrically non-linear shells." In: *International Journal for Numerical Methods in Engineering* 38.24 (1995). Publisher: Wiley Online Library, pp. 4101–4122 (cited on pages 68, 69, 153).

[113] Ramon Codina. "Stabilized finite element approximation of transient incompressible flows using orthogonal subscales." In: *Computer methods in applied mechanics and engineering* 191.39-40 (2002). Publisher: Elsevier, pp. 4295–4321 (cited on pages 68, 69, 139, 178).

[114] E Castillo and Ramon Codina. "Finite element approximation of the viscoelastic flow problem: A non-residual based stabilized formulation." In: *Computers & Fluids* 142 (2017). Publisher: Elsevier, pp. 72–78. DOI: https://doi.org/10.1016/j.compfluid.2016.07.012 (cited on pages 68, 69, 123, 139, 178).

[115] Laura Moreno et al. "Logarithmic conformation reformulation in viscoelastic flow problems approximated by a VMS-type stabilized finite element formulation." In: *Computer Methods in Applied Mechanics and Engineering* 354 (2019). Publisher: Elsevier, pp. 706–731 (cited on pages 68, 69, 123, 139, 178).

[116] Inocencio Castañar, Ramon Codina, and Joan Baiges. "A stabilized mixed three-field formulation for stress accurate analysis including the incompressible limit in finite strain solid dynamics." In: *International Journal for Numerical Methods in Engineering* 124.10 (2023). tex.eprint: https://onlinelibrary.wiley.com/doi/pdf/10.1002/nme.7213, pp. 2341–2366. DOI: https://doi.org/10.1002/nme.7213 (cited on pages 68, 69, 123, 124, 130, 145, 169, 175).

[117] Arnau Fabra and Ramon Codina. "Mixed stabilized finite element methods in linear elasticity for the velocity–stress equations in the time and the frequency domains." In: *Computer Methods in Applied Mechanics and Engineering* 404 (2023). Publisher: Elsevier, p. 115777 (cited on pages 68, 69, 123, 124).

[118] Ramon Codina. "Finite element approximation of the three-field formulation of the Stokes problem using arbitrary interpolations." In: *SIAM Journal on Numerical Analysis* 47.1 (2009). Publisher: SIAM, pp. 699–718. DOI: https://doi.org/10.1137/080712726 (cited on pages 68, 70, 138, 177).

[119] Kyuichiro Washizu. "Variational methods in elasticity and plasticity." In: *International Series of Monographs in Aeronautics and Astronautics* (1968). Publisher: Pergamon press (cited on pages 69, 70, 72).

[120] D. Boffi, F. Brezzi, and M. Fortin. *Mixed finite element methods and applications*. Springer, 2013 (cited on page 85).

[121] Miguel Cervera, M Chiumenti, and R26721221231 Codina. "Mixed stabilized finite element methods in nonlinear solid mechanics: Part I: Formulation." In: *Computer Methods in Applied Mechanics and Engineering* 199.37-40 (2010). Publisher: Elsevier, pp. 2559–2570 (cited on pages 85, 87, 138).

[122] Savvas Saloustros et al. "Accurate and locking-free analysis of beams, plates and shells using solid elements." In: *Computational Mechanics* 67.3 (2021). Publisher: Springer, pp. 883–914 (cited on pages 85, 91, 102, 130).

[123] Ralf Hauptmann, Karl Schweizerhof, and Stefan Doll. "Extension of the 'solid-shell' concept for application to large elastic and large elastoplastic deformations." In: *International Journal for Numerical Methods in Engineering* 49.9 (2000). Publisher: Wiley Online Library, pp. 1121–1141 (cited on page 92).

[124] Hexin Zhang and Jun Shang Kuang. "Eight-node Reissner–Mindlin plate element based on boundary interpolation using Timoshenko beam function." In: *International Journal for Numerical Methods in Engineering* 69.7 (2007). Publisher: Wiley Online Library, pp. 1345–1373 (cited on page 93).

[125] A Aguirre, R Codina, and J Baiges. "A variational multiscale stabilized finite element formulation for Reissner–Mindlin plates and Timoshenko beams." In: *Finite Elements in Analysis and Design* 217 (2023). Publisher: Elsevier, p. 103908 (cited on pages 93, 98, 123, 124).

[126] Richard H Macneal and Robert L Harder. "A proposed standard set of problems to test finite element accuracy." In: *Finite elements in analysis and design* 1.1 (1985). Publisher: Elsevier, pp. 3–20 (cited on pages 100, 104, 107).

[127] Ted Belytschko et al. "Stress projection for membrane and shear locking in shell finite elements." In: *Computer Methods in Applied Mechanics and Engineering* 51.1-3 (1985). Publisher: Elsevier, pp. 221–258 (cited on page 100).

[128] Juan C Simo and David D Fox. "On a stress resultant geometrically exact shell model. Part I: Formulation and optimal parametrization." In: *Computer Methods in Applied Mechanics and Engineering* 72.3 (1989). Publisher: Elsevier, pp. 267–304 (cited on page 102).

[129] Ted Belytschko, Bak Leong Wong, and Henryk Stolarski. "Assumed strain stabilization procedure for the 9-node Lagrange shell element." In: *International Journal for Numerical Methods in Engineering* 28.2 (1989). Publisher: Wiley Online Library, pp. 385–414 (cited on page 102).

[130] N. Nguyen-Thanh et al. "A smoothed finite element method for shell analysis." In: *Computer Methods in Applied Mechanics and Engineering* 198.2 (Dec. 2008), pp. 165–177. DOI: 10.1016/j.cma.2008.05.029. (Visited on 03/01/2024) (cited on page 114).

[131] Xavier J-G Élie-Dit-Cosaque, Augustin Gakwaya, and Hakim Naceur. "Smoothed finite element method implemented in a resultant eight-node solid-shell element for geometrical linear analysis." en. In: *Computational Mechanics* 55.1 (Jan. 2015), pp. 105–126. DOI: 10.1007/s00466-014-1085-2. (Visited on 02/28/2024) (cited on page 114).

[132] *An improved solid-shell element based on ANS and EAS concepts - Mostafa - 2016 - International Journal for Numerical Methods in Engineering - Wiley Online Library*. URL: https://onlinelibrary.wiley.com/doi/abs/10.1002/nme.5260 (visited on 02/28/2024) (cited on page 114).

[133] Milan Wallner, Carolin Birk, and Hauke Gravenkamp. "A scaled boundary finite element approach for shell analysis." In: *Computer Methods in Applied Mechanics and Engineering* 361 (Apr. 2020), p. 112807. DOI: 10.1016/j.cma.2019.112807. (Visited on 03/01/2024) (cited on page 114).

[134] Zhen Lei, Frederic Gillot, and Louis Jezequel. "An isogeometric Reissner–Mindlin shell element based on mixed grid." In: *Advances in Mechanical Engineering* 10.4 (2018). Publisher: SAGE Publications Sage UK: London, England, p. 1687814018766997 (cited on page 114).

[135] Sven Klinkel, Friedrich Gruttmann, and Werner Wagner. “A robust non-linear solid shell element based on a mixed variational formulation.” In: *Computer methods in applied mechanics and engineering* 195.1-3 (2006). Publisher: Elsevier, pp. 179–201 (cited on page 121).

[136] Jože Korelc, Urša Šolinc, and Peter Wriggers. “An improved EAS brick element for finite deformation.” en. In: *Computational Mechanics* 46.4 (Sept. 2010), pp. 641–659. DOI: 10.1007/s00466-010-0506-0. (Visited on 03/01/2024) (cited on page 121).

[137] G. Kikis and S. Klinkel. “Two-field formulations for isogeometric Reissner–Mindlin plates and shells with global and local condensation.” en. In: *Computational Mechanics* 69.1 (Jan. 2022), pp. 1–21. DOI: 10.1007/s00466-021-02080-8. (Visited on 03/01/2024) (cited on page 122).

[138] M Braun, M Bischoff, and E Ramm. “Nonlinear shell formulations for complete three-dimensional constitutive laws including composites and laminates.” In: *Computational Mechanics* 15.1 (1994). Publisher: Springer, pp. 1–18 (cited on page 122).

[139] Boštjan Brank, Jože Korelc, and Adnan Ibrahimbegović. “Nonlinear shell problem formulation accounting for through-the-thickness stretching and its finite element implementation.” In: *Computers & structures* 80.9-10 (2002). Publisher: Elsevier, pp. 699–717 (cited on pages 122, 152).

[140] Jie Zhang, Donghuan Liu, and Yinghua Liu. “Degenerated shell element with composite implicit time integration scheme for geometric nonlinear analysis.” In: *International Journal for Numerical Methods in Engineering* 105.7 (2016). Publisher: Wiley Online Library, pp. 483–513 (cited on page 122).

[141] E. M. B. Campello, P. M. Pimenta, and P. Wriggers. “An exact conserving algorithm for nonlinear dynamics with rotational DOFs and general hyperelasticity. Part 2: shells.” en. In: *Computational Mechanics* 48.2 (Aug. 2011), pp. 195–211. DOI: 10.1007/s00466-011-0584-7. (Visited on 03/01/2024) (cited on page 122).

[142] P. M. Pimenta, E. M. B. Campello, and P. Wriggers. “A fully nonlinear multi-parameter shell model with thickness variation and a triangular shell finite element.” en. In: *Computational Mechanics* 34.3 (Aug. 2004), pp. 181–193. DOI: 10.1007/s00466-004-0564-2. (Visited on 03/01/2024) (cited on page 122).

[143] F. Gruttmann and W. Wagner. “An advanced shell model for the analysis of geometrical and material nonlinear shells.” en. In: *Computational Mechanics* 66.6 (Dec. 2020), pp. 1353–1376. DOI: 10.1007/s00466-020-01905-2. (Visited on 03/01/2024) (cited on pages 122, 123, 154).

[144] Werner Wagner and Friedrich Gruttmann. “An improved quadrilateral shell element based on the Hu–Washizu functional.” In: *Advanced Modeling and Simulation in Engineering Sciences* 7.1 (June 2020), p. 28. DOI: 10.1186/s40323-020-00162-5. (Visited on 03/01/2024) (cited on pages 122, 123, 154).

[145] Daniele Boffi, Franco Brezzi, Michel Fortin, et al. *Mixed finite element methods and applications*. Vol. 44. Springer, 2013 (cited on pages 123, 135, 163, 175).

[146] Ernesto Castillo and Ramon Codina. "Dynamic term-by-term stabilized finite element formulation using orthogonal subgrid-scales for the incompressible Navier–Stokes problem." In: *Computer Methods in Applied Mechanics and Engineering* 349 (2019). Publisher: Elsevier, pp. 701–721. DOI: https://doi.org/10.1016/j.cma.2019.02.041 (cited on page 123).

[147] Inocencio Castañar et al. "Topological derivative-based topology optimization of incompressible structures using mixed formulations." In: *Computer Methods in Applied Mechanics and Engineering* 390 (2022). Publisher: Elsevier, p. 114438 (cited on pages 123, 124, 218).

[148] Michele Chiumenti, Miguel Cervera, and Ramon Codina. "A mixed three-field FE formulation for stress accurate analysis including the incompressible limit." In: *Computer Methods in Applied Mechanics and Engineering* 283 (2015). Publisher: Elsevier, pp. 1095–1116 (cited on pages 130, 138).

[149] Camilo Andrés Bayona Roa, Joan Baiges, and Ramon Codina. "Variational multiscale finite element approximation of the compressible Navier-Stokes equations." In: *International Journal of Numerical Methods for Heat & Fluid Flow* 26.3/4 (2016). Publisher: Emerald Group Publishing Limited, pp. 1240–1271 (cited on page 138).

[150] Javier Bonet et al. "A first order hyperbolic framework for large strain computational solid dynamics. Part I: Total Lagrangian isothermal elasticity." In: *Computer Methods in Applied Mechanics and Engineering* 283 (2015). Publisher: Elsevier, pp. 689–732 (cited on page 145).

[151] Antonio J Gil et al. "A first order hyperbolic framework for large strain computational solid dynamics. Part II: Total Lagrangian compressible, nearly incompressible and truly incompressible elasticity." In: *Computer Methods in Applied Mechanics and Engineering* 300 (2016). Publisher: Elsevier, pp. 146–181 (cited on page 145).

[152] Yavuz Başar and Yunhe Ding. "Finite-rotation elements for the non-linear analysis of thin shell structures." In: *International Journal of Solids and Structures* 26.1 (1990). Publisher: Elsevier, pp. 83–97 (cited on page 148).

[153] Zhi Li et al. "An unsymmetric 8-node hexahedral solid-shell element with high distortion tolerance: Geometric nonlinear formulations." In: *International Journal for Numerical Methods in Engineering* 120.5 (2019). Publisher: Wiley Online Library, pp. 580–606 (cited on pages 149, 150).

[154] KY Sze, WK Chan, and THH Pian. "An eight-node hybrid-stress solid-shell element for geometric non-linear analysis of elastic shells." In: *International Journal for Numerical Methods in Engineering* 55.7 (2002). Publisher: Wiley Online Library, pp. 853–878 (cited on pages 149, 150, 154).

[155] Josef Kiendl et al. "Isogeometric Kirchhoff–Love shell formulations for general hyperelastic materials." In: *Computer Methods in Applied Mechanics and Engineering* 291 (2015). Publisher: Elsevier, pp. 280–303 (cited on page 152).

[156] Nielen Stander, Anton Matzenmiller, and Ekkehard Ramm. "An assessment of assumed strain methods in finite rotation shell analysis." In: *Engineering Computations* (1989). Publisher: MCB UP Ltd (cited on page 153).

[157] Paola Causin, Jean-Frédéric Gerbeau, and Fabio Nobile. "Added-mass effect in the design of partitioned algorithms for fluid–structure problems." In: *Computer methods in applied mechanics and engineering* 194.42-44 (2005). Publisher: Elsevier, pp. 4506–4527 (cited on page 160).

[158] Yue Yu, Hyoungsu Baek, and George Em Karniadakis. "Generalized fictitious methods for fluid–structure interactions: Analysis and simulations." In: *Journal of Computational Physics* 245 (2013). Publisher: Elsevier, pp. 317–346 (cited on pages 160, 161).

[159] E Harald van Brummelen. "Added mass effects of compressible and incompressible flows in fluid-structure interaction." In: *Journal of Applied mechanics* 76.2 (2009). Publisher: American Society of Mechanical Engineers Digital Collection (cited on page 160).

[160] Sergio R Idelsohn et al. "Fluid–structure interaction problems with strong added-mass effect." In: *International journal for numerical methods in engineering* 80.10 (2009). Publisher: Wiley Online Library, pp. 1261–1294 (cited on page 160).

[161] Fabio Nobile. *Numerical approximation of fluid-structure interaction problems with application to haemodynamics*. Tech. rep. EPFL, 2001 (cited on page 160).

[162] Patrick Le Tallec and Jean Mouro. "Fluid structure interaction with large structural displacements." In: *Computer methods in applied mechanics and engineering* 190.24-25 (2001). Publisher: Elsevier, pp. 3039–3067 (cited on page 160).

[163] Matthew Hirschhorn et al. "Fluid–structure interaction modeling in cardiovascular medicine–A systematic review 2017–2019." In: *Medical Engineering & Physics* (2020). Publisher: Elsevier (cited on page 160).

[164] Michael S Sacks, W David Merryman, and David E Schmidt. "On the biomechanics of heart valve function." In: *Journal of biomechanics* 42.12 (2009). Publisher: Elsevier, pp. 1804–1824 (cited on page 160).

[165] Charbel Farhat, Kristoffer G Van der Zee, and Philippe Geuzaine. "Provably second-order time-accurate loosely-coupled solution algorithms for transient nonlinear computational aeroelasticity." In: *Computer methods in applied mechanics and engineering* 195.17-18 (2006). Publisher: Elsevier, pp. 1973–2001 (cited on page 161).

[166] Ramji Kamakoti and Wei Shyy. "Fluid–structure interaction for aeroelastic applications." In: *Progress in Aerospace Sciences* 40.8 (2004). Publisher: Elsevier, pp. 535–558 (cited on page 161).

[167] Guru P Guruswamy. "A review of numerical fluids/structures interface methods for computations using high-fidelity equations." In: *Computers & structures* 80.1 (2002). Publisher: Elsevier, pp. 31–41 (cited on page 161).

[168] Rainald Loehner et al. "Fluid-structure-thermal interaction using a loose coupling algorithm and adaptive unstructured grids." In: *29th AIAA, fluid dynamics conference*. 1998, p. 2419 (cited on page 161).

[169] Woojin Kim and Haecheon Choi. "Immersed boundary methods for fluid-structure interaction: A review." In: *International Journal of Heat and Fluid Flow* 75 (2019). Publisher: Elsevier, pp. 301–309 (cited on page 161).

[170] Cyrill W Hirt, Anthony A Amsden, and JL Cook. "An arbitrary Lagrangian-Eulerian computing method for all flow speeds." In: *Journal of computational physics* 14.3 (1974). Publisher: Elsevier, pp. 227–253 (cited on page 161).

[171] Tayfun E Tezduyar et al. "A new strategy for finite element computations involving moving boundaries and interfaces-the deforming-spatial-domain/space-time procedure: II. Computation of free-surface flows, two-liquid flows, and flows with drifting cylinders." In: *Computer methods in applied mechanics and engineering* 94.3 (1992). Publisher: Elsevier, pp. 353–371 (cited on page 161).

[172] Charles Peskin. "Flow patterns around heart valves: a digital computer method for solving the equations of motion." In: *IEEE transactions on biomedical engineering* 4 (1973). Publisher: IEEE Computer Society, pp. 316–317 (cited on pages 161, 162).

[173] HS Udaykumar, Wei Shyy, and MM Rao. "Elafint: a mixed Eulerian–Lagrangian method for fluid flows with complex and moving boundaries." In: *International journal for numerical methods in fluids* 22.8 (1996). Publisher: Wiley Online Library, pp. 691–712 (cited on page 161).

[174] Th Dunne. "An Eulerian approach to fluid–structure interaction and goal-oriented mesh adaptation." In: *International journal for numerical methods in fluids* 51.9-10 (2006). Publisher: Wiley Online Library, pp. 1017–1039 (cited on page 161).

[175] Joan Baiges and Camilo Bayona. "Refficientlib: an efficient load-rebalanced adaptive mesh refinement algorithm for high-performance computational physics meshes." In: *SIAM journal on scientific computing* 39.2 (2017). Publisher: SIAM, pp. C65–C95 (cited on pages 161, 162).

[176] Dong Han, GR Liu, and Shaaban Abdallah. "An Eulerian–Lagrangian–Lagrangian method for solving thin moving rigid body immersed in the fluid." In: *Computers & Fluids* 179 (2019). Publisher: Elsevier, pp. 687–701 (cited on pages 161, 162).

[177] Fotis Sotiropoulos and Xiaolei Yang. "Immersed boundary methods for simulating fluid–structure interaction." In: *Progress in Aerospace Sciences* 65 (2014). Publisher: Elsevier, pp. 1–21 (cited on page 162).

[178] EA Fadlun et al. "Combined immersed-boundary finite-difference methods for three-dimensional complex flow simulations." In: *Journal of computational physics* 161.1 (2000). Publisher: Citeseer, pp. 35–60 (cited on page 162).

[179] Nicholas K-R Kevlahan and Jean-Michel Ghidaglia. "Computation of turbulent flow past an array of cylinders using a spectral method with Brinkman penalization." In: *European Journal of Mechanics-B/Fluids* 20.3 (2001). Publisher: Elsevier, pp. 333–350 (cited on page 162).

[180] MP Kirkpatrick, SW Armfield, and JH Kent. "A representation of curved boundaries for the solution of the Navier–Stokes equations on a staggered three-dimensional Cartesian grid." In: *Journal of Computational Physics* 184.1 (2003). Publisher: Elsevier, pp. 1–36 (cited on page 162).

[181] Randall J Leveque and Zhilin Li. "The immersed interface method for elliptic equations with discontinuous coefficients and singular sources." In: *SIAM Journal on Numerical Analysis* 31.4 (1994). Publisher: SIAM, pp. 1019–1044 (cited on page 162).

[182] Liang Ge and Fotis Sotiropoulos. "A numerical method for solving the 3D unsteady incompressible Navier–Stokes equations in curvilinear domains with complex immersed boundaries." In: *Journal of computational physics* 225.2 (2007). Publisher: Elsevier, pp. 1782–1809 (cited on page 162).

[183] Ivo Babuška. "The finite element method with penalty." en. In: *Mathematics of Computation* 27.122 (1973), pp. 221–228. DOI: 10.1090/S0025-5718-1973-0351118-5. (Visited on 03/20/2024) (cited on page 162).

[184] Kazufumi Ito and Karl Kunisch. *Lagrange Multiplier Approach to Variational Problems and Applications*. en. SIAM, Jan. 2008 (cited on page 162).

[185] J. Nitsche. "Über ein Variationsprinzip zur Lösung von Dirichlet-Problemen bei Verwendung von Teilräumen, die keinen Randbedingungen unterworfen sind." de. In: *Abhandlungen aus dem Mathematischen Seminar der Universität Hamburg* 36.1 (July 1971), pp. 9–15. DOI: 10.1007/BF02995904. (Visited on 03/20/2024) (cited on pages 162, 163).

[186] Peter Hansbo. "Nitsche's method for interface problems in computa-tional mechanics." en. In: *GAMM-Mitteilungen* 28.2 (2005). _eprint: https://onlinelibrary.wiley.com/doi/pdf/10.100 pp. 183–206. DOI: 10.1002/gamm.201490018. (Visited on 03/20/2024) (cited on pages 162, 163).

[187] Anita Hansbo and Peter Hansbo. "A finite element method for the simulation of strong and weak discontinuities in solid mechanics." en. In: *Computer Methods in Applied Mechanics and Engineering* 193.33-35 (Aug. 2004), pp. 3523–3540. DOI: 10.1016/j.cma.2003.12.041. (Visited on 03/20/2024) (cited on pages 162, 163).

[188] Erik Burman et al. "CutFEM: Discretizing geometry and partial differential equations." en. In: *International Journal for Numerical Methods in Engineering* 104.7 (2015). _eprint: https://onlinelibrary.wiley.com/doi/pdf/10.1002/nme.4823, pp. 472–501. DOI: 10.1002/nme.4823. (Visited on 03/20/2024) (cited on pages 162, 163).

[189] Erik Burman and Peter Hansbo. "Fictitious domain finite element methods using cut elements: II. A stabilized Nitsche method." en. In: *Applied Numerical Mathematics* 62.4 (Apr. 2012), pp. 328–341. DOI: 10.1016/j.apnum.2011.01.008. (Visited on 03/20/2024) (cited on pages 162, 163).

[190] Alejandro Aguirre, Ramon Codina, and Joan Baiges. "Stress-displacement stabilized finite element analysis of thin structures using solid-shell elements - Part I: On the need of interpolating the stresses." In: *Submitted* (Aug. 2023) (cited on pages 162–164, 169, 175, 212).

[191] Alejandro Aguirre et al. "Stress-displacement stabilized finite element analysis of thin structures using Solid-Shell elements - Part II: Finite strain hyperelasticity." In: *Submitted* (Aug. 2023) (cited on pages 162, 163, 169, 212).

[192] Santiago Badia and Ramon Codina. "Unified Stabilized Finite Element Formulations for the Stokes and the Darcy Problems." In: *SIAM Journal on Numerical Analysis* 47.3 (Jan. 2009). Publisher: Society for Industrial and Applied Mathematics, pp. 1971–2000. DOI: 10.1137/08072632X. (Visited on 04/12/2024) (cited on page 177).

[193] Samuel Parada, Joan Baiges, and Ramon Codina. "A fractional step method for computational aeroacoustics using weak imposition of Dirichlet boundary conditions." In: *Computers & Fluids* 197 (Jan. 2020), p. 104374. DOI: 10.1016/j.compfluid.2019.104374. (Visited on 02/15/2024) (cited on page 178).

[194] Ramon Codina et al. "Variational Multiscale Methods in Computational Fluid Dynamics." en. In: *Encyclopedia of Computational Mechanics Second Edition*. _eprint: https://onlinelibrary.wiley.com/doi/pdf/10.1002/9781119176817.ecm2117. John Wiley & Sons, Ltd, 2017, pp. 1–28. DOI: 10.1002/9781119176817.ecm2117. (Visited on 02/15/2024) (cited on page 178).

[195] Roberto F Ausas, Fabricio S Sousa, and Gustavo C Buscaglia. "An improved finite element space for discontinuous pressures." In: *Computer Methods in Applied Mechanics and Engineering* 199.17-20 (2010). Publisher: Elsevier, pp. 1019–1031 (cited on pages 179, 181).

[196] A. H. Coppola-Owen and R. Codina. "Improving Eulerian two-phase flow finite element approximation with discontinuous gradient pressure shape functions." en. In: *International Journal for Numerical Methods in Fluids* 49.12 (Dec. 2005), pp. 1287–1304. DOI: 10.1002/fld.963. (Visited on 03/17/2024) (cited on page 185).

[197] Ramon Codina and Santiago Badia. "On the design of discontinuous Galerkin methods for elliptic problems based on hybrid formulations." In: *Computer Methods in Applied Mechanics and Engineering* 263 (Aug. 2013), pp. 158–168. DOI: 10.1016/j.cma.2013.05.004. (Visited on 04/11/2024) (cited on pages 186, 187).

[198] S. Badia et al. "Error analysis of discontinuous Galerkin methods for the Stokes problem under minimal regularity." In: *IMA Journal of Numerical Analysis* 34.2 (Apr. 2014). Conference Name: IMA Journal of Numerical Analysis, pp. 800–819. DOI: 10.1093/imanum/drt022. (Visited on 04/11/2024) (cited on page 186).

[199] R Zorrilla, A Larese, and Riccardo Rossi. "A modified finite element formulation for the imposition of the slip boundary condition over embedded volumeless geometries." In: *Computer methods in applied mechanics and engineering* 353 (2019). Publisher: Elsevier, pp. 123–157 (cited on pages 187, 195).

[200] Rubén Zorrilla et al. "An embedded Finite Element framework for the resolution of strongly coupled Fluid–Structure Interaction problems. Application to volumetric and membrane-like structures." In: *Computer Methods in Applied Mechanics and Engineering* 368 (2020). Publisher: Elsevier, p. 113179 (cited on pages 187, 195, 200).

[201] Nicolas Delaissé et al. "Quasi-Newton Methods for Partitioned Simulation of Fluid–Structure Interaction Reviewed in the Generalized Broyden Framework." en. In: *Archives of Computational Methods in Engineering* 30.5 (June 2023), pp. 3271–3300. DOI: 10.1007/s11831-023-09907-y. (Visited on 03/20/2024) (cited on page 187).

[202] Rubén Zorrilla, Antonia Larese de Tetto, and Riccardo Rossi. "A discontinuous Nitsche-based finite element formulation for the imposition of the Navier-slip condition over embedded volumeless geometries." In: *International Journal for Numerical Methods in Fluids* 93.9 (2021). Publisher: Wiley Online Library, pp. 2968–3003 (cited on pages 195–197, 199, 200).

[203] Sergio R Idelsohn, Juan M Gimenez, and Norberto M Nigro. "Multifluid flows with weak and strong discontinuous interfaces using an elemental enriched space." In: *International Journal for Numerical Methods in Fluids* 86.12 (2018). Publisher: Wiley Online Library, pp. 750–769 (cited on page 196).

[204] Zhi-Qian Zhang, G. R. Liu, and Boo Cheong Khoo. "Immersed smoothed finite element method for two dimensional fluid–structure interaction problems." en. In: *International Journal for Numerical Methods in Engineering* 90.10 (2012). _eprint: https://onlinelibrary.wiley.com/doi/pdf/10.1002/nme.4299, pp. 1292–1320. DOI: 10.1002/nme.4299. (Visited on 03/07/2024) (cited on pages 204, 206, 208).

[205] Dong Han, GR Liu, and Shaaban Abdallah. "ELL for 3D FSI problems with thin flexible structures based on the continuum-based shell element." In: *Journal of Fluids and Structures* 103 (2021). Publisher: Elsevier, p. 103281 (cited on pages 204, 206, 208).

[206] Dong Han, GR Liu, and Shaaban Abdallah. "An Eulerian-Lagrangian-Lagrangian method for 2D fluid-structure interaction problem with a thin flexible structure immersed in fluids." In: *Computers & Structures* 228 (2020). Publisher: Elsevier, p. 106179 (cited on pages 206, 208).

[207] Stefan Turek and Jaroslav Hron. "Proposal for Numerical Benchmarking of Fluid-Structure Interaction between an Elastic Object and Laminar Incompressible Flow." en. In: *Fluid-Structure Interaction*. Ed. by Hans-Joachim Bungartz and Michael Schäfer. Lecture Notes in Computational Science and Engineering. Berlin, Heidelberg: Springer, 2006, pp. 371–385. DOI: 10.1007/3-540-34596-5_15 (cited on pages 208, 210, 211).

[208] E. Castillo and R. Codina. "First, second and third order fractional step methods for the three-field viscoelastic flow problem." In: *Journal of Computational Physics* 296 (Sept. 2015), pp. 113–137. DOI: 10.1016/j.jcp.2015.04.027. (Visited on 03/23/2024) (cited on page 218).

[209] Marreddy Ambati, Josef Kiendl, and Laura De Lorenzis. "Isogeometric Kirchhoff–Love shell formulation for elasto-plasticity." en. In: *Computer Methods in Applied Mechanics and Engineering* 340 (Oct. 2018), pp. 320–339. DOI: 10.1016/j.cma.2018.05.023. (Visited on 04/16/2024) (cited on page 218).

[210] Mohamad S. Qatu, Rani Warsi Sullivan, and Wenchao Wang. "Recent research advances on the dynamic analysis of composite shells: 2000–2009." en. In: *Composite Structures* 93.1 (Dec. 2010), pp. 14–31. DOI: 10.1016/j.compstruct.2010.05.014. (Visited on 04/16/2024) (cited on page 219).

[211] J. Stegmann and E. Lund. "Discrete material optimization of general composite shell structures." en. In: *International Journal for Numerical Methods in Engineering* 62.14 (Apr. 2005), pp. 2009–2027. DOI: 10.1002/nme.1259. (Visited on 04/16/2024) (cited on page 219).